THE UNIVERSITY OF OKLAHOMA

GRADUATE COLLEGE

HYDRAULIC FRACTURING OF POORLY CONSOLIDATED FORMATIONS: CONSIDERATIONS ON ROCK PROPERTIES AND FAILURE MECHANISMS

A DISSERTATION

SUBMITTED TO THE GRADUATE FACULTY

In partial fulfillment of the requirements for the

degree of

DOCTOR OF PHILOSOPHY

by

IVAN GIL

Norman, Oklahoma

2005

Downloaded from SHAREOK. Persistent Handle URL: https://hdl.handle.net/11244/818

UMI Number: 3152841



UMI Microform 3152841

Copyright 2005 by ProQuest Information and Learning Company.
All rights reserved. This microform edition is protected against unauthorized copying under Title 17, United States Code.

ProQuest Information and Learning Company
300 North Zeeb Road
P.O. Box 1346
Ann Arbor, MI 48106-1346

HYDRAULIC FRACTURING OF POORLY CONSOLIDATED FORMATIONS: CONSIDERATIONS ON ROCK PROPERTIES AND FAILURE MECHANISMS

A DISSERTATION APPROVED FOR THE

MEWBOURNE SCHOOL OF PETROLEUM AND GEOLOGICAL ENGINEERING

BY

_____

Dr. Jean-Claude Roegiers (Chairman)

_____

Dr. Richard Hughes

_____

Dr. Roy Knapp

_____

Dr. Subhash Shah

_____

Dr. Luther White

© Copyright by Ivan Gil, 2005

All Rights Reserved

To my parents and unconditional friends, who taught me that anything is possible; thank you Luis and Dora

To Sandra, my support and partner in life

To a little bundle of energy and source of inspiration called Gabriel

To my sister Adriana and my brother Ronald

Acknowledgements

I would like to express my heartfelt appreciation and gratitude to Dr. Jean-Claude Roegiers, my advisor and mentor. His support, guidance, and encouragement made the completion of my studies possible. It was through him that I started enjoying the absorbing world of rock mechanics. I have been honored to receive from Dr. Roegiers, priceless lessons in both technical and personal aspects. Throughout my work with him, I have certainly grown both as a professional and as a human being. I sincerely hope that many more generations of rock mechanics professionals have the opportunity of being inspired by his infectious enthusiasm and generosity.

Thanks are also due to Dr. Richard Hughes, Dr. Roy Knapp, Dr. Subhash Shah, and Dr. Luther White for kindly consenting to serve as members of my doctoral advisory committee.

I am also deeply indebted to many individuals and institutions, and the contributions of some are mentioned with grateful appreciation. Chyrl Yerdon, Debbie Sipes, Lisa Parks, and Mike Shaw at the MPGE for their friendship and

always welcomed help. The Mewbourne School of Petroleum and Geological Engineering for its financial assistance during the last few years.

Last, but certainly not least, I would like to thank my wife, Sandra, and my son Gabriel, for their patience, understanding, and sacrifices, without which the completion of this study would not have been possible.

Contents

1 Introduction 1

2 Unconsolidated formations – physical properties 4

2.1 Pore compressibility 4
2.2 Porosity and Permeability 7
2.3 Pore Pressure Characteristics 27
2.4 Deformation Behavior of Unconsolidated Rocks 29
2.4.1 Uniaxial Compression Strength 30
2.4.2 Strength as function of confining pressure - Triaxial Compression Tests 32
2.4.3 Elastic moduli and their dependency on applied stress 36
2.4.4 Shear Strength 46
2.4.5 Creep 50
2.5 Effects of changes in saturation on rock mechanical properties 56
2.6 Comments on the mechanical properties of unconsolidated rocks 75

3 Reliability of the measurement of mechanical properties in unconsolidated formations 86

3.1 Core Damage Caused by Stress Relaxation 88
3.2 Core Damage Induced by Freezing 96
3.2.1 Background on Soil/Rock Freezing 97
3.2.2 General experimental results on the effect of freezing / thawing on rock mechanical behavior 107
3.2.3 Influence of mineralogy on frost alteration of the rock 112
3.2.4 Influence of freezing rate on frost heaving 114
3.2.5 Influence of freezing direction on measured rock properties 118
3.3 Comments on the reliability of the measured rock properties from unconsolidated cores 124

4 Hydraulic fracturing stimulation in poorly consolidated, highly-permeable formations.....129

4.1 OPERATIONAL PROBLEMS COMMONLY ASSOCIATED WITH POORLY CONSOLIDATED FORMATIONS..... 129
4.1.1 Problems during drilling..... 130
4.1.2 Problems during production..... 139
4.1.3 Problems during stimulation..... 151
4.2 STANDARD HYDRAULIC FRACTURING SIMULATORS 158
4.2.1 Hydraulic fracturing simulators based on linear elastic fracture mechanics..... 164
4.2.1.1 FracproPT®: 165
4.2.1.2 MFrac®:..... 173
4.2.1.3 Stimplan®:..... 179
4.2.2 Alternative approaches to hydraulic fracture propagation..... 184
4.2.2.1 Continuum Damage Mechanics (Valkó and Economides, 1993): 184
4.2.2.2 Apparent Fracture Toughness (Shlyapobersky et al., 1988):.. 185
4.2.2.3 Crack-Layer and Process Zone Model (Chudnovski et al., 1996): 189
4.2.2.4 Crack Tip Plasticity (Martin, 2000):..... 190
4.3 PROPOSED APPROACH 191
4.3.1 The Discrete Element Method (DEM) 192
4.3.2 General formulation in PFC^{3D}..... 196
4.3.2.1 Law of motion..... 203
4.3.2.2 Contact constitutive method 204
4.3.2.3 Bonding models 204
4.3.2.4 Fluid flow coupling..... 209
4.3.2.5 Advantages of PFC^{3D} 212
4.3.2.6 Limitations of PFC^{3D} 212

5 Hydraulic fracturing modeling using PFC^{3D} 214

5.1 OBJECTIVES OF THIS MODELING STUDY..... 215
5.2 NATURE OF THE CONSTRUCTED MODELS..... 215
5.3 PROBLEM-SPECIFIC DATA SETS 216
5.3.1 Antler sandstone - Core model 217
5.3.1.1 Model particle size distribution and porosity - Validation 217
5.3.1.2 Mechanical properties of the model - Validation 222
5.3.1.3 Comments on the validation of the model mechanical properties 239

5.3.1.4 Hydraulic properties of the model - Validation 244
5.3.1.5 Comments of the validation of the model hydraulic properties ……..251
5.3.2 Antler sandstone - Field model 252
5.3.2.1 Testing and results 257
5.3.2.2 Comments on the results obtained from the field model 265

6 Conclusions 268

7 Recommendations.....281

References 285

APPENDIX A – Fish routines used during the validation of the model mechanical properties.....300

APPENDIX B – Fish routines used during the validation of the model hydraulic properties 307

APPENDIX C – Fish routines used during the hydraulic fracturing tests.....335

APPENDIX D – Results of numerical experiments using the field model.....347

List of Figures

Figure 2-1. Pore volume compressibility vs. applied stress, GOM sample (after Ostermeier, 1993). 6
Figure 2-2. Pore volume compressibility as a function of mean effective stress, unidentified unconsolidated sample (after Pauget et al., 2002) 6
Figure 2-3. Comparison of porosity reduction as function of the amount of cement, for two rocks at different depths (after Scherer, 1987). 8
Figure 2-4. Compressional and shear wave velocities as a function of porosity, in dry frozen unconsolidated Otawa sand, poorly consolidated, and Berea sandstone samples (data from Tutuncu et al., 1997)..... 9
Figure 2-5. Effect of pore pressure on porosity gradient – South Louisiana sandstones (after Selley, 1978). 11
Figure 2-6. Porosity and permeability vs. time as response to applied effective stress, GOM sample (after Ostermeier, 1993). 12
Figure 2-7. Measured oil permeability vs. porosity, GOM sample (after Ostermeier, 1993). 14
Figure 2-8. Porosity as function of differential pressure - North Sea samples; data from Domenico (1977), Sclater and Christie (1980), and Prasad (2002). 15
Figure 2-9. Porosity prediction for North Sea unconsolidated sandstones (after Scherer, 1987). 15
Figure 2-10. Effect of isostatic stress cycling on rock porosity, unconsolidated samples from the GOM (after Ostermeier, 1993). 16
Figure 2-11. Porosity vs. vertical depth – a). Northern Adriatic Basin (data from Marsala et al., 1994); b). Highly over-pressured samples from the GOM (after Ostermeier et al.; 2001). 17
Figure 2-12. a). Oil permeability vs. median grain size, GOM sample (after Ostermeier, 1993); b). Oil permeability vs. (median grain size/std. dev.)^2 data from Ostermeier (1993). 18
Figure 2-13. Thin section and its corresponding grain size distribution, GOM sample (after Ostermeier, 1995). 18
Figure 2-14. . Relative Reduction in permeability when hydrostatic stress was increased from 500 to 5000 psi (data from Kilmer et al., 1987; Yale, 1984; and Holt, 1990). 19

Figure 2-15. a). Axial and radial stress vs. axial strain during anisotropic loading of Red Wilmoor Sandstone ; b). Corresponding permeability, perpendicular to bedding (after Holt, 1990). 21
Figure 2-16. Salt Wash Sandstone - SEM image (after Bruno et al., 1991). 22
Figure 2-17. Castlegate Sandstone - SEM image (after Bruno et al., 1991)..... 23
Figure 2-18. Kern River Sandstone - SEM image (after Bruno et al., 1991). 23
Figure 2-19. Variation of permeability as function of axial and radial stresses, Castlegate Sandstone (after Bruno et al., 1991)..... 25
Figure 2-20. Variation of permeability as function of axial and radial stresses (constructed with data from Bruno et al., 1991). 26
Figure 2-21. Relative magnitude of shallow water flow hazard (after Ostermeier et al., 2001). 28
Figure 2-22. Sandstone strength and behavior as function of cementing material (after Jeremic, 1981). 29
Figure 2-23. UCS on unconsolidated sandstones, 1 mstr = 0.001 (modified from Wu and Tan, 2000). 31
Figure 2-24. Stress-strain curves of Antler Sandstone under different confining pressures (after Wang et al., 1995). 33
Figure 2-25. Variation of rock response as function of the confining stress (data from Morita and Ross, 1993). 34
Figure 2-26. Stress-strain relationships from triaxial tests – Western Taiwan sandstone samples (after Huang et al., 2000). 35
Figure 2-27. Stress-strain relationships from triaxial tests, brittle to ductile transition (after Marsala et al., 1994). 36
Figure 2-28. Static and dynamic Poisson's ratio as function of shear stress (data from Larsen et al., 2000). 38
Figure 2-29. Dynamic Poisson's ratio as function of shear stress – North Sea samples (modified from Larsen et al., 2000). 39
Figure 2-30. Static vs. dynamic Young's moduli as function of stress – North Sea samples (after Fjær, 1999). 40
Figure 2-31. Young's modulus vs. effective mean stress for different values of K, starting at P_C=5400 psi and P_P=2000 psi (after Franquet and Economides, 1999). 42
Figure 2-32. Poisson's ratio vs. differential stress for different values of P_C with constant P_P=2000 psi (after Franquet and Economides, 1999) 43
Figure 2-33. "Strength" log showing the estimated values of cohesion and internal friction angle, IFA (after Ong et al., 2000). 44
Figure 2-34. Wave velocity ratio as function of differential pressure (after Lee, 2003) data from Prasad (2002); and Huffman and Castagna (2001). 45
Figure 2-35. Wave velocity ratio as function of shear wave velocity (after Lee, 2003) data from Prasad (2002); and Huffman and Castagna (2001). 46

Figure 2-36. New shear failure criterion – Sacramento River sand (after Ramamurthy, 2001). 49
Figure 2-37. New shear failure criterion – Chattahoochee River sand (after Ramamurthy, 2001). 50
Figure 2-38. Axial strain vs. time for three 750 psi axial stress step increase uniaxial creep tests on Brazos River samples, Max. axial stress = 8000 psi (after Dudley et al., 1998). 51
Figure 2-39. Axial strain vs. normalized time: a). Brazos River sand, same data as in Fig. 2.37; b). GOM reservoir sand for axial stress increment to 4300 psi (after Dudley et al., 1998) 52
Figure 2-40. Uniaxial compaction coefficient Cm vs. axial stress: a). Brazos River sand; b). GOM reservoir sand (after Dudley et al., 1998). 54
Figure 2-41. Constant load creep tests: a). Wilmington sand; and b).South Eugene Island sand (after Chang and Zoback, 1998). 55
Figure 2-42. Polyaxial creep test, South Eugene Island sand (after Chang and Zoback, 1998). 56
Figure 2-43. Dry and water saturated compressional and shear wave velocities at 30 MPa (4350 psi) (after Strandenes and Blangy, 1991) 57
Figure 2-44. Effect of non-aqueous phase saturation on compressional wave velocity (data from Seifert et al., 1998). 59
Figure 2-45. UCS vs. rock moisture content: Ecca series quartzitic sandstone, ϕ =15% (after Colback and Wiid, 1965). 59
Figure 2-46. Variation of the Coulomb failure envelope as a function of water saturation: a).Jeppestone quartzitic shale, ϕ=0.28%; and b). Ecca series quartzitic sandstone, ϕ=15% (after Colback and Wiid, 1965). 61
Figure 2-47. UCS reduction (related to its oil-saturated value) vs. water saturation; sandstone sample, initial oil-saturated UCS equal to 1,116 psi (data from Wu and Tan, 2001) 63
Figure 2-48. Results of a series of triaxial tests (dots) and uniaxial compression tests (squares), (after Rhett and Lord, 2001) 64
Figure 2-49. Sandstones UCS reduction (related to its dry value) as function of fluid saturation (data from Wu and Tan, 2001). 66
Figure 2-50. UCS of water-saturated and oven-dried vs. stress rate: a). Quartzite (98% quartz); and b). Pennant sandstone (50% quartz + 25% clay), (after Hadizadeh and Law, 1991). 66
Figure 2-51. UCS reduction vs. total clay content. Strength reduction is defined as percentage of oil-saturated strength (data from Wu and Tan, 2001). 67
Figure 2-52. Uniaxial compressive strength vs. surface tension of the saturating fluid (after Colback and Wiid, 1965). 70
Figure 2-53. Young's modulus reduction due to water saturation, UK sandstones (built with data from Hawkins and McConnell, 1992). 73

Figure 2-54. Interaction of water with quartz surfaces and associated surface free energy changes (after Parks, 1984). 74
Figure 2-55. Typical mechanical properties of unconsolidated sandstone (blue circle), plotted using Deer and Miller rock classification (Deer and Miller, 1966). 78
Figure 2-56. Average fracture width vs. fracture half length as a function of Young's modulus (modified from Franquet and Economides, 1999). 80
Figure 2-57. Average fracture width vs. fracture half length as a function of Poisson's ratio (after Franquet and Economides, 1999) 81
Figure 2-58. Variation of the magnitude of Young's modulus (left) and Poisson's ratio (right) as a fucntion of the applied differential stress (after Franquet and Economides, 1999). 83
Figure 3-1. CT Scan image of a damage non-cemented core (after Pauget et al., 2002). 88
Figure 3-2. Stress field applied on the rock at different stages of the coring process, valid only for vertical coring (after Pauget et al., 2002). 90
Figure 3-3. Stress paths defining the rock stress conditions: (Type A)"virgin" formation; and (Type B) standard stress history of cored sample, (after Holt et al., 1994). 92
Figure 3-4. Compaction curves for the samples simulating a North Sea Reservoir, cemented at 15 MPa and 7.5 MPa horizontal and vertical stresses (after Holt et al., 1994). 92
Figure 3-5. Stress path during coring and testing with constant vertical stress applied inside the core barrel (after Brignoli et al., 1998). 93
Figure 3-6. Effect of applied bias stress on the failure tendency of synthetic sands with in-built weakness planes (after Brignoli et al., 1998). 95
Figure 3-7. Axial stress vs. axial and radial strain during proportional loading ($\sigma_t=2\sigma_r$) of core samples from the Adriatic Sea (after Brignoli et al., 1998). 96
Figure 3-8. Extreme example of soil heaving: pipkrake near the trans-Alaska pipeline on Alaska's North Slope (in Davis, 2001) 98
Figure 3-9. Soil moisture characteristic curves for several clay samples (originally in Williams and Smith, 1989) 100
Figure 3-10. Soil freezing characteristic curves for several samples (originally in Williams and Smith, 1989) 100
Figure 3-11. Suction pressure as function of rock temperature, A). Data measured on fine-grained soils (originally in Williams and Smith, 1989); and B). Data measured on clay (original data from Dash et al., 1995) 102
Figure 3-12. Segregation ice forming in repeating layers, with thickness increasing with depth (in Davis, 2001) 104

Figure 3-13. a). Experimental setup for pore pressure measurement during rock freezing; and, b). typical results from the experiments (after Fukuda, 1983). 107
Figure 3-14. Effect of freezing and thawing on the UCS of several sandstones (data from Hale and Shakoor, 2003). 111
Figure 3-15. Effect of freezing and thawing on the UCS of several sandstones (data from Hale and Shakoor, 2003). 112
Figure 3-16. a).Segregation potential as a function of the mean particle size diameter for different lithologies; and b). Product of segregation potential and specific surface area vs. mean particle diameter (after Konrad, 2000). 114
Figure 3-17. Cumulative value of net heat flow and moisture flow vs. time (after Penner, 1960). 117
Figure 3-18. Heave rate vs. frost penetration rate for several lithologies (after Penner, 1972). 117
Figure 3-19. Heave rate vs. rate of frost penetration for a sand sample (after Penner, 1972). 118
Figure 3-20. Influence of temperature on: a). lateral strain, and b). water content for Twente sand (after Côté et al., 2000). 120
Figure 3-21. Radial constrains within the samples, caused by freezing (after Côté, 2003). 120
Figure 3-22. Comparison between the results of drained and undrained freezing tests for Twente sand samples (after Côté et al., 2000). 121
Figure 3-23. Results of uniaxial compression, triaxial compression, and uniaxial tension tests performed on frozen Twente sand (after Côté, 2003). 122
Figure 3-24. Variation of the UCS of frozen Twente sand because of changes in the freezing direction (data from Côté, 2003). 124
Figure 4-1. Pore pressure (PP), minimum principal stress (Sv), and fracture gradient (FG) curves for highly under-compacted (HUC) and moderately-compacted (MUC) rocks (after Willson et al., 2003). 133
Figure 4-2. Cross section of the Pompano field, GOM (after Willson et al., 2003). 136
Figure 4-3. Days vs. depth plt for the discovery well MC582#1 on the Medusa field (after Chhajlani et al., 2002). 138
Figure 4-4. Reservoir compaction curve (after Dusseault et al., 1998). 142
Figure 4-5. Compacting reservoir bedding plane slip (after Dusseault et al., 1998). 143
Figure 4-6. Localized deformation in well damage within overburden at Wilmington field, with approximately 10” lateral offset on 10 ¾” casing from 1,707 to 1,712 ft depth (after Frame, 1952). 145
Figure 4-7. Damage to weak sandstones during perforation (after Dusseault and Santarelli, 1989). 147

Figure 4-8. Elastoplastic model as postulated by Risnes et al. (1982). 149
Figure 4-9. 3D model of the Matagorda Island 623 field (after Li et al., 2003). 150
Figure 4-10. Siph-D sand/fluid production rates, and pressure, Matagorda Island field (modified from Li et al., 2003). 151
Figure 4-11. Simulated production after fracpack treatment for a well with an original skin equal to 40 (after Roodhart et al., 1993). 155
Figure 4-12. Effect of fracturing induced damage on the well productivity (L= 25 ft, r_e=1500 ft), built from equation 4.2. 157
Figure 4-13. Griffith crack (after Broek, 1986). 160
Figure 4-14. a). Ideal fracture in LEFM; b). More realistic sketch of a hydraulically induced fracture. 162
Figure 4-15. The Cleary et al. model (1991). 172
Figure 4-16. Fluid streamlines across a fracture vertical section, after Weng (1991). 183
Figure 4-17. Effects of confining pressure, water saturation, and temperature on the magnitude of fracture toughness (data from Roegiers and Zhao, 1991). 188
Figure 4-18. Increment in fracture toughness as function of confining pressure, water saturation, and temperature (data from Roegiers and Zhao, 1991)... 189
Figure 4-19. MIMES simulation of a Uniaxial Compression Test (after Sandia Nat. Lab., 2004). 194
Figure 4-20. Superquadric and arbitrary-shaped particles for DEM simulations (after Sandia Nat. Lab., 2004). 196
Figure 4-21. Ball-ball contact in PFC^{3D} , from PFC^{3D} manual (Itasca Consulting Group, 2004). 198
Figure 4-22. Ball-wall contact in PFC^{3D} (left), determination of the normal direction of the contact (right); from PFC^{3D} manual (Itasca Consulting Group, 2004) 200
Figure 4-23. Parallel bond (from PFC^{3D} manual, Itasca Consulting Group, 2004). 206
Figure 5-1. Grain size distribution curves of natural Antler sandstone (generated with data from Wang et al., 1995) 218
Figure 5-2. Dimensions and number of particles in the first modeling attempt. 220
Figure 5-3. Schematic of model used for the validation of the mechanical properties of the "virtual" sample 222
Figure 5-4. Plot of stress (in Pa) vs. strain; corresponding to Test 1-1 (inter-particle friction only). 226
Figure 5-5. Curve of stress (in Pa) vs. strain for virtual Test 2-1 (listed in Table 5.3) 228
Figure 5-6. Curve of stress (in Pa) vs. strain for Test 2-3, see Table 5.3. 229

Figure 5-7. Curve of stress (in Pa) vs. strain for Test 3-3, with σ_{conf} = 1,000 psi (6.9 MPa), b_kn=6.9*10^{10} Pa (10^7 psi), and b_ks=0 Pa (0 psi), see Table 5.4 231
Figure 5-8. Curve of stress (in Pa) vs. strain for Test 4-2, with σ_{conf} = 1,000 psi (6.9 MPa), b_kn=9.4*10^{10} Pa (13.6*10^6 psi), and b_ks=4.0*10^{10} Pa (5.8*10^6 psi), see Table 5.5. 233
Figure 5-9. Curve of stress (in Pa) vs. strain for Test 4-8, with σ_{conf} = 1,000 psi (6.9 MPa), b_kn=9.4*10^{10} Pa (13.6*10^6 psi), and b_ks=4.0*10^{10} Pa (5.8*10^6 psi), see Table 5.5. 234
Figure 5-10. Curve of stress (in Pa) vs. strain for Test 5-3, with σ_{conf} = 5,000 psi (34.5 MPa), b_kn=9.4*1010 Pa (13.6*10^6 psi), and b_ks=4.0*1010 Pa (5.8*10^6 psi), see Table 5.6..... 235
Figure 5-11. Curve of volumetric strain vs. axial strain for Test 5-3, with σ_{conf} = 5,000 psi, b_kn=9.4*1010 Pa (13.6*106 psi), and b_ks=4.0*1010 Pa (5.8*106 psi), see Table 5.6. 237
Figure 5-12 . Secondary electron images of the Antler sandstone; a). bonded grains showing what appears to be clay cement (x132);and, b). bonded grains showing white coatings of cementing material (x368), after Wang et al. (1995). 242
Figure 5-13. EDS-Spectrum display of the cementing materials in a sample of the Antler sandstone (after Wang et al., 1995). 243
Figure 5-14. Normal and shear stiffness of the minerals in the rock cement and of the simulated model (built with data from University of Kansas (2004) and Efunda (2004). 243
Figure 5-15. Normal and shear strength of the minerals in the rock cement and of the simulated model (built with data from University of Kansas (2004) and Efunda (2004). 244
Figure 5-16. Pressure vs. distance (along the model axis) distribution, hydraulic properties validation..... 248
Figure 5-17. Schematic of the "virtual" plane used for permeability measurement (left); snapshot of the model during a permeability test (right)..... 249
Figure 5-18. Snapshots of the field model used in this study: left, particle assembly; right, particle assembly + pipe network. 257
Figure 5-19. Number of cracks vs. time (red → tensile, blue → shear, black → tensile+shear), ΔP = 0.689 MPa= 100 psi & μ = 1 mPa.sec = 1 cP (Test 8-1). 260
Figure 5-20. Number of cracks vs. time (red → tensile, blue → shear, black → tensile+shear), ΔP = 0.689 MPa= 100 psi & μ = 1,000 mPa.sec = 1,000 cP (Test 8-4)..... 261

Figure 5-21. Number of cracks vs. time (red → tensile, blue → shear, black → tensile+shear), ΔP = 0.689 MPa= 100 psi & μ = 200 mPa.sec = 200 cP (Test 8-2). 261
Figure 5-22. Final number of induced tensile cracks – field model. 262
Figure 5-23. Final number of induced shear cracks - field model. 263
Figure 5-24. Final percentages of shear and tensile cracks induced by fluid injection..... 265

List of Tables

Table 2-1. Sample texture and mineralogy for Salt wash, Castlegate and Kern River Sandstone (modified from Bruno et al., 1991)..... 22
Table 2-2. Uniaxial compression data for Jurassic 3, Salt Wash and Red Wilmoor formations (modified from Nicholson et al., 1998). 32
Table 2-3. Friction angle and cohesion values – unconsildated sands from North West Italy (modified from Berardi et al., 1994) 47
Table 2-4. Friction angle and cohesion values – Ust-Illim Plant samples- Russia (modified from Sapegin et al., 1981) 48
Table 2-5. Some physical properties of the samples used by Chang and Zoback (1998). 55
Table 2-6. Creep parameters obtained during triaxial test (modified from Chang and Zoback, 1998). 55
Table 2-7. Surface-energy decrease of quartz in various saturated vapors (after Boyd and Livingston, 1942). 70
Table 2-8. Variation of elastic moduli as a function of water saturation (modified from Wu and Tan, 2001)..... 73
Table 3-1. Results of petrographic analyses based on 50 grains of each sandstone sample before freezing (after Hale and Shakoor, 2003). 108
Table 3-2. Average values for the engineering properties of several sandstones before freezing (modified from Hale and Shakoor, 2003)..... 109
Table 3-3. Effect of freezing and thawing on UCS of sandstones (after Hale and Shakoor, 2003). 110
Table 3-4. Description of the samples used in the study by Penner (1960)..... 116
Table 4-1. Major operational problems experienced on the exploratory phase of the Medusa field (after Chhajlani et al., 2002). 139
Table 4-2. Fracture toughness (in Kpsi/ft$^{0.5}$) as function of specimen and aggregate size (data from Shlyapobersky et al., 1998) 186
Table 5-1. Particle size distribution for natural Antler sandstone (calculated from the data by Wang et al., 1995) 219
Table 5-2. Initial set of simulations under σ_{conf} = 14.5 psi (0.1 MPa), only contact bonds. 224
Table 5-3. Second set of simulations, with σ_{conf} = 14.5 psi (0.1 MPa), it included both parallel and contact bonds..... 226

Table 5-4. Third set of simulations; with σ_{conf} = 1,000 psi, b_kn=6.9*10^{10} Pa (10^7 psi), and b_ks=0 Pa (0 psi)..... 230
Table 5-5. Fourth series of simulations; with σ_{conf} = 1,000 psi (6.9 MPa), see footnotes..... 231
Table 5-6. Fifth series of simulations; with σ_{conf} = 5,000 psi (34.5 MPa), b_kn=9.4*10^{10} Pa (13.6*10^6 psi), and b_ks=4.0*10^{10} Pa (5.8*10^6 psi)..... 235
Table 5-7. Calibration of the normal and shear strength of the inter-particle contacts, with constant values of stiffness for both spheres and contacts (see Table 5.6). 237
Table 5-8. Calibrated values for the mechanical interaction parameters used in this study. 238
Table 5-9. Summary of the tests performed for model permeability calibration.250
Table 5-10. Summary of the values of fluid viscosity and pressure differential evaluated in this study..... 258
Table 5-11. Summary of the results obtained from the field model. 259
Table D-1. Results of the numerical experiments performed on the field model..... ……..347

Abstract

This dissertation addresses the issue of hydraulic fracturing stimulation of poorly consolidated formations. First, a complete review about the mechanical properties of such formations was performed. Typical ranges of properties such as Young's modulus, Poisson's ratio, and uniaxial compression strength (UCS) were identified. In addition, the characteristic shape of the stress-strain curve was also recognized. Given their friable nature, weakly consolidated sands exhibit very low values of Young's modulus, and UCS. They could be located in the lower end of the sandstones trend in the Deere and Miller rock classification. Subsequently, a study on the reliability of the measurements of the rock mechanical properties for unconsolidated rocks was conducted. The effects of coring, freezing and testing were studied. It was concluded that coring-induced stress relaxation may cause permanent alterations of the rock mechanical behavior. However, the data about freezing-induced alteration of cores were deemed inconclusive and more research on this issue was recommended.

Finally, a discrete element model was built and calibrated in order to reproduce the mechanical and hydraulic responses of a selected unconsolidated sandstone.

The hydraulic fracturing process was simulated and the relative importance of different failure mechanisms was evaluated. A remarkable finding by exercising such a model was that in the case of the Antler Sandstone (and possibly in more unconsolidated formations), shear failure seems to be more important than tensile failure during the hydraulic fracturing process. This conclusion is a clear contradiction to what has been traditionally accepted in the oil and gas industry.

Chapter 1

Introduction

Hydraulic fracturing is a technology that has been utilized for more than 50 years in the oil and gas industry. It was originally used for stimulating hard, brittle formations which typically exhibited low permeabilities and roughly behaved as linear elastic materials. Nonetheless, an increasingly important segment of the industry currently is stimulating very soft and poorly consolidated formations; where the assumptions of ideal elasticity and relatively small fluid leak-off fail to hold (e.g. Gulf of Mexico, West Africa, Alaska, East China Sea). In these rock types, hydraulic fracturing stimulation has been mostly used to control and solve critical production problems such as sanding and formation damage (caused during completion and/or drilling operations).

Most hydraulic fracturing projects carried out in unconsolidated formations render rather unexpected results: standard numerical models tend to underpredict fracturing pressures. A recent worldwide survey on fracturing pressures by the Delft Fracturing Consortium (Papanastasiou, 1997) indicated that net pressures encountered in the field commonly are 50% to 100% higher than their

corresponding values predicted by conventional fracturing simulators; the difference is even higher for the case of poorly-consolidated formations (Pak, 1997). The implementation of hydraulic fracturing operations in this type of rocks has not been accompanied by modeling techniques tailored specifically for this kind of formations. In most cases, such models undergo a period of "calibration", in order to reproduce the results obtained in the field. Thus, a trial-and-error approach is commonly used to design and perform the treatments, avoiding major operational problems although without optimizing the field operation.

As part of this work, a comprehensive review about the mechanical properties of poorly consolidated formations was conducted. Typical ranges of properties such as Young's modulus, Poisson's ratio, and uniaxial compression strength (UCS) were defined. In addition, the distinctive shape of the stress-strain curve was recognized. A study on the reliability of the measurements of the rock mechanical properties for unconsolidated rocks was conducted as well.

For this particular study, experimental data provided by Wang et al. (1995) were used. In their paper, they reported the results of several triaxial tests performed on Antler sandstone samples, a weakly-consolidated formation that outcrops near Ardmore, Oklahoma. The poorly-consolidated nature of the Antler sandstone is

apparent, as dried samples of this rock may be reduced to fine loose grains by merely applying hand pressure.

This study aimed at determining the importance of shear as a failure mechanism during hydraulic fracturing processes involving highly-permeable, poorly-consolidated rocks. This modeling work consisted of two main phases: i) construction of a calibration model, using the discrete element method, to mimic both the mechanical and hydraulic behavior of the Antler sandstone; and ii) construction of a field model (based on the results obtained during the first stage) to infer the behavior of the rock modeled in the previous step during high pressure fluid injection.

Chapter 2

Unconsolidated Formations – Physical Properties

2.1 Pore compressibility

Changes in rock porosity are influenced by the applied stress and the pore compressibility. In unconsolidated formations[1], the magnitude of the pore compressibility sensitivity to stress varies considerably depending upon the lithology. In clean sands with little cementation, the stress-strain behavior is believed to be dominated by Hertzian-type elastic, inter-granular contacts. However, additional inelastic deformations may be caused by slippage and rotation of relatively rigid sand grains. In this case, the overall rock frame shows small values of compressibility, which vary little with stress. On the other hand, as the relative amount of ductile components increases (e.g. clay), the effect of stress on pore compressibility, $-d\ln(V_P)/dP$, becomes more noticeable. The rock exhibits a low value of compressibility at low stress; but as load increases, the material becomes more compressible (probably due to yielding of the ductile

[1] The term "unconsolidated" hereby refers to rocks with UCS less than 25 MPa (3,625 psi), (ISRM, 1981)

components of the formation). Pore compressibility increases until it reaches a certain stress threshold, beyond which the rock starts to show strain hardening (Fig. 2.1). In this figure, the compressibility of Prospect A increases as stress augments; but when stress becomes larger than 2,000 psi, the rock starts to exhibit strain hardening. The same behavior may be expected for Prospects B and C. However, the compressibility of Prospect D (the sample with less clay content) seems to be rather unaffected by variations in the effective applied stress. The behavior of Samples A, B, and C may be explained by the fact that as the ductile components deform, they squeeze between rigid sand grains, transferring load to them (Ostermeier, 1993).

Similar conclusions were drawn by Pauget et al. (2002), from mechanical testing unconsolidated formations. Plastic behavior was also sometimes observed in samples subjected to large isostatic stresses (Fig. 2.2); while few others behaved elastically throughout most of the tested stress range. In Fig. 2.2, the sample was initially loaded from point C to point A; the coring process was simulated by the stress path ABC, with the sample returning to its original porosity conditions after it was unloaded (elastic deformation). However, as the sample was loaded to higher values of stress (points D and E), the rock failed to return to its original conditions, even after relieving all the applied stress (plastic/permanent deformation).

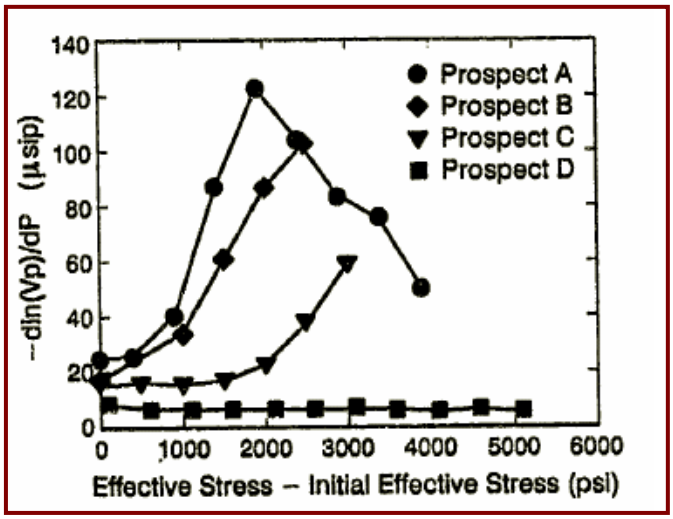

Figure 2-1. Pore volume compressibility[2] vs. applied stress, GOM sample (after Ostermeier, 1993).

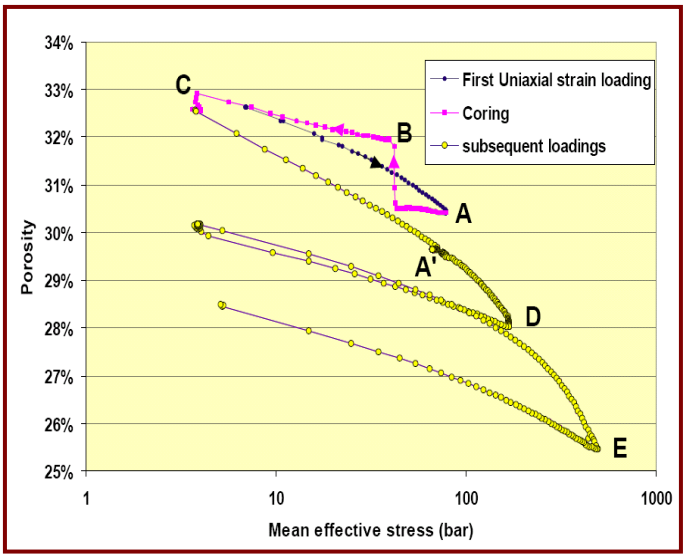

Figure 2-2. Pore volume compressibility as a function of mean effective stress, unidentified unconsolidated sample (after Pauget et al., 2002)[3]

[2] The pore volume compressibility is defined as $-d\ln(V_P)/dP$

[3] 1 bar = 14.504 psi

2.2 Porosity and Permeability

The mode of sand deposition, its environment, and the site of accumulation itself determine the permeability and porosity characteristics of sedimentary rocks. The most important parameters affecting porosity are: framework mineralogy (mainly quartz relative content), age, grain sorting, cementation and burial history of the rock. Cementation and leaching are interrelated with many other parameters, such as pore chemistry, temperature, and fluids saturation (Schmidt et al., 1977). It has been observed that the importance of some parameters changes with depth of burial, e.g. equivalent increments in the amount of cementing material have more effect on porosity in a shallow rock than in a deeper one (Fig.2.3). At surface conditions, the presence of a certain volume of cement reduces the porosity by almost the same volume. Nevertheless, if cementation occurs at depth, porosity will be affected by both compaction and cementation: the presence of cement tends to hinder additional rock compaction (Scherer, 1987).

Unconsolidated formations are, in general, geologically young sediments with low cement content, and quartz as their main mineral component. This type of rock is generally associated with high-energy sedimentary environments, where rapid deposition shortens the lithification process; i.e. high sedimentation rates create accumulations that are buried before they become competent rocks.

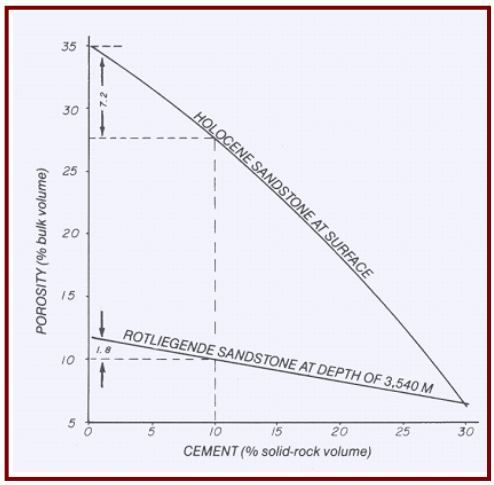

Figure 2-3. Comparison of porosity reduction as function of the amount of cement, for two rocks at different depths (after Scherer, 1987).

Results of rock characterization studies on North Sea Paleocene turbidite sands showed that they occur either with slight contact cementation, or as completely uncemented and friable rocks, yielding dramatically different seismic responses (Fig. 2.4). It was also established that clay content and sorting affect the seismic properties of these turbidite sands, and that rock physics diagnostics may be used to quantify clay content and degree of sorting (Avseth et al., 2000). Since the weight of the overlying rock drives the packing, compaction, and cementation phenomena (Schön, 1996); unconsolidated rocks are normally found at shallow depths where the overburden stress is not large enough to cause effective sediment compaction. As explained above, unconsolidated formations may also be found at great depth in high energy depositional environments; where the

interstitial fluids are trapped within the rock by overlying sediments deposited shortly afterwards.

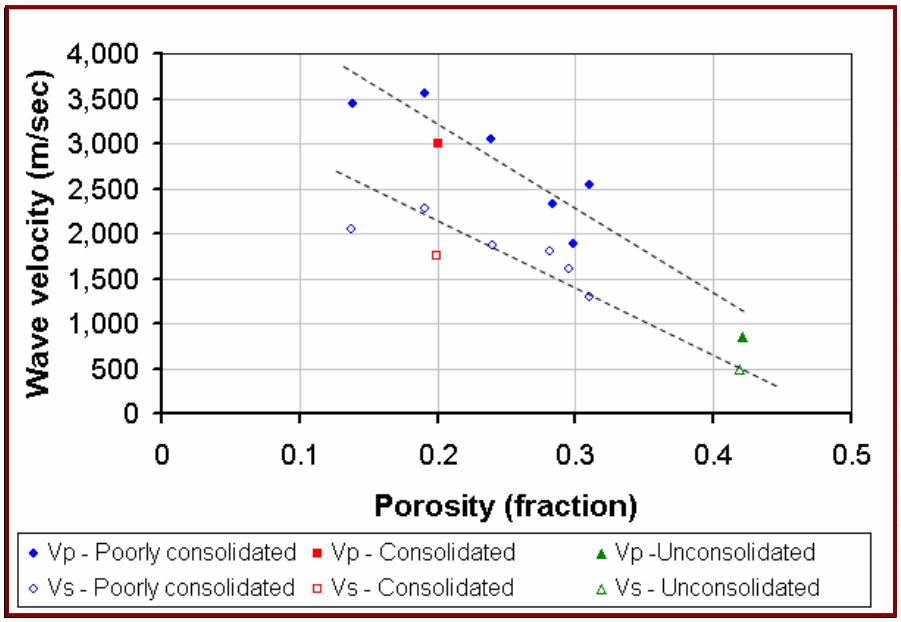

Figure 2-4. Compressional and shear wave velocities as a function of porosity, in dry frozen unconsolidated Otawa sand, poorly consolidated, and Berea sandstone samples (data from Tutuncu et al., 1997).

Compaction affects reservoir performance by reducing the pore volume and by reducing permeability. A reduction in porosity may aid in the production process by maintaining reservoir pore pressure, and literally squeezing hydrocarbons out of the rock. On the other hand, any permeability impairment caused by compaction decreases the rock ability of delivering fluids into the well. Additional compaction effects are ground subsidence (which may have important effects on surface structures), and casing/wellbore integrity; e.g. in lenticular

reservoirs, compaction increases the shear stress acting on the interface of the structure and neighboring formations. This effect could lead to casing shearing, and eventually to total well loss.

Fatt (1958) presented some of the earliest data on the behavior of moderately permeable consolidated sandstones; he showed reductions in permeability from 20% to 60% for samples subjected to stresses up to 100 MPa (14,500 psi). The effects of pressure on compaction, i.e. on porosity, have been thoroughly studied (Selley, 1978; Scherer, 1987; Ostermeier, 1995); experimental results show a correlation between pore pressure and porosity. Normal hydrostatic pressure gradients, about 0.45 psi/ft, are linear with depth. However, abnormally high pore pressures may decrease substantially the effective stress acting on the grain contacts; thus, impeding the compaction process. Data from overpressured Tertiary deposits in Louisiana illustrate this point (Fig. 2.5). The porosity gradient calculated by Atwater and Miller (1965) for normally pressured formations was 1.265% / 1,000 ft; whereas for overpressured sandstones it was only 0.960% / 1,000 ft. Thus, the normally pressured rocks compacted in average 0.305% more for every 1,000 ft increase in depth (Selley, 1978). Studies involving samples from weakly-consolidated North Sea sandstones showed that these rocks could retain approximately 1.9% more porosity for every 1,000 psi of pore overpressure during compaction. However, this number should be used with

caution, since the effect of pressure also depends on the stage of lithification at which the overpressure appeared. And it includes a time component as compaction appears to continue under overpressure conditions, although at a lower rate (Scherer, 1987).

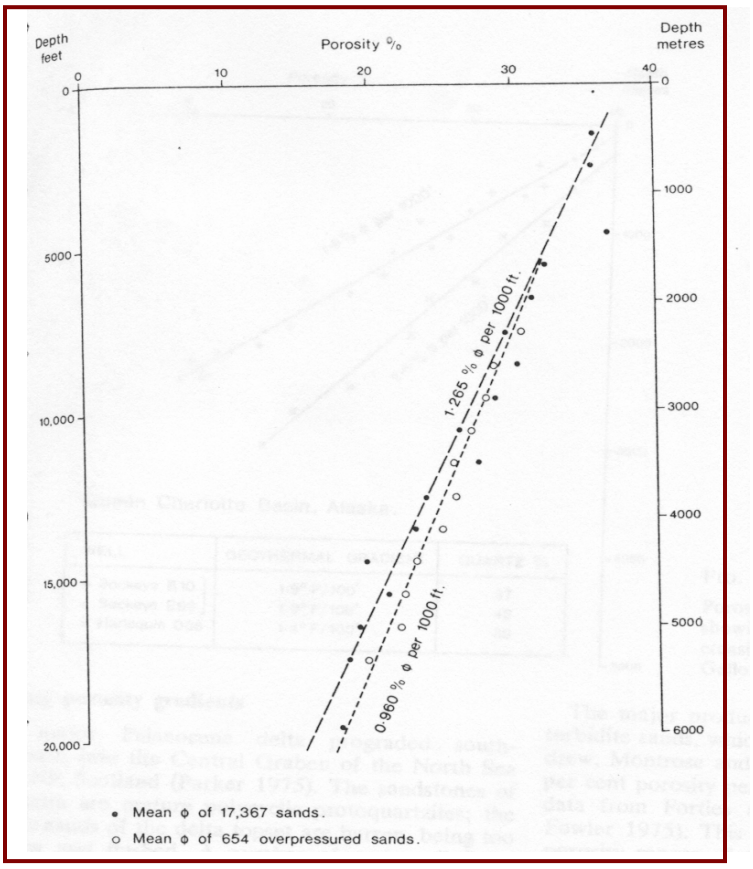

Figure 2-5. Effect of pore pressure on porosity gradient – South Louisiana sandstones (after Selley, 1978).

Detailed studies on the effect of compaction on porosity and permeability were also conducted for deep water turbidites in the Gulf of Mexico. Such sands are,

normally, over-pressured and are currently at the highest effective stress of their geological life (Ostermeier, 1993). Pore volume and sample permeability measurements were performed with the samples at S_{wi}, and maintained at isostatic stress conditions and ambient temperature (Ostermeier, 1995). The mechanical behavior of highly permeable, highly porous sedimentary rocks is greatly influenced by their mineralogy. Both increasing clay content and decreasing cementation tend to produce highly compressible, pressure-sensitive rocks (Bruno et al., 1991). Figure 2.6 shows the variation of porosity, and permeability as a function of the applied stress (equal to the effective stress in drained tests). Both porosity and permeability exhibit strong dependence upon the applied load. However, the latter was considerably more sensitive to changes in stress; in this plot, a relative decrease in porosity corresponds to about $1/10^{th}$ of its corresponding change in permeability (see Fig. 2.7).

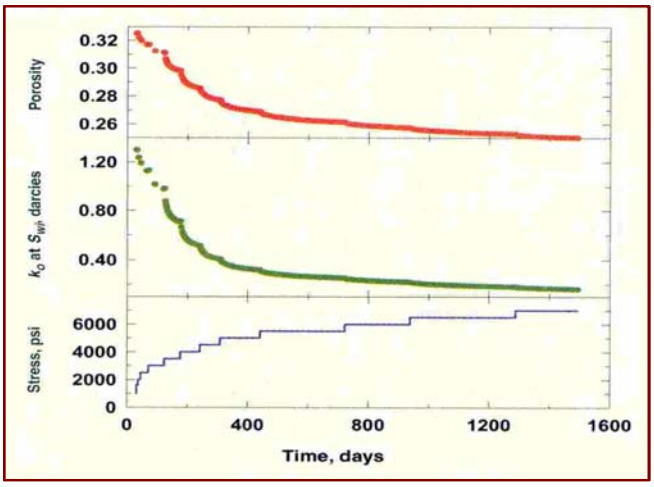

Figure 2-6. Porosity and permeability vs. time as response to applied effective stress, GOM sample (after Ostermeier, 1993).

Porosity changes for unconsolidated rocks in the North Sea may be predicted by using compaction stochastic models, such as the one proposed by Sclater and Christie (1980). This model describes offshore sand porosity as a function of its depth with respect to the seafloor (i.e mudline); the equation predicting the sandstone compaction curve in Fig. 2.8 is given by $\phi = 0.49\, e^{-2.7\, d\, /\, 10000}$, where d is the depth in meters. Here an effective stress gradient of 0.567 psi/ft or 1.86 psi/m was assumed. Porosity decreases with effective stress, i.e. with depth; however, the predictions of this theoretical model were far larger than the results obtained during testing. The cause of this discrepancy may be the inelastic nature of the compaction process; Fig. 2.8 shows that the rate of porosity reduction, i.e. the slope of the curve, changes depending upon the magnitude of the differential stress applied to the rock. Only a small amount of elastic rebound occurs when differential pressure acting on the sample is reduced (Bowers, 2002). Furthermore, the theoretical model ignores other factors that play an important role on porosity and permeability behavior such as mineralogy, grain-size distribution, and grain shape. A more comprehensive porosity prediction model, based on core measurements on sands from the North Sea, was proposed by Scherer (1987). In his model, parameters such as sorting, quartz content, depth, and age were included to give the following relation:

$$\phi = 18.60 + 4.73 \ln\left(V_{quartz}\right) + 17.38 / Sorting - 3.8\, Depth - 4.65 \ln\left(Age\right) \quad \text{.....(2.1)}$$

In the above equation, porosity is expressed in percent of bulk volume, V_{quartz} in percent of solid-rock volume, *Depth* in kilometers, *Age* in million years, and *Sorting* is defined as the Trask sorting coefficient. According to Scherer (1987), this equation is valid for sandstones with little or no cement, no leaching, a depth of burial of more than 500 m (1640 ft), older than 3 m.y., and non-tectonic sedimentary environments. Figure 2.9 presents a crossplot of measured and estimated porosities for a set of 32 samples from North Sea sandstones.

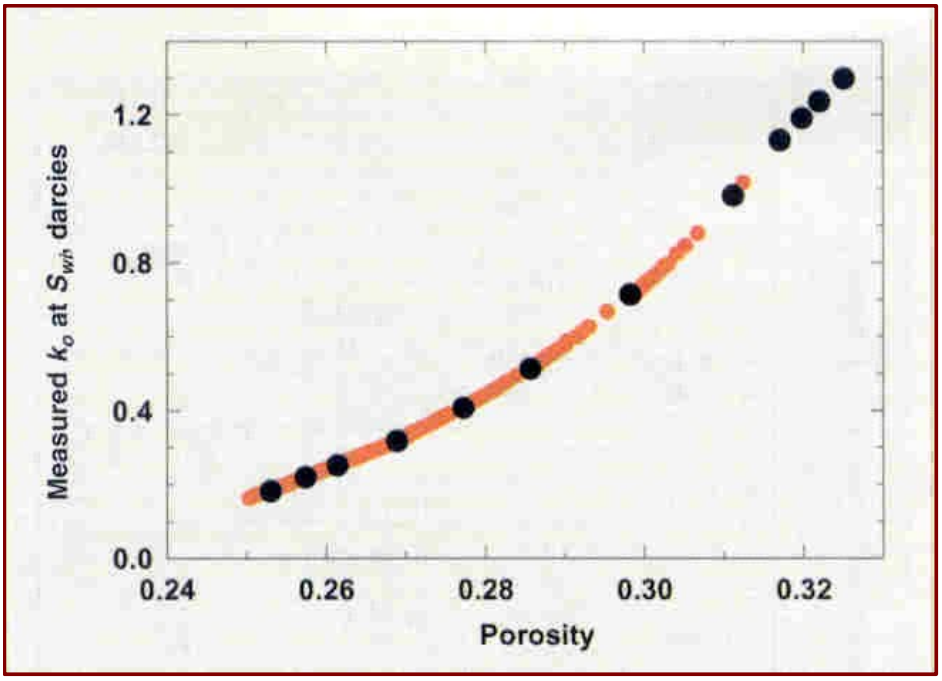

Figure 2-7. Measured oil permeability vs. porosity, GOM sample (after Ostermeier, 1993).

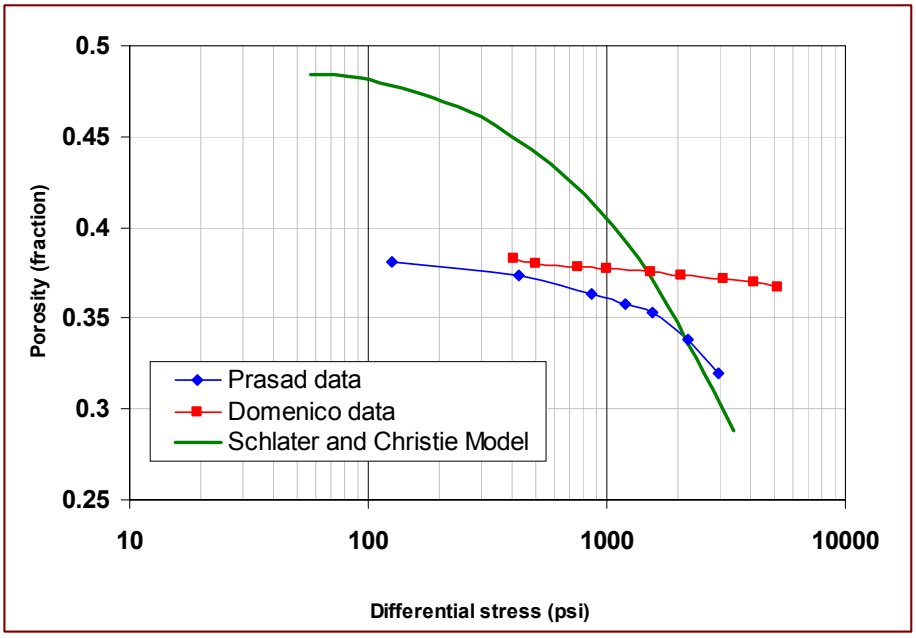

Figure 2-8. Porosity as function of differential pressure - North Sea samples; data from Domenico (1977), Sclater and Christie (1980), and Prasad (2002).

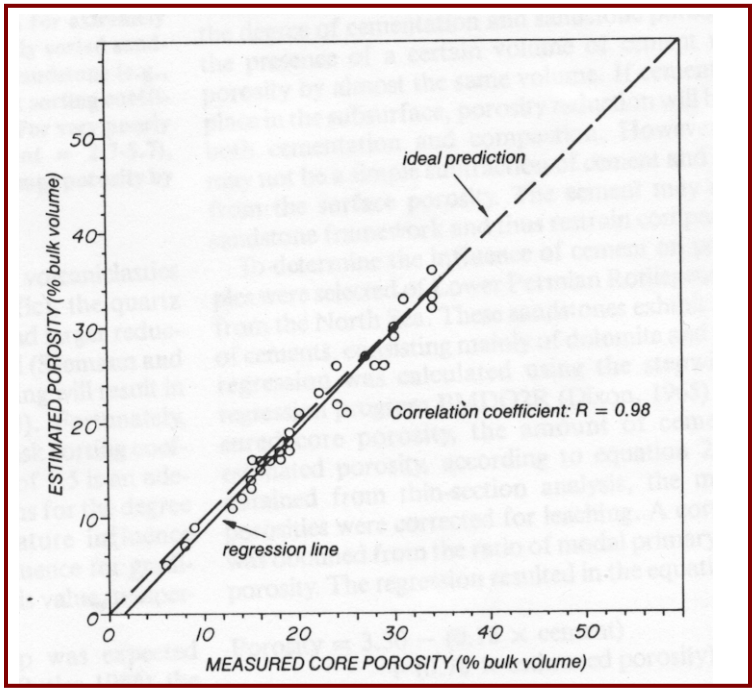

Figure 2-9. Porosity prediction for North Sea unconsolidated sandstones (after Scherer, 1987).

Ostermeier (1993) studied the permanent effects of stress cycling (hysteresis) on the porosity of unconsolidated samples from the Gulf of Mexico. Results from his study showed that hysteresis was very important, mainly during the first loading/unloading cycle; further stress cycling had little additional effects on rock porosity (Fig. 2.10). Results of drained triaxial tests performed on weakly-consolidated sandstones from the Adriatic Sea were published by Marsalla et al. (1994). These tests were run on brine-saturated samples under different stress conditions (Fig. 2.11a). The linear behavior of porosity when plotted vs. depth, suggested the basin was normally consolidated, i.e. little cementation during the compaction process. Figure 2.11b shows the variation of rock porosity as a function of depth for extremely shallow subsea sediments in the GOM.

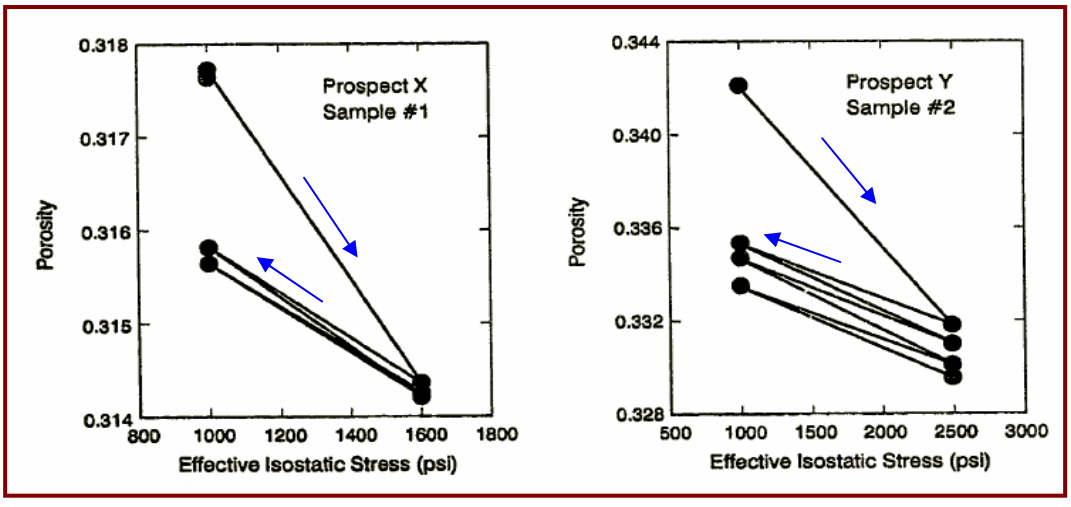

Figure 2-10. Effect of isostatic stress cycling on rock porosity, unconsolidated samples from the GOM (after Ostermeier, 1993).

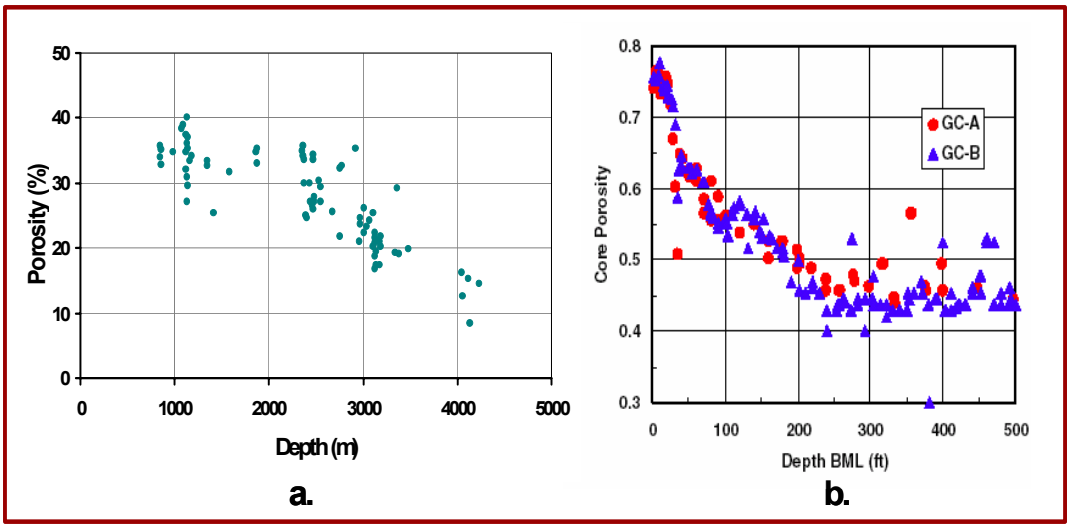

Figure 2-11. Porosity vs. vertical depth – a). Northern Adriatic Basin (data from Marsala et al., 1994); b). Highly over-pressured samples from the GOM (after Ostermeier et al.; 2001).

Physical considerations suggest that, everything else being equal, permeability varies as the square of some characteristic grain size (Ostermeier, 1995). Figure 2.12a, shows the measured oil permeability at initial average in-situ stress vs. average grain size for 13 samples from the Gulf of Mexico. It is difficult to identify any trend in this plot; similar scatter in the data is obtained if the square of the mean diameter is used instead. A more readily identifiable trend is observed if permeability is plotted against the square of the ratio d_{mean}/S_D; where d_{mean} is the average grain size and S_D is the standard deviation in the grain distribution (Fig. 2.12b). This approach follows from the consideration that permeability is also proportional to the degree of grain sorting, which is represented by the value of standard deviation; this is further illustrated in Fig. 2.13.

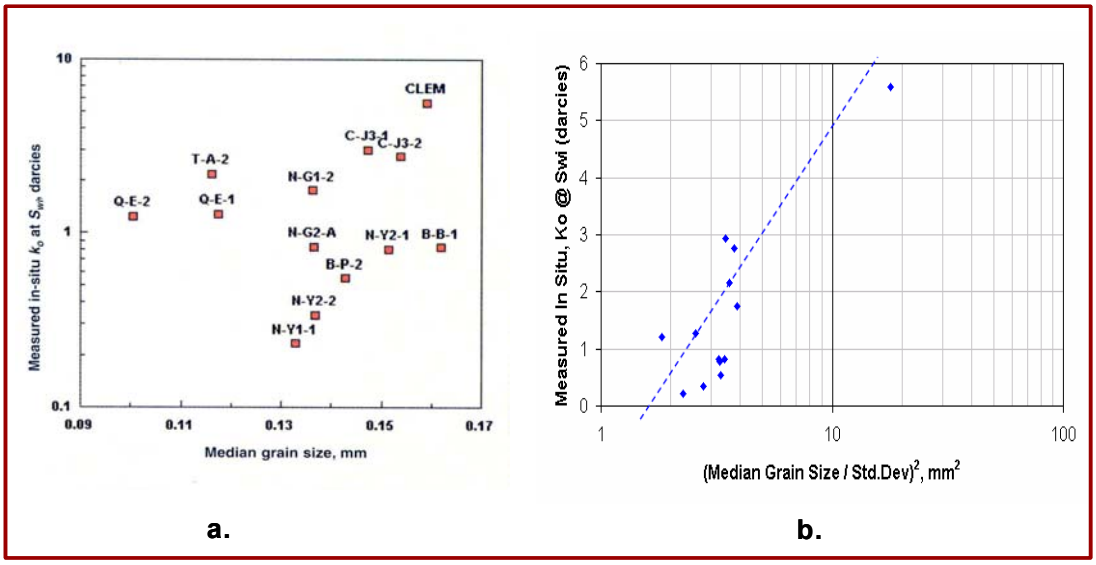

Figure 2-12. a). Oil permeability vs. median grain size, GOM sample (after Ostermeier, 1993); b). Oil permeability vs. (median grain size/std. dev.)^2 data from Ostermeier (1993).

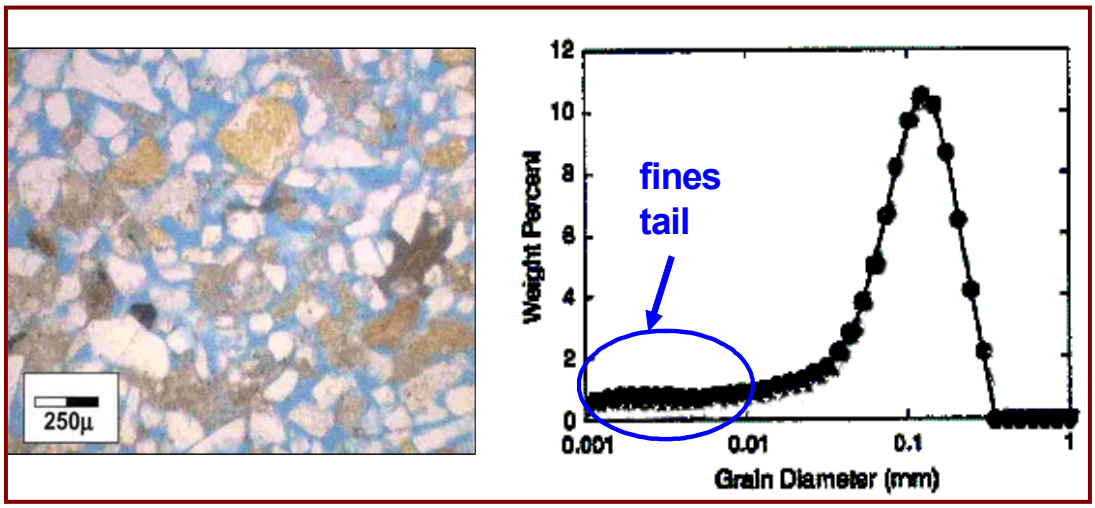

Figure 2-13. Thin section and its corresponding grain size distribution, GOM sample (after Ostermeier, 1995).

In the North Sea, the Gulf of Mexico, West Africa, and in many other poorly-consolidated fields around the world, hydrocarbon producing formations have permeabilities in excess of 1 Darcy (Holt, 1990; Ostermeier, 1993; and Joiner et al., 1999). Figure 2.14 shows measured permeability reduction as a function of the initial permeability when isotropic stress is applied to the rock. According to these results, stress should only slightly affect the production performance in highly permeable reservoirs. However, Fig. 2.14 accounts only for the effect of hydrostatic load. It has long been recognized that rocks are "stronger" when subjected to very small stress differential (Roegiers, 2004a); in contrast, high stress deviatoric can create shear loads that may cause grain rearrangement, hence permeability reduction.

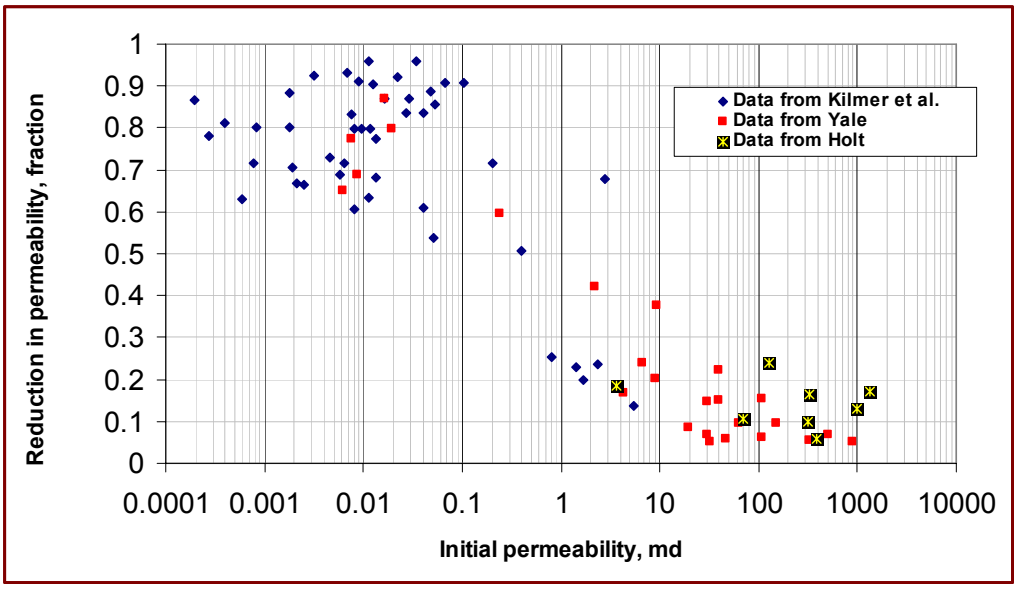

Figure 2-14. . Relative Reduction in permeability when hydrostatic stress was increased from 500 to 5000 psi (data from Kilmer et al., 1987; Yale, 1984; and Holt, 1990).

For most rocks, the ratio of horizontal to vertical permeability, k_h/k_v, is governed by stratigraphy and lithology. However, marked differences in the magnitude of the stresses acting parallel to the bedding plane may cause permeability anisotropy in the horizontal plane, i.e. in the plane of the principal horizontal stresses, σ_h and σ_H. The phenomenon of stress-induced anisotropy was first identified in low-permeability, fractured reservoirs; nonetheless, in-situ stress may also cause changes in the permeability of soft/unconsolidated sediments (Holt, 1990). Anisotropy in the in-situ stress field is commonly found in hydrocarbon fields (Roegiers, 2004a), this is particularly true for basins located within tectonically active regions, such as East China, US West Coast, South America, and Indonesia. Non-hydrostatic stress fields have the potential for causing permeability anisotropy within the reservoir, both perpendicular and parallel to the bedding plane. Non-hydrostatic triaxial compression tests were performed on samples of the Red Wilmoor Sandstone (a highly permeable, relatively weak formation), and single-phase permeability was found to decrease as the applied stress was increased. At low values of stress differential $|\sigma_{axial} - \sigma_{radial}|$, the decrease was consistent with the results of hydrostatic testing. Nevertheless, a dramatic drop in permeability was registered when shear stress, defined as $0.5|\sigma_{axial} - \sigma_{radial}|$, was large enough for yielding to occur; see blue arrow in Fig. 2.15 (Holt, 1990).

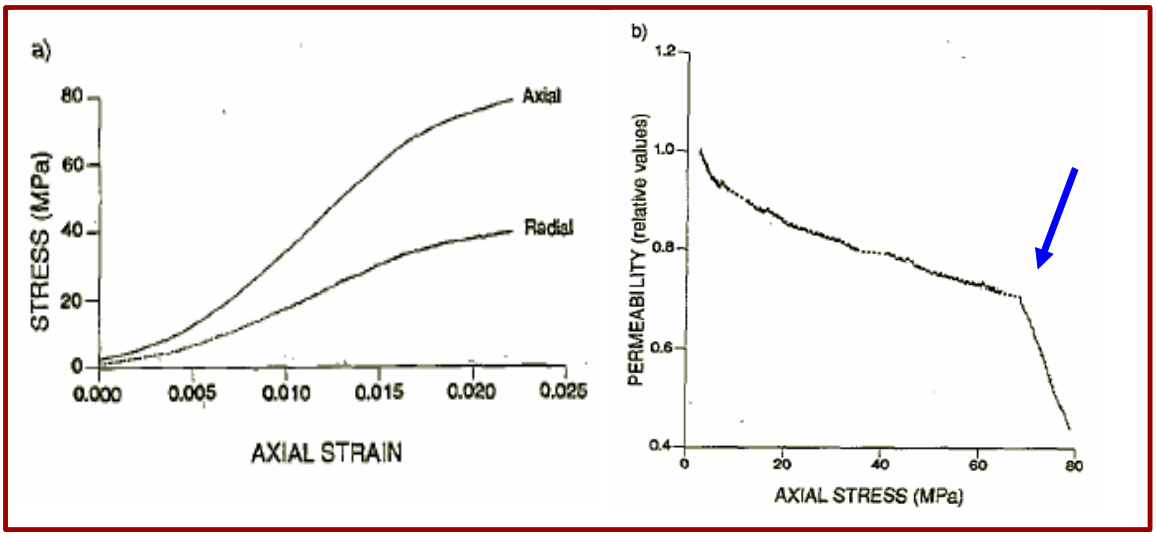

Figure 2-15. a). Axial and radial stress vs. axial strain during anisotropic loading of Red Wilmoor Sandstone, b). Corresponding permeability, perpendicular to bedding (after Holt, 1990).

More recently, Bruno et al. (1991) conducted a series of permeability tests on samples from three different lithologies: Salt Wash Sandstone, Castlegate Sandstone, and Kern River Sand. Salt Wash Sandstone is a lithic arenite deposited during the Late Jurassic. It is a friable, medium-grained, well-sorted rock; and its detrital grains are subangular to rounded. The Castlegate Sandstone is a formation from the Late Cretaceous: very friable, very fine-grained, well-sorted, and composed of angular to subrounded grains. The Kern River is Late Pliocene aged, relatively shallow (about 650 ft), and poorly consolidated to unconsolidated. It is a medium-grained, poorly-sorted rock; composed of angular to subangular grains (Bruno et al., 1991). Table 2.1 presents a summary of

mineralogy properties for these three lithologies; in addition, SEM images of all three samples are shown in Figs. 2.16 through 2.18.

	Salt Wash	Castlegate	Kern River
Age	Late Jurassic	Late Cretaceous	Late Pliocene
Quartz grains (%)	35	56	12
Feldspar grains (%)	5	5	18
Lithic fragments (%)	22	8	30
Authigenic clays (%)	8	4	10
Silica cement (%)	0	1	0
Calcite cement (%)	5	0	0
Grain size (μm)	250-500	65-125	250-500
Sorting quality	Very well	Well	Poor
Oil permeability (md)	600-800	850-950	300-500
Porosity (%)	25	26	30

Table 2-1. Sample texture and mineralogy for Salt wash, Castlegate and Kern River Sandstone (modified from Bruno et al., 1991).

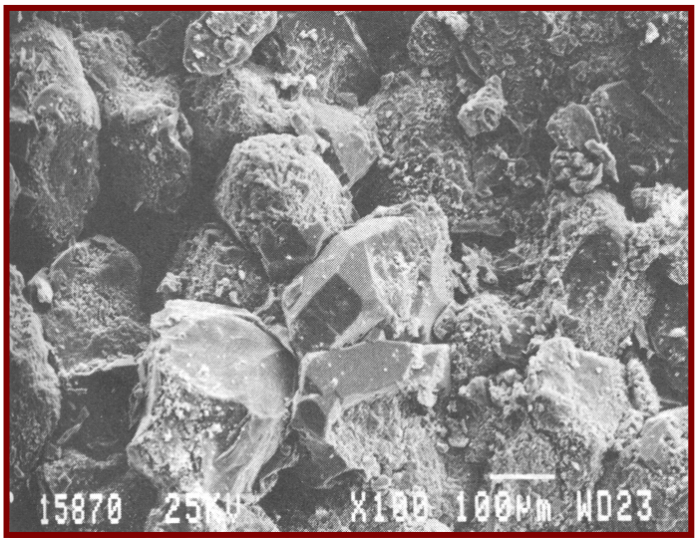

Figure 2-16. Salt Wash Sandstone - SEM image (after Bruno et al., 1991).

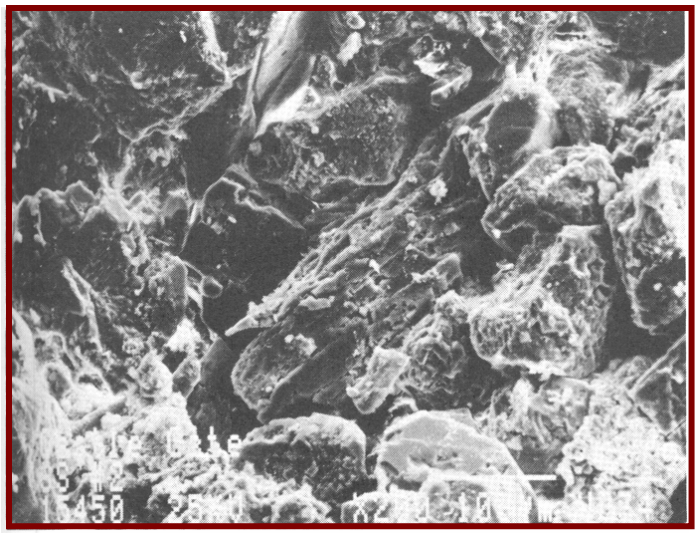

Figure 2-17. Castlegate Sandstone - SEM image (after Bruno et al., 1991).

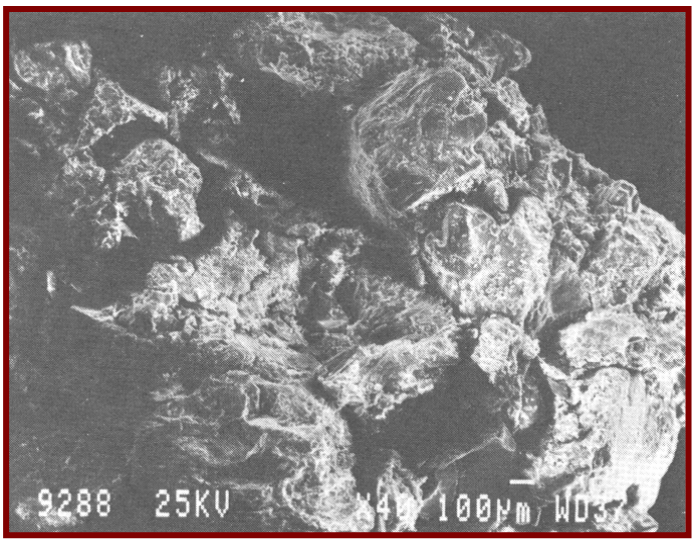

Figure 2-18. Kern River Sandstone - SEM image (after Bruno et al., 1991).

For their experiments, Bruno et al. (1991) loaded hydrostatically unconsolidated sandstone samples to a pressure of 3 MPa (450 psi), and measured their initial axial permeability. Subsequently, the axial load was increased up to about 15

MPa (2,175 psi), after which the samples were unloaded to 3MPa (450psi). This loading-unloading cycle was repeated, increasing the radial load on the sample while keeping the axial load constant; axial permeability was recorded throughout the test (Fig. 2.19). The rock permeability was reduced only slightly when samples were loaded in a direction parallel to the fluid flow path, i.e. in the axial direction. On the other hand, loading the sample perpendicular to the direction of flow had considerably more effect on permeability. In the case of the Castlegate Sandstone, axial loading caused a permeability reduction of about 5%, while radial loading provoked a permeability drop of almost 38%. Similar behavior was observed in the results obtained from the testing on the Salt Wash and Kern River specimens (Fig. 2.20); moreover, radial loading caused more irreversible permeability damage after the samples were unloaded.

Material microcracking is often mentioned as one the major mechanisms for permeability alteration in competent, low permeability formations (Kilmer et al., 1987). However, unconsolidated rocks often have mostly large pores with very low aspect ratios. Hence, microcracking is likely to occur only in a minor portion of the flow channels, namely in hydraulically irrelevant pores. It is apparent from Fig. 2.20 that the Kern River sample is more sensitive to changes in stress than the Castlegate specimen; and the latter shows more stress-sensitivity than the Salt Wash sample. The amount of "hard" minerals such as quartz, feldspar, and lithic

components was very similar for all the samples in this study (see Table 2.1). On the other hand, the total amount of cement was 5%, 1% and 0% for the Salt Wash, Castlegate, and Kern River sands, respectively. These are relatively large variations in cement content, since the amount of cement in competent sandstones is usually in the order of 10% (Proctor, 1974). This behavior agrees with former researchers (e.g. Bruno et al., 1991) who suggested that stress-sensitivity decreases with both the degree of consolidation and the amount of cement present in the rock. It is logical to expect loosely-cemented grains to rearrange and move more easily than those firmly held within the rock matrix; thus, lowering the value of rock permeability.

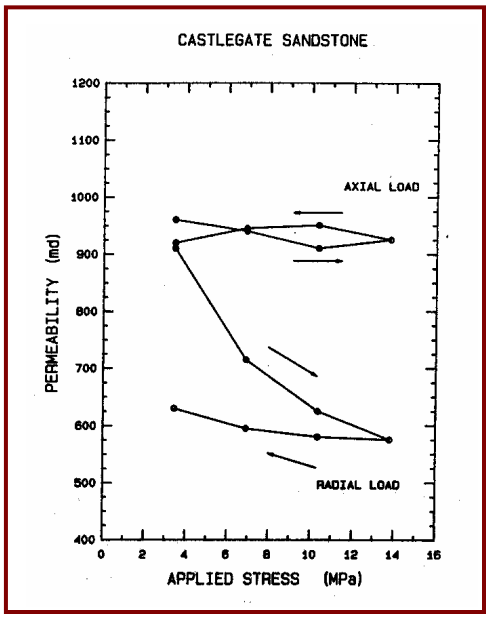

Figure 2-19. Variation of permeability as function of axial and radial stresses, Castlegate Sandstone (after Bruno et al., 1991).

The difference in the sensitivity of the samples permeability to changes in the applied stress, as observed in Fig. 2.20, may also be explained by the higher potential for fines migration inherent to poorly sorted rocks. The well-sorted Salt Wash sand exhibits less permeability impairment due to stress increment than the poorly sorted Kern River specimen. No data on permeability measurements during backflow were provided by Bruno et al. (1991); thus, this hypothesis could not be verified.

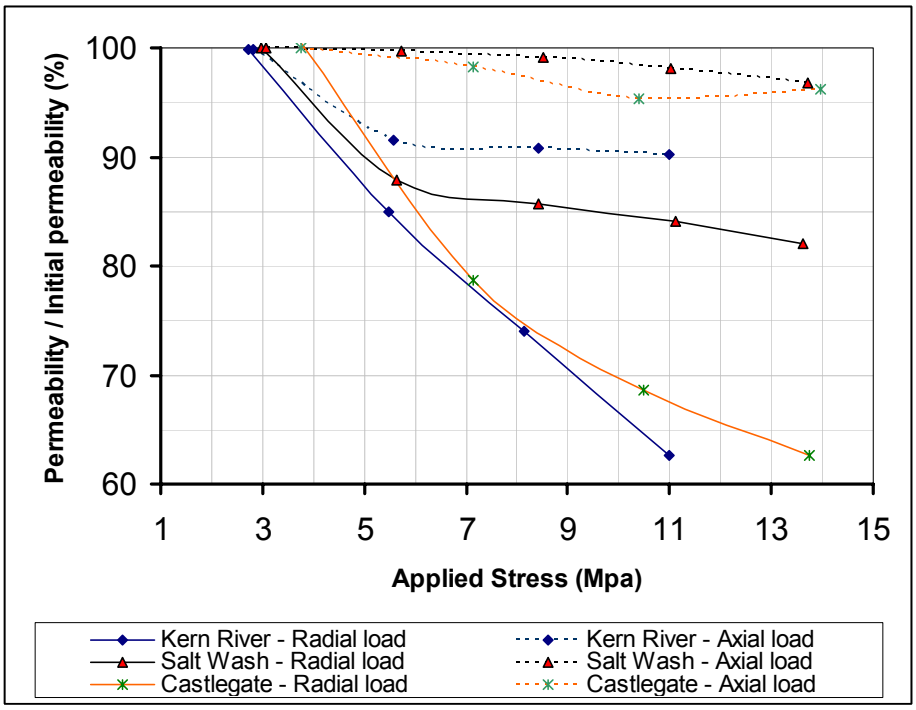

Figure 2-20. Variation of permeability as function of axial and radial stresses (constructed with data from Bruno et al., 1991).

2.3 Pore Pressure Characteristics

Because of their nature, unconsolidated reservoirs tend to be over-pressurized; this is especially factual for offshore reservoirs. Sedimentation occurred in high energy environments, where rapid deposition of sediments increased the probability of trapping the fluids that originally transported the consolidating rock fragments. Clay particles deposited on top of previously accumulated immature sands may have created a hydraulic seal, which would potentially trap the fluids still present within the sand. Consequently, the load being applied to the sand rock frame (i.e. the effective stress) is lower than in normal conditions, decreasing the rate of rock consolidation.

Amongst the many operational problems caused by pore overpressure, Shallow Water Flow (SWF) has been, and still is, a critical issue in offshore locations[4]. SWF occurs in shallow sands that are over-pressured due to rapid sedimentation. Small changes in pressure at these relatively shallow depths on virtually unconsolidated materials with high porosities and low effective stresses can lead to significant water flows. These water flows can cause formation collapse and massive sanding into a well. SWF sands have been observed in water depths

[4] Independent estimates have concluded that occurrences of SWF have cost offshore operators more than $1 billion through lost time, casing and drill string damage, and in extreme cases, the loss of the hole (WesternGeco website, 2004).

ranging from 1,300 to 8,200 ft, and at depths between 200 and 3,300 ft below the mudline.

An excellent study about SWF in the GOM, its severity and possible causes was published by Ostermeier et al. (2001). They found the existence of distinct regions of low, medium and high SWF risk. These regions were consistent with regional variations in sedimentation deposition rate in the Mississippi River Delta during the Late Pleistocene. They also identified these regions from variations in the topography of the sea floor (Fig. 2.21).

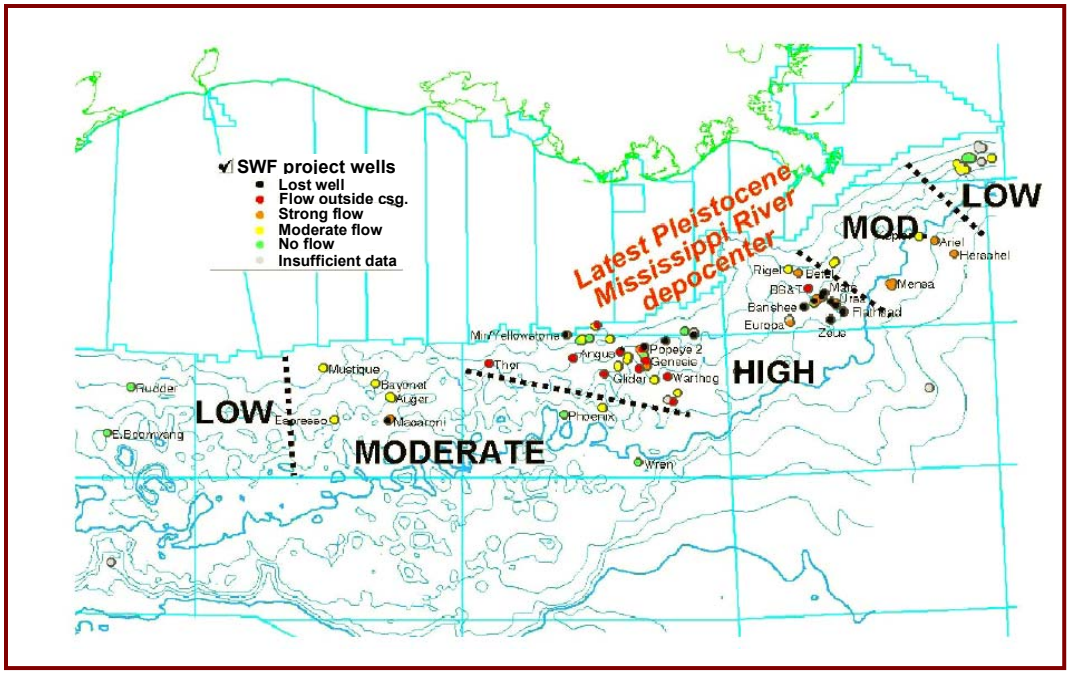

Figure 2-21. Relative magnitude of shallow water flow hazard (after Ostermeier et al., 2001).

2.4 Deformation Behavior of Unconsolidated Rocks

The strength properties of clastic sediments like sandstones are equally influenced by the amount of cement and by its clay mineralogy. Calcite-cemented sandstones have higher strengths and elastic moduli than clay-cemented sediments with equal amounts of cement. In addition, different types of clay have different mechanical behaviors: kaolinite, for example, is the stiffest clay mineral, whereas bentonite behaves as the most ductile one (Fig. 2.22).

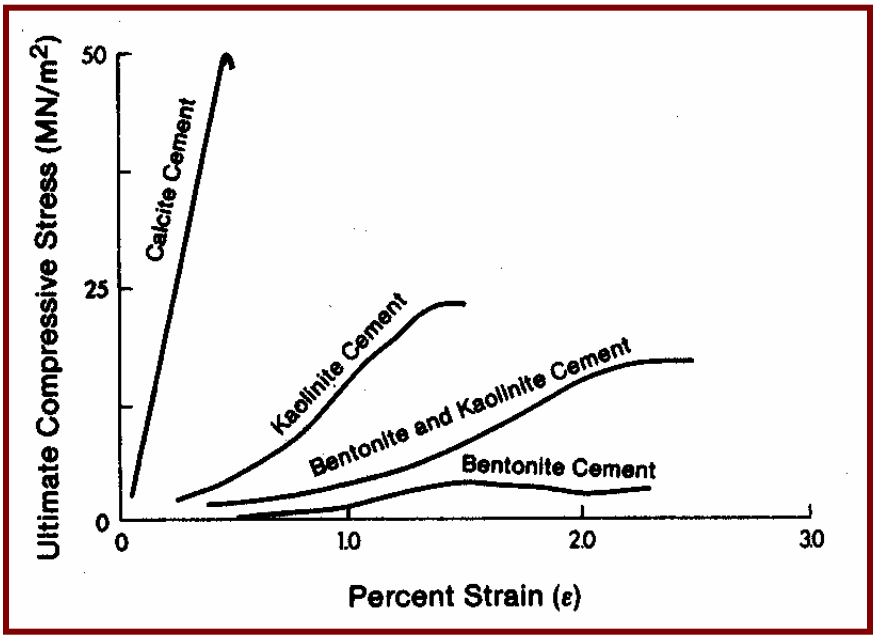

Figure 2-22. Sandstone strength and behavior as function of cementing material (after Jeremic, 1981)[5].

[5] 1 MN/m^2 = 1 MPa = 145.04 psi

2.4.1 Uniaxial Compression Strength

Given the friable characteristics of poorly and un-consolidated formations, uniaxial compression tests are very difficult to perform. Thus, very few reports were found in the literature referring to the Uniaxial Compressive Strength (UCS) of weakly consolidated rocks. Uniaxial compressive strengths for unconsolidated sandstones could be as little as 80 psi, as reported by Morita and Ross (1993). A comprehensive study on the mechanical strength and sanding potential of sandstones was recently published by Wu and Tan (2000). Their work involved mechanical testing on samples with uniaxial compressive strength ranging from 870 to 13,500 psi, i.e. ranging from poorly/weakly consolidated formations to competent high strength rocks; Fig. 2.23 shows the results of uniaxial compression tests for a couple of poorly-consolidated samples. It is important to notice that dilatancy[6] is not observed on the behavior of this type of rocks. This may be due to the fact that dilatancy is associated with the creation and extension of microcracks within an elastic, brittle material. However, unconsolidated rocks are not brittle in nature and behave more plastically throughout the failure process.

[6] Increase in volume with compression relative to the behavior of a linear, elastic material; that is, a relative negative volumetric strain with compression (Jaeger and Cook, 1976).

Nicholson, et al. (1998) presented results of uniaxial compression tests run on samples from three different weakly-consolidated formations around the world: Jurassic 3, a sandstone outcrop on the south coast of England; Saltwash South, a sandstone outcrop from south-eastern Utah; and Red Wildmoor, a Triassic Sherwood sandstone from Wildmoor (Bromsgrove, UK). Table 2.2 shows a summary of these results. From the data corresponding to Jurassic 3 samples, it was observed that rock strength was about three times higher for oven-dried than for fluid saturated specimens. This effect may be the consequence of "water weaking" of clay minerals present in the matrix of the rock[7]. On the other hand, differences in saturated fluid (i.e. water vs. kerosene) had little effect on material strength.

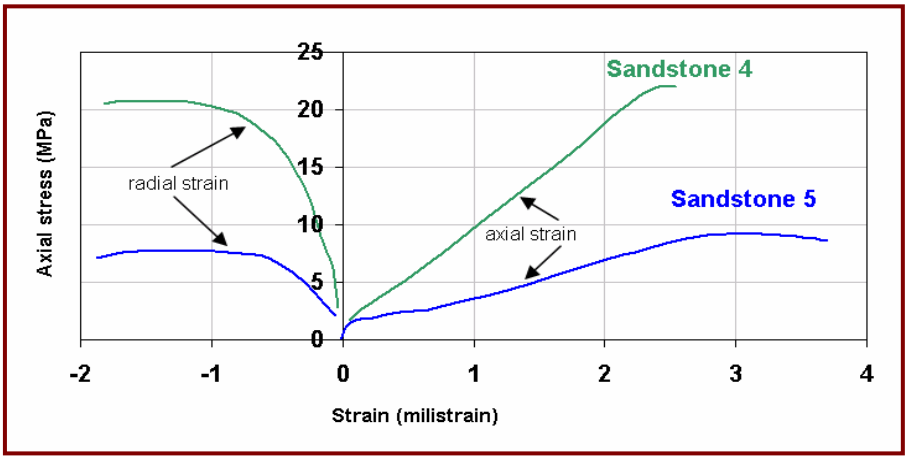

Figure 2-23. UCS on unconsolidated sandstones, 1 mstr = 0.001 (modified from Wu and Tan, 2000)[8].

[7] Currently, there is controversy on the cause(s) of this well documented water-induced weaking effect.
[8] 1 MPa = 145.04 psi.

Sample	Condition	UCS, MPa (psi)	Young's modulus, GPa (psi)	Yield Strength, MPa (psi)
Jurassic 3-H2	Kerosene saturated	2.25 (326)	0.25 (50,750)	2.00 (290)
Jurassic 3-H5	16%vol. water	2.00 (290)	0.33 (47,850)	1.80 (261)
Jurassic 3-G2	Water saturated.	2.10 (304)	0.33 (47,850)	1.70 (246)
Jurassic 3-G4	Oven dried	6.10 (884)	0.71 (102,950)	4.70 (681)
Salt Wash South- N1-3	As received (16%vol. water)	3.40-6.00 (493-870)	0.80 – 1.40 (116,000-203,000)	3.30 – 5.60 (478-812)
Salt Wash South- N4-6	Kerosene	3.20-3.70 (464-1,116)	1.50-1.90 (27,500-275,500)	3.50-7.30 (507-1,058)
Salt Wash South- P7	16%vol. water	4.00 (580)	1.0 (145,000)	3.90 (565)
Red Wilmoor – RP1-3	As received (16%vol. water)	19.00-22.00 (2,755-3,190)	3.40 (493,000)	20.00 (2,900)
Red Wilmoor RP4-6	Kerosene saturated	20.40 (2,958)	3.50 (507,000)	18.50 (2,682)

Table 2-2. Uniaxial compression data for Jurassic 3, Salt Wash and Red Wilmoor formations (modified from Nicholson et al., 1998).

2.4.2 Strength as function of confining pressure - Triaxial Compression Tests

Triaxial compression testing allows for the evaluation of changes on rock strength as a function of the confining stress. Thus, the parameters defining the Coulomb failure criterion for a sample can be readily attained. Triaxial testing conducted at different confining pressures for samples of Antler Sandstone are presented in Fig.2.24. These results were obtained under 1,000; 2,000; and 5,000 psi confining stress. Changes in the slope of the stress-strain curves at different confining pressures indicated stress-sensitivity of the specimen Young's modulus, *E*. The

value of E increased from 0.65 to 3 Mpsi. Furthermore, peak stress was also affected by variations in the confining applied stress, ranging from about 4,000 psi (at σ_3 = 1,000 psi) to more than 12,000 psi (at σ_3 = 5,000 psi). It was also possible to observe increments in the yield point (i.e. the point where the stress-strain curves start to deviate from an ideal straight line) as the confining pressure was increased.

The deformation behavior of weakly- and poorly-consolidated sandstones in the North Sea have also been thoroughly studied. Norita and Ross (1993) presented the outcome of several triaxial tests that showed the relative strengthening of the rock due to increments in the confining stress applied during testing (Fig. 2.25).

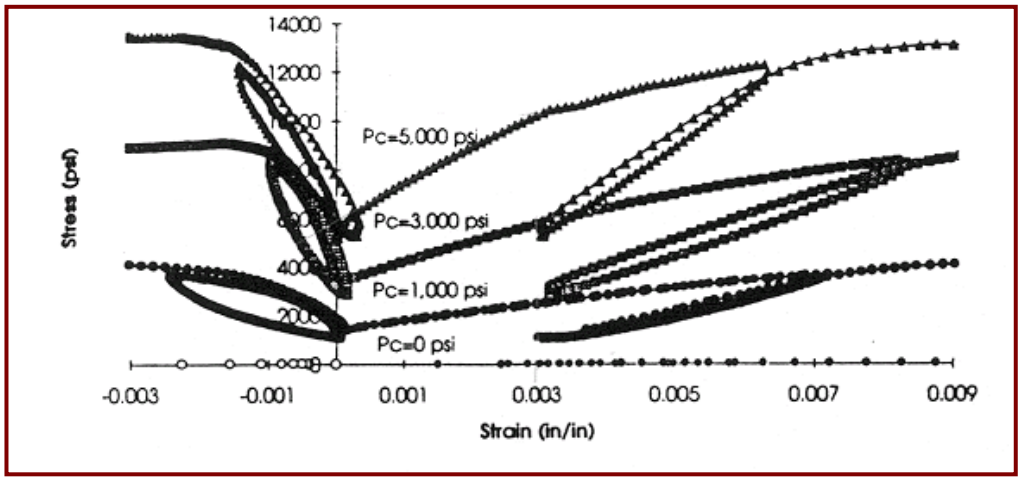

Figure 2-24. Stress-strain curves of Antler Sandstone under different confining pressures (after Wang et al., 1995).

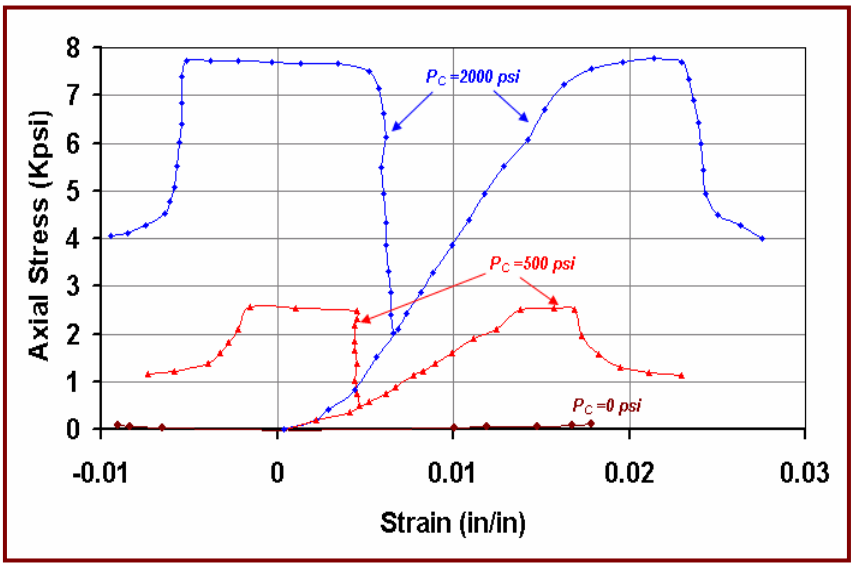

Figure 2-25. Variation of rock response as function of the confining stress (data from Morita and Ross, 1993).

Results from triaxial tests may also be presented as a function of the stress difference during the test. Figure 2.26 depicts curves of the deviatoric stress $(\sigma_1 - \sigma_3)$ normalized with respect to UCS, σ_c, versus axial strain. The lines in this plot correspond to triaxial tests run on weak sedimentary rock samples from Western Taiwan; a rather ductile behavior was evident in most of these results. Further interpretation of these data, following Coulomb's failure criterion, resulted in drained internal friction angles ranging from 30.5º to 36.9º; and effective cohesion values between 0 and 100 psi (Huang et al., 2000). The values of UCS, σ_c, used for constructing Fig. 2.26 ranged from 50 to 420 psi. Triaxial

tests also allow for the identification of the transition from brittle to ductile behavior.

Figure 2.27 presents the results from a series of triaxial compression tests performed on unconsolidated cores from the Adriatic Sea; the minimum effective in-situ stress on these samples was about 20 MPa (2900 psi). It was evident that the brittle-ductile threshold occurred when the axial deviatoric stress overcame this in-situ value, i.e. the curves became non-linear at deviatoric stresses larger than 20 MPa. Marsala et al. (1994) concluded that this was an indication of the Northern Adriatic Sea being a normally consolidated basin.

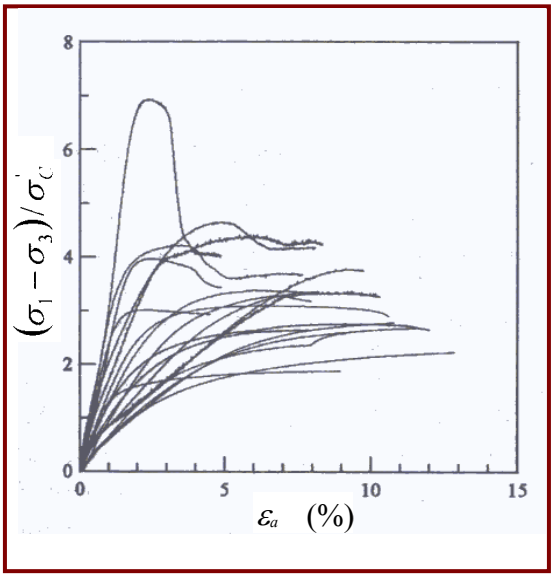

Figure 2-26. Stress-strain relationships from triaxial tests – Western Taiwan sandstone samples (after Huang et al., 2000).

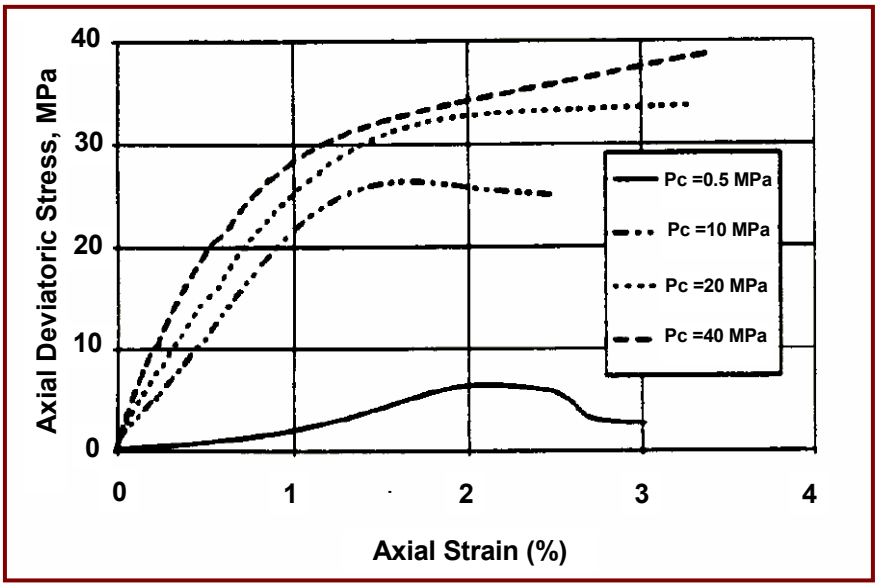

Figure 2-27. Stress-strain relationships from triaxial tests, brittle to ductile transition (after Marsala et al., 1994)[9].

2.4.3 Elastic moduli and their dependency on applied stress

Poisson's ratio, ν, is a very important rock mechanical parameter used to determine the magnitude of the deformations in a direction perpendicular to the applied stress, as related to the deformations parallel to the load. The static Poisson's ratio is defined as the ratio between the change in radial strain and the change in axial strain during a uniaxial compression test (Jaeger and Cook, 1976), thus:

$$\nu = \frac{-\Delta\varepsilon_r}{\Delta\varepsilon_z} \quad \text{.....(2.2)}$$

[9] 1 MPa = 145.04 psi

This value is considered "static" because of the low loading rate normally used during a uniaxial compression test on a core sample. However, cores are expensive and not always available; thus, an estimate based on the velocities of *P*- and *S* –waves is often used. This is called dynamic Poisson's ratio and is calculated as follows:

$$\nu_d = \left[\frac{1}{2}\left(\frac{V_P}{V_S}\right)^2 - 1\right]\left[\left(\frac{V_P}{V_S}\right)^2 - 1\right]^{-1} \quad \text{.....(2.3)}$$

where V_P and V_S are the velocities of the *P*- and the *S*-waves, respectively. It has been found that there may be a large difference between static and dynamic Poisson's ratio values (Fjær et al., 1989; Roegiers, 2004b). Dynamic moduli are obtained through high frequency (small amplitude) oscillations, whereas static moduli are attained using very low frequency perturbations (relatively large amplitude) caused by small variations of stress over time. Experimental results also evidence the fact that the value of static moduli varies during the stress history of the sample: measured Poisson's ratio values change during subsequent loading cycles (Fjær, 1999). Figure 2.28 shows the values of Poisson's ratio measured during a triaxial test on a dry, weak sandstone sample. The acoustic measurements in this figure were performed with broadband ultrasonic transducers at 500 kHz. It is also evident from Fig. 2.28, that the difference between dynamic and static moduli is not a simple constant shift or a constant

ratio. The dynamic Poisson's ratio exhibited little variation throughout the test and behaved almost linearly; whereas the static Poisson's ratio ranged between 0.1 at the beginning of the test, and more than the unity[10] at rock failure (Larsen et al., 2000). The linear behavior of the dynamic Poisson's ratio may be more readily identified in Fig. 2.29; in this plot, the observed Poisson's ratio appears to increase as the shear stress on a sandstone core plug is augmented. The porosity of the rock sample was 25%, and the confining pressure was 15 MPa (2175 psi).

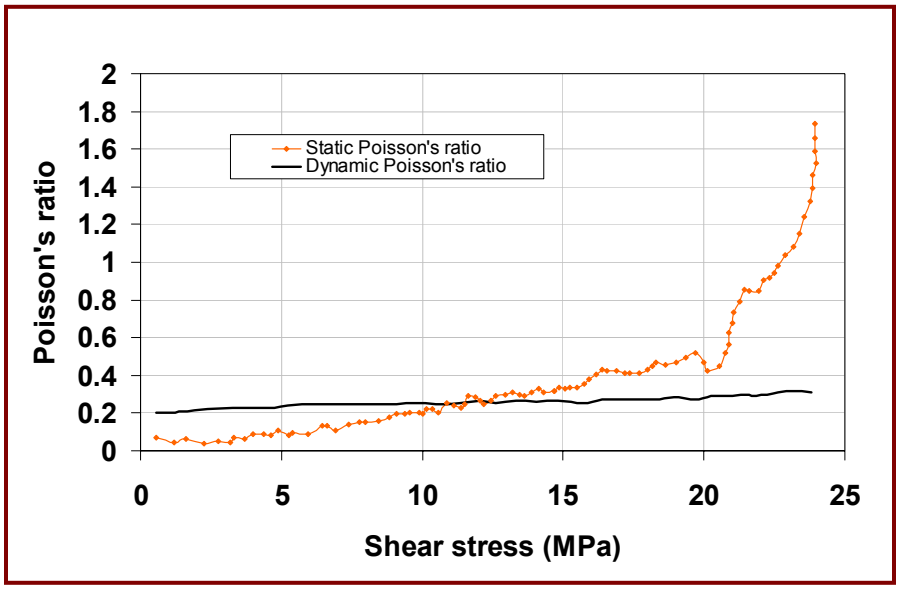

Figure 2-28. Static and dynamic Poisson's ratio as function of shear stress (data from Larsen et al., 2000).

[10] This value is theoretically impossible for a homogeneous material.

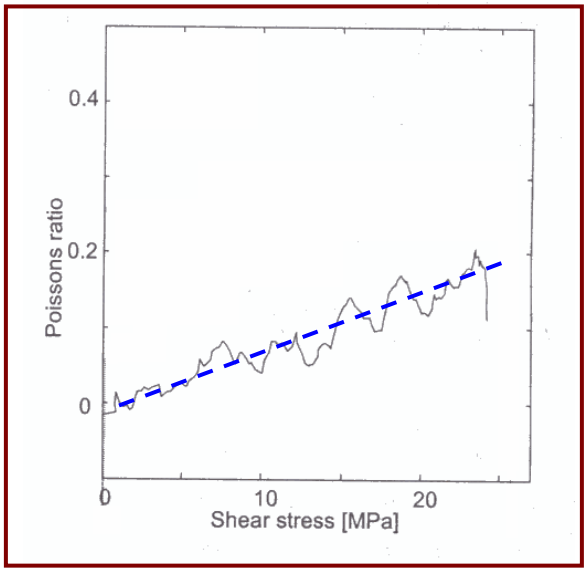

Figure 2-29. Dynamic Poisson's ratio as function of shear stress – North Sea samples (modified from Larsen et al., 2000).

Fjær (1999) analyzed the results of a series of triaxial tests carried out on samples from weak sandstones of the North Sea; he compared the magnitudes of dynamic and static Young's moduli (Fig. 2.30). This figure presents a stress-strain curve for one of his samples under large confining stress. It is apparent, once again, that the relation between static and dynamic moduli was not defined by a constant or a constant ratio; the two moduli appeared to vary rather independently as stress was increased[11]. The dynamic Young's modulus exhibited small variations, even at peak stress conditions. On the other hand, static Young's modulus was very sensitive to changes in stress and changed dramatically throughout the test;

[11] It has been found that, under similar conditions of stress and temperature, the ratio of static to dynamic rock elastic properties measured in the lab is equal to the ratio found in the field, i.e. $(E_S / E_d)_{lab} = (E_S / E_d)_{field}$, (Roegiers, 2004a).

ranging from 2.175 Mpsi (15GPa) at the beginning of the deformation process to almost zero at peak stress.

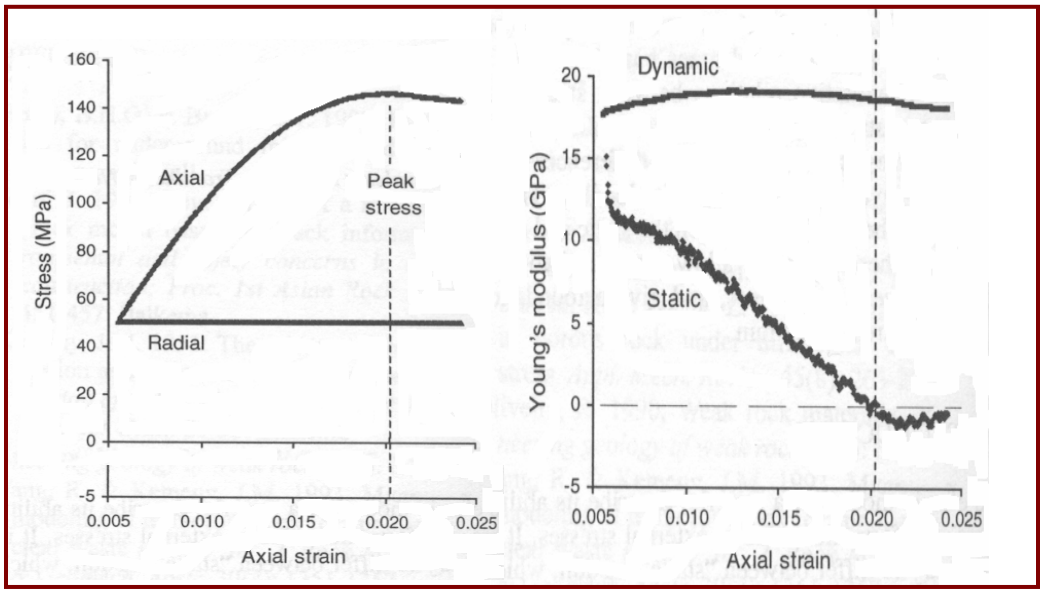

Figure 2-30. Static vs. dynamic Young's moduli as function of stress – North Sea samples (after Fjær, 1999)[12].

The values of Young's modulus and Poisson's ratio have also been found to be a strong function of both the effective mean stress, $P = (\sigma'_1 + 2\sigma'_3)/3$, and the loading stress-path (Figs. 2.31 and 2.32). According to these results, the magnitude of the Young's modulus for an unconsolidated rock may be sharply decreased when the corresponding loading stress path, K[13], is equal to zero. On the other hand, the value of Young's modulus may be dramatically augmented

[12] 1 GPa≈ 145,000 psi and 1 MPa ≈ 145.04 psi

[13] The stress path, K is defined as: $K = (d\sigma'_3 / dt)/(d\sigma'_1 / dt)$

when the sample is subjected to a loading stress path equal to 1, i.e. both the confining pressure and the axial load are increased at the same rate. Similarly, Poisson's ratio may experience large variations in magnitude as the conditions of stress and loading path are altered. A potential cause for this behavioral dependency on the loading stress path may be severe rock sensitivity to changes in shear stress. Thus, for a corresponding loading path, K^{13}, equal to zero the increment in shear stress is maximized and the rock suffers certain degree of "weakening" during the deformation process. On the other hand, when the corresponding loading path is equal to one there is no increment in the value of shear stress, and the rock appears to retain its strength.

These variations on rock mechanical moduli may cause important changes in the geometry of hydraulically induced fractures in weakly-consolidated materials. If the Young's modulus of the rock is assumed to be proportional to the applied stress and the value of Poisson's ratio is taken as constant, the hydraulically induced fractures will tend to be shorter and wider than those created assuming constant Young's modulus formations. This point is further illustrated at the end of this chapter in the comments section.

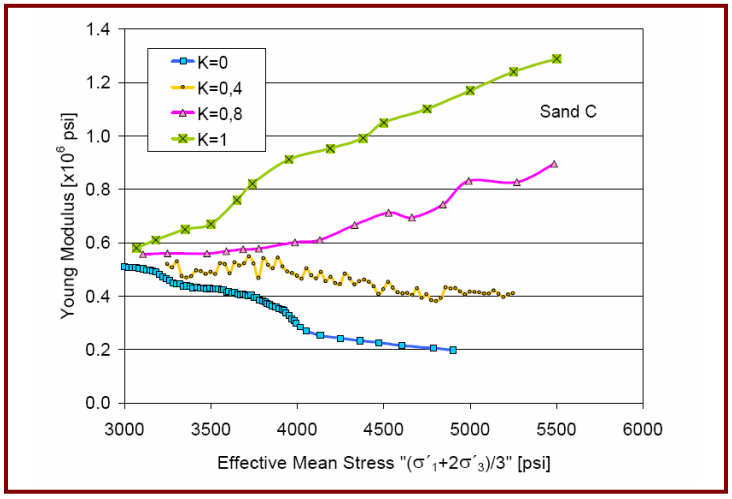

Figure 2-31. Young's modulus vs. effective mean stress for different values of K, starting at P_C=5400 psi and P_P=2000 psi[14] (after Franquet and Economides, 1999).

Accurate characterization of sand strength is critical during the discovery, development, and productive life of a weak/unconsolidated formation. Currently, techniques based on correlations allow the estimation of cohesion and internal angle of friction from well log responses. The validity of such an approach depends greatly on the rock types and conditions used to develop these correlations, and whether those conditions are similar to the ones where the correlation is to be applied. Figure 2.33 shows a "strength log" synthetically built from analyses of the formations sonic response; the left plot shows the input data and the log on the right represents the correlation output. In order to build this plot, Ong et al. (2000) used a theoretically based model; which was integrated with statistically obtained correlations accounting for variations in lithology and

[14] P_C = confining pressure and P_P= pore pressure

porosity. The main limitation of this approach is determined by the applicability of these lithology correlations; however, little additional information is provided in Ong et al.'s publication as this is a company owned model.

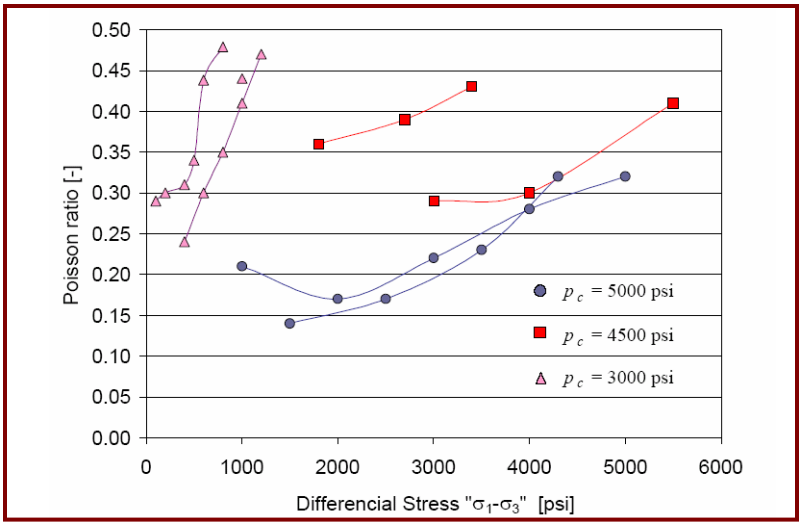

Figure 2-32. Poisson's ratio vs. differential stress for different values of P_C with constant P_P=2000 psi (after Franquet and Economides, 1999)

High pore pressure is commonly associated with poorly-consolidated formations; this is due to their immature geological nature. In these rocks, the consolidation process is halted by the deposition of overlying sealing sediments (shales), which impedes the ejection of the fluids saturating the compacting rock. The final result is that an abnormally large portion of the overburden stress is transferred to the interstitial fluid (increasing the pore pressure). Overpressured zones in sediments can be detected by observing a decrease in elastic velocities (V_P and V_S),

accompanied by an increase in Poisson's ratio. Moreover, in highly overpressured sands, the *P*- to *S*-wave velocity ratio increases, being as high as 10 and even higher, due to the uncemented nature of the rock (Lee, 2003). Experimental results showed that the velocity ratio, V_P/V_S, may be expressed as a function of the differential pressure (Lee, 2003). Figure 2.34 shows a composite of data published by different authors, where velocity ratio exhibits a linear behavior for differential pressures ranging between 0.5 and 50 MPa (72-7200 psi).

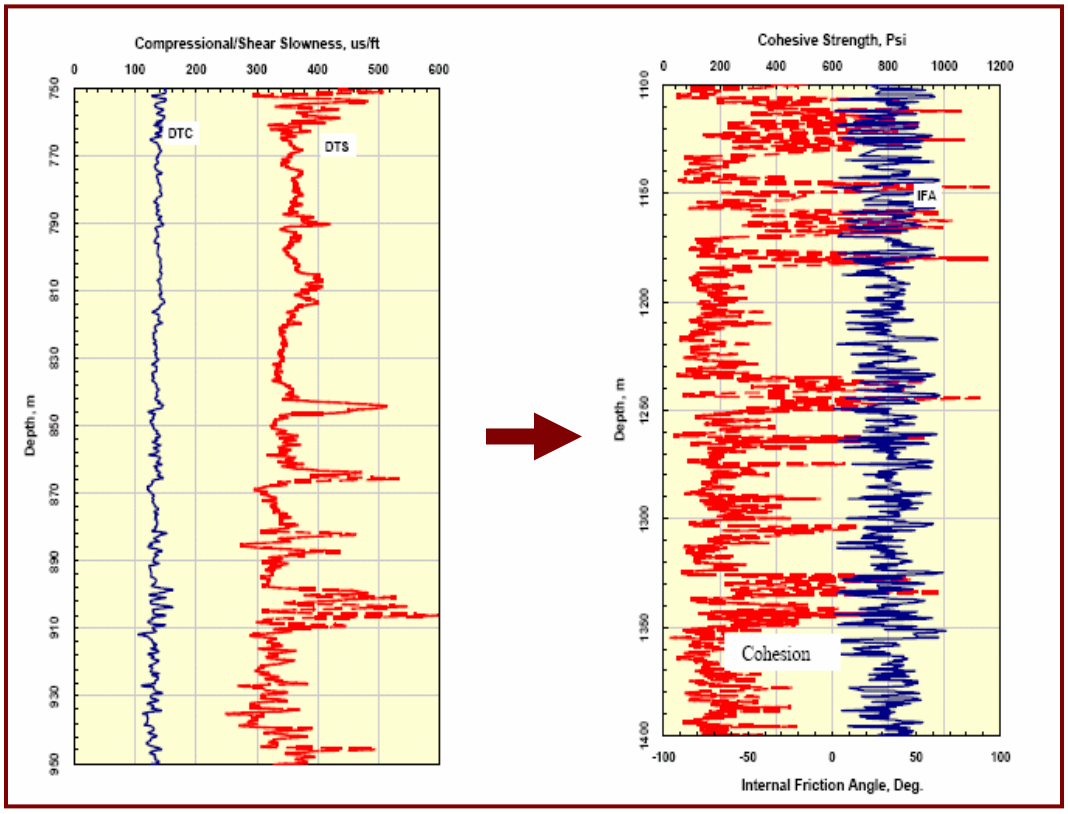

Figure 2-33. "Strength" log showing the estimated values of cohesion and internal friction angle, IFA (after Ong et al., 2000).

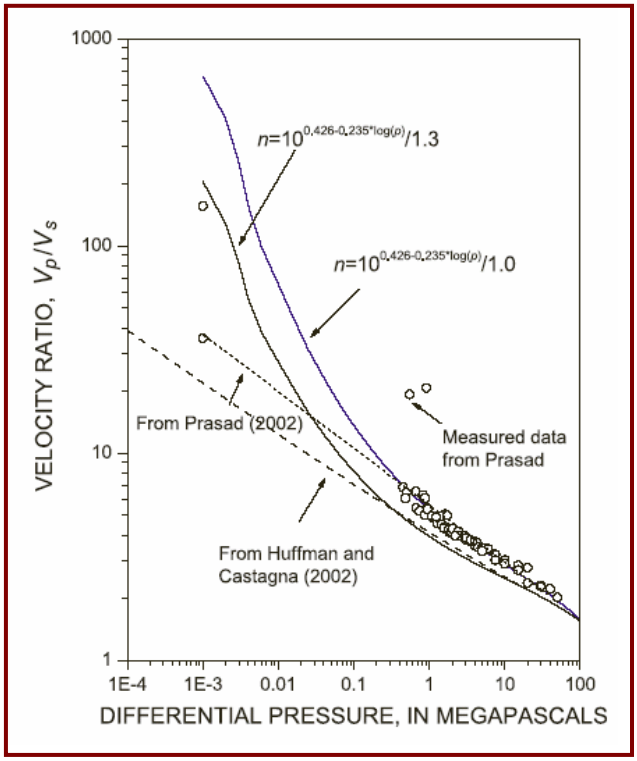

Figure 2-34. Wave velocity ratio as function of differential pressure (after Lee, 2003) data from Prasad (2002); and Huffman and Castagna (2001).

Differential pressure, clay content, porosity, degree of consolidation, and other parameters influence the values of V_S, V_P, and their ratio in rocks. Figure 2.35 presents the wave velocity ratio as a linear function of shear wave velocity, V_S. The plot of V_P/V_S against differential pressure (Fig. 2.34) shows some scattering in the data presented by several authors; whereas the plot of wave velocity ratio vs. V_S (Fig.2.35) exhibits a unique trend for the published data from all authors.

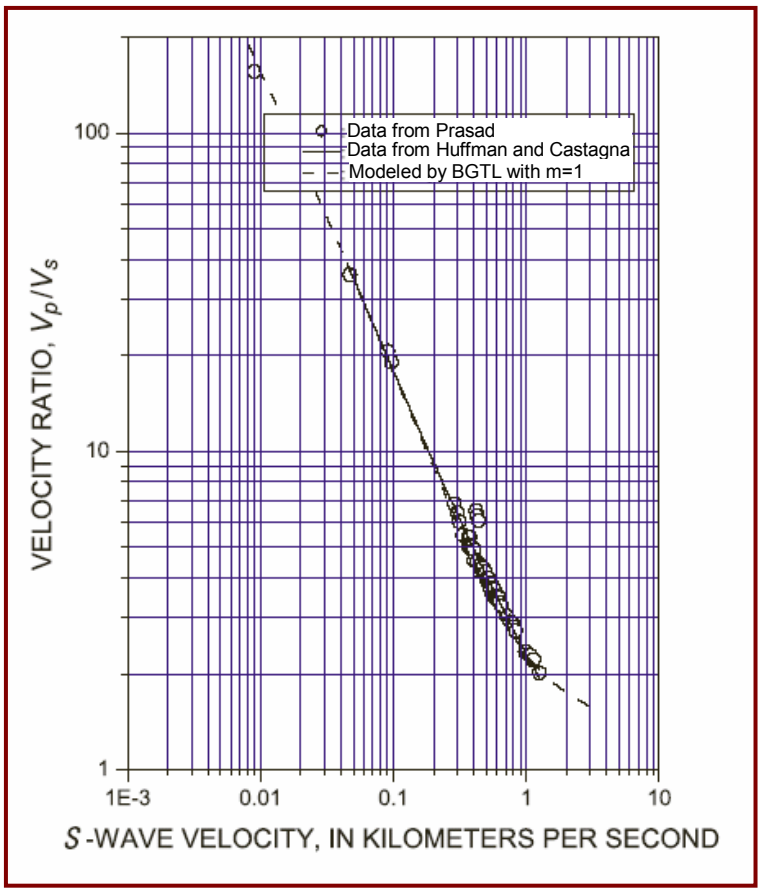

Figure 2-35. Wave velocity ratio as function of shear wave velocity (after Lee, 2003) data from Prasad (2002); and Huffman and Castagna (2001).

2.4.4 Shear Strength

The shear strength of rocks is often defined by the Mohr-Coulomb theory; linear variation of strength is assumed to occur throughout a wide range of applied stress. Thus, only two rock strength parameters are used to define the rock failure stress region: cohesion, *c,* and angle of internal friction, ϕ:

$$\tau = c + \sigma_n \tan\phi \quad \text{.....(2.4)}$$

where, τ = shear stress

σ_n = normal stress

Berardi et al. (1994) published values of these two parameters for weak rocks from the Langhe region in Italy; Table 2.3 presents a summary of their results. Studies on the mechanical properties of some weak rocks in Russia were presented by Sapegin et al. (1981); they measured the variations on the values of cohesion and internal friction angle parallel and perpendicular to the rock layering (Table 2.4). It is apparent that the value of cohesion is not relevant for poorly-consolidated formations; i.e. cohesion values in the order of a few psi are negligible when it comes to stress and failure analysis of underground rock structures.

Site	**ϕ (°)**	***residual* ϕ (°)**	**Cohesion (psi)**	**Residual cohesion (psi)**
Gottasecca	29.0	29.0	29.0	24.7
Gottasecca remolded	30.0	30.0	14.5	14.5

Table 2-3. Friction angle and cohesion values – unconsolidated sands from North West Italy (modified from Berardi et al., 1994)

Shearing direction , rock description	ϕ (°)	Cohesion (psi)	Rock pressure (psi)	
			Vertical	*Lateral*
Along layers, weak rock, air dry	31.8	18.6	9.86	4.50
Along layers, weak rock, saturated	25.6	14.6	10.59	5.94
Across layers, weak rock	27.0	56.26	10.44	5.51

Table 2-4. Friction angle and cohesion values – Ust-Illim Plant samples- Russia (modified from Sapegin et al., 1981)

The Coulomb criterion for shear failure is very easy to apply because of its simplicity; however, it has been pointed out that shear strength variation with confining pressure is a non-linear process (Ramamurthy, 2001). Thus, a single set of cohesion and friction values may not be sufficient to describe the rock behavior throughout a wide range of stress. Several other compressive failure criteria have been proposed over the years: Tresca, Hoek & Brown, von Mises, and octahedral shear among others (Roegiers, 2004b). Some of these criteria account for a three-dimensional system of stresses acting on the rock; however, their use demands prior knowledge of rock properties that are not always easy to obtain. In more recent years, a new model, which accounts for the non-linearity of the shear strength function, was proposed by Ramamurthy (2001); i.e.

$$\frac{\sigma_1^{'} - \sigma_3^{'}}{\sigma_3^{'} + \sigma_t} = B\left(\frac{\sigma_c}{\sigma_3^{'} + \sigma_t}\right)^{\alpha} \quad \text{.....(2.5)}$$

where,

- σ_1'and σ_3'= effective principal stresses acting on the rock
- σ_c = uniaxial compressive strength of the material
- σ_t = rock tensile strength
- B and α = strength parameters (material constants)

The parameters B and α can be obtained from linear regression as a log-log plot of $(\sigma_1' - \sigma_3')/(\sigma_3' + \sigma_t)$ vs. $(\sigma_c)/(\sigma_3' + \sigma_t)$ is built with lab data from triaxial tests. α is the slope of the fitted straight line, and B becomes its intercept at x=1. Figures 2.36 and 2.37 present some experimental results obtained on samples from weakly-cemented soils. In cohesionless, uncemented rocks, such as is the case of poorly-consolidated formations, the value of the tensile strength is negligible; thus, Equation 2.5 reduces to:

$$\frac{\sigma_1' - \sigma_3'}{\sigma_3'} = B\left(\frac{\sigma_c}{\sigma_3'}\right)^{\alpha} \quad \text{.....(2.6)}$$

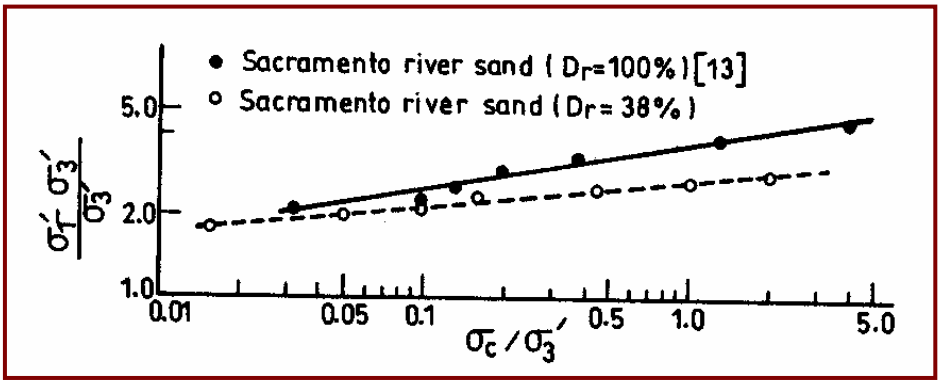

Figure 2-36. New shear failure criterion – Sacramento River sand (after Ramamurthy, 2001).

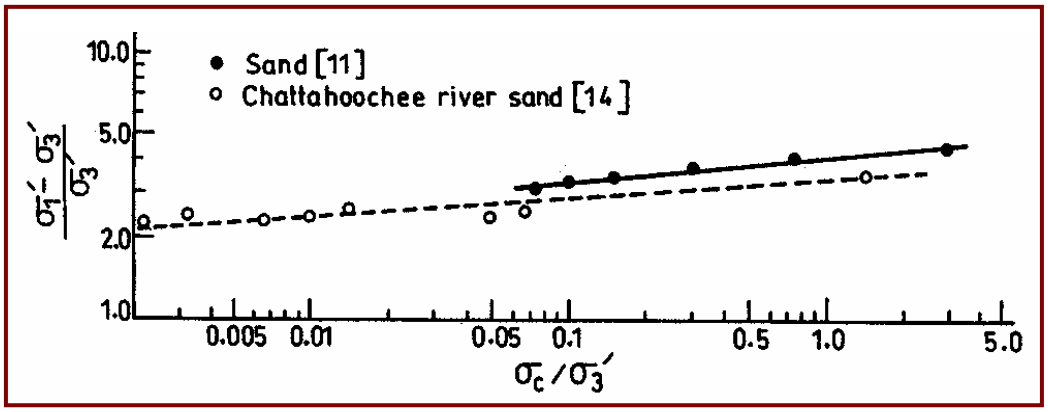

Figure 2-37. New shear failure criterion – Chattahoochee River sand (after Ramamurthy, 2001).

2.4.5 Creep

Significant creep (i.e. time-dependent strain) has been reported from testing unconsolidated and very weak core material (Ostermeier, 1993). Uniaxial-strain compaction tests performed on Brazos River Sand and on GOM samples were published by Dudley et al. (1998). In their experiments, they evaluated the effect of changes in the duration of the stress-hold period (Fig. 2.38). The longest test shows substantial creep, although the final strains achieved by all three tests were similar. The magnitude of strain during each stress hold period varied from about half to more than ten times the strain measured during each stress-ramp step. Figure 2.39a shows an alternative way to analyze the data of Fig.2.38: this time the axial strain was plotted against a normalized time function, defined as the ratio of time and step duration. In this figure, the deformation behavior observed during the three tests was very similar, suggesting creep strain time-scaling. The

initial deviation of the 1.5-hour period data from the other two tests was attributed to the time required for the stress increase ramp (7% of the total step interval). Figure 2.39b presents the same analysis for samples from a GOM reservoir; again, some data deviation for the test with 1.5 hour period was evident.

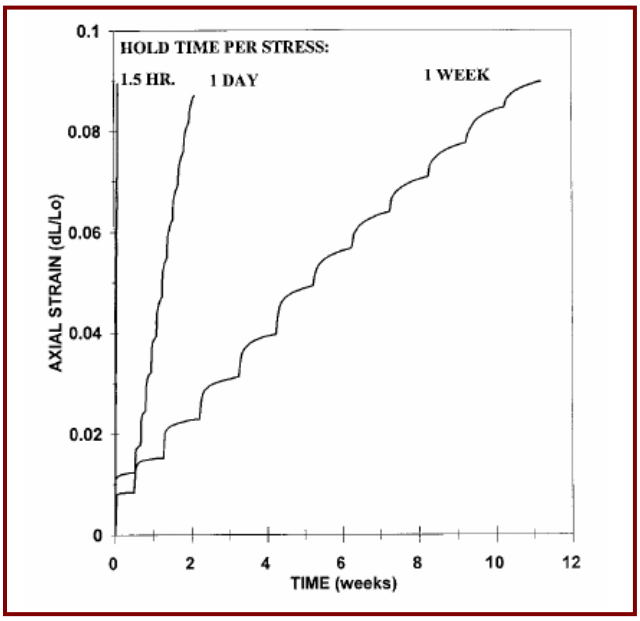

Figure 2-38. Axial strain vs. time for three 750 psi axial stress step increase uniaxial creep tests on Brazos River samples, Max. axial stress = 8000 psi (after Dudley et al., 1998).

The uniaxial compaction coefficient C_m, defined as $d\varepsilon_z / d\sigma_z$, is plotted as a function of axial stress for both the Brazos River sand (Fig. 2.40a). In this case, the compaction coefficient is large at the beginning of the loading, but decreases exponentially as the stress is increased (probably due to crushing of the pore structure). In contrast, the compaction coefficient for the GOM sand is relatively

low for small values of applied load (Fig. 2.40b), and it increases considerably as the rock yields under increasing load. This plastic deformation continues until the ultimate strength of the material is reached; then, the compaction coefficient decreases again as the pores get crushed.

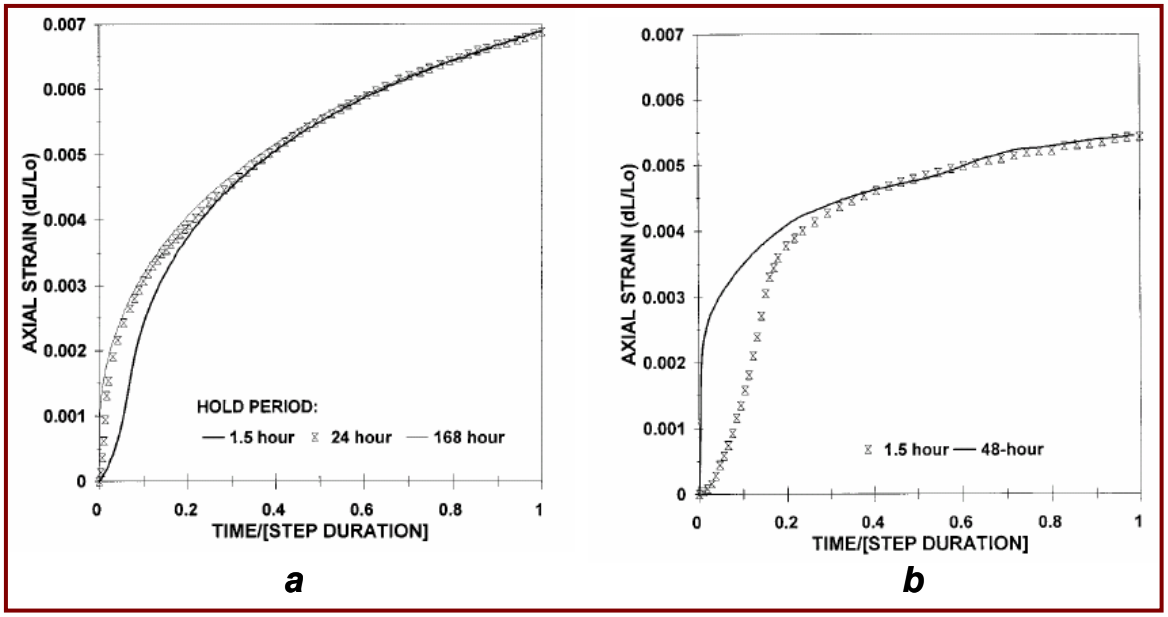

Figure 2-39. Axial strain vs. normalized time: a). Brazos River sand; b). GOM reservoir sand for axial stress increment to 4300 psi (after Dudley et al., 1998)

Pure creep[15] has been observed in laboratory tests under drained conditions and constant effective stress. Uniaxial compaction causes rock stiffening, observed as an increased quasi-consolidation pressure. In order to cause further material consolidation, the applied stress must exceed this value of quasi-consolidation

[15] Creep is defined as the occurrence of time-dependent deformation under constant load. If load is applied to a rock with creeping characteristics, the resulting deformation is not instantaneous but increases with time. The magnitude of this increment depends on the loading magnitude relative to the rock strength (Roegiers, 2004b).

pressure or yield stress. Yield pressure increases as the time of consolidation augments, i.e. the rock appears to become stiffer with time/age (Lade, 1999). This is expected as compaction and cementation are processes that occur over long periods of time, i.e. older rocks are more likely to undergo more complete cementation and compaction. Results from triaxial compression and uniaxial strain testing on unconsolidated samples from the Wilmington Field (California) and the South Eugene Island Field (GOM) were published by Chang and Zoback (1998). Table 2.5 presents a summary of some physical characteristics of the samples used during their study. They performed constant load creep tests on the specimens by first raising the axial load at a rate of 10 MPa/min (1450 psi/min) and then holding the load constant while keeping a constant (servo-controlled) confining pressure. Creep response was observed for all samples; Fig. 2.41 shows the results for the Wilmington and South Eugene Island samples. Based on these results, the values of the relaxation times were calculated for both rocks and are reported in Table 2.6.

The relaxation times for the South Eugene Island sand were shorter than those obtained for the Wilmington sand. These results are not surprising, as the sample from the South Eugene Island had a clay content which is about half of the clay content for the Wilmington specimen. Creep is usually associated to plastic materials such as clay and salt.

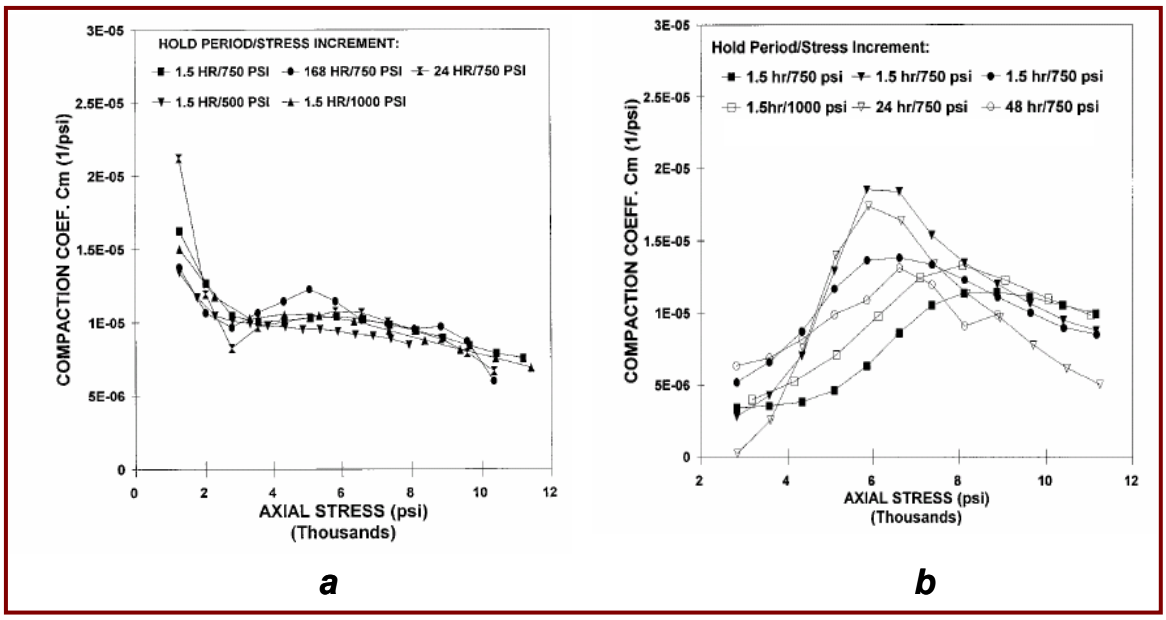

Figure 2-40. Uniaxial compaction coefficient Cm vs. axial stress: a). Brazos River sand; b). GOM reservoir sand (after Dudley et al., 1998).

In addition, pore fluid compression experiments were performed on the samples in order to study the transient increase of pore pressure associated with creep compaction under polyaxial stress. The South Eugene Island specimen exhibited a time-dependent raise in pore pressure, along with pore volume reduction under constant loads (Fig. 2.42). Pore pressure increased transiently, and almost reached the value of the confining stress, P_C. The results for Wilmington sand also showed creep; however, the deformation behavior was not always stable, possibly due to the lag between strain changes and stress perturbations in the sample.

Sample	Porosity (%)	Avg. grain size (μm)	Clay content (%)	Grain morphology
Ottawa sand	34	500	5-10	Rounded, well sorted
Wilmington sand	35-39	300	<10	Angular, poorly sorted
South Eugene Island Lentic sand	36	100	<5	Angular, well sorted

Table 2-5. Some physical properties of the samples used by Chang and Zoback (1998).

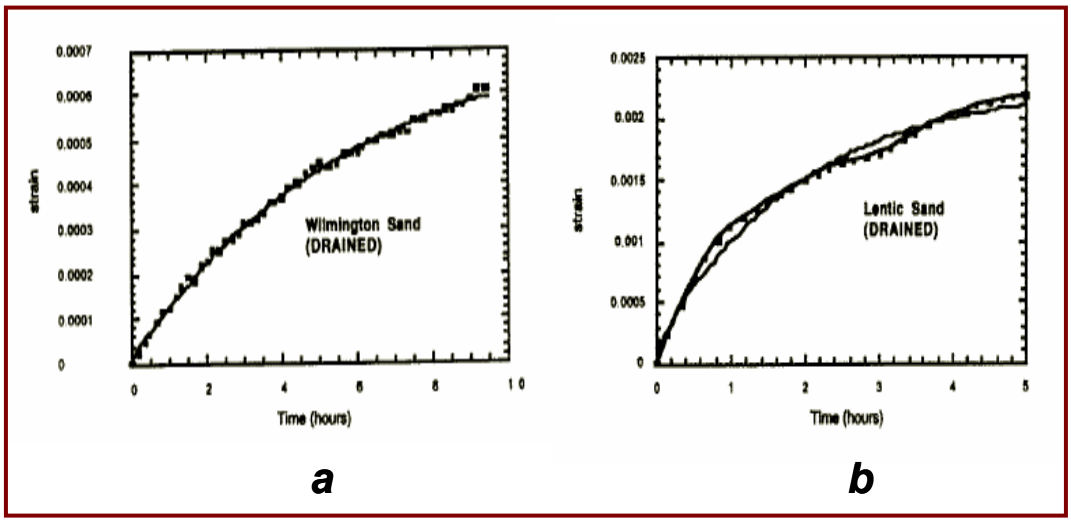

Figure 2-41. Constant load creep tests: a). Wilmington sand; and b).South Eugene Island sand (after Chang and Zoback, 1998).

Sample	Relaxation time (hrs)	P_C (psi)	σ_1 (psi)
Wilmington sand	5.70	3190	3625
South Eugene Island Lentic sand	1.88	1450	2610

Table 2-6. Creep parameters obtained during triaxial test (modified from Chang and Zoback, 1998).

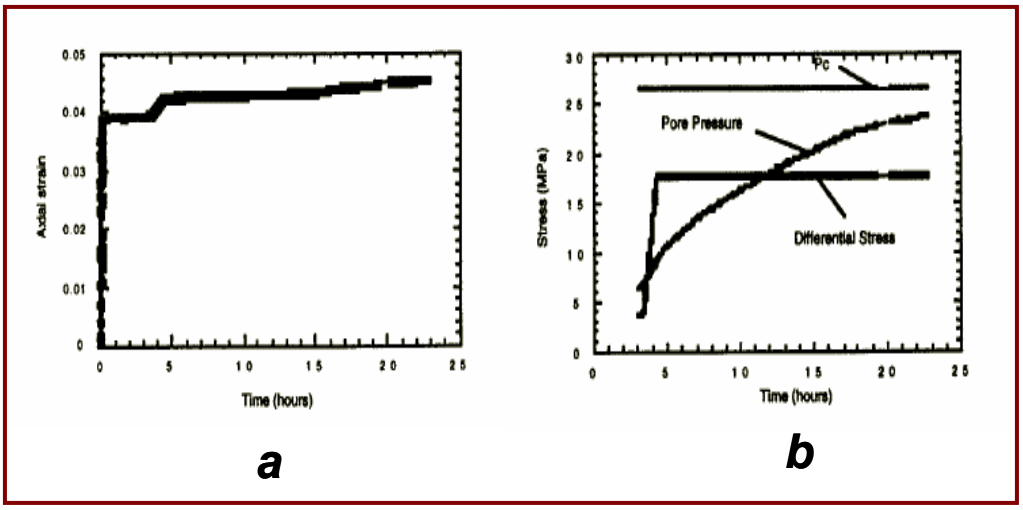

Figure 2-42. Polyaxial creep test, South Eugene Island sand (after Chang and Zoback, 1998).

2.5 Effects of changes in saturation on rock mechanical properties

The values of V_P, V_S, and their ratios are affected by rock saturation, and also by the sample porosity. Dry and water-saturated compressional and shear velocities on unconsolidated North Sea sandstones, were measured at values of effective stress ranging between 5 and 30 MPa (725 to 4,350 psi) by Strandenes and Blangy. (1991). When the magnitude of effective stress was equal to 30MPa (4,350 psi), the dry V_P varied between 2,100 m/s (6,900 ft/s) and about 2400 m/s (7,875 ft/s) for the samples porosity range (Fig. 2.43). Noticeable variations took place on V_P and V_S upon water saturation: increment in magnitude ranged between 5% and 21% for V_P, whereas V_S decreased between 2% and 19%. This saturation effect may be caused by fluids other than water, as demonstrated by

Seifert et al. (1998). In their experiments, several non-aqueous phase liquids, such as n-dodecane, iso-octane, and freon were used to saturate unconsolidated sands; *P*- and *S*-wave velocities were measured throughout the tests (Fig. 2.44).

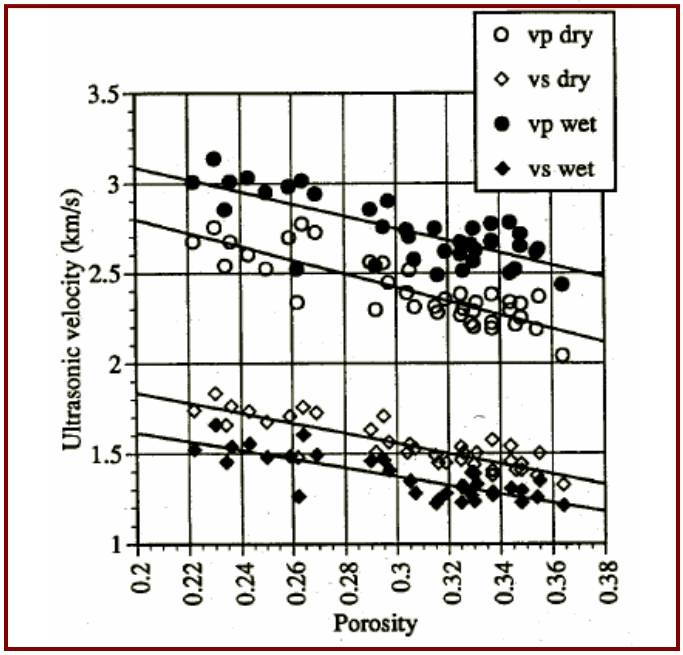

Figure 2-43. Dry and water saturated compressional and shear wave velocities at 30 MPa (4350 psi) (after Strandenes and Blangy, 1991)

The increments in liquid saturation cause the *P*-wave velocity to augment, as expected; the velocity of a compressional wave traveling through a liquid being higher than its velocity traveling through air. In contrast, the *S*-waves transmission becomes more difficult as the wetting fluid increments the bulk density of the rock; thus, decreasing the wave velocity according to the equation:

$$V_S = \sqrt{G/\rho} \quad \text{.....(2.7)}$$

Knowledge of the effects of water-rock interactions on the mechanical properties of rocks is critical in all aspects of rock engineering. This is especially true in the case of poorly and un-consolidated formations in petroleum engineering; as they are weak materials, and even relatively small changes in rock strength could translate in serious productivity losses and even borehole failure. The consequences of changes in water saturation on rock mechanical properties have been comprehensively studied in the past (Dyke and Dobereriner, 1991; Hawkins and McConnell, 1992; Baud et al., 2000).

It is well known that many water-saturated rocks exhibit lower values of strength when compared to their magnitudes measured under "dry" conditions (Wu and Tan, 2001). In some rocks, increments in water saturation may cause dramatic decrements on the rock compressive strength as published by Colback and Wiid (1965). They performed a set of uniaxial compression tests, under eight moisture content conditions, on a quartzitic sandstone specimen (Fig.2.45). The uniaxial compressive strength of the water-saturated sandstone was about 50% lower than of its dry counterpart; whereas for the shale specimens, the strength dropped almost 40% as the sample was saturated with water[16]. In addition, triaxial tests were carried out on the same types of rocks; results are shown in Fig. 2.46.

[16] As shales are mostly saturated by water, one could question these results. Possible rock alterations due to contact with air, could be responsible for this "saturation effect".

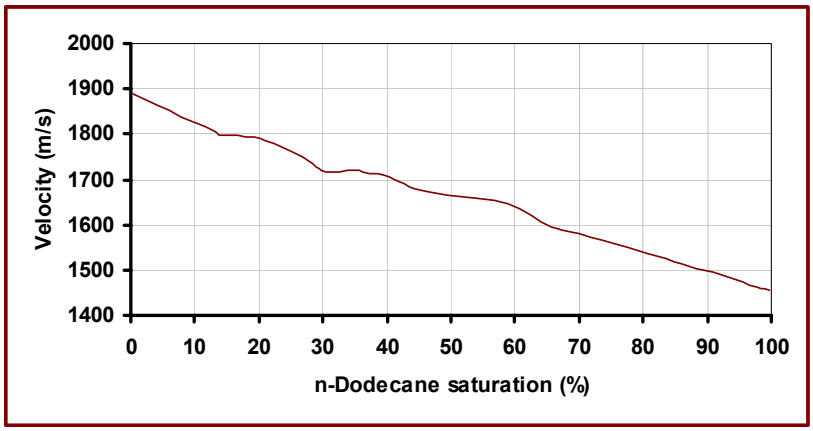

Figure 2-44. Effect of non-aqueous phase saturation on compressional wave velocity (data from Seifert et al., 1998).

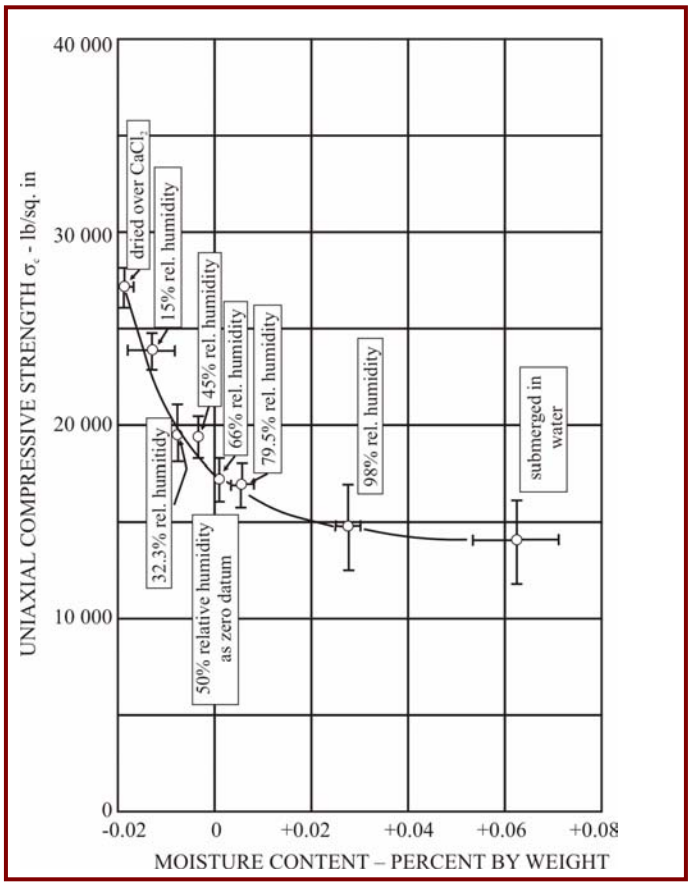

Figure 2-45. UCS vs. rock moisture content: Ecca series quartzitic sandstonę, ϕ =15% (after Colback and Wiid, 1965).

The value of inherent cohesion in the Coulomb failure envelopes appear to diminish as the water saturation increases. This provides experimental evidence that an effective weakening process occurs in the rock, as consequence of the water presence. On the other hand, the coefficient of internal friction, i.e. the envelope inclination, seems to be rather insensitive to changes in the rock moisture content. Thus, it has long been accepted that the reduction in rock strength with increasing moisture content is caused by changes in the molecular cohesive strength of the material. In these experiments, the sample moisture content was calculated, relative to a datum condition, as follows:

$$Moisture\ content\ (\%) = \frac{W_t - W_O}{W_O} * 100 \quad \text{.....(2.8)}$$

where, W_O: weight of the specimen at the datum condition (50% humidity)

W_t: weight of the specimen at the time of testing

Although the results shown in Figs. 2.45 and 2.46 were not performed on unconsolidated formations, they provide a useful insight on the mechanical behavior of sandstones when subjected to changes in water saturation. Similar conclusions were published by Wu and Tan (2001), based on the outcome of a series of UCS and triaxial tests carried out on sandstones ranging from weakly/poorly consolidated to highly cemented. Figure 2.47 presents the results

obtained during a series of tests conducted on a weakly consolidated sand with 26.5% porosity, and 1,116 psi initial oil-saturated strength. These results showed that strength reduction, in the case of this weak sand, was a strong function of water saturation. It was also observed that most of the strength reduction occurred for $S_w < 60\%$, i.e. at moisture content of 8% for this sandstone.

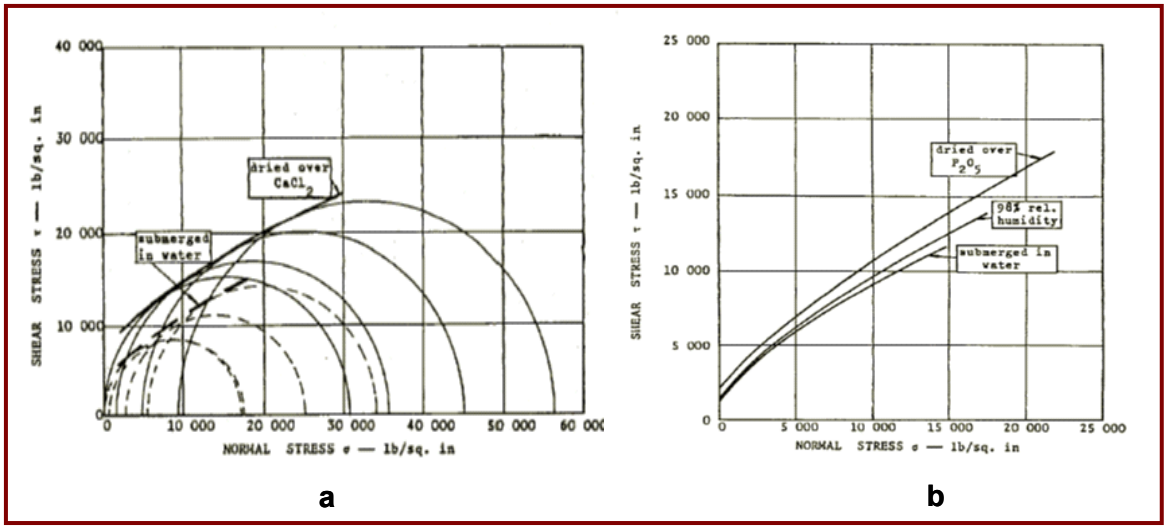

Figure 2-46. Variation of the Coulomb failure envelope as a function of water saturation: a).Jeppestone quartzitic shale, ϕ=0.28%; and b). Ecca series quartzitic sandstonę, ϕ=15% (after Colback and Wiid, 1965).

A study, focused on the effect of water on the strength of weak sandstones, was published by Rhett and Lord (2001). In their paper, the outcome of ten triaxial tests performed on 24-25% porosity reservoir sandstones was presented. These samples were cleaned using alternate extractions of methanol and toluene, then oven dried and saturated with 3% KCl solution. The cohesive strength for these water-saturated rocks was 480 psi, their internal angle of friction ranged between

24 and 25°, while the value of Young's modulus was equal to $7.7*10^5$ psi (see dots in Fig. 2.48). In addition, they presented the results of several uniaxial strain compression tests carried out on the samples from the same cores used for the set of triaxial tests. These specimens were cleaned following the same procedure outlined above; however, they were saturated with decane instead of 3% KCl solution. Each sample was then brought to 7,000 psi pore pressure, 7,100 psi confining pressure and 7,600 psi axial stress on a triaxial loading cell. This was the starting point for the uniaxial strain loading; subsequent to this, each sample was loaded along a stress path of 0.25, i.e. σ_c / σ_v was kept equal to 0.25 at all times. Loading of the specimens was stopped at different levels of stress (see open squares in Fig. 2.48). Each plug was then injected with one pore volume of 3% KCl solution. After this, plug 5 immediately failed in shear, along a high-angle fracture. Most of the other samples showed rapid axial and radial deformation, and finally prolonged axial creep behavior. Plugs 6, 7, and 8 were failed by increasing the pore pressure while maintaining a constant stress field; the unloading path until failure occurred is shown by the arrows in Fig. 2.48.

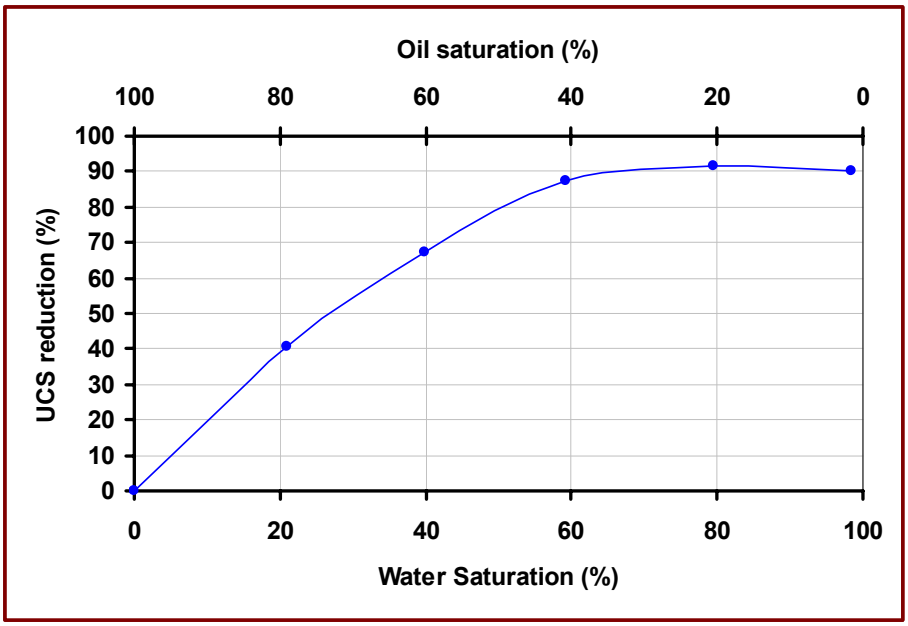

Figure 2-47. UCS reduction (related to its oil-saturated value) vs. water saturation; sandstone sample, initial oil-saturated UCS equal to 1,116 psi (data from Wu and Tan, 2001)

It has been observed that the effect of water on rock strength varies widely for different kinds of rock. Dyke and Dobereiner (1991) studied the changes in uniaxial compressive strength as a function of moisture content on three different sandstones. They concluded that, overall, the strength sensitivity of the rock to increments in water saturation was inversely proportional to its dry unconfined compressive strength, i.e. the weaker the original rock, the higher its strength reduction when water-saturated.

An analogous conclusion may be drawn from the results by Wu and Tan (2001), as they observed that the amount of strength reduction due to water saturation was

decreased as the rock dry strength increased (see blue dotted line in Fig. 2.49). Oil saturation has a far less important impact on the rock strength, and a trend on its weakening effect as a function of dry strength is not readily identifiable (see green dots in Fig. 2.49). This correlation between the severity of the water weakening effect and the dry strength of the rock is not always identifiable as concluded by Hawkins and McConnell (1992).

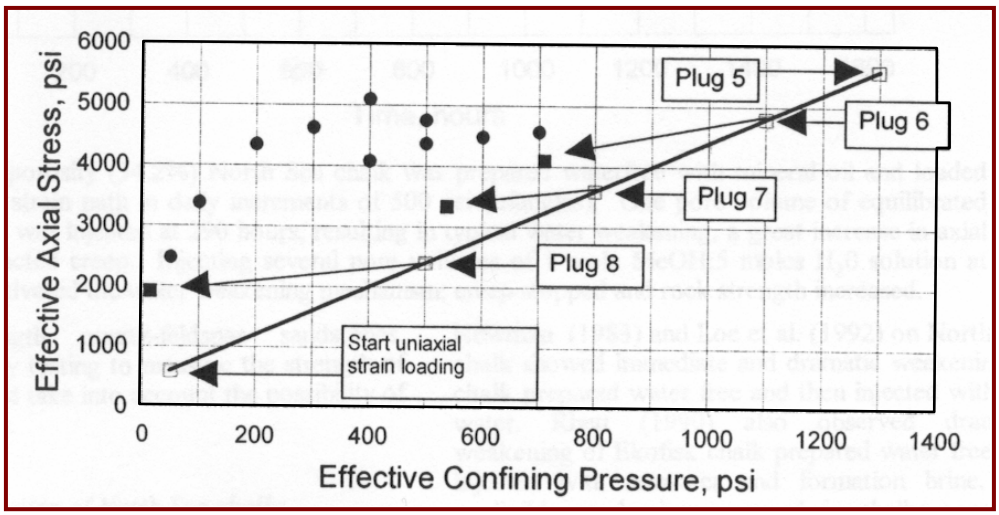

Figure 2-48. Results of a series of triaxial tests (dots) and uniaxial compression tests (squares), (after Rhett and Lord, 2001)

The effect of loading rate on the water weakening process on sandstones was examined by Hadizadeh and Law (1991). In their study, uniaxial compression tests were carried out on samples from Oughtibridge ganister and Pennant sandstone. The first is a relatively pure quartzite of Devonian age from the English Midlands; it is mainly composed of quartz (98%), plant remains, and oxide inclusions. The latter rock, on the other hand, is an impure, poorly-sorted

sandstone of Upper Carboniferous age from South Wales; its main mineral components are quartz (50%), feldspar and mudstone clasts (25%), and clay mineral cemented by ferruginous/calcareous material (25%). The results of the experiments failed to show a clear dependence of the water weakening effect on the stress and strain rate (Fig 2.50). However, these results suggested that one of the key parameters in determining the magnitude of the water weakening effect on sandstones was the rock mineralogy. The tests on quartzite showed a gentle weakening trend for water-saturated samples as the stress rate decreased. However, there was no apparent difference in the magnitude of the strength loss between the dry and the water-saturated specimens (Fig. 2.50a). In contrast, striking differences were observed between the strength of oven-dried and water-saturated samples for the Pennant sandstone. The UCS of the water-weakened material being about 55% of the dry rock UCS at all applied stress levels (Fig. 2.50b). Hadizadeh and Law (1991) also pointed out, that although the strength of the rock was dramatically reduced in the water-saturated samples, the shape and magnitude of the axial, circumferential and, to a lesser extent, volumetric strain curves were very similar regardless of specimen saturation. They suggested the existence of a structural damage (deformation) threshold that needed to be overcome for failure to occur, regardless of the chemical process acting on the material.

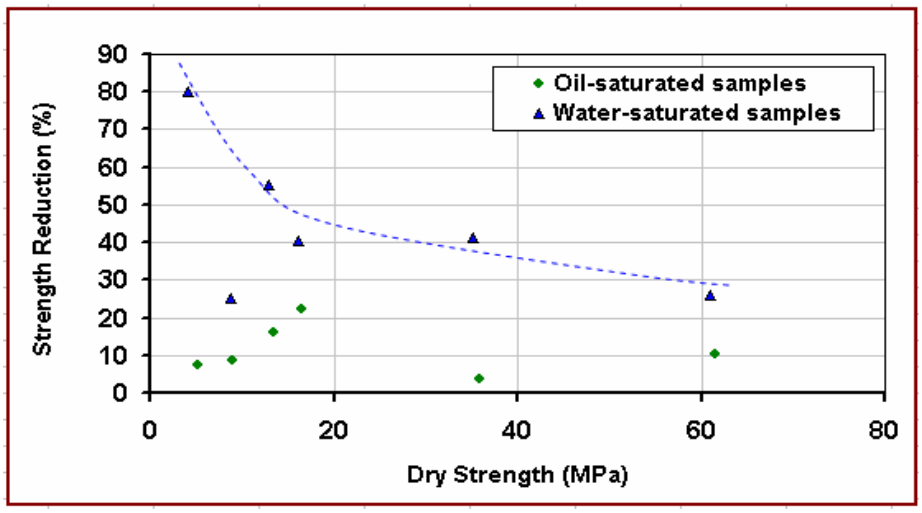

Figure 2-49. Sandstones UCS reduction (related to its dry value) as function of fluid saturation (data from Wu and Tan, 2001).

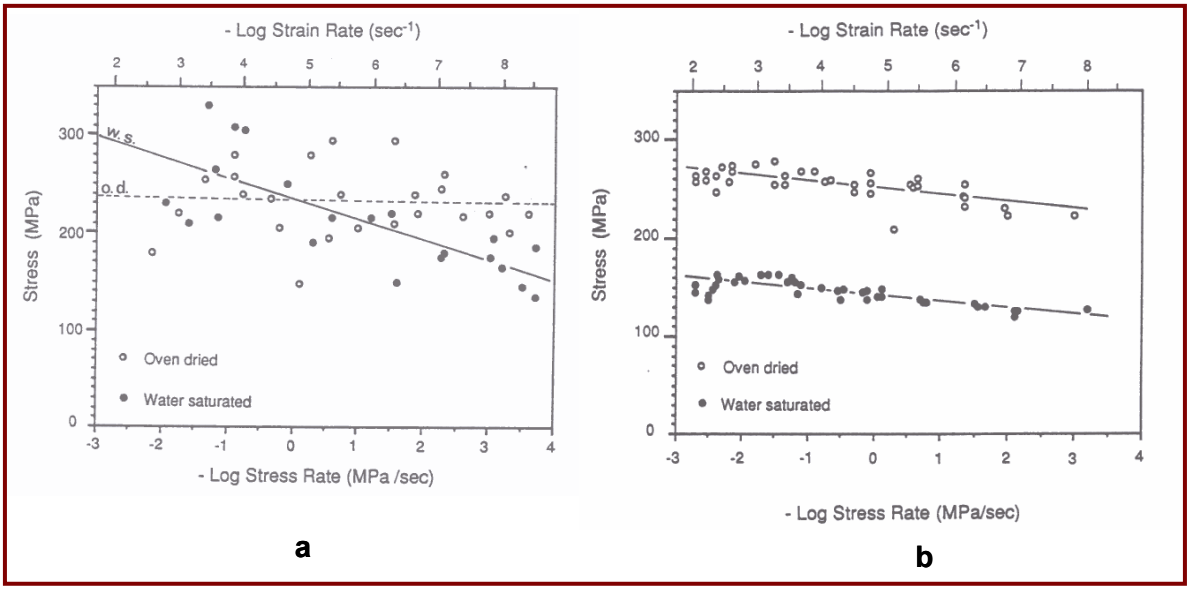

Figure 2-50. UCS of water-saturated and oven-dried vs. stress rate: a). Quartzite (98% quartz); and b). Pennant sandstone (50% quartz + 25% clay), (after Hadizadeh and Law, 1991).

Hawkins and McConnell (1992) also observed that, in general, the ratio of volumetric clay fraction to quartz content determines the amount of water

weakening suffered by a given rock. The magnitude of strength loss due to water saturation (as a percentage of oil-saturated strength) vs. total clay content, for a set of sandstones is shown in Fig. 2.51. A correlation between the clay content and the amount of water weakening was apparent in most of the samples. A comparable tendency was also obtained for samples saturated with 20% water and 80% oil. Nonetheless, no visible trend was found for the case of oil saturation-induced rock weakening. Moreover, the type of clay appeared unrelated to the strength reduction. In Fig. 2.51, the results from two specimens with low permeability appeared to fall outside the main trend (see enclosed data points in Fig. 2.51). This may be the result of both incomplete saturation due to low rock permeability, and strong capillary pressure in a partially saturated material (Wu and Tan, 2001).

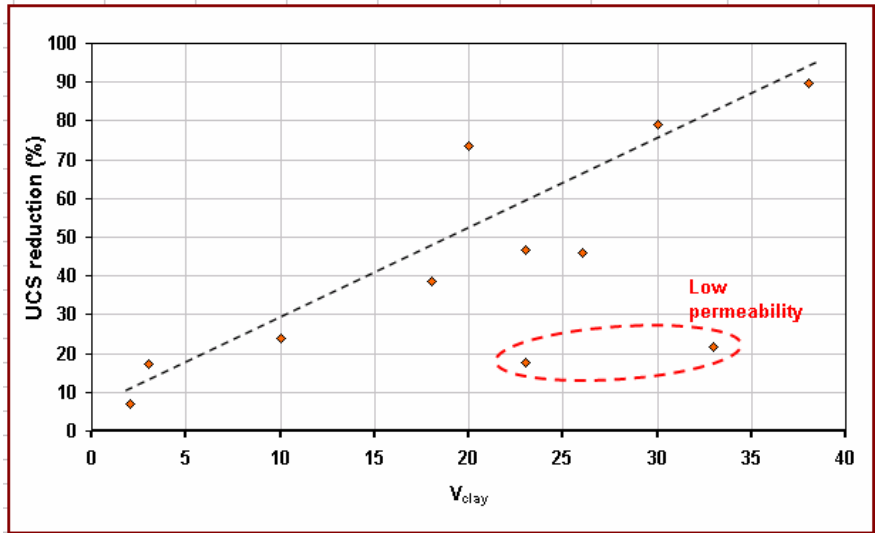

Figure 2-51. UCS reduction vs. total clay content. Strength reduction is defined as percentage of oil-saturated strength (data from Wu and Tan, 2001).

Although there is plenty of experimental evidence of their existence, the physicochemical processes involved in water-originated alterations on the rock mechanical properties are not yet fully understood. It has been suggested that at temperatures between 77 and 392 °F, the water weakening effect is caused by a reduction of the surface free-energy of the rock, stress corrosion, or a combination of both (Hadizadeh and Law, 1991). According to Colback and Wiid (1965), the reduction in rock strength with increasing moisture content is mainly caused by changes in the molecular cohesive strength of the material. As indicated by Orowan (1949), the value of the molecular cohesive strength, σ_m, for an elastic/brittle material is given by:

$$\sigma_m = \sqrt{\frac{2\gamma E}{a}} \quad \text{.....(2.9)}$$

where,
- γ = surface-free energy of the material
- E = Young's modulus
- a = spacing between neighboring atomic planes

It has long been hypothesized that the fluid environment has a major effect on the fracture strength of glass, silica, and quartz (Orowan, 1949; Rebinder and Lichtman, 1957; Cottrell, 1964). The combination of all the surface-strength interaction is referred to as the "Rebinder effect". This effect applies to all

substances, metal and non-metal, and comprises surfactant action, surface coatings, and dissolution of surface material. The surface energy[17] effect, explicitly, applies to brittle solids. This suggests that the surface energy process, in general, is important only in high quartz content and highly competent sandstones. The fluid environment changes the surface energy of solids by adsorption or desorption of surface molecules and ions. .

From Eqn. 2.9, it is evident that the rock strength varies proportional to the square root of the surface energy of the material. Colback and Wiid (1965) postulated that the rock strength was a strong function of the surface tension of the fluid saturating the rock; higher surface tension saturating fluids caused more rock strength weakening (Fig. 2.52). They concluded that changes in fluid saturation altered the value of the surface free energy within the rock. An intrinsic assumption in their conclusion was that the values of Young's modulus and atomic spacing remained constant throughout the saturation process (Eqn. 2.9). The effect of adsorbed vapors of water and organic liquids on the surface energy of quartz is shown in Table 2.7; the reported change is referenced to the value of surface-energy measured at vacuum conditions.

[17] The surface free energy of a solid is the amount of work required to produce a unit area of surface by a reversible and isothermal process (Swolfs, 1971).

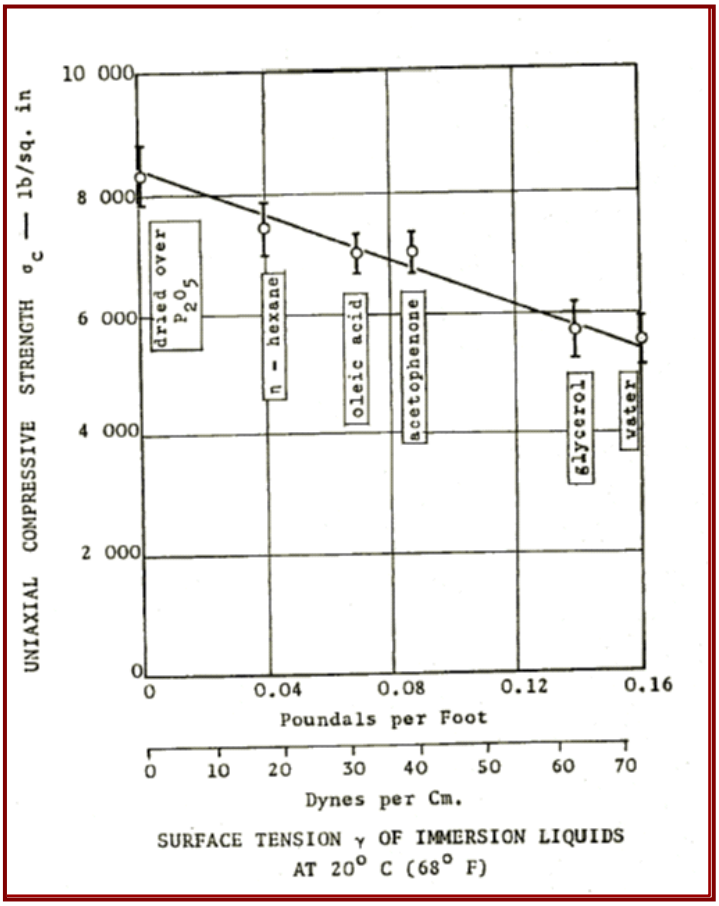

Figure 2-52. Uniaxial compressive strength vs. surface tension of the saturating fluid (after Colback and Wiid, 1965).

Saturated vapor	Surface-energy decrease, *ergs/cm²*
Water	244
n-propylacohol	110
Acetone	85
Benzene	52

Table 2-7. Surface-energy decrease of quartz in various saturated vapors (after Boyd and Livingston, 1942).

Based on the assumption of constant mechanical moduli throughout the saturation process, Colback and Wiid (1965) singled out the surface free energy as the only parameter sensitive to changes in water content (see Eqn. 2.7). Nevertheless, visible changes in both Young's modulus and Poisson's ratio were observed for weakly consolidated formations[18] (see items in Table 2.8). In general, the value of Young's modulus decreased as water saturation increased, whilst the magnitude of Poisson's ratio was proportional to the water content. The variations in the values of both parameters, Young's modulus and Poisson's ratio, seem to be consistent with a general process of weakening triggered by increments in the rock moisture content. Results of a series of uniaxial compression tests, carried out on 35 sandstones from the United Kingdom (Hawkins and McConnell, 1992), found great variations on the reduction of the Young's modulus value as the samples were saturated with water (Fig. 2.53). However, no particular trend was found between the magnitude of reduction in the value of *E* and the dry UCS of the specimens.

As stress is increased, Si-O bonds are broken due to fracturing; these broken bond ends and the surface of the created fracture are intrinsically unstable. Since quartz, amorphous silica, and glass surface hydroxylate upon exposure to water (Snoeyink and Weber, 1972), the reacting surface is dominated by SiOH or

[18] The terms "unconsolidated" or "weakly-consolidated" are hereby used for rocks with UCS less than 25 MPa (3625 psi), (ISRM, 1981).

silanol groups. Additional water adsorbs at rising water vapor pressures, hydrogen bonding to silanol until a continuous network of water molecules coats the surface. The adsorbed water adjacent to the surface is oriented and has properties (e.g. dielectric constant, and mobility) that differ from those of bulk water. These differences vanish as the thickness of the adsorbed film increases beyond the equivalent of perhaps three monolayers (Parks, 1984). Figure 2.54 illustrates schematically the hydroxylation and adsorption processes occurring at the quartz-water interface. It is apparent that the hydroxylation of the quartz surface decreases dramatically its surface free energy; hence, lowering the mechanical strength of the rock. Despite the sharp decrease in rock strength that may be caused by the quartz-water interaction, surface free energy reduction is a weakening mechanism that is important only in rocks with very high low V_{clay}/V_{quartz} ratio. On the contrary, in rocks with relatively high clay mineral content (or in rocks with clay matrix), the softer clay will be more likely to suffer most of the weakening effect. In clays, the most important deteriorating processes may be surfactant action, surface coatings, and dissolution of surface material (Swolfs, 1971).

UCS (psi)[19]	Young's modulus (psi)				Poisson's ratio			
	Dry	*Oil sat.*	*20/80 (w/o)*	*Water sat.*	*Dry*	*Oil sat.*	*20/80 (w/o)*	*Water sat.*
1,015	130,500	159,500	188,500	174,000	0.21	0.28	0.42	0.47
4,814	913,500	913,500	580,000	536,500	0.37	0.38	0.49	0.45
1,479	174,000	174,000	130,500	116,000	0.10	0.10	0.10	0.15
551	87,000	87,000	43,500	14,500	0.13	0.10	0.12	0.25
1,711	348,000	275,500	261,000	246,500	0.36	0.30	0.37	0.37
7,801	1,725,500	1,319,500	1,247,000	1,203,500	0.36	0.30	0.32	0.40
13,412	---	2,842,000	---	2,726,000	0.28	0.23	---	0.19
11,469	---	1,261,500	---	710,500	---	0.26	---	0.38
1,116	---	203,000	101,500	14,500	---	0.31	0.39	0.44
1,421	---	159,500	---	29,000	---	0.15	---	0.24
15,950	---	2,856,500	---	2,624,500	---	0.20	---	0.15

Table 2-8. Variation of elastic moduli as a function of water saturation (modified from Wu and Tan, 2001).

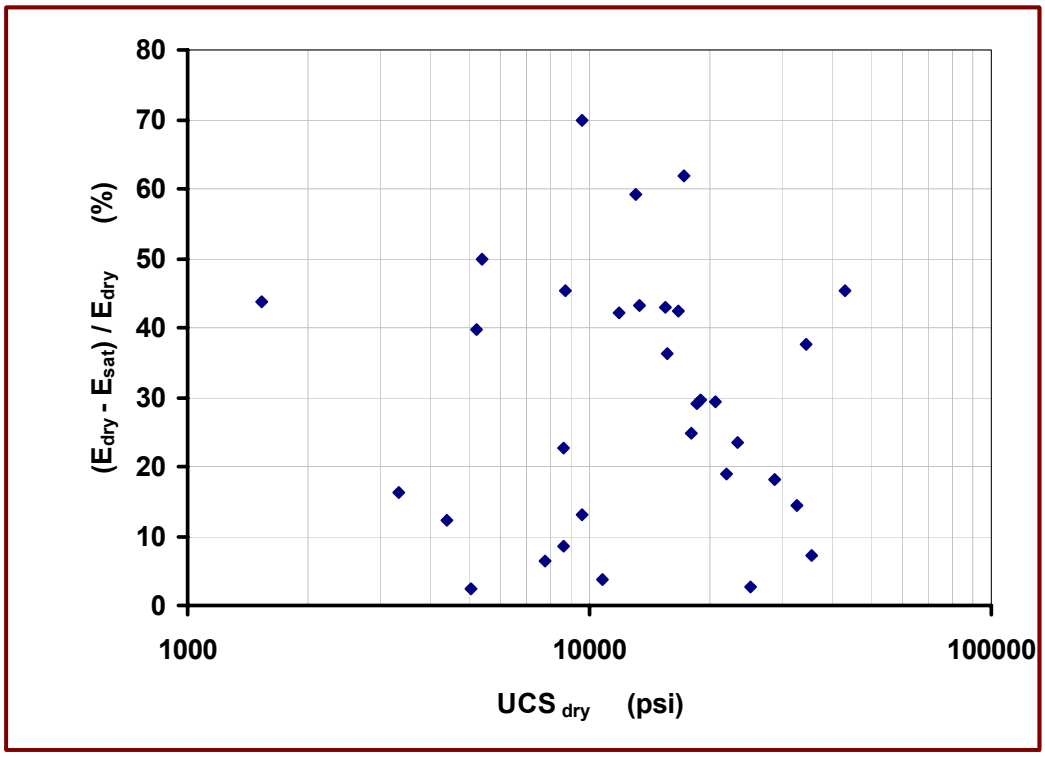

Figure 2-53. Young's modulus reduction due to water saturation, UK sandstones (built with data from Hawkins and McConnell, 1992).

[19] UCS measured under 100% oil-saturation conditions.

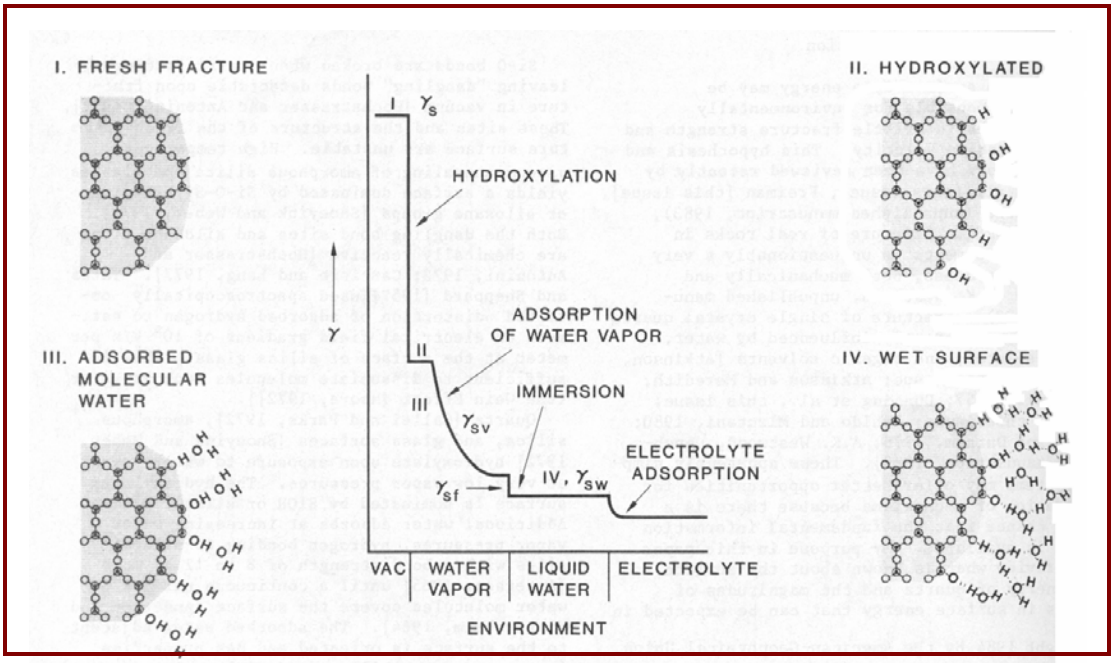

Figure 2-54. Interaction of water with quartz surfaces and associated surface free energy changes (after Parks, 1984).

Overall, the strength sensitivity to changes in water saturation is controlled primarily by the rock mineralogy, and to a lesser degree, by the rock microfabric. The relative proportion of quartz-to-clay minerals is perhaps the most important parameter determining the rock response to changes in moisture content, i.e. rocks with higher V_{clay} / V_{quartz} ratios normally suffer more strength reduction due to water saturation (Wu and Tan, 2001). Hawkins and McConnell (1992) proved that weak sandstones are not necessarily more sensitive to changes in moisture content. They published several results where high strength sandstones showed greater relative strength loss than weaker sands. From their results, they concluded that although stress corrosion is significant in quartz-rich sandstones,

clay softening becomes a more important weakening factor for clayey sandstones. This conclusion seems logical, since it is expected that the presence of water would trigger dissolution and swelling of the clay minerals present in the rock; before causing any changes in the surface of the relatively harder quartz grains.

2.6 Comments on the mechanical properties of unconsolidated rocks

Initially, most porosity and compaction models considered depth of burial as the single most important parameter determining rock porosity changes (Sclater and Christie, 1980). These early models had a marked tendency to overpredict the magnitude of compaction in unconsolidated formations. This was probably due to the inelastic nature of the compaction process. However, more comprehensive models taking into account the effects on rock porosity of changes in rock mineralogy, grain sorting, depth, and age have been proposed more recently (Scherer, 1987). The correlation obtained between these models and the results from core measurements is remarkable (Fig. 2.9). Although more inclusive, these models are normally valid only for rocks within the same depositional basin. This limitation may be originated in the fact that these rock behavior representations disregard the effects that alterations on the sedimentation environment, the stress field, and the degree of cementation could have on both porosity and

permeability. There is still need for more general models applicable to different depositional environments, and different cementation characteristics. Nonetheless, the complexities of dealing with as many inter-dependent parameters make this task a formidable challenge.

There is a general consensus on the fact that changes in rock porosity correspond to much larger variations in permeability. It is also accepted that permeability in weakly consolidated formations is far more sensitive to changes in stress deviatoric (i.e. shear stress) than to increments in the value of hydrostatic stress (Kilmer et al., 1987). In fact, it appears that poorly-consolidated materials suffer less permeability reduction than competent rocks when subjected to similar increments in hydrostatic pressure (see Fig. 2.14). This may be due to the fact that material microcracking, often believed to be the major mechanism causing permeability alteration in low permeability rocks, is not as important in high porosity, poorly-cemented formations. On the other hand, small changes in the shear stress applied to weak rocks may cause significant grain re-arrangement, and, consequently, considerable permeability alteration. Highly variable and often very low differential stress conditions are frequently found in poorly consolidated formations (Finkbeiner and Zoback, 1998). Thus, shear stress conditions ranging from high to almost non-existent can be found in nature, making permeability and porosity prediction more difficult.

Weakly consolidated formations have, typically, very low rock mechanics parameters values. Uniaxial compression strength values as low as 80 psi have been reported (Morita and Ross, 1993), whilst the magnitude of Young's modulus is normally in the order of hundreds of thousands psi. These values are normally used for predicting the deformational behavior of these formations; sometimes UCS and Young's modulus are the only input used to predict rock strength. Thus, correct rock mechanical characterization of hydrocarbon producing formations is critical throughout all stages of field development, completion and production. However, standard rock mechanics tests, such as uniaxial/triaxial compression experiments, are very difficult to perform on weakly consolidated formations given the friable nature of the samples. In addition, concerns about rock alterations suffered during the coring, handling, transport, and storage processes have been expressed by several authors (Santarelli and Dusseault, 1991; Brignoli et al., 1998). In particular, in-situ stress and pore pressure release during coring have a heavy effect on rock properties. Thus, the original in-situ rock characteristics may be considerably modified during coring, handling, and transport operations; rendering the results obtained from laboratory testing rather inadequate for representing the reservoir formation (Brignoli et al., 1996). The issue of rock "remolding" caused by coring, handling, and testing techniques will be more thoroughly studied in the next chapter of this dissertation.

Throughout this study it was found that in general, poorly consolidated sands tend to show rather low values of Young's modulus, ranging from about 1.38 GPa ($0.28*10^6$ psi) to about 10.34 GPa ($1.5*10^6$ psi). Likewise, the values of UCS are lower than 25.00 MPa (3,625 psi); sometimes as low as 0.69 MPa (100 psi). These typical ranges are plotted in Fig. 2.55 by using the Deer and Miller classification.

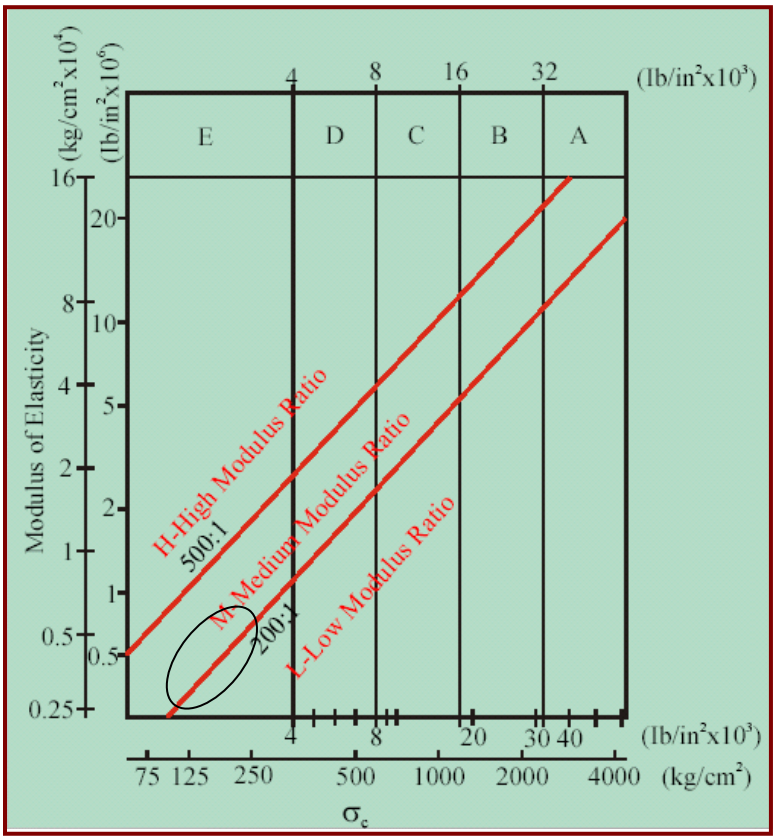

Figure 2-55. Typical mechanical properties of unconsolidated sandstone (blue circle), plotted using Deer and Miller rock classification (Deer and Miller, 1966).

Standard hydraulic fracturing simulators consider that the deformation behavior of the formations being fractured is fully characterized by the values of their Young's modulus and the minimum principal stress acting on them. Furthermore, the value of Young's modulus is assumed to be constant throughout the fracturing process, i.e. the value of Young's modulus is independent of the effective stress applied to the rock. This assumption, although valid for elastic formations, is not applicable to the case of unconsolidated rocks. Laboratory tests results have shown that the values of the elastic moduli for unconsolidated materials are a strong function of the applied stress and also of the stress-path followed during rock deformation. According to results published by Franquet and Economides (1999), the magnitude of the Young's modulus for an unconsolidated rock may decrease as much as 60% from its initial value when the corresponding loading stress path, K[20], is equal to zero. On the other hand, the value of Young's modulus may be increased by as much as 125% when the sample is subjected to a loading stress path equal to 1, i.e. both the confining pressure and the axial load are increased at the same rate (Fig. 2.31). Likewise, Poisson's ratio may experience large variations in magnitude as the conditions of stress and loading path are altered (Fig. 2.32). These variations on rock mechanical moduli may cause important changes on the geometry of hydraulically induced fractures in poorly-consolidated materials. Figures 2.55 and 2.56 show a KGD model of a

[20] The stress path, K is defined as: $K = (d\sigma'_3 / dt)/(d\sigma'_1 / dt)$

hydraulic fracture, and its expected geometry, in an unconsolidated material with stress-sensitive mechanical properties. During the construction of Fig. 2.56, it was assumed that the value of Young's modulus was proportional to the mean effective stress, i.e. the magnitude of Young's modulus decreased as the mean effective stress was reduced, and that the value of Poisson's ratio was constant. Under the same pumping schedule and leakoff conditions, the same fracture volume (area underneath the curve) is to be created for both constant and stress sensitive elastic materials. From this figure, it can be noticed that fractures induced in stress-dependent Young's modulus rocks will tend to be shorter and wider than those created in constant Young's modulus formations.

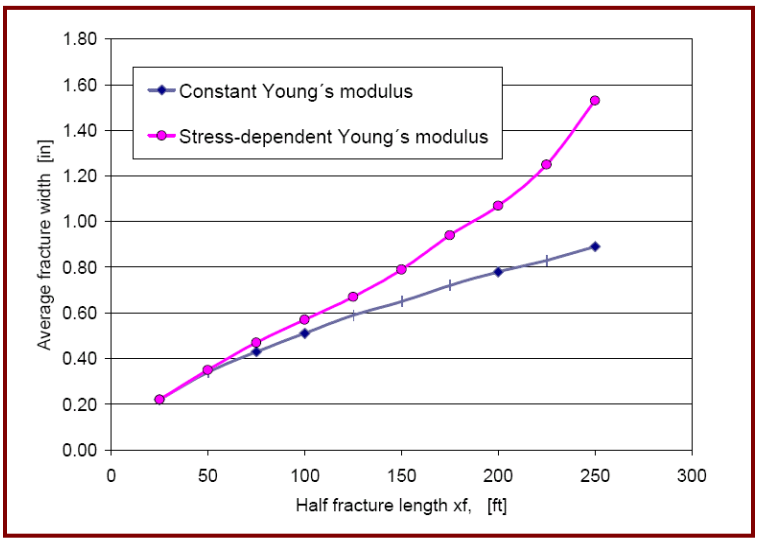

Figure 2-56. Average fracture width vs. fracture half length as a function of Young's modulus[21] (modified from Franquet and Economides, 1999).

[21] The value of Young's modulus was calculated as a function of the differential stress, q, according to the following equation: $E = aq^{-b}$, where a and b are constants.

A similar comparison is presented in Fig. 2.57 for the cases of constant and variable values of Poisson's ratio (with Young's modulus being kept constant). In this figure the trends are reversed, rocks with stress-sensitive Poisson's ratio tend to allow the creation of thinner, longer fractures than rocks with constant Poisson's ratio value. This behavior may be explained by the fact that the value of Young's modulus decreases exponentially with increasing effective stress, whereas the value of Poisson's ratio increases linearly for the same stress change (see Fig. 2.58).

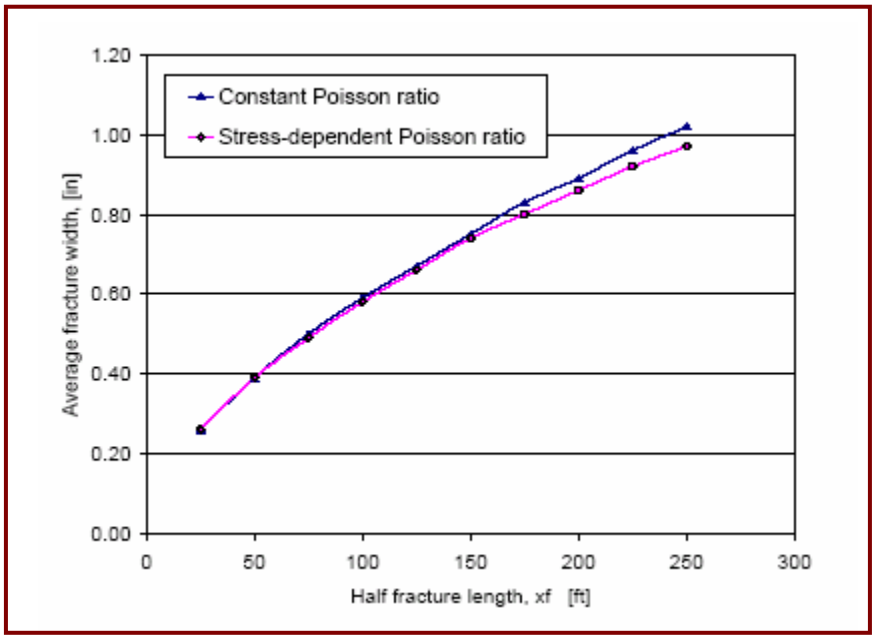

Figure 2-57. Average fracture width vs. fracture half length as a function of Poisson's ratio (after Franquet and Economides, 1999)

However, the relative difference between the curves is considerably smaller in Fig. 2.57 when compared to Fig. 2.56. Thus, it seems that Young's modulus plays a more important role in the fracturing process than Poisson's ratio. This is illustrated by the following equation, proposed by Geertsma (1979) for calculating the average fracture width[22]:

$$\overline{w} = 0.604 \left[\frac{\left(1-\nu^2\right) \mu \, C_l^2}{E} \right]^{1/5} \quad \text{.....(2.10)}$$

where,
- $\overline{w}$ = average fracture width;
- ν = Poisson's ratio;
- μ = fracturing fluid viscosity;
- C_l = fluid loss coefficient; and,
- E = Young's modulus

From a parametric analysis of the above equation, it can be inferred that changes in the magnitude of the Young's modulus would have a more important effect than corresponding variations in the value of Poisson's ratio.

[22] This equation only is valid for a KGD fracture of length x_f.

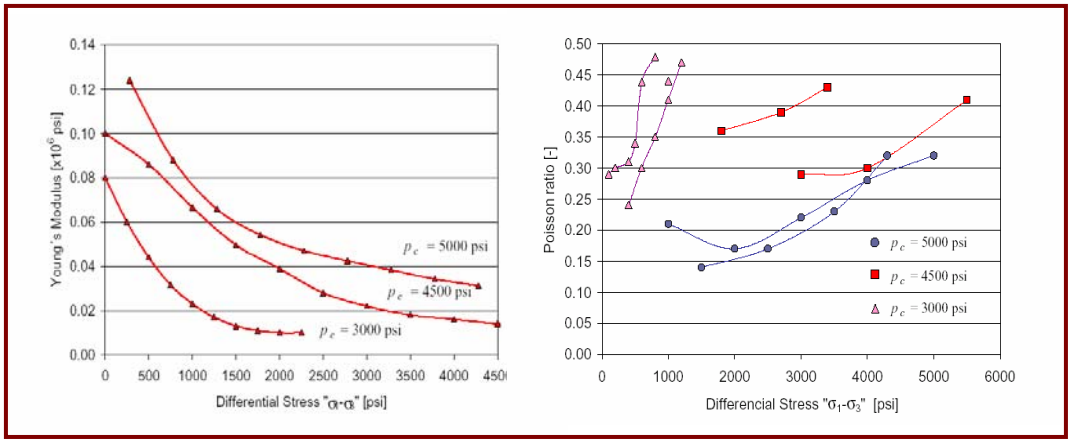

Figure 2-58. Variation of the magnitude of Young's modulus (left) and Poisson's ratio (right) as a function of the applied differential stress (after Franquet and Economides, 1999).

Core data is the most important and more accurate source of information for rock mechanical characterization. However, cores are not always available due to economical and/or technical reasons; this is especially true for weakly- and un-consolidated rocks. The use of wireline-derived sand strength for rock mechanics calculations is an alternative that has long been used in the oil and gas industry. This method consists in creating a "virtual" core from well logging data such as Δt_P, Δt_S, porosity and lithology. This "rock" is subjected to "virtual" load, allowing for the construction of stress-strain curves representing the mechanical behavior of the in-situ rock. In order to create a virtual sample, these models generally assume that the effects caused by large amplitude strains such as internal surface sliding, pore and grain deformation, and dilatancy can be related to those deformations caused during dynamic loading (i.e. small amplitude

strains). Thus, a correlation between static and dynamic properties may be derived. These correlations are obtained under the assumption that the microscopic deformation processes occurring within the rock are a function of the strain amplitude and that they may be considered as separate and independent phenomena. The relationships between rock porosity, bulk density, mineral content, rock dynamic properties, grain contact parameter, cracking factor, and dilatancy parameter are normally obtained from experimental data and theoretical considerations (Ong et al., 2000). Therefore, the range of applicability of these models is limited by the conditions used for their development.

The effects of changes in fluid saturation on rock strength have long been recognized (Colback and Wiid, 1965). It has been observed, from experimental results, that increments in water saturation may cause dramatic reductions in rock strength and also important changes in the elastic moduli of the material (E normally decreases whilst v tends to increase). Despite the mounting experimental evidence about fluid-triggered weakening processes in rocks, there is still controversy on the causes and severity of each of these mechanisms. Reduction in the surface free energy, as a result of fluid saturation, is considered to be one of the main processes affecting the rock strength and deformation behavior (Colback and Wiid, 1965; and Parks, 1984). By definition, the free surface energy is the amount of energy necessary to create a surface unit. Thus, it

is more related to cracking and fracturing of materials. This may be the case in consolidated formations, where microcracks are formed and extended as the applied stress increases. Nonetheless, processes such as matrix swelling and dissolution, and grain rearrangement also play an important role in the rock strength alteration observed in unconsolidated formations. It has been found that in highly-permeable, weakly-consolidated formations the amount of water weakening effect is strongly influenced by the clay content of the rock (Wu and Tan, 2001). There is also lack of understanding on the effect of increments in saturation of non-polar fluids, as they also seem to cause rock strength reduction, although to a lesser degree of severity. The need for more comprehensive fluid weakening models specifically designed for weakly-consolidated rocks is becoming more critical as more unconsolidated hydrocarbon reservoirs are experiencing increments in water saturation due to water injection and depletion.

Currently, hydraulic fracturing simulators assume that the value of the elastic parameters of the rock remain constant throughout the stimulation process, regardless of changes in the effective stress as well as in water saturation caused by fluid injection. There is enough experimental evidence that this is not a correct approach, as the magnitudes of both Young's modulus and Poisson's ratio vary widely as function of both effective stress and rock fluid saturation.

Chapter 3

Reliability of the Measurement of Mechanical Properties in Unconsolidated Formations

Cores are the most important source of data for hydraulic and mechanical characterization of rocks. However, core alteration and preservation are very important problems in rock testing; the consequences of inaccurate rock characterization impact the ability to predict formation behavior during all stages of reservoir development: reserves estimation, sand production, reservoir compaction, etc. This issue is even more critical when dealing with weak and naturally-fractured formations. The advantages of estimating - and avoiding - potential core damage are evident; any improvement in rock mechanical characterization may greatly enhance the quality of engineering predictions and reservoir performance.

The amount of reserves located in poorly- and un-consolidated formations, which represent most deep water and heavy oil targets, has created the need for reliable measurements of the petrophysical and mechanical properties of weak and very weak rocks. Unfortunately, the results obtained from these measurements are

regarded with skepticism. Concerns about the amount of rock alteration (i.e. remolding) caused by the coring, handling, and testing processes bring uncertainty about the ability of the rock sample to represent the behavior of the in-situ formation (Pauget et al., 2002). The problem of core quality is addressed in this chapter, different kinds of damage inflected on the core due to stress release, and freezing/thawing effects are considered.

The rock sample starts being affected from the instant the core bit releases part of the in-situ stress applied on the material. Subsequent operations such as core retrieval and handling may be the source of additional rock alterations. Direct mechanical shock and core disaggregation are both probable causes of damage. Viscous oils tend to entrain dissolved gas and swell with decompression rather than to release the gas; thus, damage imposed in the rock by expanding hydrocarbons has been a common occurrence. During the core laydown, fiberglass tube flexure or mechanical impact has been shown to cause important core alteration. The most popular wellsite core preservation technique for weakly-consolidated samples is freezing of the sediments while they are still inside the fiberglass tube. The freezing process can effectively preserve the rock fabric, since while in frozen state the grains are locked and rearrangement is very difficult. Temperatures of -58 °F (-50 °C) are necessary to completely freeze

unconsolidated rocks saturated with oil of moderate viscosity; increments in oil viscosity demand lower treatment temperatures (McGregor et al., 1991).

3.1 Core Damage Caused by Stress Relaxation

During coring operations, several changes occur in the stress field applied to the core, e.g. a rotation tensor is created by the spinning tool, and the magnitude of the stress on the rock is decreased as the core enters the coring barrel. In a standard double barrel tool, as the bit turns, the inner fiberglass sleeve is presumed to remain stationary. Thus, a rotation tensor is created at the bottom of the core section, which balances out the friction between the tool and the fiberglass sleeve. When dealing with weak formations, the possibility of grain dislocation and severe core twisting needs to be considered. Experimental evidence, suggests that this effect is not very important even in non-cemented formations (Fig. 3.1). In this figure, a CT scan image of a damaged ductile sand core shows very little perturbation on the orientation of the rock laminations.

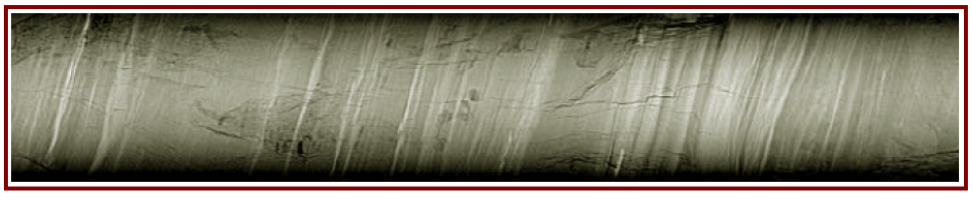

Figure 3-1. CT Scan image of a damage non-cemented core (after Pauget et al., 2002).

In addition to the rotation tensor, the coring process also involves sharp stress relaxation as the sample is being cut out of the rock mass. The unloading path during coring is not smooth; on the contrary, disturbing anisotropic stress release occurs near the rock bit, as the overburden disappears whilst the rock is still subjected to horizontal stress. In Fig. 3.2, the stress relaxation process is depicted for three locations in the reservoir: the rock at location A is being affected by the original undisturbed stress field, it is assumed here that the vertical stress is the largest principal stress[23]. The rock in region B is located near the rock bit, and due to the coring process, suffers a sharp stress relaxation in the vertical direction while its horizontal stress remains unchanged. As the rock in region C enters the coring barrel, it suffers stress relaxation both in horizontal and vertical direction. This is the stress condition affecting the rock sample until it is removed from the core barrel. Such stress alterations have the potential for causing permanent damage to the core, i.e. these changes are not reverted by reloading the core back to its original in-situ stress conditions. This rock damage may be caused by the fact that during certain stages of the coring process, the rock is subjected to a stress field where the horizontal component is higher than its vertical counterpart (e.g. location B). This condition allows for the occurrence of "artificial" differential deformations caused by the anisotropic unloading process, i.e. the anisotropy in the rock expansion is determined by the stress alteration caused by

[23] This situation is found in non-tectonic, relatively deep basins.

the coring process, rather than by the in-situ stress field. As a consequence, alteration of both the rock fabric and its pore structure may occur. The impossibility of knowing the mechanical properties of a formation before a core sample is obtained, have forced researchers to use artificial rocks in order to evaluate the effect of stress relaxation on rock mechanical behavior. Experimental results on synthetic formations have showed that the decrease in rock quality for deformation measurements is to a large extent caused by stress release during the coring operation (Holt and Kenter, 1992).

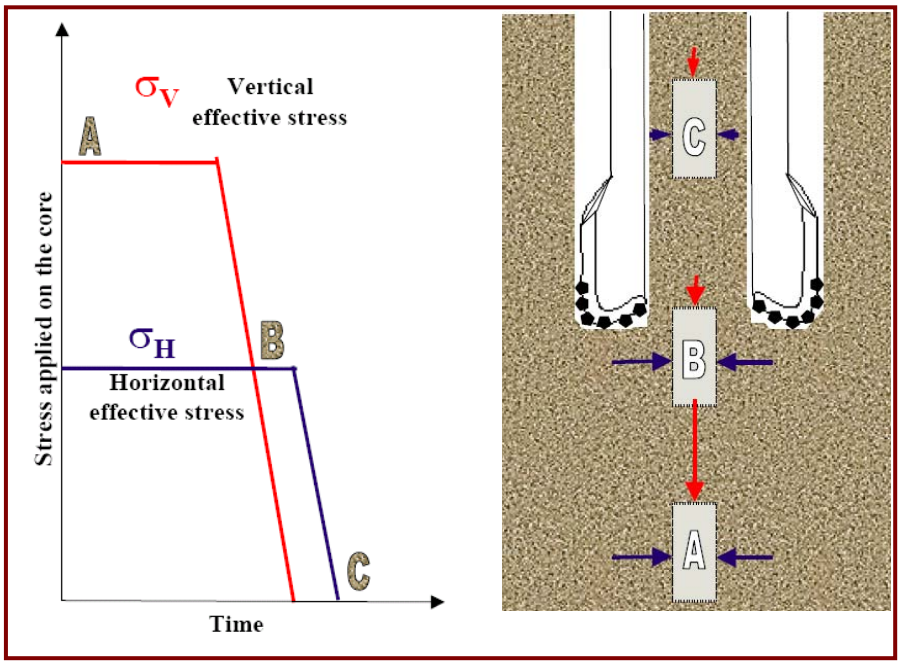

Figure 3-2. Stress field applied on the rock at different stages of the coring process, valid only for vertical coring (after Pauget et al., 2002).

The effect of stress relaxation on rock properties have been studied by comparing the behavior of a "virgin" synthetic rock, i.e. a specimen being kept under original in-situ conditions since cementation (Fig. 3.3 *Type A*), and of an analogous sample subjected to stress release (simulating coring) before testing (Fig. 3.3 Type B). During their study Holt et al. (1994), provided results from deformation analyses performed on artificial sandstones simulating rocks from two locations: the North Sea and the Adriatic Sea. The "virgin" sample (*A* curve in Fig. 3.4) exhibits a non-linear trend with slope decreasing as effective stress is increased, i.e. the rate of deformation is accelerating with depletion; whereas the "cored" specimen behaves in a more linear way (*B* curves in Fig. 3.4). It appears that the initial stiffness of the "cored" rock is much lower than of its "virgin" counterpart. This could lead to gross overestimation of rock compaction at the beginning of the depletion stage. Also from Fig. 3.4, it is apparent that the curve representing the sample that was rapidly cored (*B1f*) differs more from the behavior of the "virgin" rock than the sample that was cored at a lower rate (*B1s*). In Figures 3.3 and 3.4, the stress path *B2* represents an idealized stress path where the horizontal stress is not allowed to be larger than the overburden during the unloading process. Rocks undergoing this ideal coring unloading seem to have suffered less stress relaxation effect than both *B1* cases. The same behavior was observed for samples representing Adriatic Sea unconsolidated sandstones (Holt et al., 1994).

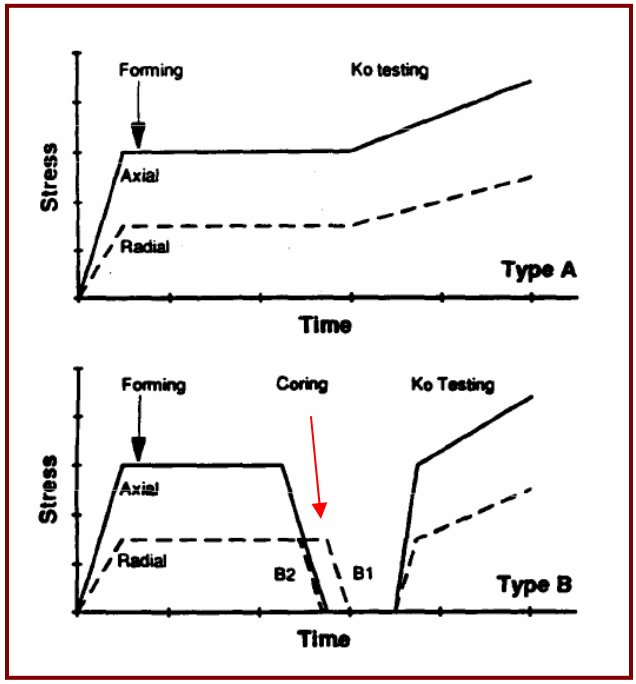

Figure 3-3. Stress paths defining the rock stress conditions: (Type A)"virgin" formation; and (Type B) standard stress history of cored sample, (after Holt et al., 1994).

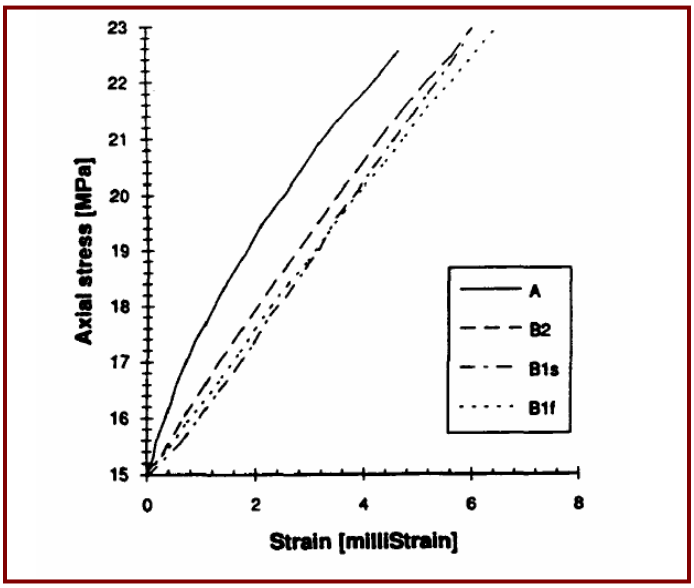

Figure 3-4. Compaction curves for the samples simulating a North Sea Reservoir, cemented at 15 MPa and 7.5 MPa horizontal and vertical stresses (after Holt et al., 1994)[24].

[24] In this figure, *s* and *f* are the conditions of slow and fast coring (unloading) rates, respectively; the labels *A, B1s, B1f*, and *B2* correspond to different unloading paths, explained in the paragraph above.

Permanent changes in rock porosity due to the simulated coring (unloading) process were calculated from radial and axial strain measurements. The results showed a permanent reduction on porosity; which for the case of the slowly sample (*B1s*) mounted to 0.5%, whereas it was about 1% for the rapidly cored specimen (*B1f*). In the case where the idealized unloading path (B2) was followed, the porosity reduction was minimal (around 0.1%). Based on these results, Brignoli et al. (1998) field-tested a coring tool that was designed to apply a constant vertical pressure (a bias stress[25]) on the core entering the coring barrel. The main idea was to reduce the level of stress anisotropy affecting the rock during the coring process; the proposed stress path is shown in Fig. 3.5.

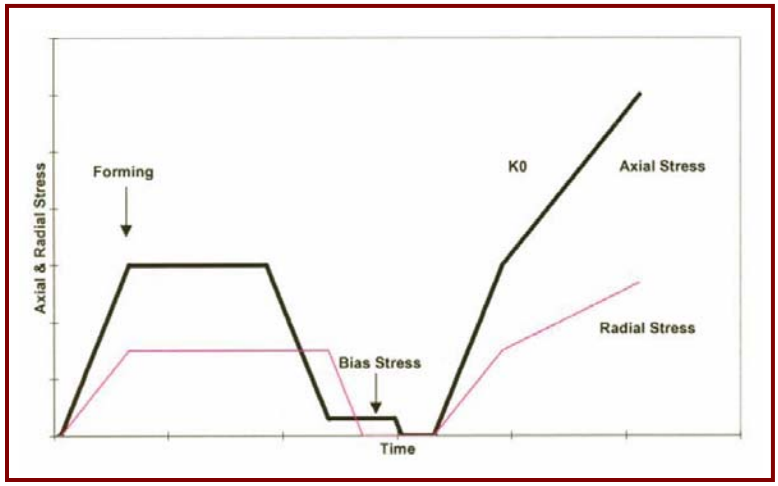

Figure 3-5. Stress path during coring and testing with constant vertical stress applied inside the core barrel (after Brignoli et al., 1998).

[25] Bias stress: constant vertical pressure applied on the sample to reduce the stress anisotropy affecting the rock during the coring process

The results obtained by Brignoli et al. (1998) showed that for weak synthetic sandstones (UCS< 725 psi), the rock damage due to stress relaxation was very small when a bias vertical stress close to 150 psi was applied on the sample, i.e. the "cored" and the "virgin" samples compacted in a very similar way. The improvement obtained when a bias vertical stress was applied to more consolidated rocks was not as important as in the case of weaker rocks. In addition, the sample tendency to disc during the unloading process was reduced by the application of the bias stress. This result is somewhat expected since discing is caused by tensile failure as the core expands unconstrained in the axial direction; the presence of a vertical stress opposing that expansion reduces the risk of failure (Fig. 3.6).

Analogous conclusions were obtained for porosity measurements: the permanent porosity loss observed in standard coring simulation experiments performed on weakly-consolidated sands was reduced by the application of a vertical bias stress. As before, the magnitude of porosity in more competent materials was just marginally affected by the coring process. However, there is a limit to the magnitude of the bias stress that should be applied to the rock during coring. The value of this stress threshold depends on the rock strength; indeed, compressive failure was usually induced when the value of the applied vertical stress was larger than 70% of the rock UCS (Brignoli et al., 1998). Field testing of this

technique was performed in an offshore gas field in the Adriatic Sea. The measured stress-strain response during the initial loading for all samples obtained in the field is presented in Fig. 3.7. The effect of the applied bias stress is evident as the samples tended to be "stronger" when a given bias stress was applied during the coring process. The variability in the response of the samples may also be attributed to rock variation, as the samples were taken in the same wells but at slightly different depths.

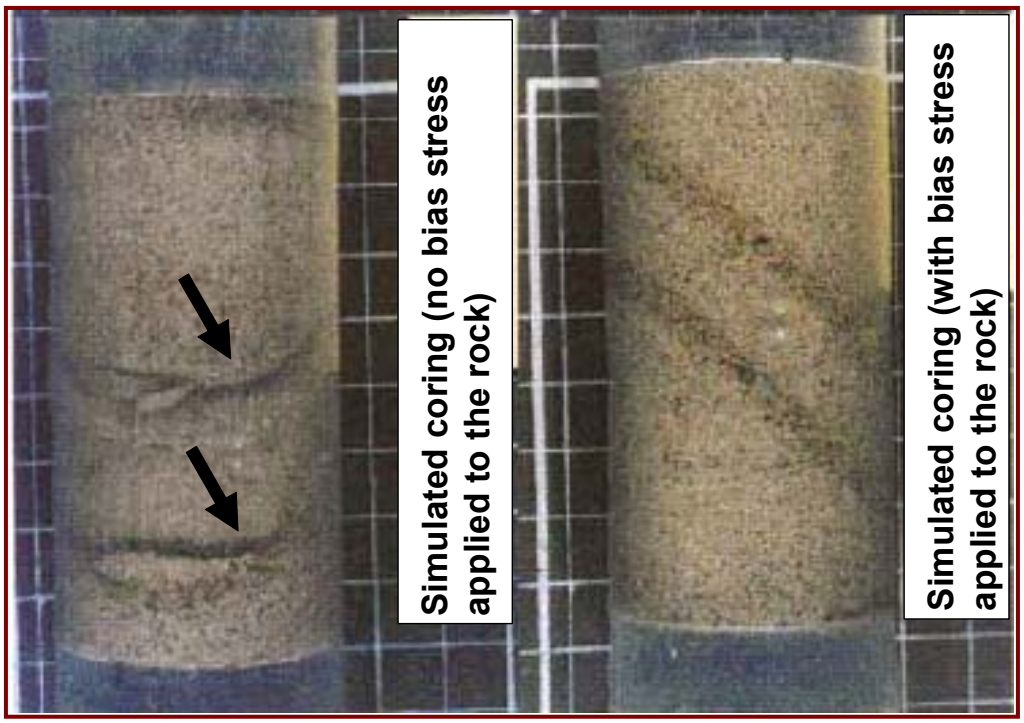

Figure 3-6. Effect of applied bias stress on the failure tendency of synthetic sands with in-built weakness planes (after Brignoli et al., 1998).

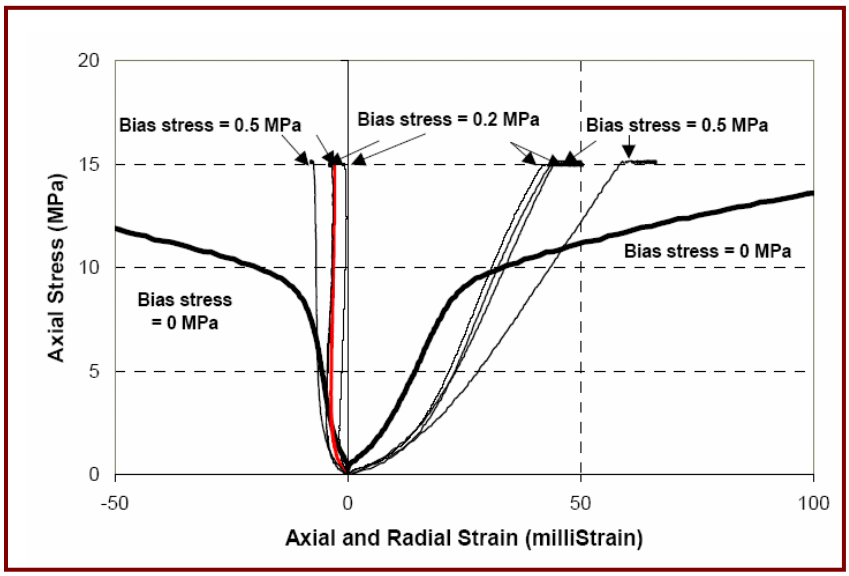

Figure 3-7. Axial stress vs. axial and radial strain during proportional loading ($\sigma_t=2\sigma_r$) of core samples from the Adriatic Sea (after Brignoli et al., 1998).

3.2 Core Damage Induced by Freezing

In the oil and gas industry, freezing is the most used sample preservation method when dealing with poorly-consolidated formations. However, the potential alterations of the rock's mechanical and hydraulic properties due to freezing and thawing are seldom addressed. Most studies concerning the degradation and weathering of rocks due to freezing/thawing cycles deal with rather competent construction materials (Ishizaki, 2000). In order to understand the effects of saturated rock freezing, a review of the basics of ground freezing is presented in the next section.

3.2.1 Background on Soil/Rock Freezing

Water has the ability to form hydrogen bonds; this in turn helps explain its abnormally strong electrical character that makes it the universal solvent. The hydrogen bonding of water not only enhances its electrical properties, but it also accounts for its abnormally high viscosity, high surface tension, and tendency to adhere to itself and to many other substances, especially those containing oxygen in their structure, i.e. organic matter, glass, and dirt. Because of the hydrogen bond, water is one of the few substances that expands upon freezing; the volume of water increases about 9% when converted to ice. Although ice always melts at 0°C (32°F), perfectly pure water may remain liquid when cooled to approximately -40°C(-40°F). This phenomenon where a substance remains liquid at temperatures below its freezing point is known as supercooling. This delicate equilibrium will be broken if the system is shaked, stirred, or a surface (which acts as a nucleating agent) is introduced in the water. Perhaps the most critical phenomenon in ground freezing is the movements of water molecules through the ground during and after freezing. Upon freezing, water expands about 9%; however, water-saturated soils may expand 100% and even more[26] (Davis, 2001).

[26] Extremely large values of soil expansion are only possible if the freezing soil is in contact with a water source large enough to sustain the expansion process.

This enormous expansion is caused by the formation of ice lenses which grow within the rock as water is fed into them; an example of this phenomenon is the formation of pipkrakes (see Fig. 3.8).



Figure 3-8. Extreme example of soil heaving: pipkrake near the trans-Alaska pipeline on Alaska's North Slope (in Davis, 2001)

The process of ice lenses growth is determined by both the soil permeability and the water saturation. The permeability affects the flow of water within the rock, and the saturation influences its availability. The pressure required to force water out of a soil is equal to the suction force holding it in. The concept of suction pressure is very useful when studying the freezing characteristics of a soil, as the freezing process itself creates pore pressure alterations that trigger water flow. Suction pressure is created as a result of the freezing process (cryosuction); this is explained as a reaction to the temperature gradient existing in the freezing rock.

The water tries to minimize its internal energy by migrating towards the coldest region of the material, namely, down the temperature gradient. The water molecules lower their internal energy and collect in the form of ice within the cold regions in the rock.

Figure 3.9 shows the soil moisture characteristic curves for several clays. From this plot, it can be observed that half of the water in the samples is released by applying about 10 atm (147 psi). This loosely held water corresponds to the fluid saturating the largest pores in the rock; whereas the water remaining within the rock is more firmly held inside small pores, where the attraction forces between the rock surface and the fluid are larger. The attraction forces between the fluid and the grains are proportional to the liquid-solid area of contact. Spherical soil particles such as sand have the lowest specific surface[27], while plate-like particles have the highest; the specific area of sand is about 0.01 times the specific area of clay (Davis, 2001). If water is contained within the pores of a rock/soil and adsorbed onto the surface of the grains, the freezing behavior is quite complex. Due to the action of the Van der Waals (attractive) forces, water may remain liquid even at temperatures well below 0°C (32°F). Curves showing the unfrozen water content of a soil as a function of temperature are presented in Fig. 3.10. These curves are also known as soil freezing characteristic curves.

[27] Specific surface area is defined as the surface area per unit weight or per unit volume

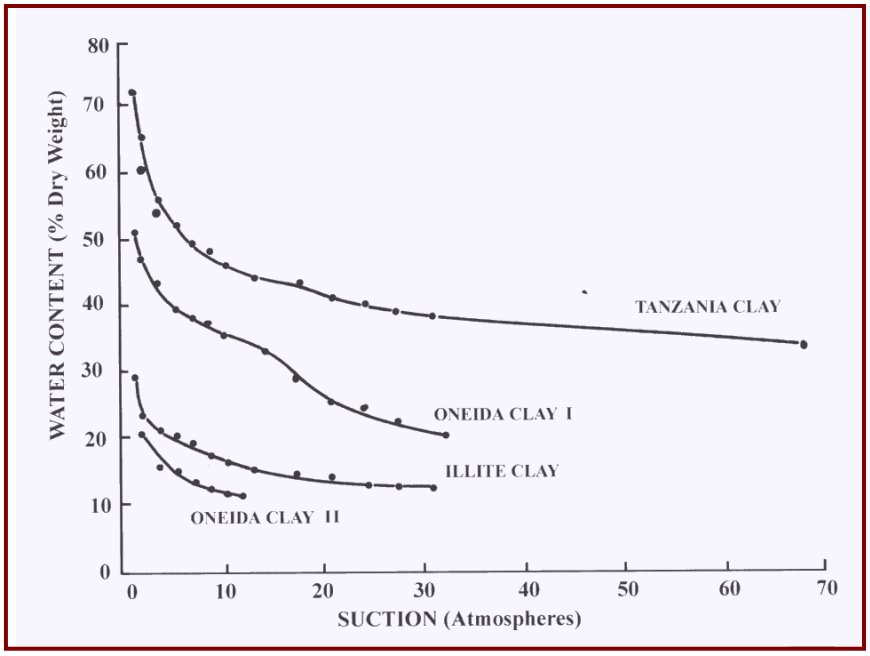

Figure 3-9. Soil moisture characteristic curves for several clay samples (originally in Williams and Smith, 1989)

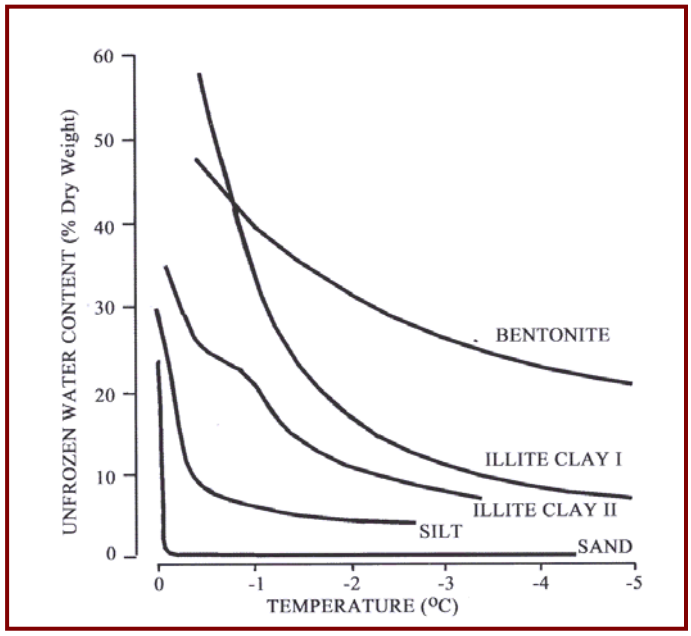

Figure 3-10. Soil freezing characteristic curves for several samples (originally in Williams and Smith, 1989)

The shapes of Figs. 3.9 and 3.10 are very similar; this is not surprising as the shape of both curves is a strong function of the size of the pores in the soil and the total surface area available for water sorption. For example, bentonite has such small pores and high specific surface, that it is able to keep 20% wt. of its saturating water in liquid state at a temperature of -5°C. It is apparent from Fig. 3.10 that the amount of water that remains unfrozen within the sand pores is negligible; a somewhat expected result as most of the pores within this rock are relatively big and the saturating water is contacting only a small amount of grain surface area, i.e. small liquid-solid contact area translates in weak attractive forces between the water and the rock.

The value of suction pressure increases as the rock temperature decreases; this may be explained by the fact that, at the beginning of the freezing process, only the most loosely-held water, i.e. the water saturating the largest pores, becomes ice. However, as the rock temperature is continuously decreased, the radii of the pores containing ice decreases rapidly too. Therefore, it becomes increasingly difficult to force water out of the rock; this behavior is readily identifiable in Figs. 3.11A and 3.11B. The magnitude of the pressure holding the water within the rock (suction pressure) increases linearly as the temperature of the rock decreases below the ice melting point.

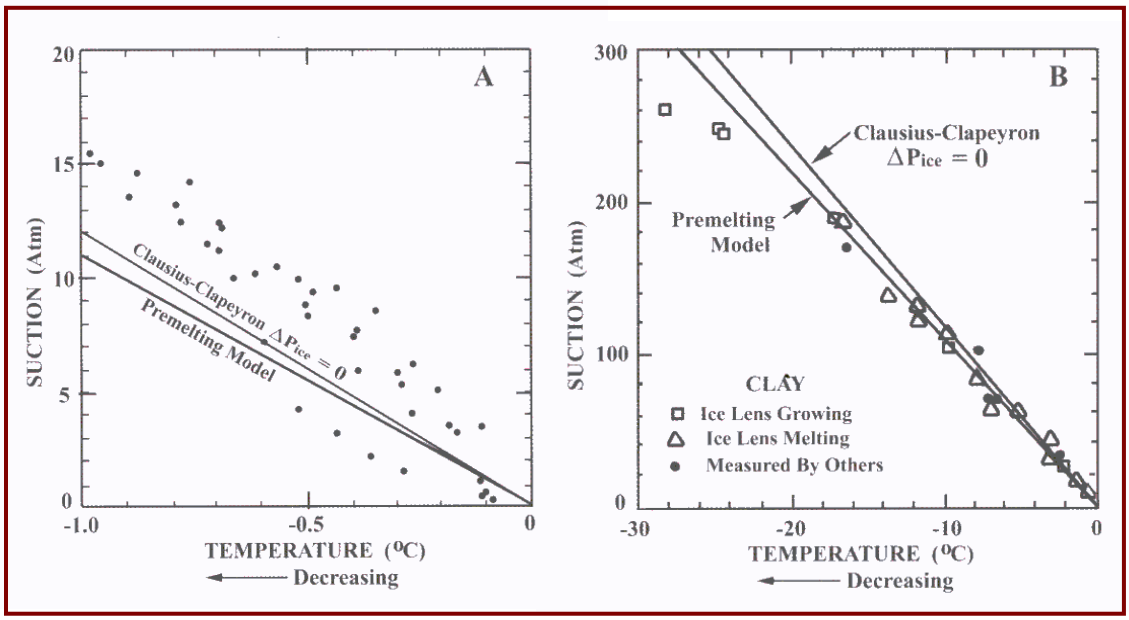

Figure 3-11. Suction pressure as function of rock temperature, A). Data measured on fine-grained soils (originally in Williams and Smith, 1989); and B). Data measured on clay (original data from Dash et al., 1995)

It is not uncommon finding frozen soils that contain layers of pure ice, called segregation ice, their thickness typically increasing with depth (see Fig. 3.12). According to the Clausius-Clapeyron principle, if a system is in stable equilibrium of pressure, volume and temperature; and a disturbance is introduced (via a change in P, V, or T), the remaining conditions will adjust trying to reach a new equilibrium. For the particular case of the water-ice system saturating a soil, this principle can be translated as (Davis, 2001):

$$\Delta T = (V_{water}\Delta P_{water} - V_{ice}\Delta P_{ice})\, T_0 / L \quad \text{.....(3.1)}$$

where,

- ΔT = change in absolute temperature, °K;
- T_0 = absolute temperature ice melting point = 273 °K;
- V_{water} and V_{ice} = specific volumes of water and ice, respectively;
- ΔP_{water} and ΔP_{ice} = pressure change on water and ice; and,
- L = latent heat of fusion of water = 80 calories per gram.

Several models that have proposed to explain the formation of segregation ice, but all of them are based on the occurrence of a temperature-dependent suction (cryosuction) in a permeable, saturated freezing soil. This suction triggers water flow within the rock, and the transported water freezes somewhere within the material, usually in layers perpendicular to the advancing freezing front. The coexistence of ice and water in the freezing rock requires the pressure in the water and the ice to be different from each other but at the same time related by the Clausius-Clapeyron equation. Thus, the difference in the magnitudes of P_{ice} and P_{water} increases as the temperature of the rock is lowered below the ice melting point. Depending upon the model of choice, the two magnitudes depart from each other at a rate between 11 and 12 Atm/°C or 291-317 psi/°F (Davis, 2001).

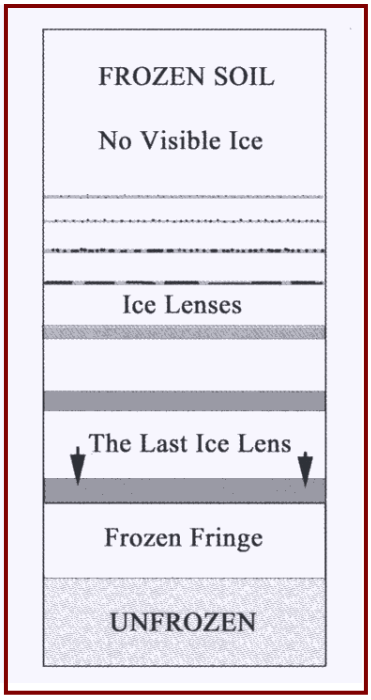

Figure 3-12. Segregation ice forming in repeating layers, with thickness increasing with depth (in Davis, 2001)

Multilayered occurrence of ice lenses suggests that rock freezing is a cyclic process that is active only when the conditions sustaining ice segregation exist. For a particular soil, two variables may change within short distances: water availability and temperature. Segregation ice starts to form when the suction pressure supplies enough water to and beyond the freezing front. This process continues until the region near the freezing front is depleted of water. Thus the ice segregation stops, and the freezing front is allowed to advance, until the conditions of suction pressure and water supply are met again and a new ice lens starts to form.

The phenomenon of "frost heave", defined as the soil volume increment caused by ice segregation forming within the material. This process (shown in Fig. 3.8, above) occurs only when the following conditions are met:

- Freezing temperature gradients and soil pore sizes permit cryosuction to appear;
- the soil is permeable enough to allow water movement to areas where it may collect as ice;
- the thermal conductivity and temperature gradient are sufficient to allow heat balance, which tends to stall the advance of the freezing front;
- water is supplied to the system at rates high enough to sustain the ice lenses growth; and,
- the suction of the water is adequate for allowing ice pressure to equal or exceed the overburden stress applied on the rock.

Conditions for frost heave are easily met at the surface of water-saturated soil when the air temperature falls below the ice melting point. Ice pipkrakes grow in loose and wet soils; thus, small magnitudes of suction pressure are enough to provide adequate water supply to the freezing front. At very shallow depths, the value of the overburden stress is low and the readily accumulating ice creates enough pressure to cause ground uplift. However, in the case of an unconsolidated rock sample where the condition of adequate water supply into the

freezing front is not met, the formation of ice lenses should not be an issue. However, alterations in rock behavior due to simple water expansion inside the rock pores could still be important; this is further discussed at the end of this chapter.

Changes in pore pressure during more than 20 freezing experiments on sedimentary rocks were recorded by Fukuda (1983). The rock used in his experiments was Neogine Tertiary Tuff, from Central Japan, a sedimentary highly porous (ϕ=36%), frost-susceptible formation. In these experiments, the samples were first wetted to ensure full water saturation. Tensiometers were installed at different distances from the top of the rock sample. The freezing process started from top to bottom of the sample, while keeping the lower end of the sample in hydraulic contact with a water reservoir. A schematic showing the experimental setup and some results obtained during these experiments are presented in Fig. 3.13. Note that the y-axis in Fig. 3.13B shows negative water pressure (suction pressure). These measurements proved the existence of cryosuction pressures in excess of 200 cm H_2O (6.56 ft H_2O), as well as the movement of water through the rock from the watertable to the freezing front. Although the experiments described in Fig. 3.13 are not representative of typical core freezing operations, they provide a useful starting point for designing experiments that could represent the freezing process of saturated, unconsolidated cores.

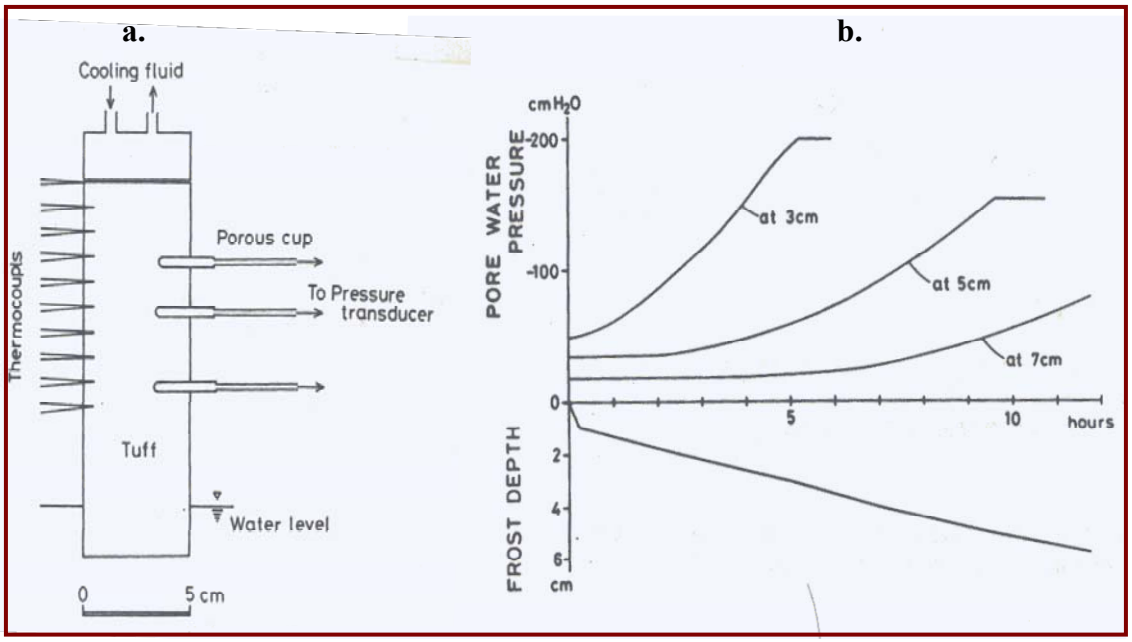

Figure 3-13. a). Experimental setup for pore pressure measurement during rock freezing; and, b). typical results from the experiments (after Fukuda, 1983)[28].

3.2.2 General experimental results on the effect of freezing / thawing on rock mechanical behavior

In general, frost susceptibility[29] is mainly reliant upon the geometry of the continuous network of unfrozen water films in the frozen fringe. As stated above, the amount of unfrozen water is a strong function of the fines content. Furthermore, given a grain-size distribution, the geometry of the interconnected pores depends also on the degree of packing of the particles. Given a pore-size

[28] The distances reported in Fig. 3.13.b were measured between the top of the sample and the location of the tensiometers.

[29] The term "frost susceptibility" is hereby used to refer to variations in rock mechanical behavior as result of freezing/thawing processes.

distribution, frost effect is a function of the relative amounts of water (both capillary and adsorbed), which depend both on the rock clay content and on the clay minerals present in the rock (Konrad, 2000).

An investigation on the effect of freezing and thawing on the unconfined strength of several sandstones was published by Hale and Shakoor (2003). In their study, the UCS was measured on about 90 sandstone cores after subjecting them to 0, 10, 20, 30, 40, and 50 cycles of freezing and thawing. Their purpose was to evaluate the effect of seasonal changes in temperature upon the strength of rock used as construction material, i.e. competent formations. The results of petrographic analyses for the samples used in their study is shown in Table 3.1; while the mean values of the engineering properties for the rocks, before freezing, are presented in Table 3.2.

	Modal composition (%)			
Sandstone	**Quartz and Feldspar**	**Clay and Matrix[30]**	**Lithic Fragments**	**Cement**
Sharon	88	10	2	0
Berea	76	12	12	12
Pottsville	70	22	8	5
Catskill	86	10	4	10
Rockwell	78	12	10	16
Tuscarora	96	4	0	20

Table 3-1. Results of petrographic analyses based on 50 grains of each sandstone sample before freezing (after Hale and Shakoor, 2003).

[30] This value included fine material indiscernible as quartz, feldspar, lithic fragments, or cement

Sandstone	Dry density (g/cc)	Bulk specific gravity	Absorption (%)	UCS (psi)	Porosity (%)	Slake durability Index[31] (%)
Sharon	2.14	2.12	5.76	2,636	12.32	89.4
Berea	2.12	2.09	6.58	3,162	13.94	96.1
Pottsville	2.44	2.39	2.85	7,580	6.94	97.1
Catskill	2.60	2.51	1.55	16,899	4.00	98.6
Rockwell	2.62	2.61	0.32	14,224	0.86	99.1

Table 3-2. Average values for the engineering properties of several sandstones before freezing (modified from Hale and Shakoor, 2003).

The effects of freezing/thawing on rocks result from the freezing of pore-saturating fluid. Upon expansion, water experiences a 9% volume increase; this value may increase up to 13.5% in a closed system, i.e. when fluids are not allowed to leave the rock. As the freezing front advances into the rock, it forces water to migrate further into the material; this fluid flow is caused by the pressure differential between the ice and water, $P_{ice} - P_{water}$. If this value is high enough, hydraulic fracturing may be induced within the freezing rock (Lienhart, 1988). However, as stated before, certain conditions regarding water content and permeability should be met in order for suction pressure to occur. In the work by Hale and Shakoor (2003), all samples were frozen according to ASTM method C666[32] (ASTM, 1990). The results of their experiments are presented both in Table 3.3 and Fig. 3.14. As it can be observed from this figure, a dramatic reduction on UCS was registered for the samples with the lowest vales of porosity

[31] Second-cycle slake durability test (%)
[32] A modified version of test ASTM C666 was performed: the modification consisted of using a single sleeve to hold six cores during each cycle.

($\phi < 0.05$); whereas the results for the more porous specimens oscillate around the original UCS value. Research on the effect of porosity upon the freezing and thawing degradation has been published by Lewis et al. (1953), Shakoor et al. (1982), and Fitzner (1990). The latter concluded that pore spaces were the places most susceptible to weathering reactions. Litvan (1984) found pore-size distribution to be critical when assessing frost susceptibility; conclusion that was supported by Shakoor et al. (1982) who noted that freezing effects were more important for rocks with larger percentages of small pores (< 0.1 mm). It is believed that only the smaller voids allow significant hydraulic pressure to develop in the pores during freezing.

Sandstone	**Mean Unconfined Compressive Strength (psi) by Number of Freezing and Thawing Cycles**					**Correlation coeff. (r)**
	0	**20**	**30**	**40**	**50**	
Sharon	2,636	1,480	2,214	743	1,723	-0.69
Berea	3,163	4,152	1,696	2,687	3,715	-0.09
Pottsville	7,580	6,543	7,597	4,506	5,777	-0.81
Catskill	16,899	16,264	12,963	10,896	8,186	-0.95
Rockwell	23,739	19,567	16,021	18,885	15,724	-0.98
Tuscarora	14,224	14,947	11,933	16,500	9,878	-0.37

Table 3-3. Effect of freezing and thawing on UCS of sandstones (after Hale and Shakoor, 2003).

These results, although very interesting, are not very relevant for the case of a single freezing/thawing cycle, as it is the situation during coring operations of unconsolidated formations. Thus, an alternative way to analyze the results in

Table 3.3 is to plot the variation of UCS (in % $UCS_{initial}$ / cycle) vs. rock porosity (see Fig. 3.15). In this figure, no apparent trend was found in the behavior of UCS variation as a function of porosity. The two samples with the highest porosity (Berea and Sharon), have the lowest and highest freezing susceptibility, respectively. However, it was evident that the effect of a single freezing/thawing cycle on the rock strength was minimal; in the worst case, the UCS was only reduced about 1.3% per cycle.

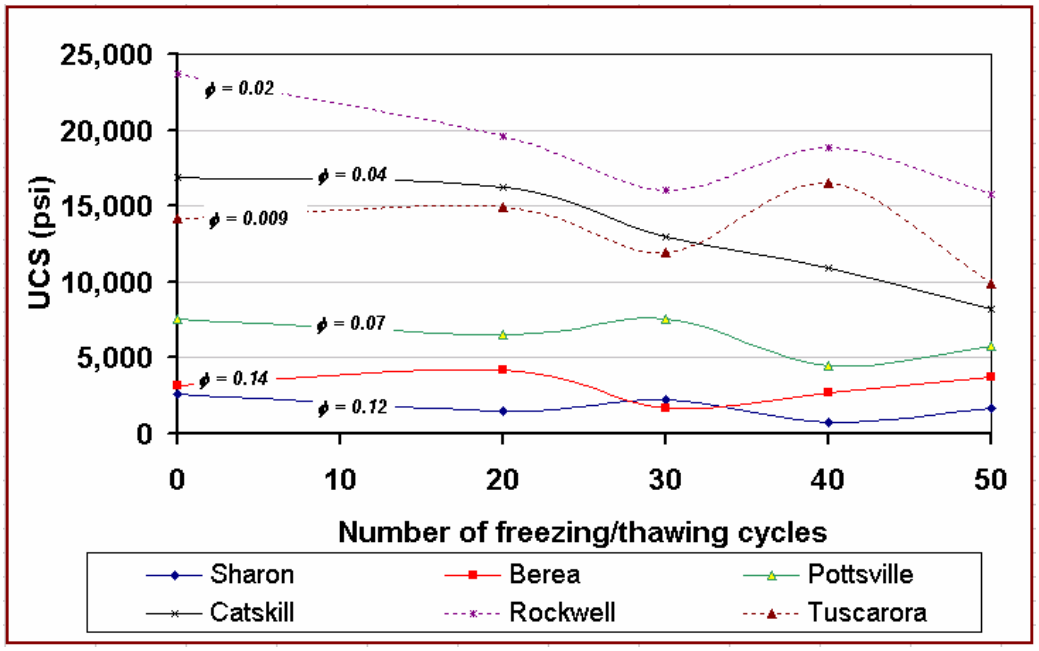

Figure 3-14. Effect of freezing and thawing on the UCS of several sandstones (data from Hale and Shakoor, 2003).

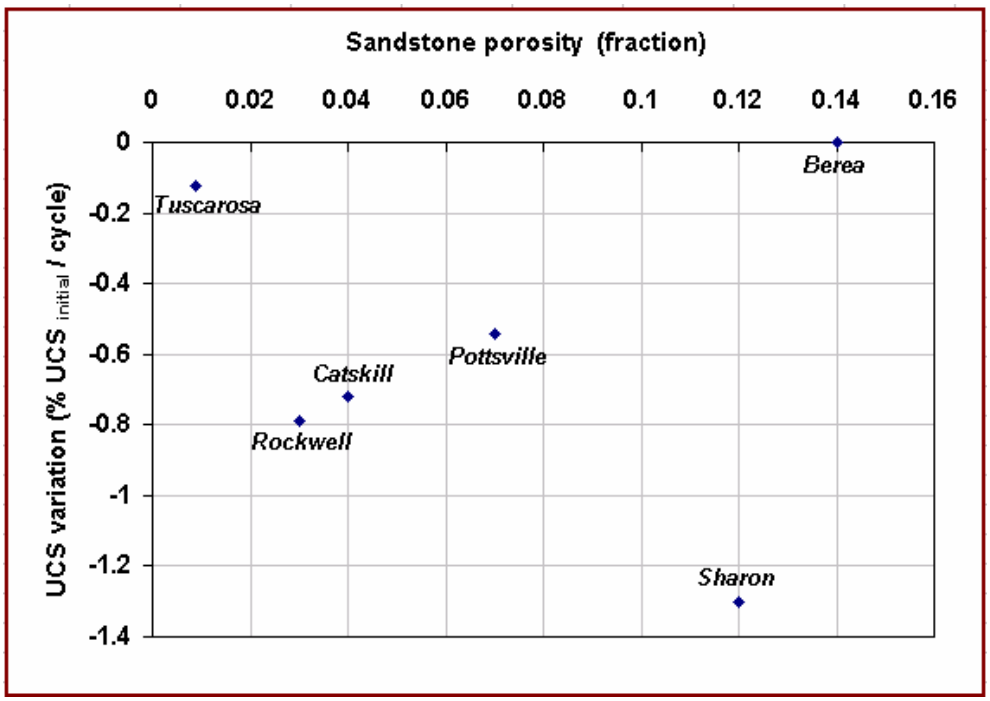

Figure 3-15. Effect of freezing and thawing on the UCS of several sandstones (data from Hale and Shakoor, 2003).

3.2.3 Influence of mineralogy on frost alteration of the rock

The potential of segregation[33], $SP_{o,}$ is related to the rock tendency to allow the formation of ice lenses; hence, to the occurrence of heaving. Figure 3.16A presents the results of the segregation potential threshold, obtained experimentally for silty sands containing up to 20% fines. In the case where kaolinite was the main clay component, the magnitude of the segregation potential was considerably higher than for the case of montmorillonite. It is also evident that the segregation potential is inversely proportional to the mean particle diameter in

[33] Defined as the ratio of the rate of moisture migration to the temperature gradient in a frozen soil near the 0°C isotherm.

the rock, i.e. rocks with smaller particles exhibit more frost susceptibility than larger ones.

Unfrozen water occurs both in the macro-pores (comparatively far from the influence of the rock surface), and trapped in micro-pores (in close contact with the mineral surface of the grains). Thus, water mobility is far greater within relatively large capillary channels (macropores) than in the adsorbed films normally found in the micropores (Hoekstra, 1969). The cause of this double-dependency may be that the size of the macropores determines the radius of the ice-unfrozen water interface; hence, of the amount of capillary unfrozen water, whereas clay mineralogy influences the thickness of the adsorbed (unfrozen) water layer. The main mechanism responsible for ice lenses growth and heaving is water transport through the freezing rock. It is normally assumed that the rate of water flow is related to the magnitude of effective porosity (Konrad, 2000). The fact that different clays show different freezing susceptibility may be explained by variations in the magnitude of their specific surface area. This variable may be included in the analysis by plotting the product of segregation potential and specific surface area vs. the mean particle diameter (Fig. 3.16b). In this figure, the effect of rock fabric vanishes, and the results from different clays follow the same trend, this will be found as long as the fines fill uniformly the rock pores (Konrad, 2000).

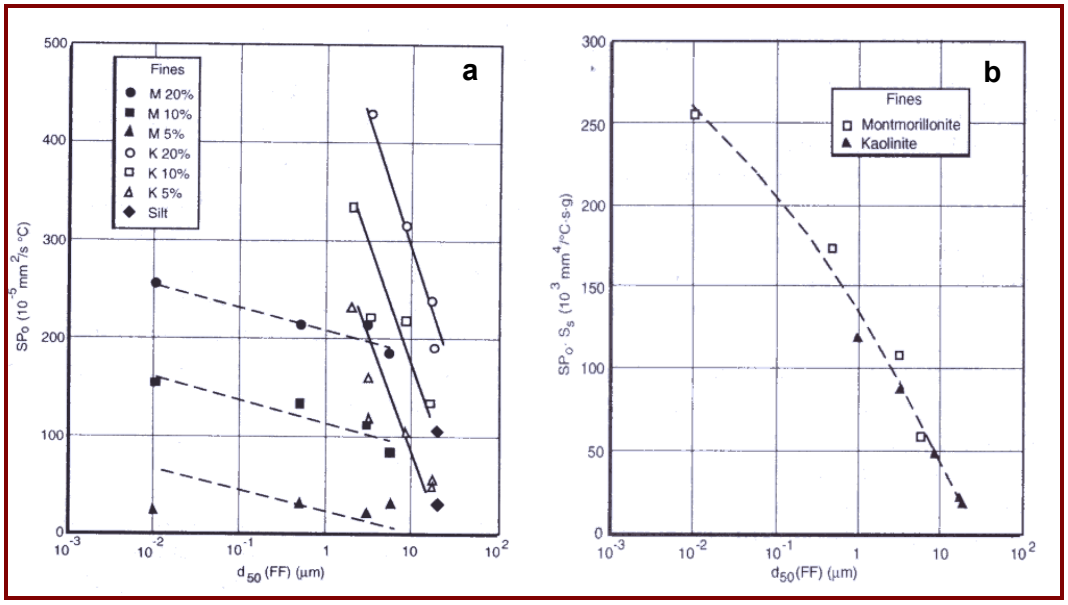

Figure 3-16. a).Segregation potential as a function of the mean particle size diameter for different lithologies; and b). Product of segregation potential and specific surface area vs. mean particle diameter (after Konrad, 2000).

3.2.4 Influence of freezing rate on frost heaving

The results of laboratory experiments to evaluate the frost susceptibility of soils/rocks have been shown to be strongly influenced by the freezing procedure (Penner, 1972). He concluded that, in general, increments in the rate of heat removal caused the heaving rate to rise to a maximum followed by a reduction that intercepts the in-place pore water phase-change expansion. In his paper, the ice segregation efficiency parameter[34], $\mathcal{E}$, was used to assess the rock tendency to suffer frost heaving. He studied the consequences of changes on the thermal

[34] defined as the ratio of heat removed from the freezing front, that is attributable to ice lens formation; if $\mathcal{E}$ =1 all the heat removed involves ice lens formation, while $\mathcal{E}$=0 means no ice lens growth (Arakawa, 1966).

conditions upon the rock reaction to freezing processes; namely, the effect of the soil freezing rate on its heaving characteristics. The reliance of the heaving rate on the freezing rate has not always been recognized: Beskow (1947) postulated that, under constant load conditions, the soil heaving rate was not a function of the rate of freezing. This conclusion was obtained based on the results of experiments conducted on highly permeable soils; hence, it is not applicable to rocks/solid where the freezing front may become stationary. Likewise, the U.S. Army Corps of Engineers (1958) found that the rate of heave was not related to the rate of freezing; they arrived at this conclusion after running tests on soils at freezing rates varying between ¼ and ¾ in/day. These early results proved to be very limited and valid only under certain conditions of freezing rate and rock permeability. More recent studies by Penner (1960), showed strong dependence of heaving rate upon the sample freezing rate, Table 3.4 shows some characteristics of the samples used in his study. Figure 3.17 presents the results of a series of experiments where different heat rates were imposed onto the rocks; simultaneously, the water flowrates into the samples were also recorded. In this figure, moisture flow was plotted in terms of the latent heat of fusion by using standard values of 80 cal/gr of water (144 Btu/lb of water). The effect of freezing rate is readily identified, higher freezing rates provoked higher water inflow rates; hence, more rock heaving. It is important to notice that, in these experiments, a water reservoir was in permanent hydraulic contact with the samples, thus

ensuring water supply. The impact of changes in the freezing front advance rate on the rock heave rate is also evident in Fig. 3.18. The upper curves represent the total heave, due to the summation of the expansion of the in-situ water as it freezes and the additional water moved into the freezing front. The lower curves correspond to the heave rate expected as a result of in-situ water freezing alone.

Sample	Clay (%)	Silt (%)	Sand (%)	Dry density (lb/ft^3)	Moisture (%)
Leda clay	64	36	--	91	33.2
PFRA silt	9	43	48	110	19.2
Lindsay sand	7	13	80	137	8.2

Table 3-4. Description of the samples used in the study by Penner (1960).

Similar behavior was reported by Kaplar (1968) from laboratory experiments; he found a correlation between the frost-penetration rate and the heave rate. According to his observations, the heave rate was dependent on the rate of heat extraction, up to some critical rate whose value is a function of the rock permeability (Fig. 3.19). Hence, it is generally accepted that the freezing front penetration rate should be an important consideration when performing frost susceptibility studies on rocks/soils. The effect of freezing rate varies for different lithologies, as it is evident in Fig. 3.18; however, the available evidence suggests that the heave rate on highly permeable rocks is less sensitive to changes in the frost advancement rate.

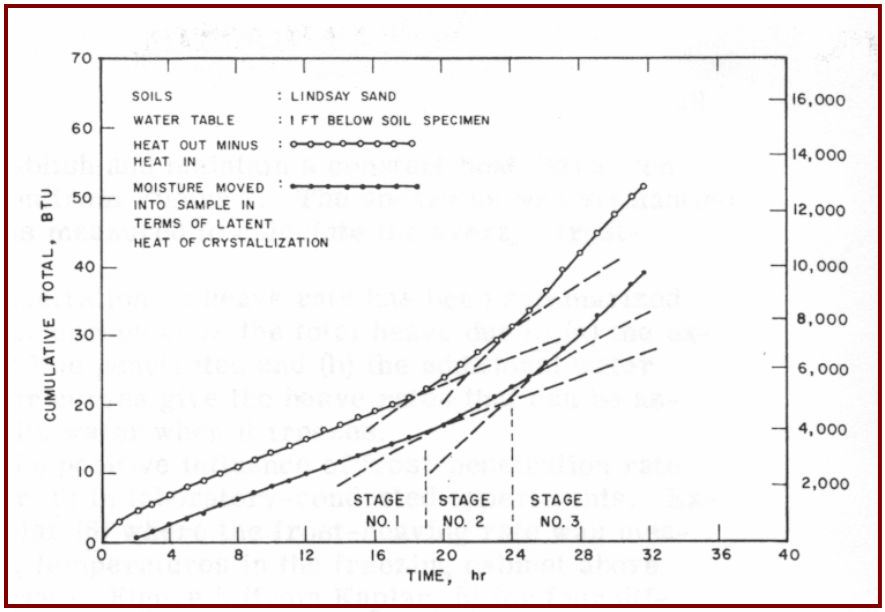

Figure 3-17. Cumulative value of net heat flow and moisture flow vs. time (after Penner, 1960).

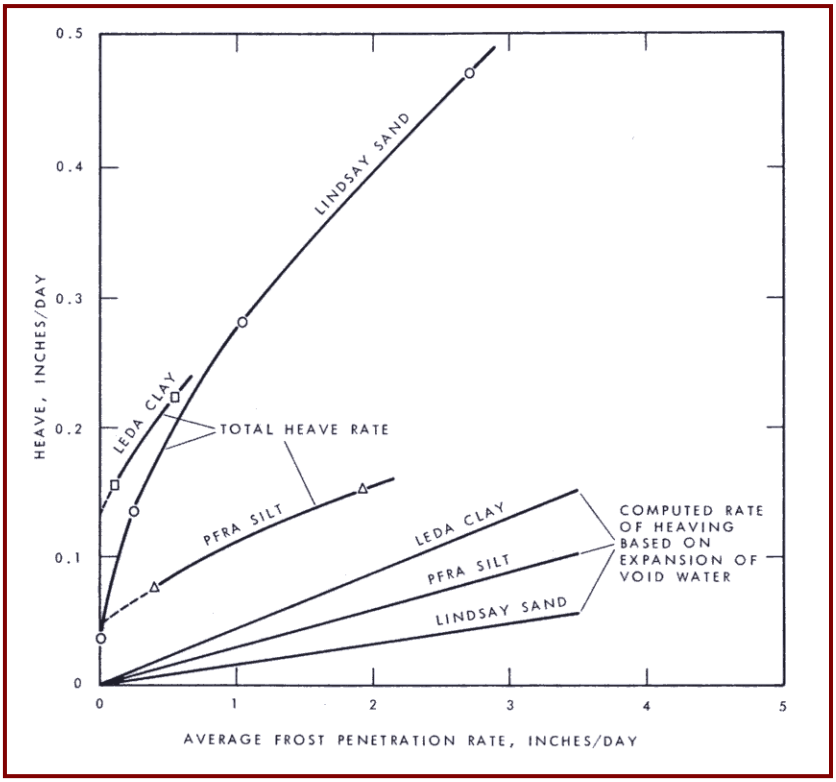

Figure 3-18. Heave rate vs. frost penetration rate for several lithologies (after Penner, 1972).

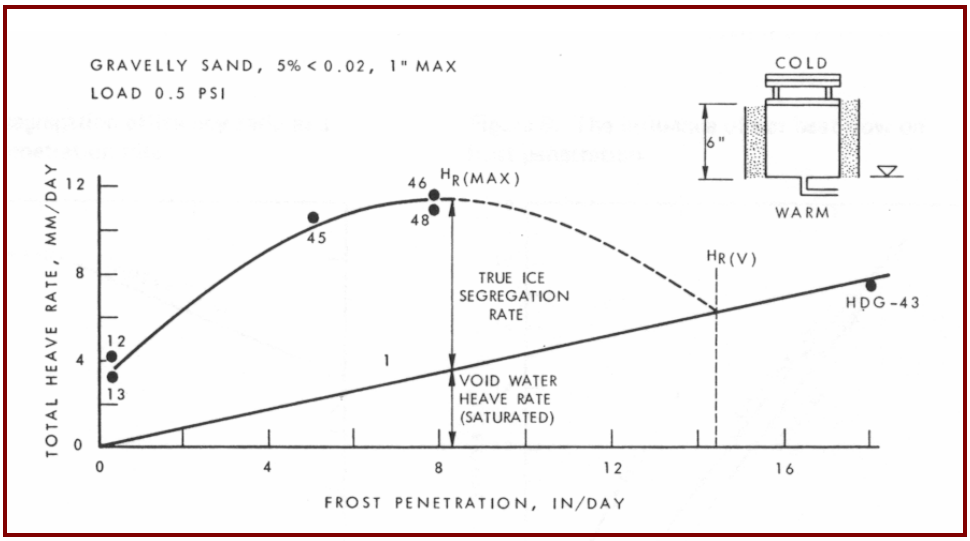

Figure 3-19. Heave rate vs. rate of frost penetration for a sand sample (after Penner, 1972).

3.2.5 Influence of freezing direction on measured rock properties

Despite an extensive literature search, it was not possible to find studies regarding the effect of the direction of freezing on the mechanical properties of samples undergoing freezing/thawing cycles. Nonetheless, variations on the mechanical response of frozen samples due to changes in the freezing procedure were published by Côté et al. (2000), and Côté (2003). In their paper, Côté et al. (2000) presented the deformation behavior of Twente sand and Boom clay samples during an internal radial freezing process, i.e. the rock was frozen by circulating a chilled fluid though an inner borehole drilled axially at the center of the sample. For Twente sand, at the beginning of the process, the sample suffered some contraction and expelled part of the saturating water. However, the

contraction stabilized rapidly as the temperature profile became steady. Figure 3.20 shows the behavior of lateral deformation and water content throughout the freezing process for two cooling fluid temperatures. At the beginning of the test, a frozen cylinder forms around the inner hole of the sample. As the freezing front advances outwards the saturating water expands; for this particular soil, only the 9% water content volume variation due to phase change is driving the expansion. The expansion of the frozen region creates a lateral stress, which acts on the unfrozen part of the rock (see Fig. 3.21). This lateral pressure causes an increase in pore pressure that forces some water to be expelled from the sample (in drained tests). Despite the fact that the diameter of the frozen zone is increased, the outer diameter of the specimen decreases as freezing continues. Thus, the unfrozen region in the sample is subjected to cryconsolidation, i.e. temperature-induced consolidation. This phenomenon is important at the beginning of the test but its magnitude decreases as the temperature profile stabilizes. A comparison of the outcome of drained and undrained freezing experiments is shown in Fig. 3.22. For undrained conditions, large deformations were recorded both in the axial and lateral directions; the sample compressed dramatically throughout the test[35]. This behavior suggests that core freezing in the field should be performed under drained conditions to avoid sample heaving and to decrease the magnitude of rock damage due to frost action.

[35] For this series of tests, the samples were frozen radially inwards

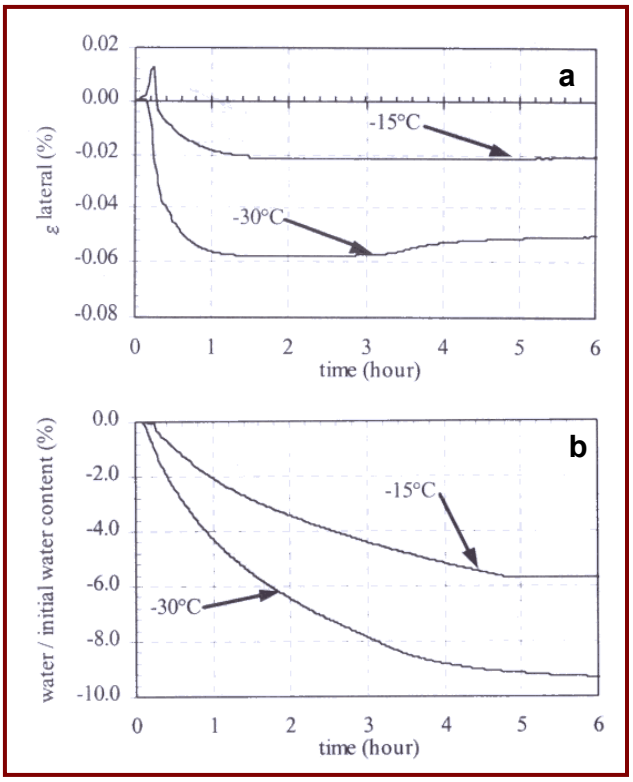

Figure 3-20. Influence of temperature on: a). lateral strain, and b). water content for Twente sand (after Côté et al., 2000).

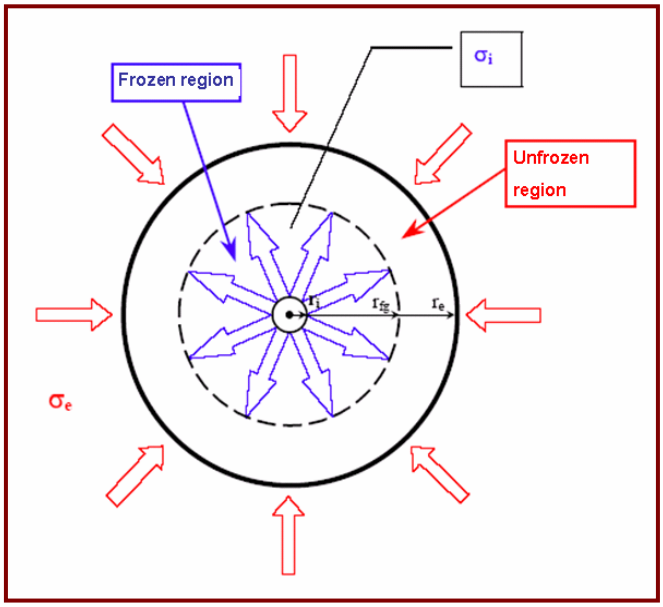

Figure 3-21. Radial strain within the samples, caused by freezing (after Côté, 2003).

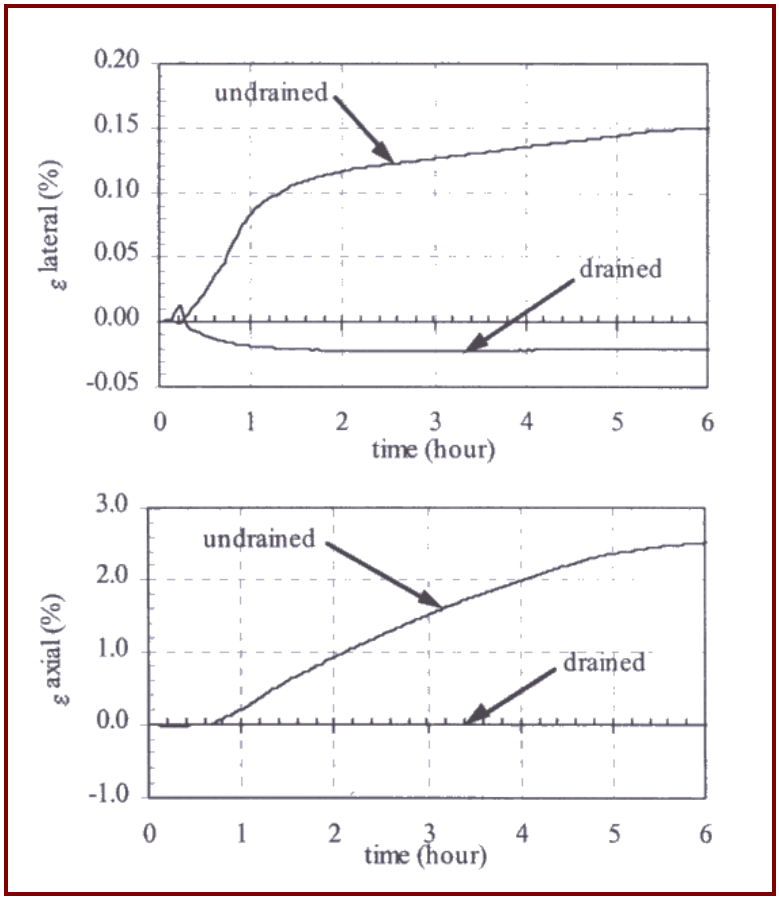

Figure 3-22. Comparison between the results of drained and undrained freezing tests for Twente sand samples (after Côté et al., 2000).

The results obtained by Côté (2003) from Brazilian and uniaxial compression tests were higher than those resulting from triaxial compression tests. Similar observations were reported by Thimus (1989) from experiments performed on Boom clay. The origin of this discrepancy could be the freezing method applied on the samples (orientation of the crystals of ice according to the direction of freezing, speed of cooling) or differences in the rates of deformation. The

samples used for the uniaxial and Brazilian tests underwent unidimensional freezing along their longitudinal axis. Whereas the cores utilized on the triaxial compression tests were radially frozen, i.e. from the outside towards the interior. Figure 3.23 presents a summary of the results obtained for all the tests; each point represents a test: uniaxial compression ($\sigma_3 = 0$), triaxial ($\sigma_3 > 0$) or Brazilian test ($\sigma_3 < 0$). A comparison of the changes in the UCS measured for the Twente sand due to changes in the freezing procedure is shown in Fig. 3.24.

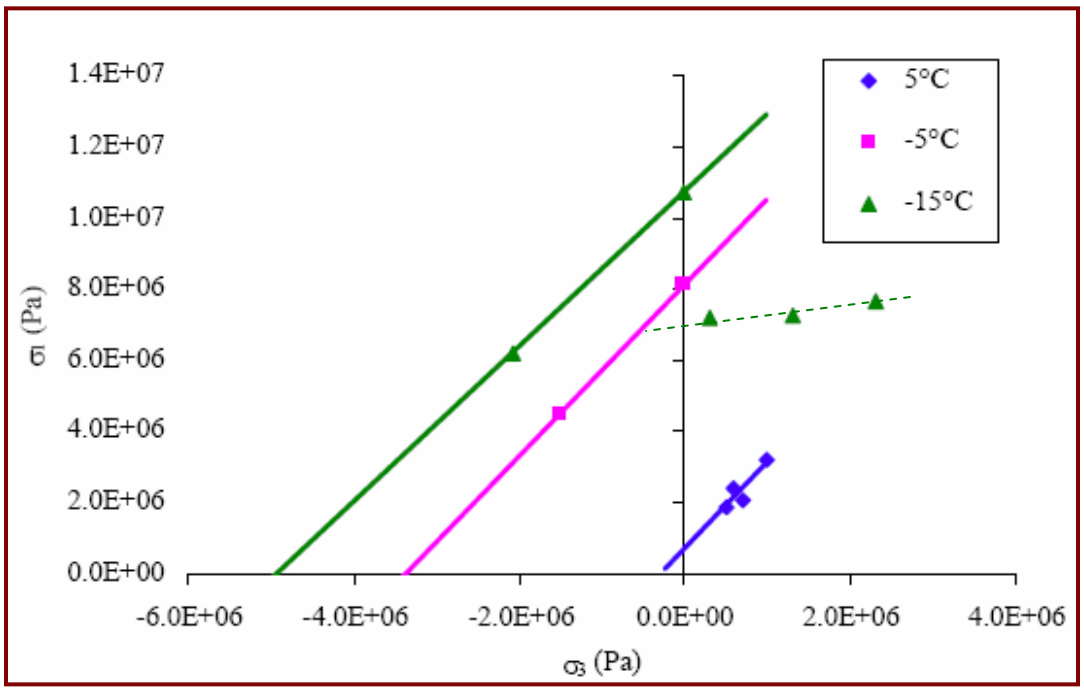

Figure 3-23. Results of uniaxial compression, triaxial compression, and uniaxial tension tests performed on frozen Twente sand (after Côté, 2003).

From Figs. 3.23 and 3.24, it is evident that the direction of freezing affected the mechanical strength of the frozen samples. The specimens that were frozen in

axial direction appear to be stronger than those frozen in radial (inwards) direction. This result is somewhat expected as during the inwards radial freezing procedure, the outermost rock layer is frozen first; creating an inwards stress that acts on the internal (unfrozen) region of the sample. As the freezing process continues, the volume of the unfrozen rock decreases; thus, one may expect the freezing-induced stress to build up until the whole sample is frozen. This temperature-induced stress may cause alterations in the way the ice crystals are formed; hence, modifying the mechanical strength of the frozen sample. On the contrary, the samples being frozen in the axial direction may expel part of their saturating water; hence, compensating for the occurrence of the freezing-induced stress and suffering less alteration during the freezing process.

Currently, most unconsolidated samples in the field are frozen inwards in the radial direction; thus, creating the conditions for the occurrence of freezing-induced "remolding" of the rock. It seems less disturbing to freeze the samples in axial direction, allowing part of the saturating fluid to escape. This new procedure would minimize the amount of freezing-induced stress that may be exerted on the sample during the freezing process. This conclusion seems logical, and follows from the results and conclusion suggested by Côté et al. (2000) and Côté (2003). Nonetheless, more specific research studying the effect of freezing

direction on the mechanical response of the core samples is critically needed in order to reach more definitive conclusions.

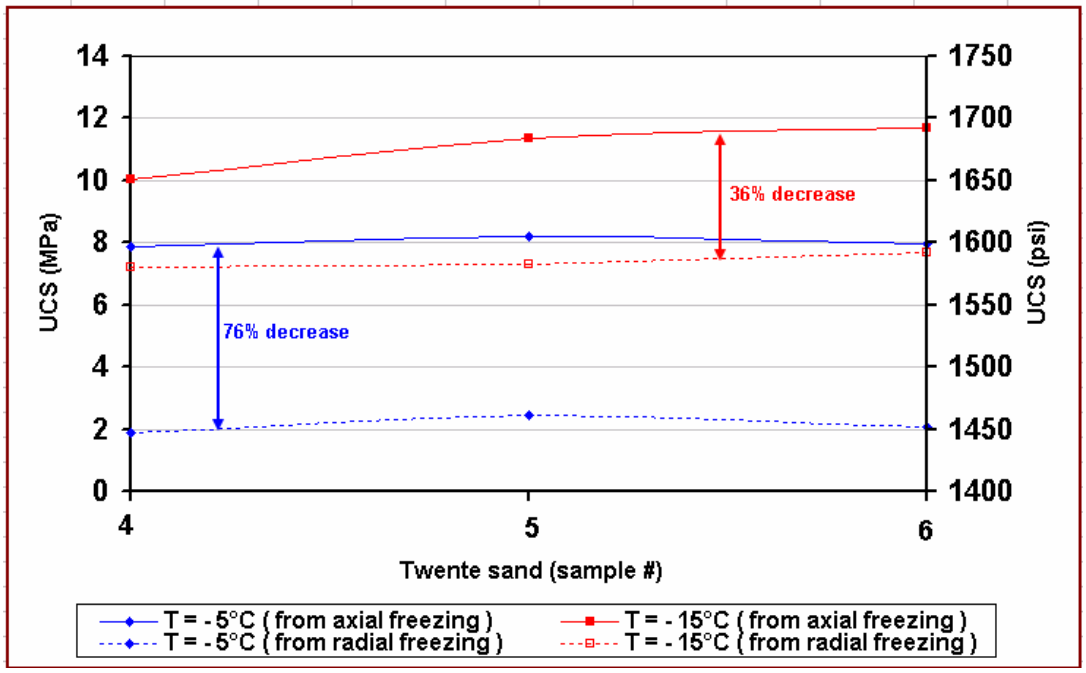

Figure 3-24. Variation of the UCS of frozen Twente sand because of changes in the freezing direction (data from Côté, 2003).

3.3 Comments on the reliability of the measured rock properties from unconsolidated cores

Stress relaxation during coring, handling and testing procedures has been found to cause important permanent changes in the porosity and mechanical behavior of some core samples. Alterations on the in-situ stress field applied on a rock, due to coring, have the potential to cause permanent "remolding" or rearrangement of

the rock fabric and of its pore structure; thus, a "new material" may be created. The magnitudes of the rock properties measured on this altered material may not necessarily represent the behavior of the in-situ formation. Techniques such as the application of an axial bias stress, inside the core barrel, show a great potential for core damage prevention. The existence of this artificial stress restrains the expansion of the rock in the axial direction, whereas the lateral expansion of the sample is limited by the core barrel itself. Nevertheless, some knowledge about the strength of the formation is necessary, prior to coring, in order to optimize the magnitude of the axially applied bias stress (if the bias stress is too large, compressive failure may be induced within the specimen).

Core damage may also be induced in a core due to freezing/thawing processes. It has been found that, even at temperatures well below 0° C (32° F), some of the saturating water may remain liquid. This liquid phase has the ability of migrating through the rock and collecting as ice somewhere within the pore network. These ice layers are believed to be responsible for extreme rock expansion, sometimes as high as 100% of the initial rock volume (Davis, 2001). The relative amount of unfrozen water is a function of the amount of fines in the rock, its pore size distribution, and the clay mineralogy. Even at frost temperatures, clays have the tendency to keep relatively large amounts of unfrozen water within their pores; whereas in sands, the amount of liquid water is almost non-existent.

In order for "frost heave" to occur, water needs to be supplied to the system at rates large enough to sustain the ice lenses growth. This is only possible if a large source of unfrozen water is accessible; either from unfrozen water saturating the rock or from the environment. The amount of unfrozen saturating water in "clean" sand cores is rather limited (see Fig. 3.10); as the attraction forces between the grains and the water phase are very small due to the small interfacial contact area. During standard core freezing operations, a sleeve containing the specimen is set in contact with a cooling medium (either liquid or gas) for several hours to induce rock freezing (ASTM C666, 1990). This procedure ensures minimal alteration of saturation conditions in the rock. Therefore, frost heaving is not expected to occur in sandstones with low shale content, during standard freezing operations.

However, in the case of rocks with high clay content, their freezing behavior is more difficult to predict because relatively larger amounts of unfrozen water may be available within the pores for migrating through the sample. On the other hand, higher clay content translates into lower rock permeability, which tends to hinder waterflow; hence, slowing ice lenses growth (i.e. it is more difficult for the water supply to move through the rock and reach the ice lenses). For these reasons, frost heaving appears to be rather improbable during core freezing operations (unless a large water source is in contact with the sample during the

cooling process). Nonetheless, a definitive conclusion cannot be reached at this time due to the lack of published experimental evidence. More specific studies on the effect of freezing on the mechanical properties of cores as function of the clay content are critical to clarify this issue. This would also bring more confidence to the laboratory results that need to be used in the rock characterization process.

As frost heaving[36] is probably not an issue in core freezing procedures, the normal expansion of water due to freezing, which is about 9% of its initial volume, could change the mechanical properties of rock. The effects of changes in the freezing direction on the strength of the rock have been marginally studied (Côté et al., 2000; Côté, 2003). It has been reported that the mechanical response of frozen samples probably changes due to alterations in the freezing directions on the samples. Radially frozen samples seemed to be weaker than those frozen in axial direction. The cause of this discrepancy appears to be the presence of stress caused by water expansion during the freezing process. In the radial case, the freezing front advances inwards increasing the pore pressure and locking the saturating fluids within the sample. This condition alters the stress field exerted on the rock and may cause material "remolding". In contrast, the samples being frozen in axial direction, contract slightly and expel part of the saturating fluids during the process; eliminating any stress induced by the freezing procedure. The

[36] Extreme rock expansion due to freezing, sometimes it could be as much as 100% of the rock thawed volume.

results published by Côté et al. (2000) and Côté (2003), were obtained under frozen conditions only, and no comparison to the unfrozen mechanical responses of the specimens was performed. Thus, their findings are inconclusive and additional research on the issue is needed.

Chapter 4

Hydraulic Fracturing Stimulation in Poorly Consolidated, Highly-Permeable Formations

As the world energy demand rises, hydrocarbon exploitation is driven further away into increasingly difficult environments, e.g. offshore fields, tectonically active settings. Consequently, field operations have become more complex, expensive and time-sensitive; thus, requiring optimum design of all variables involved in well planning. When dealing with weakly consolidated formations, comprehensive geomechanics studies have become necessary to address concerns such as: i) wellbore stability and damage issues during drilling operations; ii) completion issues relating to sand production; and, iii) pore pressure management for reservoir performance and subsidence control.

4.1 Operational problems commonly associated with poorly consolidated formations

Given their friable nature, weakly and un-consolidated rocks are particularly prone to exhibit problems such as wellbore stability, sand production, fluid losses, casing damage, and surface subsidence. High pore pressures and low mechanical

strength (characteristic of unconsolidated formations) create the conditions for narrow mud weight operational windows; thus, making drilling operations more difficult. The problems of reservoir compaction, and its associated bedding plane slip and overburden shear[37] have caused severe damage to hundreds of wells around the world (Bruno, 2002). In addition, stimulation procedures become less efficient as severe formation damage, due to large leakoff, may be induced. Furthermore, the created "fracture(s)"[38] is (are) not always planar and their geometry and dimensions may become very difficult to predict. The most common problems encountered while drilling, completing, and producing poorly-consolidated formations are discussed in the following sub-sections.

4.1.1 Problems during drilling

Current offshore reservoir development schemes normally call for highly-deviated and horizontal boreholes to be drilled in highly permeable, poorly consolidated formations. The prediction of the proper mud weight to be used for each drilling stage determines the success or failure of these wells. Over-designed mud densities increase fluid loss and damage, and the possibility of differential sticking. On the other hand, if the density of the mud to be used is too low, well

[37] Shear stress caused on the interlayer contact by the overburden rock moving downwards (during compaction).
[38] Hereby, the term "fracture" is used for referring to one or more features (not necessarily planar) caused by pore pressure increase due to fluid injection into the formation.

collapse may occur. Furthermore, this operational mud weight window for failure avoidance may be very narrow, and sometimes even inexistent (Chhajlani et al., 2002); mainly due to the tendency of weakly consolidated formations to show high values of pore pressure while having very low shear/tensile strength. The standard linear elasticity approach, traditionally used in the oil industry, tend to predict unnecessarily high values of mud density to prevent borehole collapse, limiting even further the options for well design. In addition, different mud densities may be required along the stratigraphic column of the well. Weak formations need low mud weight to avoid borehole fracturing and to limit fluid loss; while adjacent shales call for high mud weight in order to control rock burst or borehole sloughing issues. This is often the case when a horizontal or highly inclined well is drilled through a weak formation. Thus, when it is not possible to meet both density requirements simultaneously, one of the formations fails. Field experience shows that borehole failure normally takes place in the weak lithologies or in the cap rock (Morita and Ross, 1993).

One of the most important challenges in drilling deepwater wells, especially for exploratory wells, is the prediction of fracture gradients and pore pressures. As a consequence of the slim pore pressure - fracture gradient gap, multiple casing strings are often used in order to reach the target formations. In environments such as sub-salt formations, pore pressure predictions may become inaccurate as

salt formations obscure the seismic response of the underlying rock. A further complication that may appear in deepwater environments is the fact that extended reach wells experience variation of the water depth along their trajectory, i.e. the ocean floor depth may vary along wells drilled near undersea slopes. This is the case of the Mad Dog and the Atlantis fields, which lie beneath the Sigsbee Escarpment, where horizontal distances of only 2 miles may translate in water depth variations of up to 2,000 ft (Willson et al., 2003). In this case a one-dimensional calculation of pore pressure (as function of depth) is not accurate; a calculation including depth and the horizontal variation of the sea floor level would be more adequate.

Deepwater basins are normally associated with high energy deposition environments, where rocks tend to be under-consolidated due to the fact that rapid accumulation of sediments hindered the compaction process. As rocks remain under-compacted, saturating fluids are not allowed to escape the formation, and conditions for the occurrence of over-pressure are given. The final consequence is a narrow pore pressure-fracture gradient operational window during drilling operations. Figure 4.1 shows a comparison between the pore pressure and fracture gradient curves for a moderately under-compacted (MUC) formation, and a highly under-compacted rock (HUC).

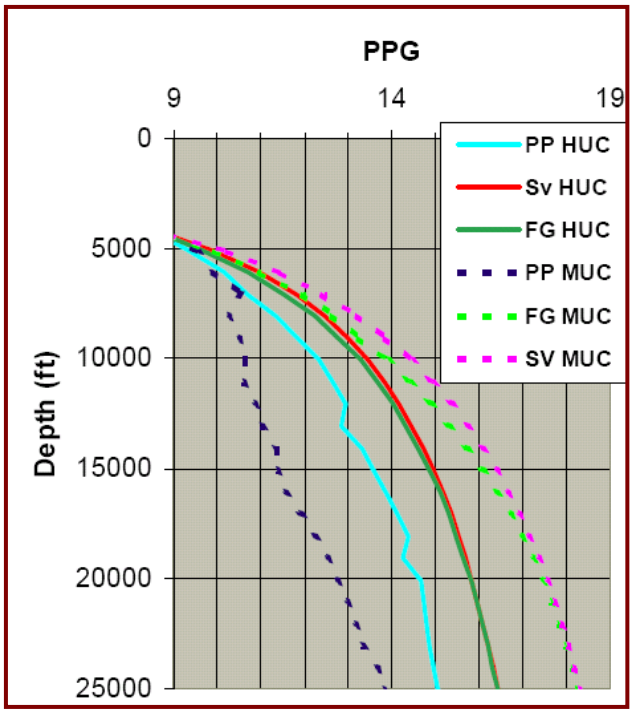

Figure 4-1. Pore pressure (PP), minimum principal stress (Sv), and fracture gradient (FG) curves for highly under-compacted (HUC) and moderately-compacted (MUC) rocks (after Willson et al., 2003).

In addition to the naturally narrow operational window normally found in unconsolidated environments, infill/deeper development drilling may experience further difficulties: as producing formations become depleted, the associated fracture gradient decreases. This effect is well recognized from hydraulic fracturing treatments in mature wells and has been repeatedly reported in the literature (Addis et al., 2001; Jones et al., 2001; and Chan and Zoback, 2002). Reductions in the fracture gradient appear to be a cause of major mud losses during drilling operations, with several thousands barrels being reported in some wells (Willson et al., 2003). This problem seems to be more severe when using

oil-based muds. The standard approach for overcoming this problem includes both a reduction of the fluid losses and the control of the equivalent circulating density during the drilling process (Fu et al., 1992). An alternative way of dealing with this fracture gradient reduction is to chemically consolidate the depleted sand zones (van Oort et al., 2003).

The complexity of typical offshore geological settings and their well design is evident from Figure 4.2, which presents a cross-section of the Pompano field in the GOM. The well TB-03 (marked by a red arrow) was drilled to access the M85 and M83 sands at depths of 9,900 ft TVD (10,820 ft MD) and 10,100 ft TVD (11,950 ft MD), respectively. At the time of drilling, the objective sands were depleted from the original reservoir pressure, 6,572 psi (12.64 ppg), down to about 4,000 psi (7.97 ppg). The overlying shales were overpressured; thus, demanding the use of 13 ppg mud in order to avoid instability. However, the fracture gradient was estimated to be only 12.45 ppg. Casing was set at 6,643 ft MD, and a 13.1 ppg mud had to be used for controlling well influx at 9,777 ft MD. Total fluid loss occurred at 11,280 ft MD when drilling the M85 sand. The drill pipe became stuck, and the losses continued, leading to the loss of the bottom-hole-assembly (Willson et al., 2003).

Another problem is a phenomenon known as "ballooning"; it may occur in any environment but is often encountered in deepwater reservoirs, mainly because of narrow mud weight window conditions. Well "ballooning" happens when mud losses are observed with operating pumps, and mud returns are registered after circulation is stopped. This phenomenon is also referred to as wellbore breathing and losses/gains (Edwards et al., 2002). It was originally explained as a balloon-like expansion of the wellbore, caused by the mud circulation (concept of equivalent circulating density[39], ECD). As the wellbore expanded, it required more mud volume; but after circulation was stopped, the borehole returned to its original geometrical condition causing extra mud returns. This concept was later revised as the volumes observed in the field were excessively large (up to 100's of barrels) to be explained as "elastic" borehole deformation. Recent publications (Bratton et al., 2001; and Edwards et al., 2002) have proven that the opening and closing of drilling-induced fractures are responsible for the "ballooning" effect. These fractures are forced open by the fluid injected during mud circulation, thus explaining the mud losses; conversely, when the pumps are stopped, the fluid filling the fractures is squeezed out and mud return is observed. An increment in the volume of the mud may be wrongly interpreted as a kick, with possible consequences on the mud weight design (Willson et al., 2003). Any increase in

[39] ECD is the total pressure exerted at the formation face during pumping; it is equal to the hydrostatic pressure (ρgh) plus the pump pressure.

mud density aimed at controlling this "kick" may translate into uncontrollable fluid losses as the induced wellbore fractures are extended.

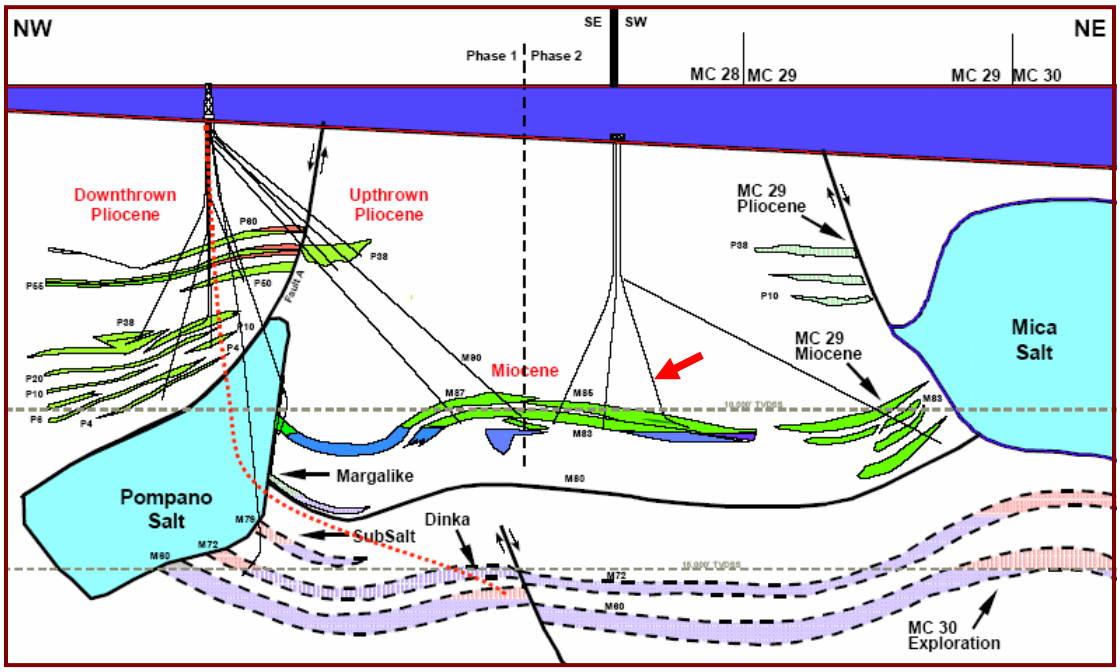

Figure 4-2. Cross section of the Pompano field, GOM (after Willson et al., 2003).

The low geothermal gradients, also common in deepwater reservoirs, allow for the deposition of thick layers of smectite-rich shales. These called "gumbo shales" tend to be highly reactive to water-based fluids, i.e. shale swelling and time-dependent stability are common problems. Such problems are normally prevented by using oil-based muds, although new water-based mud formulations have showed the shale inhibition characteristics of synthetic-based muds without sacrificing drilling penetration rate (Klein et al., 2003). In their paper, field data are presented comparing the drilling performance of water-based muds (WBM)

and of synthetic-based[40] muds (SBM). The WBM's were able to deliver SBM-like shale inhibition without using any salts, through a specifically designed combination of a shale inhibitor, a polymeric encapsulator and a given anti-accretion[41] agent. In addition, the reported rates of penetration were up to 85% higher for WBM than those obtained by using SBM. A brief description of the components of a new generation WBM is as follows: i) a multi-functional complex amine-based molecule, which acts as shale hydration suppressant and PH buffering agent; ii) a low molecular weight co-polymer that prevents shale dispersion by encapsulating the clay surfaces; iii) a specifically designed blend of surfactants and lubricants that coat drill cuttings and metal surfaces, thus reducing accretion problems; iv) a rheology control agent, normally Xanthan gum; and, v) a filtration controller, such as ultra-low viscosity PAC (Klein et al., 2003).

Chhajlani et al. (2002) reported several problems encountered during the drilling stage on several offshore wells in the Medusa field (GOM). The discovery well, MC582#1, was drilled deep into both target sands (packages X and XX), and plugged back after breaking into salt. A second geological sidetrack (MC538#1), was deserted due to severe circulation losses and to a kick. A bypass (MC538#1BP#1) was also abandoned due to the fact that the logging tools got

[40] In synthetic-based muds, the continuous phase is either oil or paraffin, or a combination of both (Klein et al., 2003)
[41] Accretion = drill bit balling

stuck. A total of four sidetracks were drilled, two of them for geological reasons and two due to operational problems (see Fig. 4.3). Well MC238#2, drilled near the discovery well also reported a kick and four sidetracks. In addition to the previously mentioned problems, episodes of tight hole, pack off, and liner running issues were also reported in these wells. Table 4.1 summarizes the most important problems encountered during the drilling operation in these two wells.

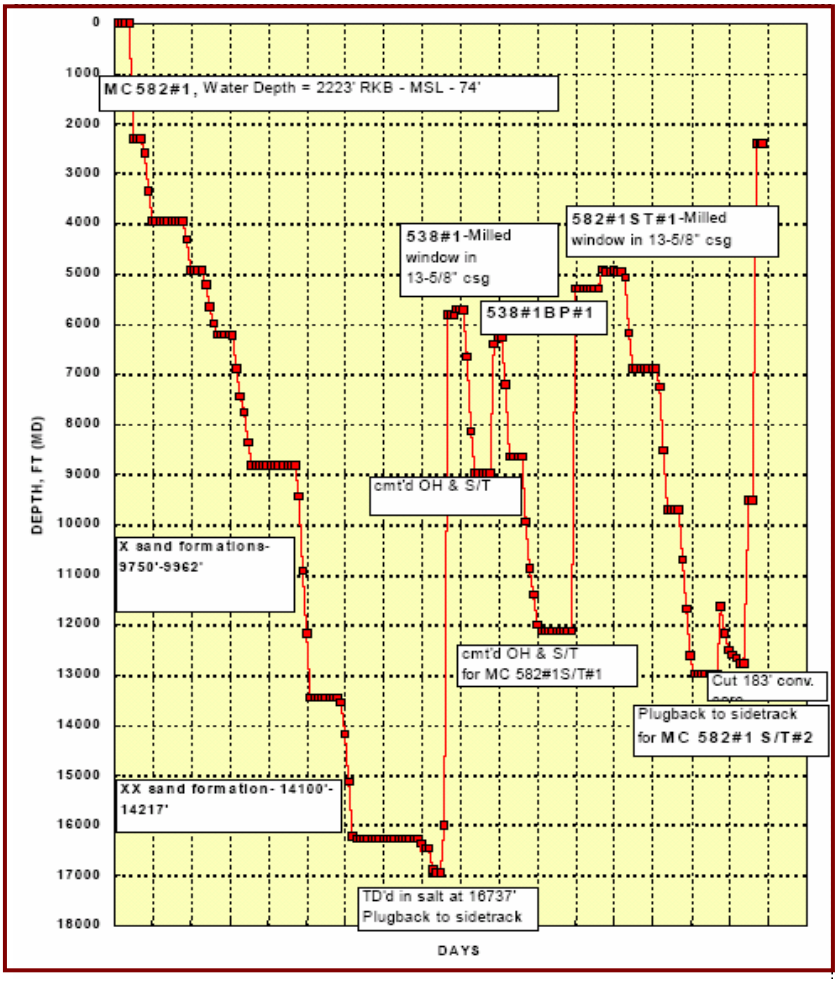

Figure 4-3. Days vs. depth plt for the discovery well MC582#1 on the Medusa field (after Chhajlani et al., 2002).

Well	Hole section	MD (ft)	TVD (ft)	Operational problem
MC582#1	10 5/8"x12 ¼"	13462-TD	12,750- TD	Well flowing and no returns while running/cementing 9 7/8" casing
MC538#1	12 ¼"	7952 8981	7734 8394	Tight hole and losing returns while drilling. Kick and losses. Set plug. No returns while 9 5/8" casing cementing
MC538#1 BP#1	12 ¼" 8 ½"	8536 11707- 12115	8094 10170- 10446	Tight hole while POOH. Could not get 9 5/8" casing to TD. Well ballooning initially while drilling. Lost mud at 12115', stable later. Run logs. Well starts flowing and then tools get stuck.
MC538#1 BP#1	12 ¼" x14 ¾" 10 5/8"	9121 10263	8421 9254	11 ¾" casing stuck off bottom and lost return while running liner. 9 7/8" casing stuck off bottom.

Table 4-1. Major operational problems experienced on the exploratory phase of the Medusa field (after Chhajlani et al., 2002).

4.1.2 Problems during production

Significant subsidence and casing damage have been reported to occur in several fields throughout the world: Gulf of Mexico, North Sea, South America, Southeast Asia, California, and Canada (Bruno, 1992; Dusseault et al., 1998, Li et al., 2003). These problems may be especially critical in deep offshore locations, where well costs are an order of magnitude higher than in onshore environments, and where difficult reach targets are to be developed.

Problems such as loss of pressure integrity, production tubing collapse, or difficulty to lower tools in the borehole are consequences of casing damage. Rock displacements along bedding or faulting planes are transferred to the casing

causing plastic deformation. These displacements are shear failures triggered by changes in the rock volume as a result of production or injection of fluids from or into the rock. Three critical forms of well damage involving shear have been recorded rather commonly: i) localized shear at weak lithology interfaces overlying the pay horizon due to compaction, e.g. Wilmington field (Bruno, 2002); ii) casing buckling and shear along the producing formation, e.g. Cold Lake in Canada (Dusseault et al., 1998); and, iii) localized horizontal shear at the top of the production or injection intervals due to pore pressure-induced volume changes, e.g. Ekofisk. According to Terzaghi's law, the effective stress acting on the matrix of a rock is equal to the applied stress minus the saturating fluid pore pressure (Jaeger and Cook, 1976). Tectonic and overburden stresses are constant; therefore, any change in the value of effective stress is determined only by a variation of the pore pressure, i.e. the effective stress varies in the same amount the pore pressure is depleted (as throughout production) or increased (as during injection)[42]. Production-related depletion leads to reservoir compaction, i.e. volume reduction of the pay zone. A producing reservoir compacts uniformly or uniaxially depending upon the in-situ stress and the sedimentary basin characteristics. A change in the rock bulk volume, V, is related to the bulk compressibility, C_b, and the pore pressure change, Δp, as shown in the equation below (Bruno, 2002):

[42] Assumes that Biot's coefficient is equal to 1; hence, it is only valid at rock failure.

$$\frac{\Delta V}{V} = C_b \, \Delta p \quad \text{.....(4.1)}$$

This equation intrinsically assumes that the rock compressibility is both, constant and independent of the magnitude of the applied stress, which is not always true as already explained in Chapter 2. Hydrocarbon extraction lowers the pore pressure within the producing rock; this depletion causes an increase in the inter-granular load (effective stress), as a result the grains rearrange to withstand the change in the applied stress magnitude. The new relative position of the grains will increase the inter-granular contact area; thus, lowering the rock porosity, and decreasing its overall volume. If the formation is assumed to behave as a linear-elastic material, a single value of compressibility would suffice for describing the whole reservoir compaction curve. However, poorly-consolidated rocks are far from linear-elastic media; as they may experience severe plastic deformation because of depletion. A more realistic compaction curve for weakly consolidated reservoir rocks is presented in Fig. 4.4. In this plot, a porosity reduction of about 5% is observed after total drawdown (path A-B); in other words, the rock interval looses about $1/20^{th}$ of its original height due to production-related depletion. When high-pressure fluid injection is utilized in the reservoir for pressure restoration, the porosity rebounds following the red curve (path B-A-C) (Dusseault et al., 1998).

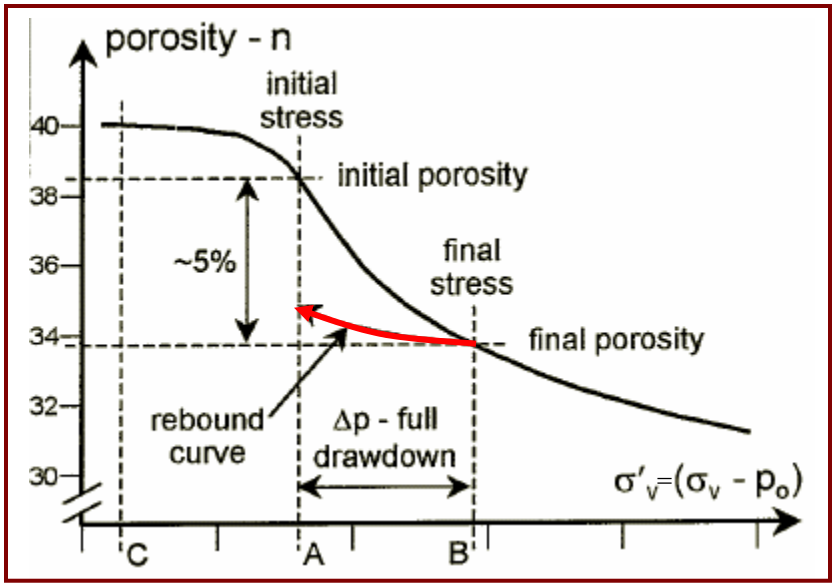

Figure 4-4. Reservoir compaction curve (after Dusseault et al., 1998).

Hydrocarbon traps are commonly associated with lenticular structures; this is also true for poorly-consolidated formations. Thus, compaction translates into a combination of inwards-downwards deformation. As a consequence, the crestal section of the reservoir undergoes an increase in the magnitude of the minimum horizontal principal stress, σ_h. Simultaneously, the remote flanks of the structure experience a drop in the value of σ_h. By the same token, the rocks overlying the shoulders tend to slip, causing the shear stress on them to increase (refer to Fig. 4.5).

Nonetheless, the position of the overburden damage seems to be determined by the location of weak interfaces rather than by the location of the areas of high shear stress (Bruno, 2002). This is supported by the fact that induced shear stress seems to be distributed over large depth intervals, while reported casing damage is generally localized with depth (see Fig. 4.6). Furthermore, overburden casing damage in the Valhall, Arun, Belridge, Lost Hills and Cold Lake fields seems to indicate that shearing damage is widely distributed over the entire reservoir structure, and not only at the flanks as it would be expected (Dale et. al, 1996; Fredich et al., 1996). On the other hand, evidence of high concentration of casing failure around the structure flanks has been found in the Ekofisk field, and to some degree in the Wilmington field (Bruno, 2002).

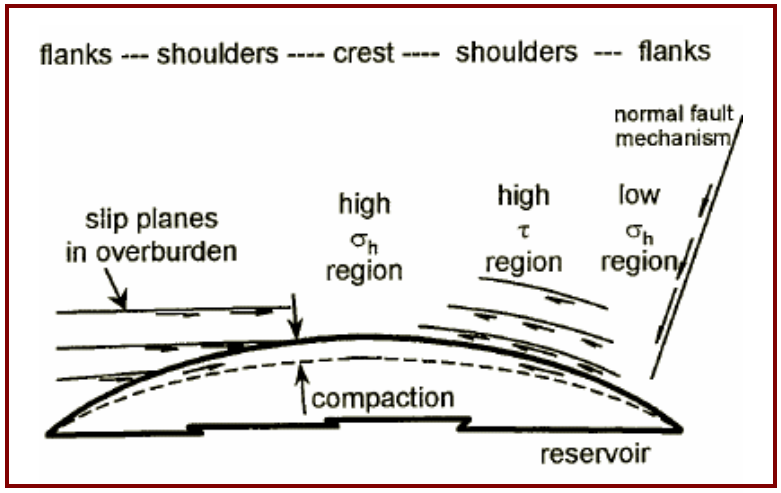

Figure 4-5. Compacting reservoir bedding plane slip (after Dusseault et al., 1998).

The standard method used in the oil industry for compaction prevention and control is the injection of fluids at high pressure into the compacting formation. The pore pressure in the pay zone changes rapidly because of its high permeability; hence, its effective stress drops swiftly. However, this is not the case of its surrounding seal formations; the pressure of the fluids saturating the relatively impermeable bounding strata remains almost unchanged. Whereas the pay zone tends to expand due to an increase in pore pressure, the volume of the surrounding rock stays constant. This effect causes the shear stress exerted on the reservoir limits to augment; if this increment overcomes the shear strength of the rock, slip ensues and casing failure is likely to occur. In addition, increments of the pore pressure may lead to fault reactivation as the effective stress acting on the discontinuity plane is reduced.

Another very important problem normally associated to hydrocarbon production from weakly consolidated formations is sand production. Sand inflow accompanying the produced fluids causes problems such as tubing/facilities wear, casing collapse, and surface handling problems. Severe solids production may lead to critical operational problems like sand bridging, wellbore plugging, and tubular erosion; all of which increase the required workover frequency. In addition, collapse or serious deformation of the casing may be caused by solids production (Dusseault and Santarelli, 1989).

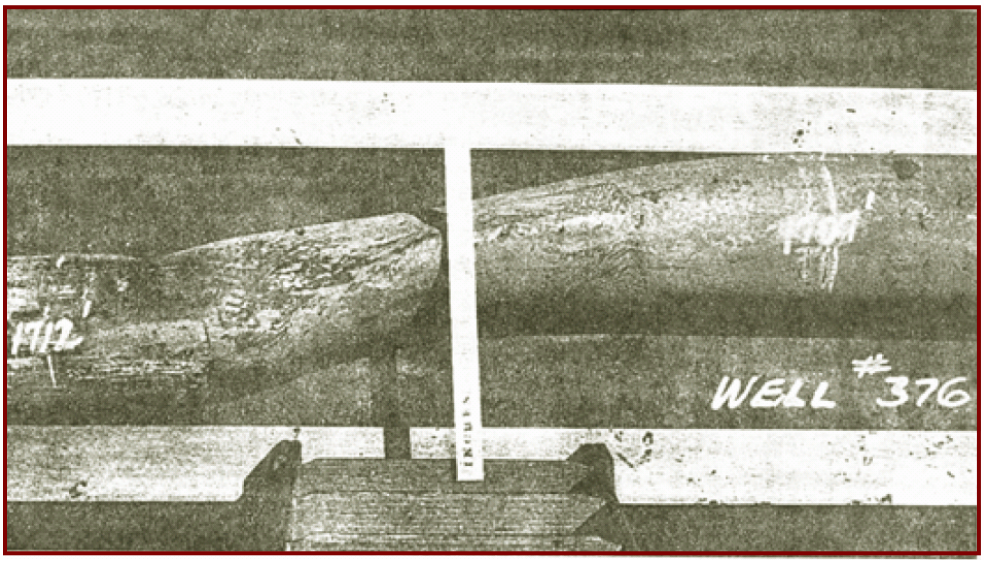

Figure 4-6. Localized deformation in well damage within overburden at Wilmington field, with approximately 10" lateral offset on 10 ¾" casing from 1,707 to 1,712 ft depth (after Frame, 1952).

The deformation history of the rock is important when it comes to determining its potential for solids production. The mud-rock interaction during drilling and completion operations plays a major role on rock stability during production: if a cake-building drilling mud is used, its hydrostatic pressure brings support to the borehole. On the contrary, using highly-invasive muds would increase the formation pore pressure; hence, increasing the possibility for the creation of shear/ tensile failure surfaces. Furthermore, it has been proven that increments in water saturation may provoke dramatic reductions in the mechanical strength of the rock (see Chapter 2). If the borehole wall yields during drilling, caving may follow as loose, broken material contributes little to the overall rock stability and is readily removed by the mud (Santarelli, 1987). Given the brittle nature of most mineral

cements; strain magnitudes as little as 0.3% may lead to cohesion loss and rock failure (Dusseault and Santarelli, 1989).

Completion operations may also cause significant alterations to the in-situ rock: cement contraction lowers the radial stress, σ_r; thus decreasing the support on the borehole wall. Expandable cements and inflatable packers are considered a good alternative for avoiding this "shrinkage" effect (Suman et al., 1983). In addition, perforating also disrupts the material cohesion as a region of crushed grain is created by the penetrating explosive charge. Around it, an elastoplastic region with varying degrees of alteration is induced; and further away from the perforation, a region with little or no damage corresponding to the virgin state of the rock exists (Fig. 4.7).

After the completion of a well in poorly consolidated formations, solids production may be observed at the beginning of the productive life of the reservoir or after a certain production time lapse. The production of solids is seldom a continuous development but an intermittent process where particulate material bursts are followed by solids-free fluid inflow. Sand production is a function of the rock strength, the in-situ stress field, the production flowrate and the perforation scheme (perforations size and orientation relative to the principal stresses).

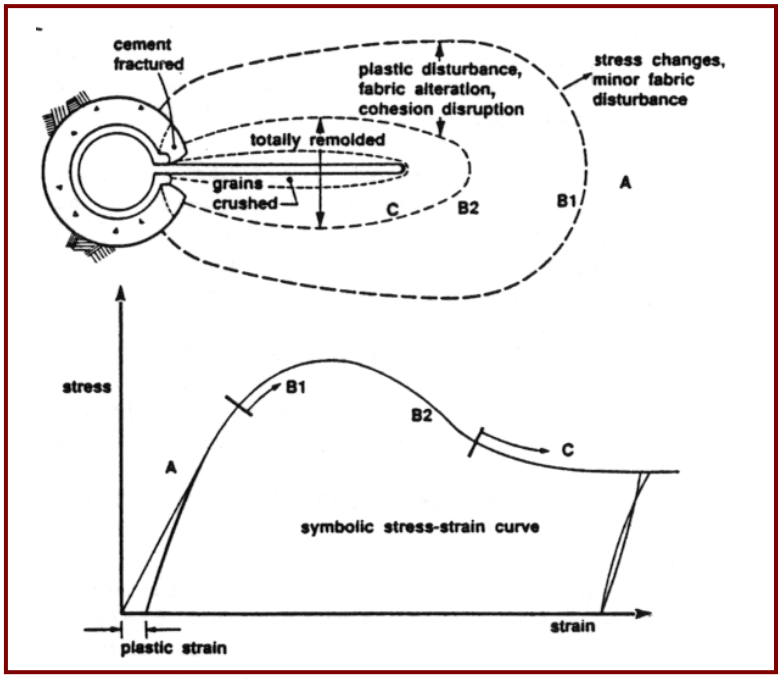

Figure 4-7. Damage to weak sandstones during perforation (after Dusseault and Santarelli, 1989).

Previous studies (Bratli and Risnes, 1981; Fahrenthold, 1984; and Fahrenthold and Cheatham, 1986) have shown that, in mechanically weak or unconsolidated formations, in-situ stresses will cause a shear failure region to develop around a cavity located within the material. If fluid flows towards the cavity, additional stresses (due to fluid drag forces) are induced in the rock, causing the shear failure region to extend farther away from the cavity in an attempt to reach overall equilibrium. These drag forces are a function of the rheology and flowrate of the fluid being produced through the porous medium. Theories indicate that, for a given rock, there is a maximum flowrate (for a specific fluid), beyond which the

shear zone would extend uncontrollably; thus, causing catastrophic failure and massive solids production (Perkins and Weingarten, 1988). In an attempt to predict the magnitude of this flow threshold, elastoplastic models were postulated; such as the one published by Risnes et al. (1982). These models assumed the existence of two axially symmetric regions around the wellbore: a plastic region nearest to the well, and an elastic (intact) zone further away into the reservoir (see Fig. 4.8). These models also included assumptions such as, isotropy and homogeneity in the rock properties, fluid incompressibility and steady-state conditions (Roegiers, 2004a). The following equation was provided by Risnes et al. (1982) to estimate the magnitude of the flow threshold for rock failure:

$$q = \frac{4\,C\,\tan(\alpha)\,\pi\,h\,k_p}{\mu} \quad \text{.....(4.2)}$$

Where,
- q: fluid flow rate;
- C: cohesive strength;
- α: internal friction angle;
- h: producing formation height;
- k_p: plastic region permeability; and,
- μ: fluid viscosity.

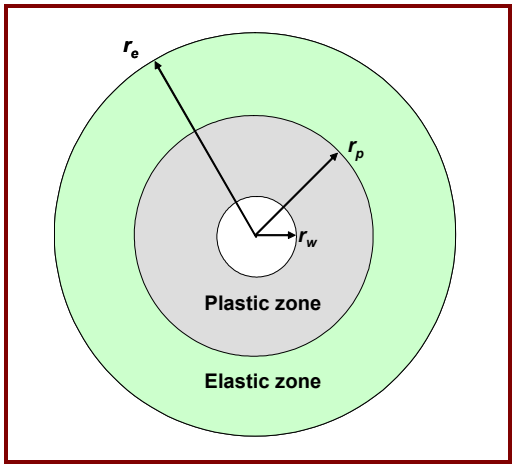

Figure 4-8. Elastoplastic model as postulated by Risnes et al. (1982).

The Matagorda Island-623 gas field is located offshore southeast Texas in the Gulf of Mexico. All of its 17 development wells have experienced some form of well failure or casing damage throughout their production life of about 16 years; Fig. 4.9 shows a 3D model of this field. The main reservoir in Matagorda Island is the Siph-D sand with a maximum gross pay thickness of 500 ft. This sand was initially developed between 1982 and 1985 with the drilling of six wells, which had cased and perforated completion schemes. Two additional wells, the E1 and the MI635#1, were later drilled and completed with cased hole-gravelpack completions. A second development phase has taken place since 1995, as nine replacement wells were drilled to replace the initial wells, which had failed, and to maintain production. Figure 4.10 presents the well life together with completion type and production rate for both Phase I and Phase II wells (Li et al., 2003).

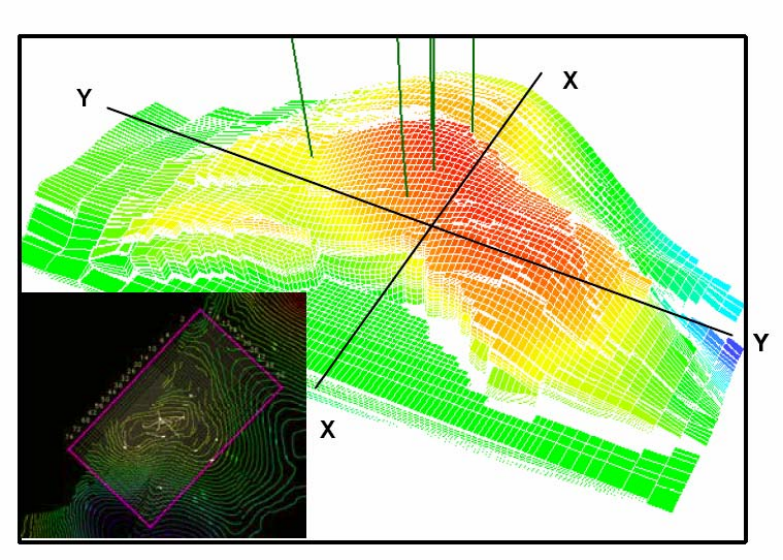

Figure 4-9. 3D model of the Matagorda Island 623 field (after Li et al., 2003).

A strong correlation can easily be identified between well life and peak production rate. The wells in Phase II (circled in red in Fig. 4.10) had a noticeable shorter lifespan, probably due to the fact that their higher production rates impacted the formation bonding and ultimately led to sand disintegration. A second conclusion in this case, is that gravelpack completion provided no extra benefits for the wells, i.e. gravel-packed wells were not able to produce neither more nor longer than those that were cased and perforated. Fracpack completions provided higher production rates and almost eliminated the problem of sand production, although their productive life was a lot shorter than in the case of conventionally completed wells.

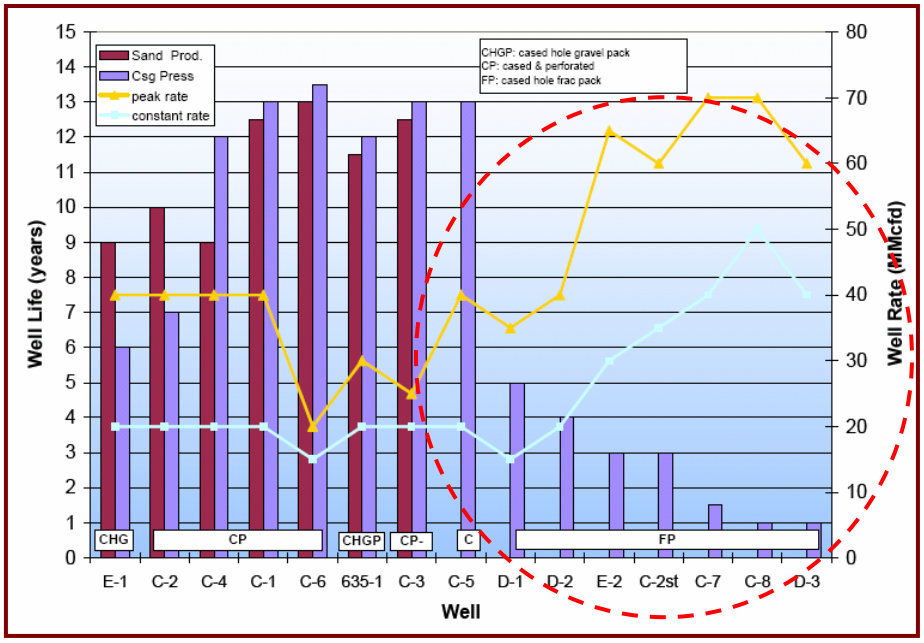

Figure 4-10. Siph-D sand/fluid production rates, and pressure, Matagorda Island field (modified from Li et al., 2003)[43].

4.1.3 Problems during stimulation

The objective of hydraulic fracturing stimulation in low permeability formations is to create a high conductivity channel able to reach reserves located away from the wellbore. Nonetheless, in highly permeable formations, bypassing the drilling/completion-induced damage zone and reducing the pressure drawdown are the main goals of any stimulation operation. A relatively short, highly conductive fracture, induced in a highly permeable reservoir, will breach near-

[43] The original plot in Li et al. (2003) provided no indication on the magnitude of the sand production problem. The red circle marks the wells with the highest production rates and shortest lifespans.

wellbore damage; thus, reducing the pressure drawdown, lowering flow velocity, and increasing the effective wellbore radius. This type of technology is a combination of gravelpack and fracturing technique and for that reason is commonly dubbed "fracpack" (Roodhart et al., 1993). Fracpacking has become an extensively used sand control technique for offshore GOM operators (Mullen et al., 1994); and its success has been thoroughly documented in the literature (Stewart et al., 1995; Powell et al., 1997). Currently, this technology is being effectively applied for a wide range of fracture sizes in various reservoirs around the world, including California, Alaska, South America, West Africa, and Southeast Asia (Reimers and Clausen, 1991; Gulrajani et al., 1997; Fan et al., 2001).

Fracpack operations involve two phases: fracture creation (terminated at tip-screen-out[44]), and fracture widening and packing. During the first stage, the fracture design is aimed at creating a short fracture. Once the desired fracture length is achieved, tip-screen-out is induced with sand; subsequent pumping increases the fracture width and allows for fracture packing with high conductivity proppant (Smith et al., 1987). The success of the fracpack technique relies mainly on the creation of a highly conductive fracture; its length affects only slightly the potential performance of the treatment (Roodhart et al., 1993).

[44] TSO occurs when the sand slurry starts to dehydrate at the tip of the fracture, bridging and impeding further fracture propagation in the lateral direction.

Hence, the objective of the stimulation treatment is to maximize the fracture conductivity by increasing the fracture propped width and the permeability of the proppant, i.e. using larger, more uniform-sized proppant particles translates into higher fracture permeability.

The success or failure of the treatment will be determined by the accuracy of the design parameters used. Fracpack operations involve severe risk of premature screen-out and also of failure in achieving TSO. Therefore, special calibration tests (e.g. mini-fracturing) are normally carried out before the treatment implementation. Perhaps, the most critical factor involved in fracture design of TSO hydraulic fracturing treatments, is the fluid leak-off coefficient (Smith et al., 1987). In order to predict the fluid loss behavior of the rock/gel system, it is customary to perform a minifrac test using the pad gel. In their paper, Smith et al. (1987) present a complete example of one of these calibration treatments performed in a chalk field in the North Sea.

It is crucial for maximum well productivity that the fracture conductivity is not significantly impaired by sand/fines invasion of the proppant pack. The presence of sand or fines within the proppant pack may lead to significant permeability reduction; hence, to lower production potential. The use of small size proppant limits the possibility of sand/fines inflow; however, it also limits the ability of the

proppant to allow fluid production (see Fig. 4.11). The Saucier's criterion establishes that the average proppant diameter should be less than 6 times the average diameter of the formation sand (Saucier, 1974). Although this standard was developed for gravelpack design, it is also used as the selection criterion for proppant size in fracpacks. It is important to notice that the fluid velocities normally handled by a gravelpack are orders of magnitude higher than those expected in a fracpack. Hence, it is reasonable to conclude that Saucier's standard is excessively restrictive and tends to unnecessarily limit the production potential of fracpack completions (Roodhart et al., 1993). Figure 4.11 presents a series of theoretical estimates of the effect of proppant size on well production rate, for various fracture widths and proppant concentrations, in a well with original skin equal to 40. For a fracture width of 5 mm (about 1/5 in) and propped with 20/40 mesh sand, the expected production rate is about 65% higher than the one that would be obtained by using 40/60 mesh sand. This conclusion is supported by field data published by Hainey and Troncoso (1992); in their paper, encouraging results are reported from two fracpacked oil wells completed with 16/20 and 16/30 mesh sand rather than with the 40/60 proppant recommended by the conventional selection criterion. Initial production data indicated that completions using larger proppant perform well, without sacrificing their sand control capabilities.

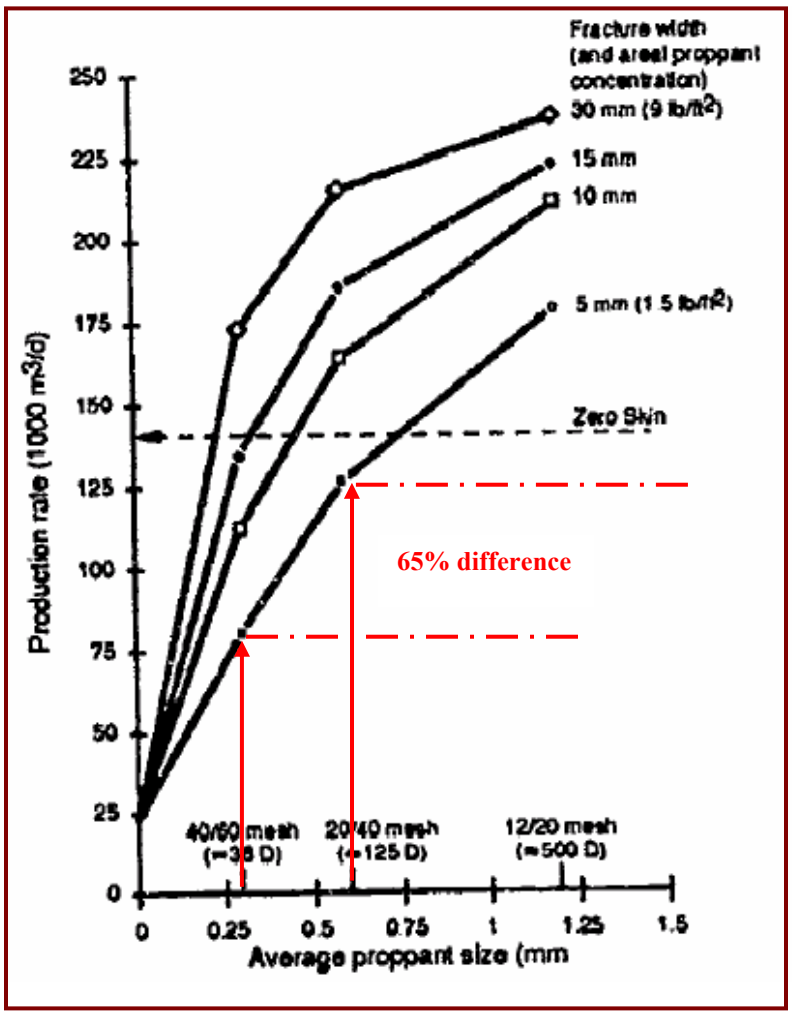

Figure 4-11. Simulated production after fracpack treatment for a well with an original skin equal to 40 (after Roodhart et al., 1993).

Another important concern during the implementation of fracpack treatments in high permeability sands is the fact that excessive fracturing fluid leak-off may lead to severe formation damage. The existence of an impaired permeability region along the fracture wall is mainly caused by the leak-off of fracturing fluid

filtrate and/or unbroken polymer. The effect of this damage zone was first evaluated by Prats (1961); who provided a relationship for comparing the production rate of the reservoir with and without the presence of skin:

$$\frac{Q_{Damaged}}{Q_{Undamaged}} = \frac{1}{1+\left[\frac{k}{k_d}-1\right]\frac{4\,W_d}{\pi\,L\,\ln\left(2r_e\,/\,L\right)}} \quad \text{.....(4.3)}$$

where,

- r_e : reservoir radius;
- L : fracture length;
- W_d : width of the damaged zone; and,
- k/k_d : ratio of original to damaged rock permeability.

Figure 4.12 is a graphical representation of Prats' equation; the production potential of the well appears to be sensitive to both the severity of the damage and the depth of the invasion bank. However, reasonable combinations of permeability damage and invasion depth (e.g. k/k_d = 0.01 and W_d = 0.2 ft) render reductions of well productivity that are less than 15%. This confirms the theory that the performance of fracpacks is determined by the fracture conductivity rather than by the induced formation damage (Roodhart et al., 1993).

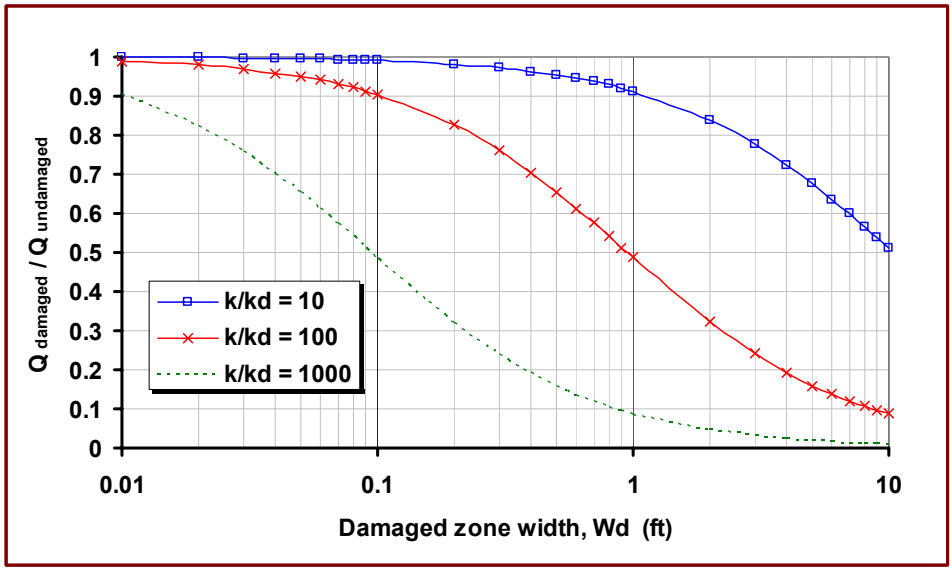

Figure 4-12. Effect of fracturing induced damage on the well productivity (L= 25 ft, r_e=1500 ft), built from equation 4.3.

The friable nature of unconsolidated formations creates additional complications during the stimulation treatment. Large amounts of proppant flowback have been reported in several fields subjected to fracpack stimulation. According to Reimers and Clausen (1991), fracpack treatments in Prudhoe Bay (Alaska) have shown pronounced tendency to produce large amounts of proppant flowback, in some cases up to 20% of the total pumped proppant mass. This problem is more common in previously produced reservoirs with sanding incidents. It is believed that sizable voids may be created around the casing/cement during the production stage before the stimulation. This theory is further supported by the fact that large cement volumes are normally needed during squeeze-cementing operations, and

also by the abnormally high porosities reported by cased-hole neutron logs (Reimers and Clausen, 1991). During the hydraulic fracturing operation, these voids fill with proppant, which may be easily produced during the well flowback. One of the most puzzling problems during fracpack operations is the calculation of the expected bottomhole pressure during the treatment. Accurate prediction of the pressure is not always possible; some authors have reported unexpectedly high values of treatment pressure (Shlyapobersky, 1985; Palmer and Veatch, 1987; Economides et al., 2002), while some other have found that the expected pressure was indeed higher than the one measured in the field (Roodhart et al, 1993; Smith, 2004) and in the laboratory (van Dam et al., 2000). This issue is further addressed in the next section.

4.2 Standard hydraulic fracturing simulators

The first meaningful analytical approach to studying the mechanics of fracture propagation was proposed by Griffith, in the 1920's. The "Griffith Crack" concept is the basis for the development of the LEFM theory (Broek, 1986), and is expressed by:

$$\frac{\delta U}{\delta a} = \frac{2\pi \sigma^2 a}{E} = 2G \text{ ……...…….(4.4)}$$

where U is the elastic energy, a is the characteristic fracture length (Fig. 4.13), σ is the far field stress, G is the energy release rate, and E is Young's modulus. Hence, Eqn. 4.3 allows the calculation of the amount of energy necessary to make a crack extend from a length a to $a+\delta a$. Griffith made an important assumption in developing this relationship: no energy absorption takes place at the crack tip. Energy is used either to elastically deform the rock or to rupture the material. An intrinsic assumption in Griffith's analysis is that the deformation is infinitesimally small. The Griffith failure criterion assumes that $\delta U/\delta a$ is a material constant. Thus, there is a critical value of stress, σ_c, at which the material will experience instantaneous catastrophic failure. This value is given by:

$$\sigma_c = \sqrt{\frac{EG_{IC}}{\pi a}} \quad \text{.....(4.5)}$$

The critical energy release rate, G_{Ic}, is considered a material property, even though it changes with temperature and setup geometry. This equation also reveals the existence of a critical crack length above which failure will occur. Considering the plain strain condition, and the case where $a >> r$, then the stress σ_{yy} can be defined by:

$$\sigma_{yy} = \frac{K}{\sqrt{2\pi r}} \quad \text{..... (4.6)}$$

Analyzing this equation for a zone close to the fracture tip, i.e. $r \rightarrow 0$, it can easily be observed that σ_{yy} tends to infinity. This numerical singularity shows an essential flaw in the LEFM theory. The equation fails within a zone of most interest throughout the failure process. K is the stress intensity factor, which is a quantity that characterizes the stress concentration. Furthermore, K will be the only factor affecting the magnitude of the stress at a given distance from the fracture.

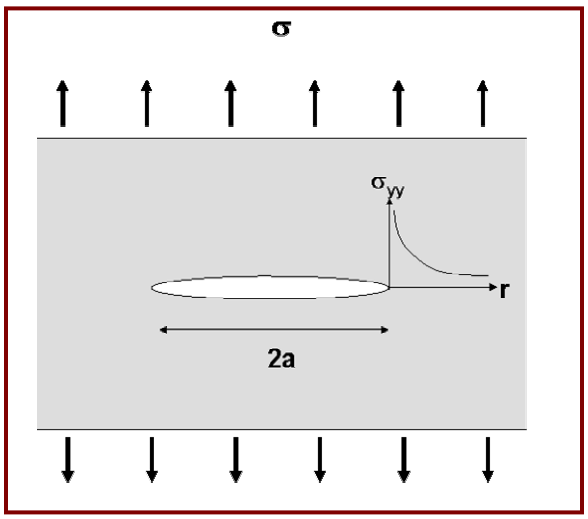

Figure 4-13. Griffith crack (after Broek, 1986).

At failure onset, σ_c, can be expressed in terms of a "critical stress intensity factor" (also known as fracture toughness); i.e.

$$\sigma_c = \frac{K_{Ic}}{\beta\sqrt{\pi a}} \quad \text{..... (4.7)}$$

This is the principal equation on which the LEFM theory is based; here, the parameter β is a geometrical factor. Fracture toughness is a controversial concept in view of the fact that it predicts that the energy necessary to propagate a fracture is inversely proportional to its length; the opposite has been commonly observed in the field (Economides et al., 2002). This discrepancy might be explained by the fact that the LEFM theory assumes that the fracture walls are in contact only at the tip, and that fracture containment is not taken into account in the model.

However, it is more probable that what is assumed to be a single fracture is, instead, a series of sub-parallel fractures separated by areas of contact between the crack walls (Fig. 4.14). Thus, the "wedge" effect at the fracture tip is lost, making the failure process more difficult. It is also possible that the "macrocrak" is created as a consequence of the coalescence of micro shear fractures in the process zone. By the same token, the fluid being injected at the wellbore perforations will have to flow through a more difficult path in order to reach the tip, as the crack propagates. Other factors, such as back-stresses[45] are not considered by LEFM, although they might be very important during the rock fracturing process.

[45] Changes in the original in-situ stress field, caused by the presence of the hydraulic fracture itself.

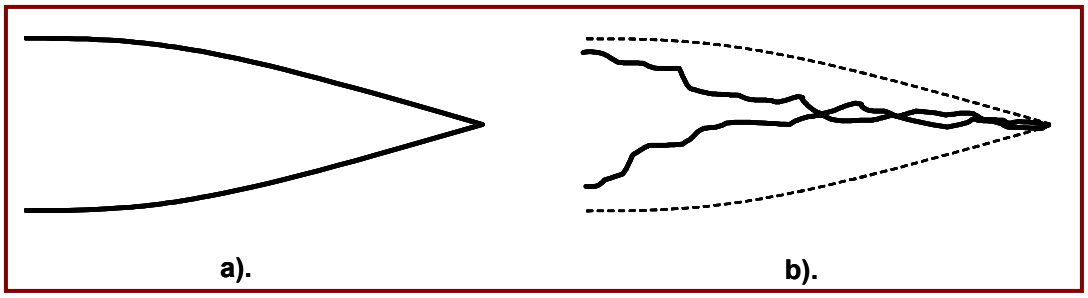

Figure 4-14. a). Ideal fracture in LEFM; b). More realistic sketch of a hydraulically induced fracture.

The vast majority of fracture modeling is carried out by using simulators that are largely derived from LEFM. Evaluation of hydraulic fracturing operations data have revealed discrepancies between predicted and observed responses. Several authors (Shlyapobersky, 1985; Palmer and Veatch, 1987; Economides et al., 2002) have reported that the measured field net pressure is larger than predicted by fracturing simulators. It was also found that simulated net pressure was rather insensitive to rate variation and fluid viscosity. Furthermore, direct observations of mined-back hydraulic fractures revealed multiple strands rather than a single crack (Warpinski and Teufel, 1987). Additionally, when standard simulators are run on unconsolidated formations, it is apparent that neither tip-over-pressure effects nor geometry variations can be accounted for. These discrepancies may be explained by considerations not included in the LEFM theory, such as:

- Non-linear stress-strain relationships for rock behavior, as unconsolidated rocks tend to behave plastically, even under small magnitude loads. Thus,

characterizing their mechanical behavior by using only linear elastic parameters (Young's modulus and Poisson's ratio) seems rather insufficient.

- Large strains caused by loading of low modulus rock, as is the case in very weak formations. Substantial rock deformations render the assumption of infinitesimal strain during hydraulic fracturing invalid. Thus, even second order deformation terms (e.g. $\partial^2 u/\partial x^2$) become important and should be taken into account.

- High fluid leak off into high permeability/high porosity formations; Carter's unidimensional leak-off model fails to represent the fluid loss process into high permeability formations. A fully 3D model such as those used in reservoir simulation would likely be more accurate.

- Shear failure as one of the main failure mechanism; in unconsolidated formations, shear fractures have been reported to occur in the laboratory. Given their low value of cohesion, unconsolidated rocks are likely to fail in compression (shear) much before their stress become tensile. Current standard simulators assume that all hydraulically induced fractures are the result of tensile failure. In the present study, a model was built using the Discrete Element Method (DEM) to represent both the mechanical and hydraulic behavior of poorly consolidated sands. This model allowed for both tensile and shear failure to occur; thus, a comparison on the relative importance of each mechanism was made possible.

- Variations in effective net pressure[46], as a consequence of changes in pore pressure. As fluid leaks off into the rock, its pore pressure increases. Thus, the fracture effective stress acting on the rock reduces as established by Terzaghi's law[47]. Changes in the effective load affecting the rock cause deformations of the pore structure and alterations of the rock porosity and permeability. As a consequence, the characteristics of the fluid leak-off process are changed. This two-ways relationship (coupling) between flow and mechanical deformations is not normally included in standard hydraulic fracturing simulators.

4.2.1 Hydraulic fracturing simulators based on linear elastic fracture mechanics

Traditionally LEFM has been the basis of almost all fracturing simulators; even modern models still assume the validity of original LEFM postulates. Most fracture models currently available use one of two approaches: Meyer et al. (1990), and Cleary et al. (1991). There are several commercial simulators that have been developed by consulting and service companies, and are available commercially. In this subsection the theoretical bases and limitations of three of the most currently used simulators are presented: FracproPT®, MFrac®, and Stimplan®.

[46] Effective net pressure = fluid pressure within the fracture – effective confining stress.
[47] Effective stress on the rock matrix = total applied stress – pore pressure.

4.2.1.1 FracproPT®:

This software is based on the model published by Crockett et al. (1986a), and Cleary et al. (1991). Only the module calculating the fracture creation, extension, shut-in, and closure is reviewed here. This component is a general integrated 3D model, which incorporates the essential physics of the fracturing process. It includes the mechanics of rock deformation and failure, the slurry flow inside the fracture, and the fluid/heat exchange between the fracture and its surroundings. One of the fundamental equations in this module is obtained through the mass conservation principle:

$$M - 2\,M_L = \rho_F\ \gamma_v\ w\,(2H)\,L \quad \text{..... (4.8)}$$

where M and $2M_L$ are the injected and lost fluid masses, ρ_F is the fracturing slurry density, and γ_v is a shape factor describing the crack shape. The fracture width, half-height and half-length are represented by the symbols w, H, and L. The fracture width is a function of the net pressure, the mechanical properties, and the shape of the fracture:

$$w = \gamma_1 \frac{P_{net}\ l}{E'}; \qquad with \quad P_{net} = P_f - \sigma_C \quad and \quad l = \begin{cases} H & if \quad H \le L \\ L & if \quad L \le H \end{cases} \text{..(4.9)}$$

where,

- P_{net} : net pressure;
- P_f : fracture fluid pressure;
- σ_C : closure stress;
- γ_1 : coefficient accounting for fracture geometry and rock structural variation; and,
- E' : crack-opening modulus = E / [4(1-v^2)] for isotropic homogeneous rock.

The net pressure inside the fracture is determined by both the flowrate and the rheological characteristics of the fracturing fluid; thus,

$$\left(\frac{\dot{M}_i}{\rho_F}\right)^n = -\gamma_{i4}\frac{w^{2n+1}}{\overline{\mu}}\frac{\partial P_F}{\partial x_i}; \quad i = 1,2 \qquad \text{.....(4.10)}$$

where,

- $\dot{M}_i$: lateral/vertical mass flow rate per unit height/length, i=1,2;
- n : power-law behavior index;
- γ_{14} : shape coefficient, explained in more detail in eqn. 4.13; and,
- x_i: spatial coordinate in the lateral, vertical, and normal directions to the fracture.

The symbol $\overline{\mu}$ is the effective channel flow viscosity defined, for power-law fluids, by:

$$\overline{\mu} = 2K\left(4 + 2/n\right)^n \quad \text{.....(4.11)}$$

Where K is the fluid consistency index; the lateral/vertical mass flow rates per unit height/length, $\dot{M}_1$ and $\dot{M}_2$, respectively, may be expressed as:

$$\dot{M}_1 = \dot{M}/(2H) \quad \text{.....(4.12)}$$

$$\dot{M}_2 = \frac{d}{dt}\left[\rho_F\ \gamma_{23}\ w\ H\right] + \gamma_{25}\ \dot{M}_L / L \quad \text{.....(4.13)}$$

In this equation, γ_{23}, *and* γ_{25} are the vertical cross-section and fluid loss shape factors[48], respectively. Equation (4.10) is embedded in a spatially distributed model to numerically determine the 3D pressure gradient vector. The values in this vector may be represented by the coefficients γ_{i2} and used in the following equation:

$$\frac{\partial P_F}{\partial x_i} = -\gamma_{i2}\frac{P_{net}}{L_i};\quad i = 1,2;\quad L_1 = L\ and\ L_2 = H \quad \text{.....(4.14)}$$

[48] There is no physicall justification for the use of these "shape factors". They appear to be nothing but correction multipliers.

The pressure gradient coefficient γ_{i2} reflects all of the complexities associated with stratification, fluid rheology, frictional drag, and earth stress gradients (Crockett et al., 1986b). In their paper, all the equations in this section (Eqns. 4.8-4.14) were combined to obtain two governing first order differential equations in length (L_1) and height (L_2):

$$\frac{d}{dt}\left(L_i^N\right) + B_i L_i^N = A_i \quad \text{.....(4.15a)}$$

where,

$$N = \left(\frac{3n+6}{n}\right) \quad \text{.....(4.15b)}$$

$$A_i = N\left[\frac{\gamma_{i2}\,\gamma_{i4}}{\gamma_1\,\gamma_{i3}^n}\,\frac{E'}{\overline{\mu}}\left(\frac{M-2M_L}{2\rho_F\,\gamma_v}\,\frac{L_i}{L_k}\right)^{n+2}\frac{L_i}{l}\right]^{1/n} \quad \text{.....(4.15c)}$$

and,

$$B_i = N\frac{\gamma_{i5}\,\gamma_v}{\gamma_{i3}}\frac{2\dot{M}_L}{\left(M-2M_L\right)}; \qquad i=1,2;\ k=2,1 \quad \text{.....(4.15d)}$$

For the case of a penny-shaped fracture, and with Newtonian fluid ($n = 1$), the geometry of the fracture and its net pressure may be calculated as a function of time by:

$$R = \left[\frac{9}{4}\,\frac{\gamma_{12}\,\gamma_{14}}{\gamma_1\,\gamma_{13}}\,\frac{E'}{\overline{\mu}}\left(\frac{\dot{Q}}{2\gamma_v}\right)^3\right]^{\frac{1}{9}} t^{\frac{4}{9}} \quad \text{.....(4.16a)}$$

$$w = \left[\left[\frac{4}{9}\frac{\gamma_1\gamma_{13}}{\gamma_{12}\gamma_{14}}\frac{\bar{\mu}}{E'}\right]^2\left[\frac{\dot{Q}}{2\gamma_v}\right]^3\right]^{\frac{1}{9}} t^{\frac{1}{9}} \quad \text{.....(4.16b)}$$

$$P_{net} = \frac{E'}{\gamma_1}\left[\frac{4}{9}\frac{\gamma_1\gamma_{13}}{\gamma_{12}\gamma_{14}}\frac{\bar{\mu}}{E'}\right]^{\frac{1}{3}} t^{\frac{-1}{3}} \quad \text{.....(4.16c)}$$

Similar equations can be found for the case of Newtonian fluid and constant height fracture, i.e. in a complete confined environment. In these equations, the effect of the coefficients γ_{ik} is apparent. In FracproPT®, these gamma factors are used to account for the influence of confining stress variation, frictional drag, geometric effects, etc.; some of these factors may be calculated as follows:

$$\begin{aligned}
&\gamma_1 = S_0 S_d S_g \gamma_1^0 \\
&\gamma_{i2} = S_{si} S_{di} S_{\mu i} S_{pi} \gamma_{i2}^0 \;; \quad i = 1,2 \quad \text{.....(4.17)} \\
&\gamma_{i5} = S_{Li} \gamma_{i5}^0 \;; \quad i = 1,2
\end{aligned}$$

where the shape factors, *S*, represent the effects on fracture development caused by: confining stress variation (S_S), modulus stratification (S_d), spatial variation of fracturing fluid viscosity (S_μ), frictional drag induced by proppant (S_p), stratified fluid loss (S_L), and geometric effects (S_g). According to the software manual (FracproPT manual, 2003), all these shape factors are calculated from careful numerical simulations and comparison with laboratory and field data (Lam et al.,

1986; Crockett et al., 1986b). The model also suggests that any other physical phenomena that could be deemed important may be introduced as another shape factor multiplying the right hand side of equations (4.17).

The basic model behind FracproPT® was developed as an attempt to account for the most important physical mechanisms affecting fracture creation and extension during stimulation treatments. It started with the material balance equations and the equation for fluid flow through parallel plates. These strictly physical bases were later obscured by the utilization of shape factors to account for very complex processes such as fracture shape variation, stratified loss, stress field variation. From Eqn. (4.17) it can be observed that these "shape" factors are basically parameters that control the weight given to the effect caused by the physical processes they represent. FracproPT® claims that the values given to all shape factors are the results of rigorous simulations; hence, they are nothing but correlation parameters. Furthermore, the way the gamma factors are calculated involves the assumption that all the processes represented by the shape factors, *S*, are independent of the rest. This approach has a fundamental drawback: all the shape factors may be utilized by the user as "tuning knobs" to match almost any response observed in the field, without regard of the physics controlling the fracture creation and propagation process. The number of shape parameters involved on every simulation, and the way the gamma factors are calculated,

suggests that the same results could be achieved by using different input data (i.e. non-unique model input will produce the same output). This model should be used with caution, and only by users with enough experience to avoid transgressing the physics behind the fracturing process while manipulating the values of the shape factors. In addition, this approach assumes that the effect of confining stress is much more important than the effect of fracture toughness. Thus, the model disregards K_{Ic} provided that:

$$\sigma_c \sqrt{\pi R} >> K_{Ic} \quad \text{..... (4.18)}$$

where R is the radius of the fracture (a in the original LEFM equation). From Eqn. (4.18), it can be observed that fracture toughness is important for small fractures in shallow formations, such as may be the case of hydrofrac in unconsolidated formations[49]. This model assumes that a fluid lag exists at the very end of the fracture i.e. the fracture tip is considered to remain "dry" at all times (Fig. 4.15). Therefore, a very rapid change in net pressure is located at a distance, ω, from the tip of the crack;

$$\omega_d = \frac{R}{2}\left(\frac{P_{net}}{P_{net} + \sigma_c}\right)^2 \quad \text{..... (4.19)}$$

[49] Fracture toughness is also very important during fracture closure analysis, as well as during micro-fracturing tests for stress determination.

Energy is lost at the "dry" fracture tip as it deforms. It is postulated that this deformation takes place in a non-linear or inelastic manner. This additional deformation reduces the amount of energy available for fracture propagation; hence, reducing the final fracture size at any given P_{net}.

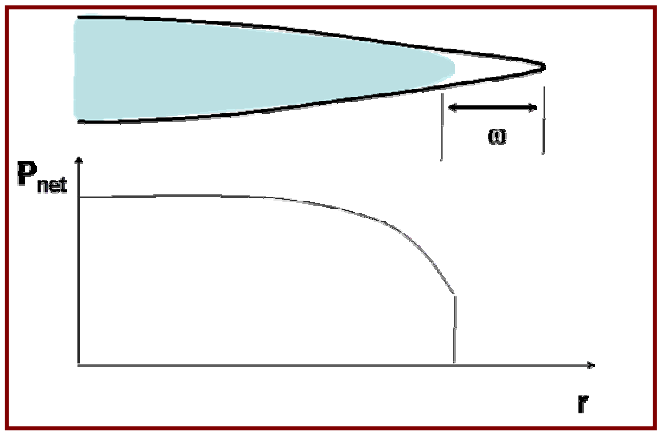

Figure 4-15. The Cleary et al. model (1991).

Simulations performed by using this model show that if lab-measured inelastic rock properties are used as input; the simulated rock failure occurs in a small zone near the crack tip. The end result of this is a negligible change in net pressure compared to the elastic solution. However, the size of the inelastic zone can be increased by reducing the values of rock strength. This indicates that tip-dilatancy and inelastic deformations are subjected to a strong scale effect. This effect, not predicted by the model, needs to be corrected through field calibration prior to model application. Furthermore, the assumption of a "dry" fracture tip in

highly permeable formation seems rather unlikely, as the fluid readily leaks off into the formation, leaving no time for fluid lag to occur.

4.2.1.2 MFrac®:

This program is based in the model published by Meyer (Meyer, 1989; Meyer et al., 1990); it is a pseudo-3D numerical representation of the mechanisms affecting fracture creation and growth. The governing equations in this simulator were obtained through application of the principles of mass, continuity, and momentum conservation. The governing mass conservation equation for an incompressible slurry in a fracture is given by:

$$\int_0^t q\,(\tau)\,d\tau - V_f(t) - V_l(t) - V_{sp}(t) = 0 \quad \ldots\ldots\ldots\ldots\ldots \quad (4.20)$$

where q is the injected flow rate, V_f is the fracture volume, V_l represents the fluid leaked off into the formation (without spurt), and V_{sp} is the fluid lost by spurt. The terms in Eqn. 4.20 may be calculated as:

$$\begin{aligned} V_l(t) &= 2\int_0^t\int_0^A \frac{C(A,t)}{\left[t-\tau\,(A)\right]^{\alpha_\tau}}\,dA\,dt \\ V_{sp}(t) &= 2\,S_p\;A(t) \\ \tau(A) &= t\left[A/A(t)\right]^{\alpha_a} \end{aligned} \quad \ldots\ldots\ldots\ldots\ldots\ldots \quad (4.21)$$

where,

- C : Total fluid loss coefficient;
- A : area perpendicular to the leak off flow direction;
- τ : time at which the area A is created;
- S_p : spurt volume; and,
- α_a : exponent determining relative area growth with time.

MFrac® solves the above equation by discretizing the domain and then integrating over each element of the grid (MFrac manual, 2004). The mass continuity equation may be expressed in terms of the flowrate per unit length (the product fluid velocity times fracture width, $q = \vec{v}\ w$) by:

$$\vec{\nabla}.\vec{q} + 2\ q_L + \frac{\partial w}{\partial t} = 0 \qquad \text{.....(4.22)}$$

where w is the fracture width, and q_L is the leakoff rate per unit leakoff area. Likewise, the momentum equation can be written as:

$$\rho \frac{D\vec{v}}{Dt} = -\vec{\nabla}P - \left[\vec{\nabla}.\vec{\tau}\right] + \rho\,\vec{g} \qquad \text{.....(4.23)}$$

This relationship can be generalized for laminar and turbulent steady state flow as follows:

$$\vec{\nabla}P = -\frac{1}{2}\frac{f\,\rho\,\vec{q}^{\,2}}{w^3} \quad \text{..... (4.24)}$$

where,

- f : Darcy friction factor ($f = 24/Re$ for laminar flow, and $f = f(Re, \varepsilon)$ for turbulent flow);
- Re : Reynolds Number; and,
- ε: relative wall roughness.

MFrac® utilizes a crack-opening and opening pressure equation of the form:

$$w = \Gamma_w\,(\lambda, x, z, t)\frac{2(1-\nu)}{G}H_\xi \Delta P \quad \text{..... (4.25)}$$

where,

- $w\,(x, z, t)$: fracture width;
- $\Gamma w = f\,(\lambda\text{-geometry}, x, z, \sigma(z), \nu(z), G(z), t)$: generalized influence friction;
- G : rock modulus;
- H_ξ : characteristic half height;
- $\Delta P(x,y,z)$: net fracture pressure; and,
- $\sigma\,(z)$: closure stress.

Depending upon the type of fracture (PKN, GKD, and penny-shaped), the constitutive width opening equation may be defined as:

$$\begin{aligned} PKN: &\quad w(x,0,t) = 2\frac{(1-\nu)}{G} H\ \Delta P(x,t) \\ GDK: &\quad w(0,t) = 2\frac{(1-\nu)}{G} L(t)\ \Delta P(t) \\ Penny: &\quad w(0,t) = \frac{4}{\pi}\frac{(1-\nu)}{G} R(t)\ \Delta P(t) \end{aligned} \quad \text{…….....…… (4.26)}$$

The fracture propagation criterion in this model, also a fundamental LEFM concept, states that the stress intensity factor, K, must be greater than the fracture toughness, K_{IC}, in order to allow for fracture propagation. It defines a characteristic length, H_ξ and a geometric factor, γ, hence, the original LEFM equation (see Eqn. 4.7) becomes:

$$\sigma_c = \frac{K_{Ic}}{\sqrt{\gamma H_\xi}} \text{ ……..…… (4.27)}$$

The values of H_ξ and γ are determined by the fracture geometry being used (KGD, PKN, penny-shaped), as shown above. This model claims that the total intensity factor, K_I, can be represented by superposition of the stress intensity factors caused by the net pressure ΔP, the in-situ stress variations, $\Delta\sigma$, the gravity, and contrast in moduli (Morita et al., 1988; Meyer, 1989); thus,

$$K_I = K_{I,\Delta P} + K_{I,\Delta\sigma} + K_{I,\Delta\rho h} + K_{I,G} \text{ ……..…… (4.28)}$$

where,

- $K_{I,\Delta P}$: Stress intensity factor due to the net pressure effect;
- $K_{I,\Delta\sigma}$: Stress intensity factor due in-situ stress variations;
- $K_{I,\Delta\rho h}$: Stress intensity factor due to gravity; and,
- $K_{I,G}$: Stress intensity factor due to moduli contrasts.

Equation (4.28) intrinsically assumes that net pressure, in-situ stress difference and modulus contrast, are all linear phenomena with no effect on each other. Unfortunately, this is not the case in unconsolidated highly permeable formations, as extreme leak-off affects the magnitude of the rock pore pressure; hence, the value of the effective stress and of the net pressure. Changes in the magnitude of effective stress translate also into alterations in the mechanical properties of the rock, i.e. elastic moduli tend to decrease making the rock weaker as deformation progresses. By the same token, increasing deformation affects the value of pore pressure; therefore, the magnitude of effective and closure stresses. Thus, it is apparent that in poorly-consolidated rocks, their mechanical behavior, pore pressure, and effective/closure stress are all tightly coupled during the hydraulic fracturing process; hence, Eqn. (4.28) fails to represent the rock behavior.

In addition, there is a tip-overpressure that is not accounted for in the model. The authors handle this problem by introducing an "over-pressure factor", which should be obtained empirically for each formation to be fractured; however, there is no physical justification for the use of this factor. Just as in the case of FracproPT®, this over-pressure parameter may be manipulated in MFrac® to match the well response; with the corresponding risk of loosing physicality while trying to reproduce the desired result.

Amongst the intrinsic limitations found in this model, one of the most important is the assumption of perfectly linear elastic behavior of the rock being fractured. This assumption holds for brittle and hard rocks, which fail catastrophically in an extremely rapid manner. However, in the case of unconsolidated materials the failure process is much slower with non-linear deformations playing a rather important role.

In general, MFrac® is rigorous in the way that it represents the physical processes involved in hydraulic fracturing; however, it was intended for modeling hard/brittle materials that could be approximately described as linear elastic. This software uses a pseudo-3D model of the whole phenomenon with the intrinsic sacrifice in accuracy that it represents. Thus, caution should be exercised when using MFrac® to represent hydrofrac in weak, highly permeable formations.

4.2.1.3 Stimplan®:

This software is based on the same fundamental equations used in most hydraulic fracturing simulators. It is a numerical simulator performing implicit, coupled, finite difference solutions to basic equations of mass balance, elasticity, height growth, and fluid flow mass conservation and momentum balance. The analytical model behind this simulator is as rigorous as in MFrac®; for that reason that part of the model is not revisited here. What differentiates Stimplan® from most simulators is the fact that it provides an option to run a fully-3D model and not just a pseudo-3D fracture representation. This allows for more accuracy in the calculation of fracture width, as it is calculated using 3-D elasticity, i.e., width anywhere is a function of the pressure everywhere in the fracture (Stimplan manual, 2004).

Amongst the differences between a pseudo-3D model and a fully 3D model, probably the most relevant are that in a pseudo-3D model, the height is allowed to grow with time and to vary along the pay zone (Settari and Cleary, 1982; Palmer and Carroll, 1983); and the fluid flow in the crack is assumed to be uni-dimensional. In addition, plain strain conditions are assumed to occur on the deformation of each vertical cross-section. On the other hand, fully 3D models solve a set of coupled equations governing the deformations of a 3D fracture and

the 2D (vertical and along the fracture) fluid flow (Clifton and Abou-Sayed, 1981; Abou-Sayed et al., 1984; Stimplan manual, 2004).

From linear elasticity, the crack opening as a function of the local pressure and stress may be calculated by:

$$p(x,z) - \sigma(z) = \int_{-H_L}^{H_U} \Gamma(z, z_0) \frac{dw}{dz_0} dz_0 \quad \text{..... (4.29)}$$

where σ is the minimum principal stress, H_U and H_L are the upper and lower fracture height, and Γ is an influence function. In a 1D-flow simulator, Eqn. (4.22) is solved with q being only a function of one coordinate; however, for 2D fluid flow it becomes:

$$\frac{\partial q_x}{\partial x} + \frac{\partial q_z}{\partial z} + 2\, q_L + \frac{\partial w}{\partial t} = 0 \quad \text{..... (4.30)}$$

where q_x and q_z are the flow components in the x- and z-direction, respectively. The first two terms in the equation above are of the same order of magnitude; thus, neglecting any of them may lead to significant errors in the calculation of the pressure profile and the height growth rate (Weng, 1991). For cases with some height confinement, but with "weak" barriers to vertical fracture growth, Eqn. 4.30 should be used. In Stimplan, this option (2D flow) uses an iterative solution for height growth to insure that the vertical pressure drop due to vertical

fluid flow is properly accounted for in the solution. This solution demands more computational effort but should give a more realistic solution where the vertical pressure drop due to vertical fluid flow is a significant parameter affecting the rate of height growth. This option will generally predict less height growth than the 1D option (Stimplan manual, 2004). The assumption of one-dimensional fluid flow (in the vertical direction) holds only for very elongated ($L >> H$) and contained fractures, where the flow near the edges is vertical; in this case the horizontal fluid flow near the center of the crack has little effect on the edges.

Pressure drop is greater at the narrower regions in the fracture, i.e. near the crack edges. If a vertical fracture is assumed, the flow fields near its upper and lower edges determine the height growth rate of the whole crack. Therefore, accurate representation of fluid flow at the advancing fracture edge is critical for achieving accurate crack extension prediction; fully 3D simulators perform a "sweep" of the pressure conditions near the edges at every time step. During fracture propagation, the crack edges move away from its center; thus the flow streamlines are represented as lines perpendicular to the edges (Fig. 4.16). A local radial flow field is assumed; then, the fluid flowing through each vertical cross section is originated at an imaginary source located at the distance D upstream from the element (see dashed lines). The distance between the cross-section and the source is chosen such that the streamline at the edge of the element is perpendicular to

the crack boundary. For an elliptical fracture with half length L and height H, the distance D can be calculated as follows (Weng, 1991):

$$D = X\left[\frac{H}{2L}\right]^2 \quad \text{(4.31)}$$

where X is determined by the assumed radial flow. For a penny-shaped fracture ($H=2L$), the term enclosed by brackets becomes equal to 1 and the assumed flow field matches the actual flow in the fracture (i.e. the assumed flow geometry and the flow in the fracture are both radial). For the assumed radial flow, the continuity equation becomes:

$$\frac{1}{r}\frac{\partial}{\partial r}(r\,q_r) + q_L + \frac{\partial w}{\partial t} = 0 \quad \text{(4.32)}$$

where r is the distance form the imaginary source, and q_r is the radial flow rate. This equation can be modified to make it applicable to a vertical fracture as follows:

$$\frac{\partial}{\partial z}(r\,q_r) + z\,q_L + z\frac{\partial w}{\partial t} = 0 \quad \text{(4.33)}$$

The relation between pressure gradient and and flow rate becomes (Weng, 1991):

$$-\frac{\partial p}{\partial z} = 2K'\left(\frac{4n'+2}{n'}\right)^{n'} \frac{q_r^{n'+1} q_z}{w^{2n'+1}}$$

…..…… (4.34)

$$with \qquad q_z = q_r \sin\theta$$

Stimplan® solves Eqns. 4.29, 4.33, and 4.34 to determine the pressure and width profiles and the height growth rates. This software also provides the user with the option of performing the fracture width calculations by using the finite element method instead of the finite differences method.

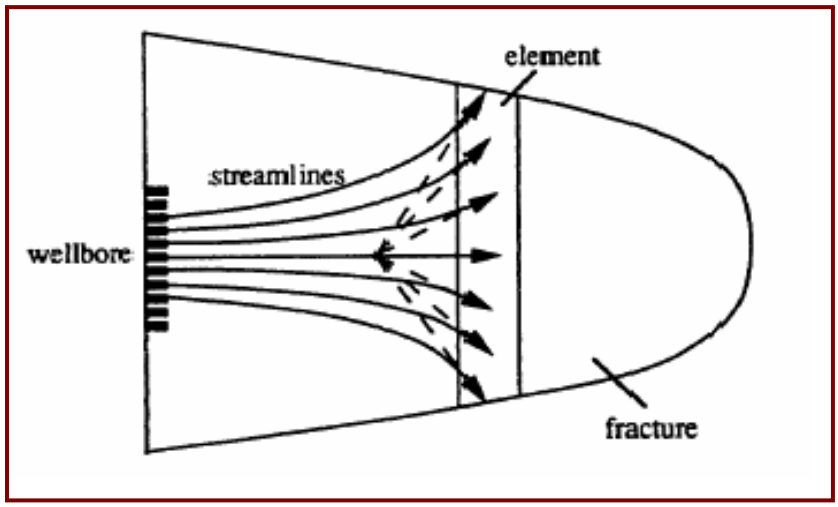

Figure 4-16. Fluid streamlines across a fracture vertical section, after Weng (1991).

In general, Stimplan® is very strict in the approach it uses for representing the physical processes involved in hydraulic fracturing of rock. This program uses the finite element technique to calculate the rock deformations leading to fracture

width/height growth; thus, it is likely to be more exact than conventional finite differences models. However, this software was built for modeling hard/brittle materials that could be approximately described as linear elastic. Albeit being a fully 3D model, it constrains the fracture to be created and extended on a plane perpendicular to the minimum principal stress. The failure mode used in this program is tension, based on the traditional LEFM concepts of fracture toughness and stress intensity factors. Therefore, non-planar geometries and compressive failure mechanisms (that may be critical in hydraulic fracturing of unconsolidated formations) are not considered.

4.2.2 Alternative approaches to hydraulic fracture propagation

Several other hydraulic fracturing models have been developed, often in an attempt to dissociate from the limitations imposed by the assumptions of the LEFM theory. Nevertheless, they have failed in achieving acceptance by the oil and gas industry; a brief analysis of some of them is provided below.

4.2.2.1 Continuum Damage Mechanics (Valkó and Economides, 1993):

The concept of Continuum Damage Mechanics considers inelastic behavior at the fracture tip. This model defines two main parameters: a scale parameter, *l,* and a

material damage parameter, C; these two parameters can be combined as Cl^2, which can be related to both stress intensity factor, K, and fracture toughness, K_{Ic}. For the case of contained fractures, the group Cl^2 is fairly easy to use (after field calibration) in order to match the net pressure. The combined parameter, Cl^2, varies greatly (about four orders of magnitude) between the values measured in the laboratory and those observed in the field. This discrepancy might be caused by problems in the scaling process, when results obtained in small cores are extrapolated for field operations prediction. Occasionally, different values of the group Cl^2 are necessary in order to match the net pressure at early-and late-times. This suggest that the value of the damage parameter, C, is a function of time throughout the fracturing process rather than a constant value, as stated in the model.

4.2.2.2 Apparent Fracture Toughness (Shlyapobersky et al., 1988):

The calibration of 2D models by using this approach, accounts for increments in the net pressure at the fracture tip; and makes pressure profiles within the fracture more uniform. Simultaneously, it reduces the sensitivity of fracture geometry and net pressure to changes in viscosity. This model corrects the critical volumetric errors found in LEFM models. Nonetheless, the values of fracture toughness obtained in the laboratory are normally much smaller than those inferred from

field calibration. Variations in the magnitudes of both fracture toughness and energy release rate have been measured in the lab as a function of sample and aggregate size dimensions. Table 4.1 shows the results reported by Shlyapobersky et al. (1998) for different specimen sizes. It can be appreciated from their results that the value of the fracture toughness tends to increase with the size of the specimen and the aggregates in the rock. The increment in fracture toughness as function of sample size may be a consequence of the relative size of the process zone[50] and the specimen, i.e. the overall behavior of large samples is less affected than relatively smaller cores are by the presence of the process zone. Given the fact that the aggregates are stronger than the rock, the extending crack will tend to go around them; thus, increasing its tortuosity and making further fracture growth more difficult (Shlyapobersky et al., 1998).

	Aggregate size, mm(in)				
Specimen size, cm (in)	**4.75 (0.19)**	**9.50 (0.37)**	**19.00 (0.75)**	**38.00 (1.50)**	**76.00 (2.99)**
10.50 (4.13)	1.25	1.30	---	---	---
21.00 (8.27)	1.10	1.24	1.36	---	---
42.00 (16.53)	1.12	1.44	1.47	1.31	---
84.00 (33.07)	1.26	1.52	1.55	1.58	1.62
105.00 (41.34)	---	1.48	1.57	1.60	---
168.00 (66.14)	---	1.63	1.46	1.78	1.73

Table 4-2. Fracture toughness (in Kpsi/ft$^{0.5}$) as function of specimen and aggregate size (data from Shlyapobersky et al., 1998)

[50] Region near the crack tip, where the material has already yielded and inelastic deformation takes place.

The calibrated values of fracture toughness are also rate-dependent and change with fracture dimensions rather than being a material property. It has been found that the net pressure measured during the fracture creation frequently remains constant during later stages of the hydrofrac, when the fracture is reopened. This contradicts the concept of fracture toughness, which is entirely based on the tensile strength of the rock.

In addition, several publications have shown that fracture toughness is severely influenced by confining pressure (Schmidt and Hurdle, 1977; Abou-Sayed, 1978; Thiercelin, 1987) and by temperature (Meredith and Atkinson, 1985). More recently, Roegiers and Zhao (1991) presented the results of a series of Chevron-notched Brazilian Tests performed on several lithologies. They investigated the effects of confining pressure, temperature and water saturation on the magnitude of fracture toughness (see Fig. 4.17). They found that the magnitude of the fracture toughness tends to increase with confining pressure; however, the magnitude of such an increment varied depending on the rock lithology. The value of fracture toughness increases almost linearly with the confining stress for both the sandstone and the limestone samples; however, this linear trend is not observed in the case of chalk (Fig. 4.18).

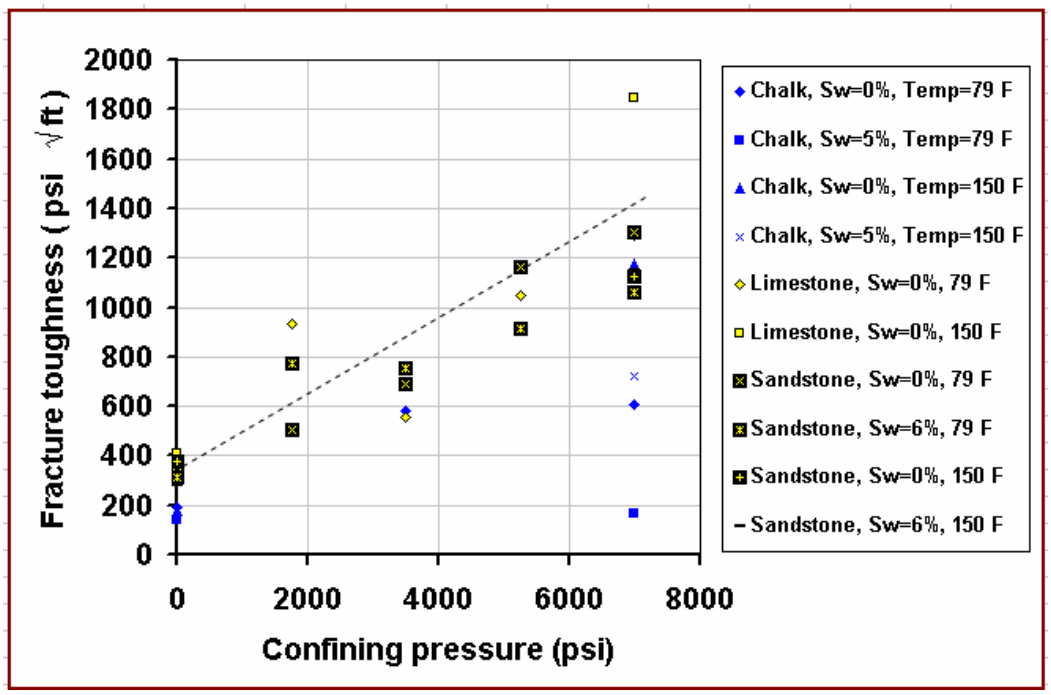

Figure 4-17. Effects of confining pressure, water saturation, and temperature on the magnitude of fracture toughness (data from Roegiers and Zhao, 1991).

From their results, Roegiers and Zhao (1991) also concluded that water saturation provided lower values of fracture toughness for dry samples. Temperature had the opposite effect; slightly higher values of fracture toughness were obtained for limestone and sandstone when the temperature increased from 79 ºF to 150 ºF. Their study provided an insight on the causes behind the discrepancies found between the values of fracture toughness measured in the lab and the magnitudes obtained in the field.

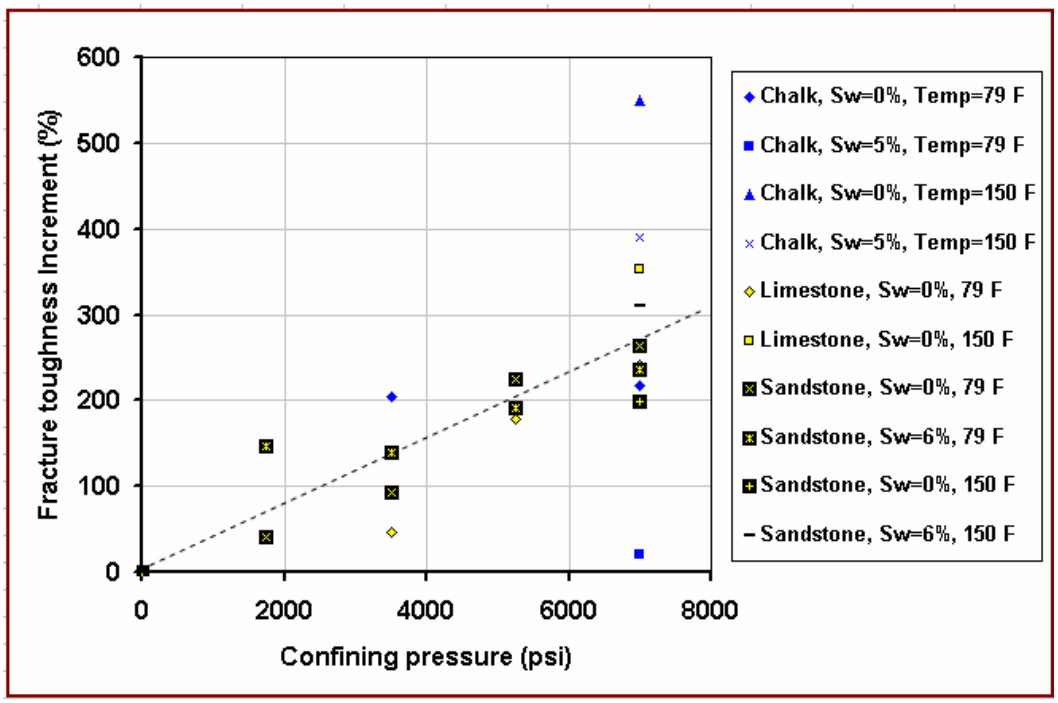

Figure 4-18. Increment in fracture toughness as function of confining pressure, water saturation, and temperature (data from Roegiers and Zhao, 1991).

4.2.2.3 Crack-Layer and Process Zone Model (Chudnovski et al., 1996):

This model introduces the concept of crack layer (CL), which is defined as a system composed of a main crack and a surrounding array of microcracks (also called process zone). It is a dynamic set with self-enhancing and self-inhibiting tendencies. The main crack tends to advance but its energy is dissipated when it encounters the process zone (PZ). The driving force within the main crack acts instantaneously, through stress concentration at the fracture tip, while the process zone is active over a finite period of time. These conditions allow for the

existence of a discontinuous series of events where steady fracture growth is followed by steady process zone development. The CL-PZ model uses energy as failure criterion, which is a very interesting approach to study the hydraulic fracturing process. However, this theory seems to be in its infancy as recognized by the authors. The problem of scaling the parameters measured in the laboratory to field operations remains a big obstacle for the application of the model.

4.2.2.4 Crack Tip Plasticity (Martin, 2000):

This method assumes a fracture tip of finite radius, with a zone of plastically deformed material around it. This plastic zone acts to absorb extra energy from the fracturing fluid, making it harder to propagate the crack through formations with significant plastic properties. As consequence, hydraulic fractures will be relatively smaller in soft/ductile formations than in hard/brittle rocks. The failure criterion used in this approach is the Von Mises one, which includes a yield stress, σ_y, for determining the onset of failure. Thus, this model eliminates the stress singularity problem for points near the crack tip. Nevertheless, the only LEFM limitation that is overcome in this model is the presence of non-elastic deformations. Moreover, no consideration to variation in the net pressure as consequence of fluid leakoff is presented.

4.3 Proposed approach

Traditionally, all hydraulic fracturing modeling has been based on LEFM theory; which was initially developed for hard, competent rocks. Thus, when standard hydrofrac simulators are run on poorly-consolidated formations; "correction factors" need to be introduced in order to fit model predictions to field data. Furthermore, the lack of reliable design and prediction tools reduces unconsolidated rock hydrofrac operations to a little more than trial-and-error procedures. The economical consequences of such an approach are enormous; unpredicted pressure requirements, lower-than-expected well productivity and operational problems are of common occurrence.

In this work, PFC^{3D}, a computer program originally built to be used in civil and mining engineering problems, was utilized to perform several simulations of the hydraulic fracturing process in poorly-consolidated formations. PFC^{3D} is a program based on the discrete element method (DEM), which allows for the creation of three-dimensional models of granular materials by tracing the motion and interactions of individual rock grains. Each particle is modeled as a discrete object with a particular geometric and physical state representation. Thus, the whole model evolves over time by tracing characteristics such as shape, size, position, contact forces, and displacements for each of the particles forming the

system. In the next subsection, a brief introduction to the basics of DEM is presented.

4.3.1 The Discrete Element Method (DEM)

The Discrete Element Method (DEM) has been developed to represent the behavior of rock, which at the microscopic level is a discontinuous bonded material rather than a continuum, as it is commonly assumed. In general, DEM is ideal for analyses of processes that involve the disaggregation and movement of particulate material. Currently, one of the most important challenges for the DEM is modeling problems coupling particle deformation and fluid flow; such problems include sand production in oil wells and hydraulic fracturing of unconsolidated, fragmenting formations. DEM has been under development since the early 1970's (Sandia Nat. Lab., 2004). The four most important components in a general discrete element simulation are: object representation, contact detection, physics, and visualization.

The discrete element method is a numerical technique which solves engineering problems that are modeled as a large system of distinct, interacting, general-

shaped (deformable or rigid) particles that are subject to the action of a physical field. Conventional continuum based procedures, like the Finite Element Method (FEM) fail to solve problems that exhibit such large scale discontinuous behavior. The discrete element procedure is used to determine the dynamic contact topology of the bodies. It accounts for intricate non-linear interaction phenomena between bodies and numerically solves the equations of motion. Given that the DEM is a very computationally demanding procedure, numerous existing computer codes are limited to modeling either two-dimensional or small three-dimensional problems that employ simple body geometries (Mustoe, 2004). Figure 4.19 shows a 2D representation of an unconfined compression test performed on a "virtual" sample. In this example, the number of particle bonds being broken is traced over time, as the top and bottom platens advance towards each other at a constant velocity.

In the discrete element method (DEM), the interaction of the particles is dealt with as a dynamic process with temporary equilibrium stages developing whenever the internal forces balance. The contact forces and displacement of a stressed system are found by tracing the movements of individual particles. Movements are the results of disturbances propagating through the model; these

disturbances may be created by specified wall and particle motion, as well as by application of body forces (Itasca Consulting Group, 2004).

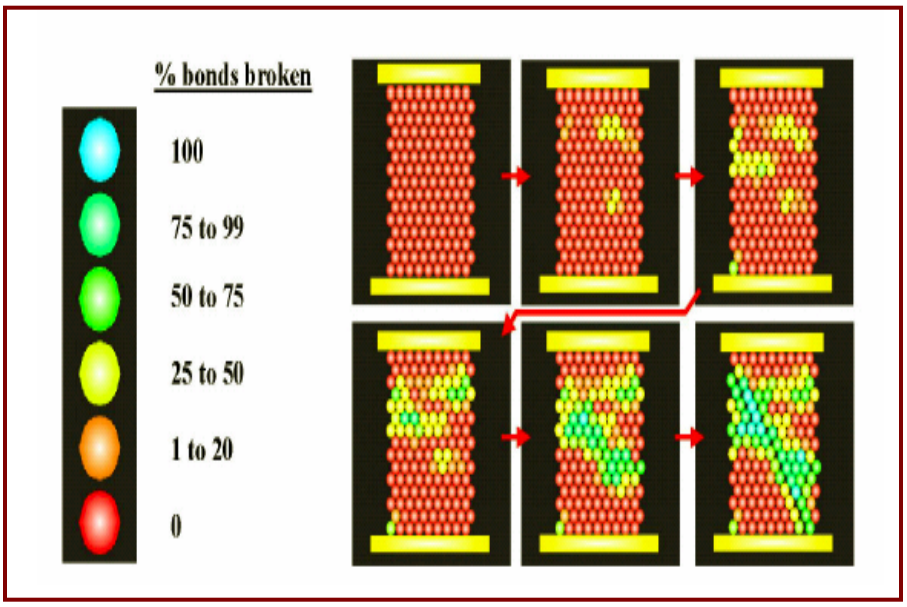

Figure 4-19. MIMES[51] simulation of a Uniaxial Compression Test (after Sandia Nat. Lab., 2004).

In order to deal with the deformation problem as a dynamic process, time steps are taken over which velocities and accelerations are assumed to be constant (Cundall, 1974). The discrete element is based upon the selection of a time step small enough to ensure that during a single step, disturbances will not propagate from any particle further than its immediate neighbors. Thus, the resultant force

[51]DEM simulator developed by Sandia National Laboratory and the Massachusetts Institute of Technology.

affecting any particle can be determined by its interaction with all the particles contacting it. As a consequence of this solution scheme, even non-linear interaction between large numbers of particles may be traced without excessive computer memory requirements (Cundall and Strack, 1979). However, the method is very intensive and the computational time required for finding a solution for a large problem may become impractical.

The calculations performed in DEM alternate between the application of Newton's Second Law[52] to the particles, and a force displacement law at the contacts. Newton's second law is evaluated to calculate the motion of each particle, as result of the contact and body forces acting upon it; where as the force-displacement law determines the change in the contact forces as consequence of the relative motion of each contact.

The general DEM can be applied by using arbitrary-shaped particles that may be treated as rigid or deformable depending upon the problem being analyzed (Itasca Consulting Group, 2004). A program called MIMES presented a new type of discrete element, which is based on the concept of superquadrics. These are obtained by changing the exponents in the elliptical equation shown in Fig. 4.20. The ability of MIMES to deal with different particle shapes is not limited to

[52] F = ma

spheres, ellipses, rectangles, and superquadrics. This program also handles particles with arbitrary shapes that are defined as n-sided polygons, see right-hand side of Fig. 4.20 (Sandia Nat. Lab., 2004).

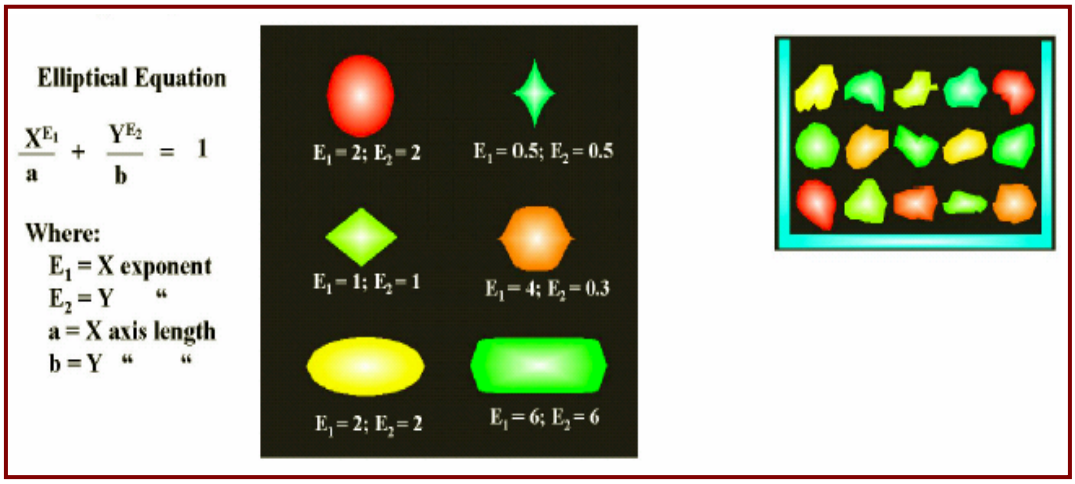

Figure 4-20. Superquadric and arbitrary-shaped particles for DEM simulations (after Sandia Nat. Lab., 2004).

4.3.2 General formulation in PFC^{3D}

A summary of the formulation in PFC^{3D} is presented hereby; for a more detailed description please refer to the software manual (Itasca Consulting Group, 2004). The PFC^{3D} program is a discrete element method model built on the following assumptions:

- The particles are rigid bodies;

- the contacts (ball-ball and ball-wall) occur over a very small area;
- behavior at the contacts may be represented by a soft-contact approach, where the rigid particles are allowed to overlap one another at contact points;
- the magnitude of the contact force is determined by the overlap through the application of the force-displacement law; all overlaps are small relative to the particle size;
- contacting surfaces may be bound to each other; and,
- spherical particles are representative of the particles in the real rock. "Clumps" may be created by agglomerating several spheres to give almost any desired shape.

The calculation cycle in PFC^{3D} is a time-stepping algorithm that requires the repeated evaluation of the law of motion for each particle, a force-displacement law for each contact, and a permanent updating of the position of every particle. The force-displacement law may be illustrated in terms of a contact point, $x_i^{[c]}$, lying on the contact plane, which is defined by its unit normal vector, n_i. The force-displacement law is defined for ball-ball and ball-wall contacts. In the first case, the contact plane between two particles (labeled A and B in Fig. 4.21), is defined by its unit normal:

$$n_i = \frac{x_i^{[B]} - x_i^{[A]}}{d} \qquad \text{with} \qquad d = \left| x_i^{[B]} - x_i^{[A]} \right| = \sqrt{\left(x_i^{[B]} - x_i^{[A]}\right)\left(x_i^{[B]} - x_i^{[A]}\right)} \qquad \text{…..... (4.35)}$$

where $x_i^{[A]}$ and $x_i^{[B]}$ are the position vectors of the centers of balls A and B, and d is the distance between the ball centers; in Figs. 4.21 and 4.22, U^n is the overlap between the different entities (balls and walls)..

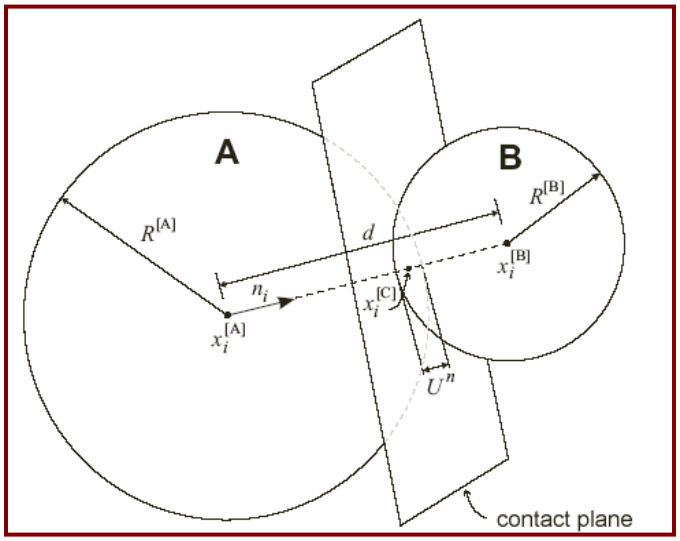

Figure 4-21. Ball-ball contact in PFC^{3D} , from PFC^{3D} manual (Itasca Consulting Group, 2004).

Figure 4.22 depicts the manner in which the direction of n_i is found for a contact between a ball and a two-dimensional wall: if the ball lies within regions 2 or 4, the procedure is straight forward and the shortest distance will be given by a

perpendicular line drawn from the wall to the ball center. However, if the sphere is located in regions 1, 3 or 5, the shortest distance will be given by a line connecting the wall endpoint (*A, B or C*) and the ball center. The overlap U^n, defined as the relative contact displacement in the normal direction is calculated as:

$$U^n = \begin{cases} R^{[A]} + R^{[B]} - d & (ball - ball) \\ R^{[b]} - d & (ball - wall) \end{cases} \quad \text{..... (4.36)}$$

Where $R^{[i]}$ is the radius of the ball *i*; by the same token, the location of the contact point is:

$$x_i^{[C]} = \begin{cases} x_i^{[A]} + \left(R^{[A]} - \frac{1}{2} U^n \right) n_i & (ball - ball) \\ x_i^{[b]} + \left(R^{[b]} - \frac{1}{2} U^n \right) n_i & (ball - wall) \end{cases} \quad \text{..... (4.37)}$$

The contact force vector F_i, representing the action of ball A on ball B (for ball-ball contact) or the action of the ball on the wall (for ball-wall contact), has both normal and shear components:

$$F_i = F_i^n + F_i^s \quad \text{..... (4.38)}$$

where the normal components may be expressed as:

$$F_i^n = K^n U^n n_i \quad \text{..... (4.39)}$$

and where K^n is the normal stiffness [force/displacement] at the contact; the value of K^n is a function of the contact-stiffness model (explained later in this subsection).

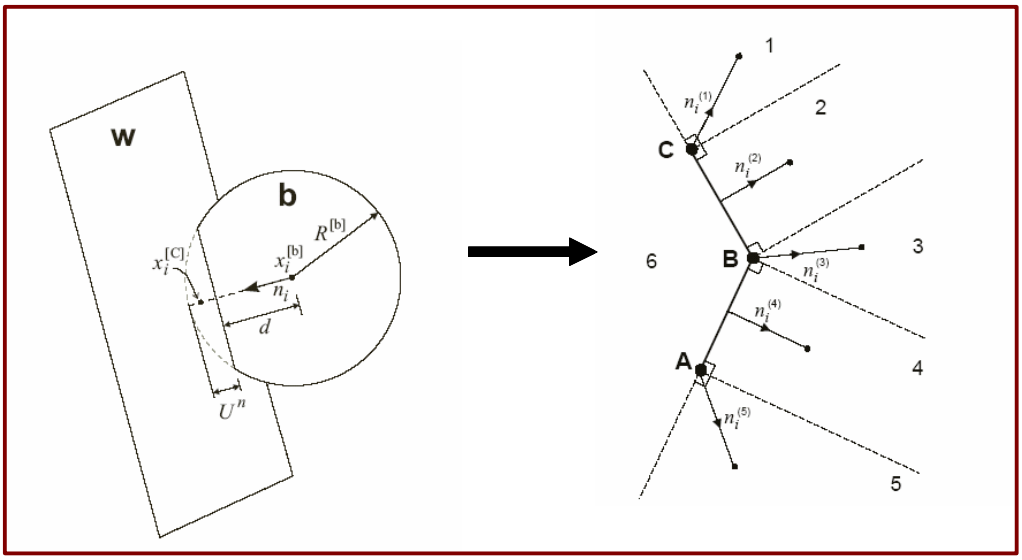

Figure 4-22. Ball-wall contact in PFC^{3D} (left), determination of the normal direction of the contact (right); (from PFC^{3D} manual; Itasca Conulting Group, 2004)

The contact shear force is calculated in an incremental manner; it is set equal to zero when the contact is formed, and updated at every time step depending upon the shear-displacement computed at every contact. The motion of every contact is accounted for by updating n_i and $x_i^{[C]}$ at every time step. F_i^s is updated by

calculating two rotations: the first one about the line common to the old and the new contact planes, and the second about the new normal direction; they are given by:

$$\begin{aligned}\left\{F_i^s\right\}_{rot.1} &= F_j^s\left(\delta_{ij} - e_{ijk}\ e_{kmn}\ n_m^{[old]} n_n\right)\\ \left\{F_i^s\right\}_{rot.2} &= \left\{F_i^s\right\}_{rot.1}\left(\delta_{ij} - e_{ijk}\ \langle\omega_k\rangle\ \Delta t\right)\end{aligned} \quad \text{..... (4.40)}$$

with $n_m^{[old]}$ being the old normal to the contact plane, and $\langle\omega_k\rangle$ being the average angular velocity of the two contacting entities about the new normal direction, it is defined as:

$$\langle\omega_i\rangle = \frac{1}{2}\left(\omega_j^{[\phi^1]} + \omega_j^{[\phi^2]}\right) n_j n_i \quad \text{..... (4.41)}$$

The Kronecker delta, δ_{ij}, and the permutation operator, e_{ijk}, are defined, respectively, as:

$$\delta_{ij} = \begin{cases} 1, & if\ i = j \\ 0, & if\ i \neq j \end{cases}$$

$$e_{ijk} = \begin{cases} 0, & if\ two\ indices\ coincide \\ +1, & if\ i, j, k \quad permute\ like\ 1,2,3 \\ -1, & otherwise \end{cases} \quad \text{..... (4.42)}$$

In Eqn. (4.41), $\omega_i^{[\phi^j]}$ is the rotational velocity of entity ϕ^j (A and B for ball-ball contacts, or b and w for ball-wall contacts); the relative velocity of the entities at the contacts is expressed as:

$$\begin{aligned} V_i &= \left(\dot{x}_i^{[C]}\right)_{\phi^2} - \left(\dot{x}_i^{[C]}\right)_{\phi^1} \\ &= \left[\dot{x}_i^{[\phi^2]} + e_{ijk}\omega_j^{[\phi^2]}\left(x_k^{[C]} - x_k^{[\phi^2]}\right)\right] - \left[\dot{x}_i^{[\phi^1]} + e_{ijk}\omega_j^{[\phi^1]}\left(x_k^{[C]} - x_k^{[\phi^1]}\right)\right] \end{aligned} \quad \ldots\ldots (4.43)$$

where $\dot{x}_i^{[\phi^j]}$ is the translational velocity of entity ϕ^j. The contact velocity may be decomposed into its normal and shear components as:

$$\begin{aligned} V_i^s &= V_i - V_i^n \\ &= V_i - V_j n_j n_i \end{aligned} \quad \ldots\ldots\ldots\ldots\ldots\ldots\ldots\ldots\ldots\ldots (4.44)$$

The shear elastic force-increment vector over a time step is defined as:

$$\begin{aligned} \Delta F_i^s &= -k^s \Delta U_i^s \\ with \qquad \Delta U_i^s &= V_i^s \Delta t \end{aligned} \quad \ldots\ldots\ldots\ldots\ldots\ldots\ldots\ldots\ldots\ldots (4.45)$$

where
- ΔU_i^s : shear component of the contact-displacement vector
- Δt : time step;
- k^s : shear stiffness [force/displacement] at the contact

The new shear contact force is calculated by adding the shear force at the beginning of the time step (old) to the shear elastic force-increment vector:

$$F_i^s = \left\{F_i^s\right\}_{rot.2} + \Delta F_i^s \quad \text{..... (4.46)}$$

4.3.2.1 Law of motion

The motion of each particle is determined by the resultant force (translational motion) and moment vectors (rotational motion) acting on it. The equation of translational motion may be described by:

$$F_i = m\left(\ddot{x}_i - g_i\right) \quad \text{..... (4.47)}$$

where
- F_i : resultant force;
- m : particle mass; and,
- g_i : body acceleration vector (e.g. gravity).

For spherical particles of radius R, the equation for rotational motion can be expressed as:

$$M_i = I\,\dot{\omega}_i = \left(\frac{2}{5}mR^2\right)\dot{\omega}_i \quad \text{..... (4.48)}$$

where $\begin{cases} I : \text{principal moment of inertia; and,} \\ \dot{\omega}_i : \text{angular acceleration about principal axis } i. \end{cases}$

4.3.2.2 Contact constitutive method

The contact stiffnesses relate the contact forces and relative displacements in the normal and shear directions as can be seen from Eqns. (4.39) and (4.45). During this work, the linear model was used to calculate the stiffness of the contact. Hence, the two entities are assumed to act in series, and the values of contact normal and shear stiffness may be calculated as:

$$K^n = \frac{k_n^{[A]} k_n^{[B]}}{k_n^{[A]} + k_n^{[B]}}$$
$$k^s = \frac{k_s^{[A]} k_s^{[B]}}{k_s^{[A]} + k_s^{[B]}} \quad \text{..... (4.49)}$$

4.3.2.3 Bonding models

In PFC^{3D} the particles are allowed to bond at the contact, this allows the simulation of the presence of cementing material between the spheres. For this

work, two bonding models were used for representing the mechanical behavior of the rock sample: contact-bonds and parallel-bonds.

In the case of contact bonds, two parameters define the mechanical behavior of the contact: normal contact bond strength and shear contact bond strength. Thus, the bond may be visualized as a couple of elastic springs with constant normal and shear stiffnesses acting on the contact point. These "springs" are assigned finite values of shear and tensile strength. Contact bonds only allow the transmission of forces at the contact point, i.e. moments are not transferred. The magnitude and sign of the normal force depends on the value of the inter-particle overlap, i.e. $U^n>0$ cause compressive forces to occur, whereas $U^n<0$ translate into tensile loads. Once the tensile/shear strength of the material is exceeded by the load applied to the contact, it breaks and the particles become free to rotate and translate in space (unless bound by other contacts).

A parallel bond is defined by the mechanical behavior of a finite-sized piece of cementing material deposited between the spheres. This type of contact is able of transmitting both force and moments. A parallel bond may be visualized as a set of elastic springs, with constant normal and shear stiffnesses. These springs are homogeneously distributed over a circular disk located on the contact plane between the particles, and centered at the contact point. Parallel bonds are

defined by five parameters: normal and shear stiffness [stress/displacement], normal and shear strength [stress], and bond radius. This contact acts parallel to the contact-bonds described before; thus, both parallel and contact bonds may coexist at the same contact plane; Fig. 4.23 shows a graphical representation of a parallel contact bond.

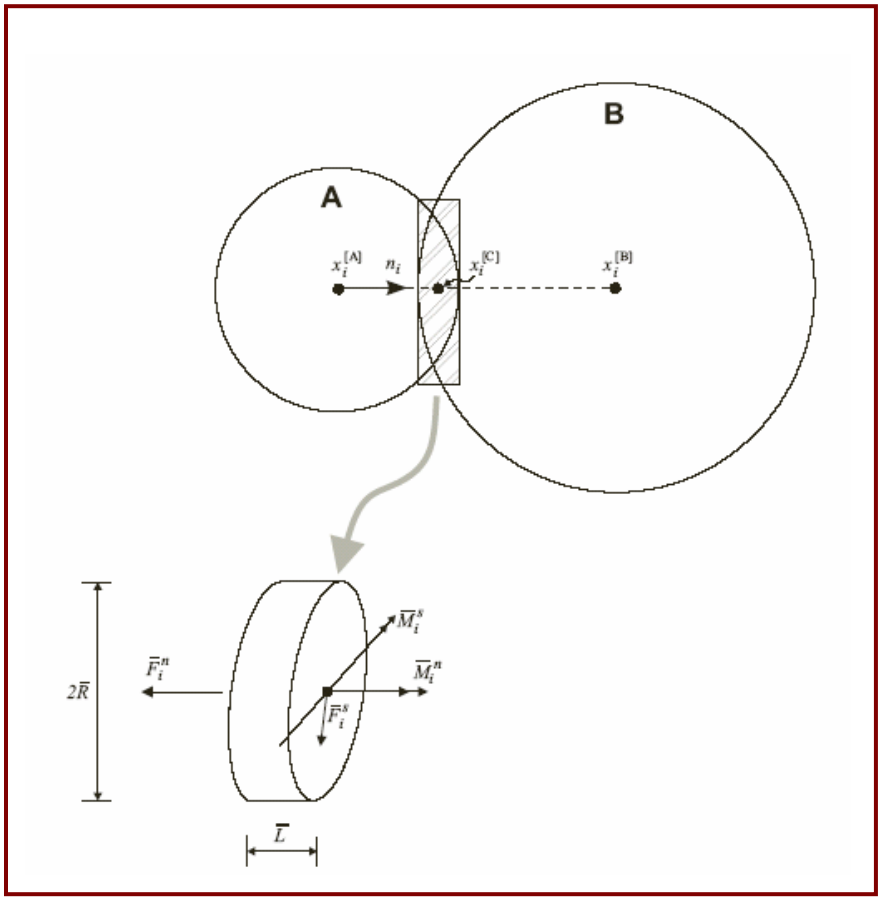

Figure 4-23. Parallel bond (from Itasca Consulting Group, 2004).

The total force, $\overline{F}_i$, and moment, $\overline{M}_i$, being transmitted through the parallel bond may be defined by the following expressions:

$$\begin{aligned} \overline{F}_i &= \overline{F}_i^n + \overline{F}_i^S \\ \overline{M}_i &= \overline{M}_i^n + \overline{M}_i^S \end{aligned} \quad \text{..... (4.50)}$$

where the superscripts *n* and *s* represent the normal and shear components of the force and moment vectors. Immediately after the parallel bond is formed, PFC^{3D} resets the values of $\overline{F}_i$ and $\overline{M}_i$ to zero; hence, the subsequent force and momentum increments caused by the movement of the particles are calculated by:

$$\begin{cases} \Delta\overline{F}_i^n = (-\overline{k}^n A \Delta U^n)\, n_i \\ \Delta\overline{F}_i^S = (-\overline{k}^S A \Delta U_i^S) \quad with \quad \Delta U_i = V_i \Delta t \end{cases}$$
$$\begin{cases} \Delta\overline{M}_i^n = (-\overline{k}^S J \Delta\theta^n)\, n_i \\ \Delta\overline{M}_i^S = (-\overline{k}^n I \Delta\theta_i^S) \quad with \quad \Delta\theta_i = (\omega_i^{[B]} - \omega_i^{[A]})\, \Delta t \end{cases} \quad \text{..... (4.51)}$$

where the area of the bond disk, *A*, the polar moment of inertia, *J*, and the moment of inertia of the disk cross-section about an axis through the contact point and in the direction $\Delta\theta_i^S$ are given by:

$$A = \pi \, \overline{R}^2$$
$$J = \frac{1}{2} \pi \, \overline{R}^4 \qquad \text{..... (4.52)}$$
$$I = \frac{1}{4} \pi \, \overline{R}^4 = \frac{J}{2}$$

The new force and moment vectors are calculated as the summation of the old values of the vectors, at the beginning of the time step, and the vector increments. Thus, the new force and moment vectors are given as:

$$\begin{cases} \overline{F}_i^n \leftarrow \overline{F}^n n_i + \Delta \overline{F}_i^n \\ \overline{F}_i^S = \left\{ \overline{F}_i^S \right\}_{rot.2} + \Delta \overline{F}_i^S \end{cases}$$
$$\begin{cases} \overline{M}_i^n \leftarrow \overline{M}^n n_i + \Delta \overline{M}_i^n \\ \overline{M}_i^S = \left\{ \overline{M}_i^S \right\}_{rot.2} + \Delta \overline{M}_i^S \end{cases} \qquad \text{..... (4.53)}$$

The maximum tensile and shear stresses acting on the bond boundaries are derived from the beam theory, and are calculated as follows:

$$\sigma_{\max} = \frac{-\overline{F}^n}{A} + \frac{\left| \overline{M}_i^S \right|}{I} \overline{R}$$
$$\tau_{\max} = \frac{\left| \overline{F}_i^S \right|}{A} + \frac{\left| \overline{M}^n \right|}{J} \overline{R} \qquad \text{..... (4.54)}$$

4.3.2.4 Fluid flow coupling

In PFC^{3D}, fluid flow through porous media is modeled as the flow occurring between "pipes" connecting neighboring pores. These pores are the void spaces inside a "domain". A domain is created by every four neighboring particles, such that each one of them is a vertice of a tetrahedron (Li and Holt, 2002). In the case of unconsolidated sandstones, the rock particles may be acceptably described as spheres; by the same token, the rock pores may be represented as the void space between the spheres. Each pipe between two contiguous domains has a small space between three neighboring particles. PFC^{3D} models these pipes as cylindrical tubes with length L, and aperture a (Itasca Consulting Group, 2004). Thus, the flow rate may be defined by the following equation (also called *Poiseuille's law*, Munson et al., 2003):

$$q = \frac{\pi\, a^4\, \Delta p}{128\, \mu\, L} = \frac{k\, a^3\, \Delta p}{L} \quad \text{..... (4.55)}$$

where,

- q : pipe flow rate;
- μ : fluid viscosity;
- Δp : pressure difference between two adjacent domains;
- L : distance between the centers of the two domains;
- a : pipe aperture; and,
- k : conductivity factor = $\pi a / 16\mu$.

The aperture of the pipe is a function of the load applied to the two contiguous domains; it varies between a_0 under zero loading conditions, and 0 as the load increases to infinite. Thus, the following empirical equation is used in PFC^{3D} to calculate the magnitude of the pipe aperture (Itasca Consulting Group, 2004) as function of compressive load:

$$a = \frac{a_0 \; F_0}{F + F_0} \quad \text{..... (4.56)}$$

where F_0 is the value of normal compressive load, F, at which the aperture decreases to $a_0/2$. For the case of normal tensile force, the aperture is computed as the summation of the residual aperture and the normal distance between the surfaces of the two particles (Itasca Consulting Group, 2004):

$$a = a_0 + m \; g \quad \text{..... (4.57)}$$

where, m : dimensionless scaling multiplier; and,

g : normal distance between the surfaces of the two particles.

Every time step, the flow rate received/produced by every domain, Σq, is calculated; and the consequent pressure disturbance ΔP is calculated as:

$$\Delta P = \frac{K_f}{V_d}\left(\Sigma q\ \Delta t - \Delta V_d\right) \ldots\ldots\ldots\ldots\ldots\ldots\ldots\ldots\ldots\ldots \quad (4.58)$$

where V_d is the apparent volume of the domain, and K_f represents the fluid bulk modulus. The solution scheme alternates between applying the flow equation to all pipes and applying the pressure equation to all domains. When a perturbation ΔP_p is induced in a domain, the flow into or out of that domain may be computed as:

$$q = N\frac{\pi\ a^4\ \Delta P_p}{16\,\mu\,\overline{L}} = N\frac{k\ a^3\ \Delta P_p}{\overline{L}} \ldots\ldots\ldots\ldots\ldots\ldots\ldots\ldots\ldots\ldots \quad (4.59)$$

where N is the number of pipes connected to the domain, and $\overline{L}$ is the average distance between the centers of the domain being evaluated and all its immediate neighbors. This fluid flow triggers a pressure response, ΔP_r, defined as:

$$\Delta P_r = \frac{K_f\ q\ t}{V_d} \ldots\ldots\ldots\ldots\ldots\ldots\ldots\ldots\ldots\ldots\ldots\ldots\ldots\ldots \quad (4.60)$$

Due to stability considerations the value of the pressure response should be less than the original perturbation, i.e. $\Delta P_r < \Delta P$. Thus, the optimum time step for the fluid flow calculation may be found from Eqns. (4.59) and (4.60):

$$\Delta t \leq \frac{\overline{L}\ V_d}{N K_f\ k a^3} \quad \text{..... (4.61)}$$

4.3.2.5 Advantages of PFC^{3D}

PFC^{3D} has several advantages, amongst which the most important are:

- There is no limitation on the magnitude of relative displacement between particles;
- From a microscopic point of view, the DEM is inherently more representative of the rock being modeled;
- It is possible for the block bonds to break, since the model is composed of independent particles; and,
- Contact detection between spherical particles is much simpler than contact detection between angular particles.

4.3.2.6 Limitations of PFC^{3D}

The way PFC^{3D} is set up, brings some inherent limitations to the way the model is built and evaluated:

- Block boundaries are not planar;

- Specification of model geometry and boundary conditions is not straightforward;
- Initial stress field is not independent of the initial packing, since forces acting on the particles arise from the relative position and interaction of the particles;
- Boundary conditions act on non-planar boundaries; and,
- The process of matching the macroscale mechanical properties of the model to those of a "real" rock is tedious and painstaking. Microscale properties are assigned to the particle assembly, and then the model is constructed and run in order to calculate the macroscale mechanical properties. This procedure needs to be repeated several times following a basic trial-and-error approach. The present study introduces a methodology for making this process much shorter and efficient.
- To the knowledge of the author, this is the first time a calibration of the macroscale hydraulic properties of a DEM model is performed. The approach developed here is explained in the next chapter.
- In order to reach stability, the magnitude of the selected time step for the fluid flow calculations is extremely small (typically about 10^{-6} sec); thus, demanding a large number of steps to model a short process, i.e. the computation time may become impractically long.

Chapter 5

Hydraulic Fracturing Modeling Using PFC^{3D}

Several steps were followed during this study in order to assess the feasibility of using Discrete Element Method (DEM) models as reliable predictive tools for describing hydraulic fracturing processes in unconsolidated formations:

i) Delineation of the objectives of the model analysis;

ii) Construction of a conceptual description of the physical system;

iii) Dvelopment and debugging of a simple and idealized model;

iv) Problem-specific data sets were obtained through calibration of the inter-particle bond and interaction parameters in the model;

v) A series of detailed model runs were performed; and,

vi) The results from the simulations were analyzed.

5.1 Objectives of this modeling study

This study aims at determining the potential and importance of shear as a failure mechanism during hydraulic fracturing processes involving highly-permeable, poorly-consolidated rocks. This modeling work consisted of three main phases: i) A first model of a core sample was constructed to mimic both the mechanical and hydraulic behavior of an unconsolidated rock sampled from the field; and ii) A field model was built to infer the behavior of the rock modeled in the first step during high pressure fluid injection.

5.2 Nature of the constructed models

The models built in this research work were aimed at describing both the mechanical and the hydraulic properties of typical poorly-consolidated formations. Thus, high porosity, high permeability, low mechanical strength rocks were used for calibration purposes. Throughout the calibration steps for the mechanical properties, parameters such as elastic modulus, Poisson's ratio, strength, and the shape of the stress-strain curve were duplicated in order to validate the results produced during the simulation runs.

For the first two phases of this study, the Antler sandstone was selected as the rock to be modeled; this formation is a weakly-consolidated rock that outcrops near Ardmore, Oklahoma. The poorly-consolidated nature of the Antler sandstone is apparent, as dried samples of this rock may be reduced to fine loose grains by merely applying hand pressure (Krishnan et al., 1994). During this part of the study, a cylindrical model was used to match the results of deformation tests available in the literature. A wealth of experimental data performed on Antler sandstone was obtained from a paper by Wang et al. (1995). Subsequently, a field-sized model was built in order to infer the behavior of the rock when subjected to high pressure injection of fluid with different viscosities.

5.3 Problem-specific data sets

The numerical modeling in this study consisted mainly of three steps: validation of the model mechanical properties, validation of the model hydraulic characteristics, and model construction and generation of results. In the first phase, parameters such as Young's modulus, Poisson's ratio, compressive strength, and shape of the stress-strain curve were duplicated by controlling the particle interaction parameters. In the second phase, the aperture of the inter-granular "conduits" created in PFC^{3D} was calibrated to reproduce the permeability

of the modeled rock. In the last phase, the model was built using the values of the interaction parameters obtained in the first two stages.

5.3.1 Antler sandstone - Core model

5.3.1.1 Model particle size distribution and porosity - Validation

Using the appropriate particle size distribution is critical when building a DEM model. In this particular study, several grain size distribution curves for Antler sandstone were available from the literature (Krishnan et al., 1994; Wang et al., 1995). The blue curve in Fig. 5.1 corresponds to the percent passing by weight for natural Antler samples, as reported by Wang et al. (1995). Applying numerical correlation techniques to these data, allowed obtaining Eqn. (5.1) (shown as the red dashed line in Fig. 5.1). The data frequency values (red solid curve) were obtained by simple derivation of the cumulative curve, see Eqn. (5.2). Table 5.1 presents the main statistical parameters obtained from the data reported by Krishnan et al. (1994).

$$Pass\ (\%) = A + \frac{B}{1 + \left(\frac{x}{C}\right)^{D}} \quad \text{.....(5.1)}$$

$$Frequency\ (\%) = -B\left[1 + \left(\frac{x}{C}\right)^{D}\right]^{-2}\left[\left(\frac{1}{C}\right)^{D} Dx^{D-1}\right] \quad \text{…….(5.2)}$$

where,

A = 99.898737;

B = -98.974718;

C = 0.21957087;

D = 4.10859700; and,

x : particle size, mm.

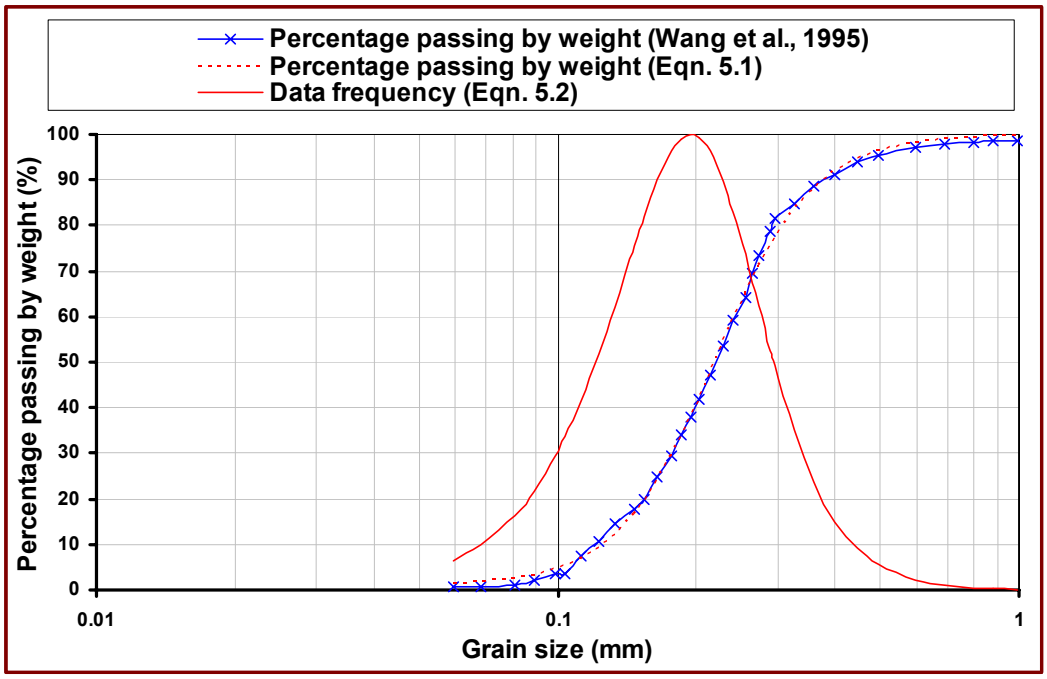

Figure 5-1. Grain size distribution curves of natural Antler sandstone (generated with data from Wang et al., 1995)

Parameter (mm)	Value
Mean	0.2980
Std. deviation	0.2391
Minimum	0.0596
Maximum	0.9903
Variance	0.0572

Table 5-1. Particle size distribution for natural Antler sandstone (calculated from the data by Wang et al., 1995)

From the Gaussian-like distribution, the limits for the maximum and minimum relevant data were found as follows: $\phi_{\max,\min} = \phi_{mean} \pm Std.deviation$. Then, the maximum and minimum values of the particle size distribution were 0.5371 mm. and 0.0589 mm., respectively.

In order to mimic the mechanical behavior of the Antler sandstone, a first cylindrical model with a length of 3 in. and a diameter of 1.5 in. was built. The particle size distribution within this "virtual" specimen was similar to the one reported for real Antler samples (see Fig. 5.1). The maximum and minimum[53] particle radii used were 0.990 mm. and 0.109 mm., respectively. The resulting model had more than 50,000 independent particles (Fig. 5.2), which made the deformation calculation process extremely slow. Thus, considering the fact that

[53] The difference between the maximum and minimum values of the distribution was later altered in the "virtual" sample in order to avoid the generation of an excessively large number of particles.

the real model would be a cylinder several times larger than this preliminary model, the need for reducing the number of particles was apparent.

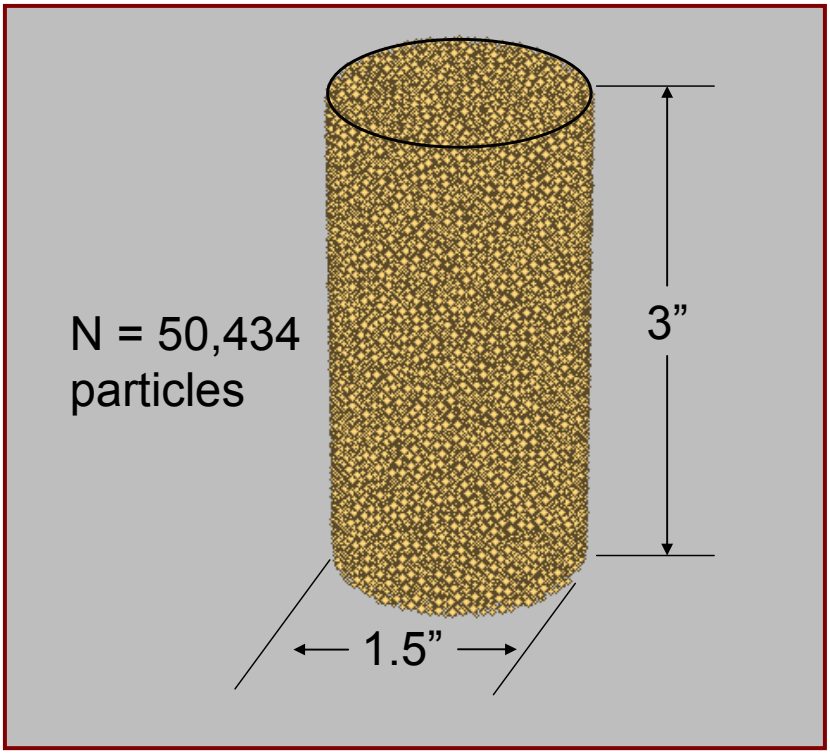

Figure 5-2. Dimensions and number of particles in the first modeling attempt.

A second “virtual” sample was generated by using the original values of particle size distribution multiplied by two; thus the maximum and minimum particle radii used for the simulation were 1.980 mm. and 0.596 mm, respectively. The result was a model composed of about 6,300 independent spheres. The reduced number

of particles made the deformation calculation process much faster; hence, the computer time necessary for each simulation was substantially shortened[54].

However, for a larger specimen (as in the case of the field model) the anticipated running time was still expected to be impractically long. Increasing the size of the particles while keeping the specimen size constant was not considered an option since the particles could become too large relative to the size of the rock sample. Thus, it was decided to increase both the size of the model and the particle size, and to deal with a "life size" problem from the beginning of the validation process. Figure 5.3 presents a view of the final model, which was a cylinder with 16.4 ft. in diameter and 32.8 ft. in length. A total of 5,626 particles with density equal to 2,650 Kg/m^3 were created, with their radii varying between 0.15 and 0.21 m.

The total porosity, measured after the sample was built, was approximately equal to 30%. This high value of porosity was used because poorly-consolidated sands tend to be under-compacted. After this step was completed, the sample was subjected to a stress field acting on axial and radial direction, simulating a triaxial test. The value of the radial stress (confining pressure) was kept constant

[54] The simulation running time for the second model was about $1/15^{th}$ of the simulation time needed to run the first model.

throughout each test, while the axial stress was increased until failure was reached; this procedure is explained in detail below.

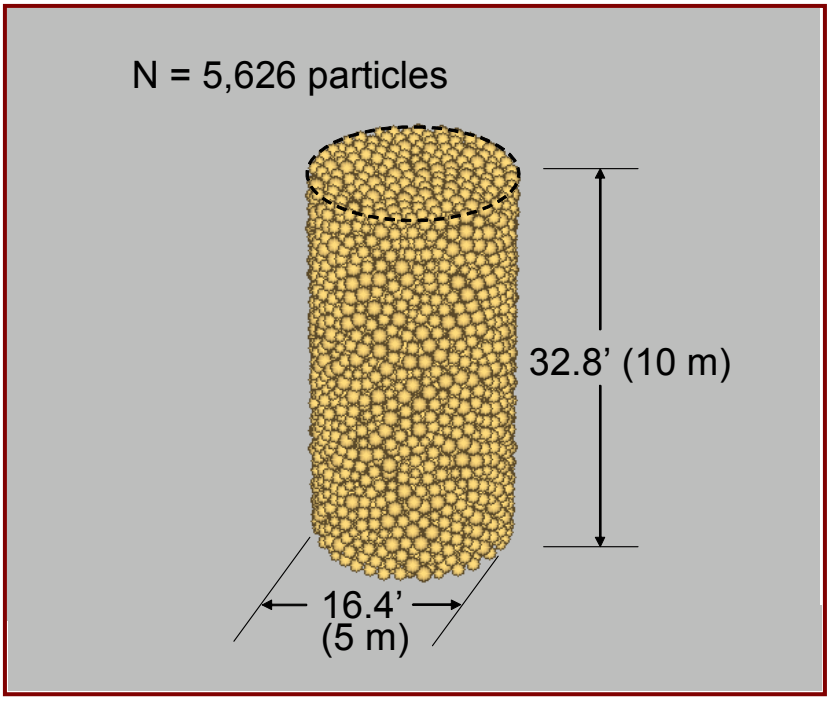

Figure 5-3. Schematic of model used for the validation of the mechanical properties of the "virtual" sample

5.3.1.2 Mechanical properties of the model - Validation

Validation of the mechanical properties of the model was performed by modifying the parameters governing the interaction between particles, i.e. type and stiffness of the contacts, bonding, and friction, amongst others. PFC^{3D} allows the construction of a model by defining these material properties at the microscopic level, and then evaluating the mechanical properties of the resulting

macroscopic model. This process is performed basically through a trial-and-error approach.

The results of a series of triaxial tests performed in the laboratory on natural and remolded Antler samples were published by Wang et al. (1995). They reported that for natural Antler Sandstone, the elastic modulus[55] ranged between 4.5 and 20.7 GPa (650,000 to 3,000,000 psi) when confining pressure increased from 6.9 to 34.5 MPa (1,000 to 5,000 psi). Whilst for Antler remolded samples the elastic modulus varied between 2.7 and 5.5 GPa (400,000 to 800,000 psi) for the same range of confining stress. The value of Poisson's ratio changed only slightly as a function of the confining load (from 0.2 to 0.3) for both the natural and the remolded specimens.

During the first few attempts to replicate the measured mechanical response of Antler sandstone, stiff spheres with linear elastic contacts and contact bonds[56] were used. The initial forces acting on the particles were consequence of both the stiffness of the material and the inter-particle "overlapping"[57] (larger magnitudes

[55] Slope of the linear region at the beginning of the stress-strain curve on a triaxial test; it is called the Young's modulus when obtained under zero confining pressure conditions (i.e. in uniaxial compression tests).
[56] A more detailed description on the type of inter-particle contact and bonding characteristics is provided in Chapter 4.
[57] Particles were created randomly in a 3D-space; thus, slight overlaps may exist. This overlapping was small compared to the particle diameter.

of overlap, and stiffer spheres cause inter-particle repulsion forces to increase). Thus, it was decided to start with particles of very low stiffness in order to evaluate the results provided by the model. The initial values of shear and normal stiffness, assigned to the spheres in the specimen were 0 Pa (0 psi) and 10^8 Pa (14,500 psi), respectively. Table 5.2 summarizes the parameters used for input during the first series of simulations, and the results obtained. Amongst the tested parameters were friction, contact normal and shear stiffness (*kn* and *ks*), and normal and shear bond strength (*n_bond* and *s_bond*).

	Simulation Input Parameters					**Simulation Results**
Test	**Friction**	**n_bond (Pa)**	**s_bond (Pa)**	**kn (Pa)**	**ks (Pa)**	**Young' modulus GPa (*psi*)**
1-1	0.5	0.0	0.0	0.0	0.0	0.023 (*3,287*)
1-2	1.0	1.0e5	1.0e5	0.0	0.0	0.106 (*15,370*)
1-3	0.5	1.0e15	1.0e15	1.0e10	1.0e10	3.067 (*444,785*)

Table 5-2. Initial set of simulations under σ_{conf} = 14.5 psi (0.1 MPa), only contact bonds.

The stress-strain curve in Test 1-1 showed an early linear-elastic region, followed by a broad peak, and finally a smooth strain-softening region (see Fig. 5.4). All tests in Table 5.2 were run under a confining pressure of only 0.1 MPa (14.5 psi); this low confining load allowed them to be considered as uniaxial compression tests. In the case of Test 1-1, the magnitude of the Young's modulus was only 22.6 MPa (3,287 psi), which is about two orders of magnitude lower than what would be expected for Antler sandstone samples. In addition, the shape of the

simulated curve was not similar to the shape of laboratory measured stress-strain plots for Antler sandstone (refer to Fig. 2.24). The plots obtained in the laboratory lack the presence of both a maximum and a strain-softening region. However, the results of this test were very instructive, as the model behaved similarly to a sample that was run with friction being the only inter-particle interaction parameter, i.e. with no inter-particle bonds. The plastic behavior observed after the peak suggested that inter-particle friction was dominant in the post-failure deformation process.

The second and third tests listed in Table 5.2 (Tests 1-2 and 1-3) produced much larger values of Young's modulus; however, the shapes of the stress-strain curves were radically different from the curves published in the literature for Antler sandstone. In these simulation runs, the stress-strain behavior was completely linear-elastic at the beginning of the test; followed by a sharp, instantaneous brittle failure. Based on the results of the first set of tests, it was decided to include both contact bonds, and parallel bonds in the second series of simulation runs. The main goal of this second series of tests was to identify the best type of bonding properties, which could provide a stress-strain curve with the same shape as the one observed in Fig. 2.24. Table 5.3 presents a summary of the simulation input parameters as well as the corresponding results for Young's modulus for this part of the study.

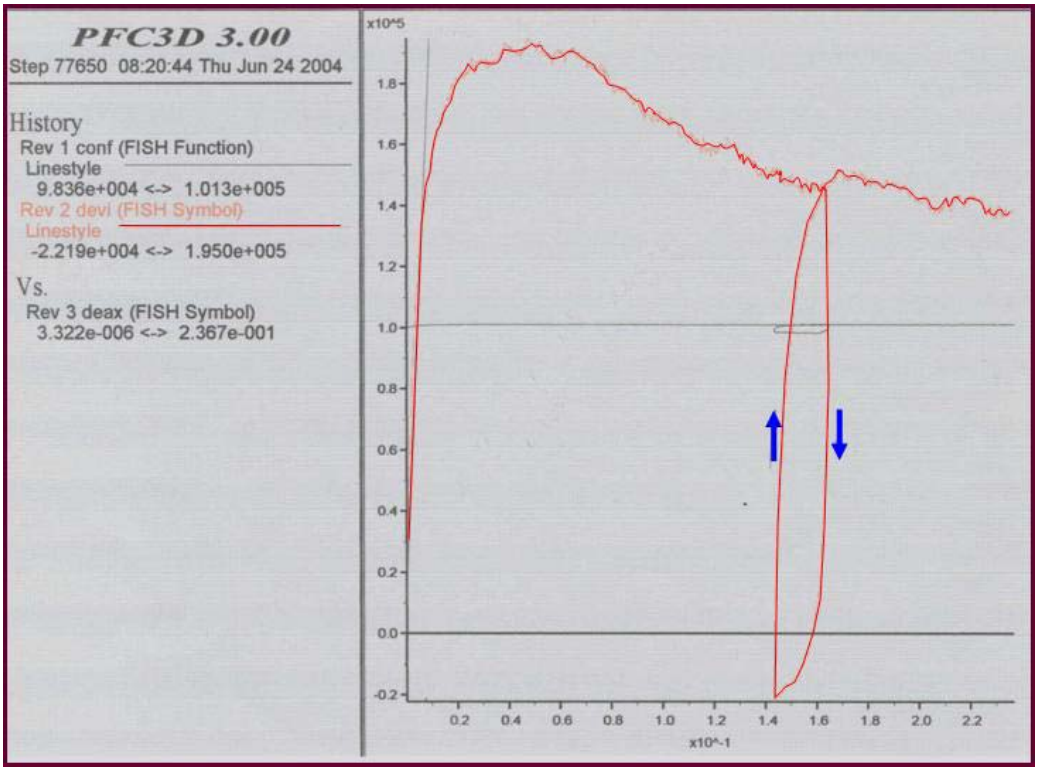

Figure 5-4. Plot of stress (in Pa) vs. strain; corresponding to Test 1-1 (inter-particle friction only).

		Test			
		2-1	**2-2**	**2-3**	**2-4**
INPUT	**Friction coefficient**	0.5	0.5	0.5	0.5
	pb_kn (10^{10}Pa)	8.0	80.0	8.0	80.0
	pb_ks (10^{10}Pa)	8.0	80.0	8.0	80.0
	pb_rad	0.1	0.2	0.1	0.2
	pb_nstren (10^{7}Pa)	1.0	10.0	1.0	10.0
	pb_sstren (10^{7} Pa)	1.0	10.0	1.0	10.0
	kn (10^{5} Pa)	1.0	1.0	10.0	10.0
	ks (10^{5} Pa)	1.0	1.0	10.0	10.0
	n_bond (Pa)	100.0	100.0	1,000.0	1,000.0
	s_bond (Pa)	100.0	100.0	1,000.0	1,000.0
OUTPUT	**Young's modulus GPa, (*psi*)**	**0.002** ***(348)***	**0.354** ***(51,283)***	**1.066** ***(154,666)***	**1.697** ***(246,060)***

Table 5-3. Second set of simulations, with σ_{conf} = 14.5 psi (0.1 MPa), it included both parallel and contact bonds.

In Table 5.3, *pb_kn* and *pb_ks* represent the normal and shear stiffness of the parallel contact, respectively; whereas *pb_nstren* and *pb_sstren* are the normal and shear mechanical strength of the parallel contact. The parameter *pb_rad* is the radius of the parallel contact[58]. The stress-strain curve produced in Test 2-1, exhibited a shape that was very similar to the shape of the measured curves in Fig. 2.24. However, the magnitudes on the stress and strain scales were shifted, i.e. for this simulation run the values of stress were very low while the corresponding magnitudes of strain were extremely large (Fig. 5.5). In Test 2-2, the values assigned to the parameters defining the parallel bonds were increased, i.e. the parallel bonds were made stiffer and stronger. The results showed a similarly-shaped curve shifted upwards on the stress scale and to the left on the strain scale. However, the generated values of Young's modulus for the material were still an order the magnitude lower than in the case of the "real" rock. Despite the fact that the magnitude of the macroscopic mechanic properties of the model were still too low, the selected micromechanical interactions were matching the general behavior (shape of the stress-strain curve) of the Antler sandstone. The values of axial stress at the beginning of the test indicated the presence of tensile load within the sample; this may be explained by the fact that confining stress (black line at the top of the plot) was increased faster than the axial stress creating some tensile deformations. This phenomenon was later avoided by increasing both the

[58] Given as a fraction of the radius of the smaller of the two spheres forming a particular contact; by definition, it is a dimensionless quantity.

axial and the radial stress at the same rate until the value of confining stress was reached. Then, the radial stress was kept constant while the axial stress was increased.

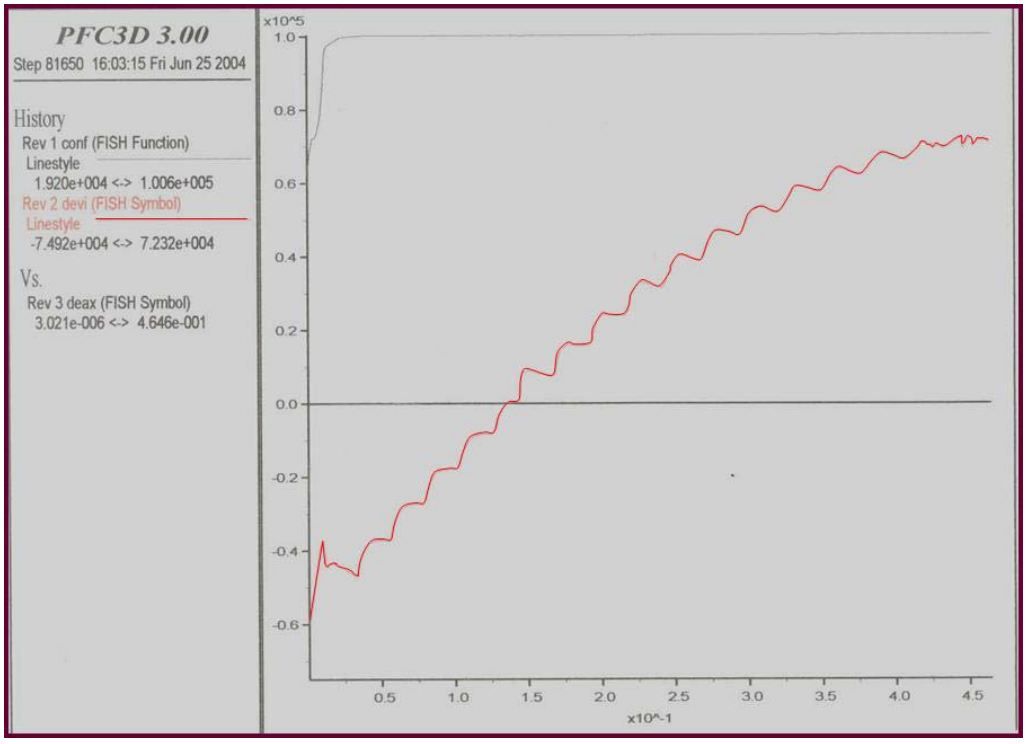

Figure 5-5. Curve of stress (in Pa) vs. strain for virtual Test 2-1 (listed in Table 5.3)

In the case of Test 2-3, the values of the parameters defining the contact bonds were increased in magnitude; as a result, a significant increase in the value of the Young's modulus for the model was observed. Nonetheless, the shape of the stress-strain curve resembled that of a brittle rock: the beginning of the curve was evidently linear-elastic, followed by very rapid failure and then by a steep stress

decline (Fig. 5.6). Test 2-4 showed the same general trend, although the value of Young's modulus increased. From the results of Tests 2-1 through 2-4, it was concluded that parallel bonds were more representative of the general mechanical behavior of the Antler sandstone: a relatively short linear-elastic region at low values of strain, followed by a smooth strain hardening inelastic region as deformation was increased.

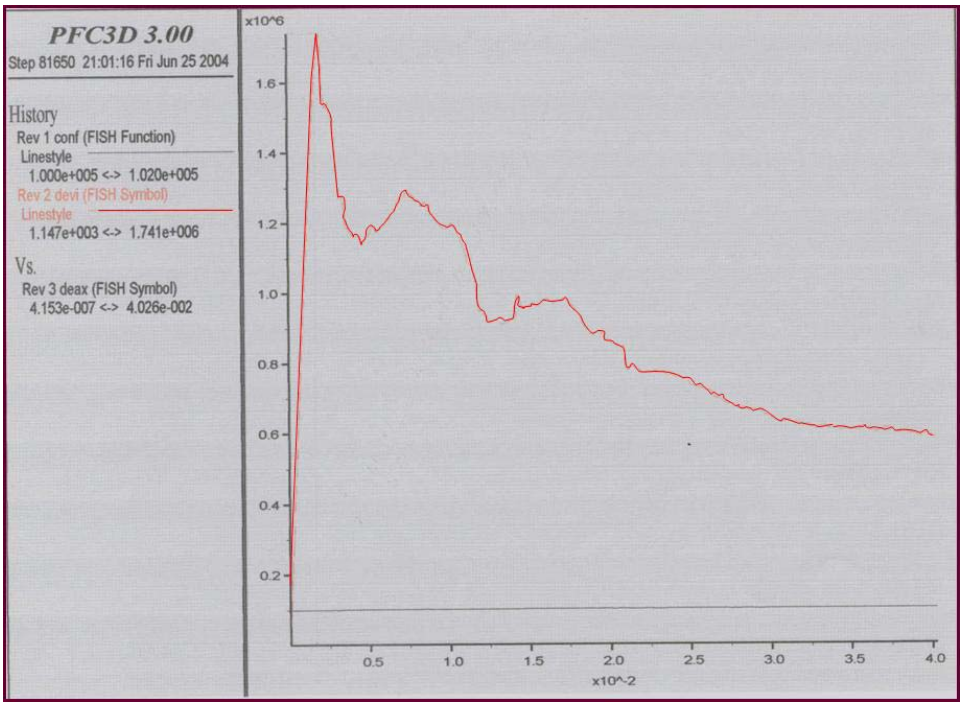

Figure 5-6. Curve of stress (in Pa) vs. strain for Test 2-3, see Table 5.3.

Based on the analysis of the results attained from the second series of simulations, it was decided to model the Antler sandstone by using only inter-particle parallel

bonds and friction, i.e. contact bonds were eliminated from the simulation model. At this point, the normal stiffness of the spheres was increased to $6.9*10^{10}$ Pa (10^7 psi); the value of the shear stiffness was still kept equal to zero. The characteristics of the new set of numerical simulations are presented in Table 5.4.

Test	Simulation Input Parameters						Results
	Frict.	pb_kn (10^{15}Pa)	pb_ks (10^{15}Pa)	pb_rad	pb_nstren (10^6Pa)	pb_sstren (10^6 Pa)	Elastic modulus Gpa (*psi*)
3-1	0.55	1.00	1.00	0.20	1.00	1.00	0.79 (*114,474*)
3-2	0.55	1.00	1.00	0.30	1.00	1.00	0.72 (*104,166*)
3-3	0.55	10.00	10.00	0.30	1.00	1.00	0.77 (*112,403*)

Table 5-4. Third set of simulations; with σ_{conf} = 1,000 psi, b_kn=$6.9*10^{10}$ Pa (10^7 psi), and b_ks=0 Pa (0 psi)[59].

The results of Test 3-3 are also presented in Fig. 5.7; for this case the obtained elastic modulus was about 0.77 GPa (112,000 psi). Although the magnitude of the model elastic modulus was only a little more than ¼ of the value reported from measurements, the shape of the obtained curve was very similar to the shape of the curves published by Wang et al. (1995). Thus, it was decided to increase the normal stiffness of the spheres as well as the stiffness and diameter of the inter-particle parallel contacts. Table 5.5 shows a summary of the values of the input parameters and the results obtained during this new series of tests.

[59] b_kn : particles normal stiffness, and b_ks: particles shear stiffness.

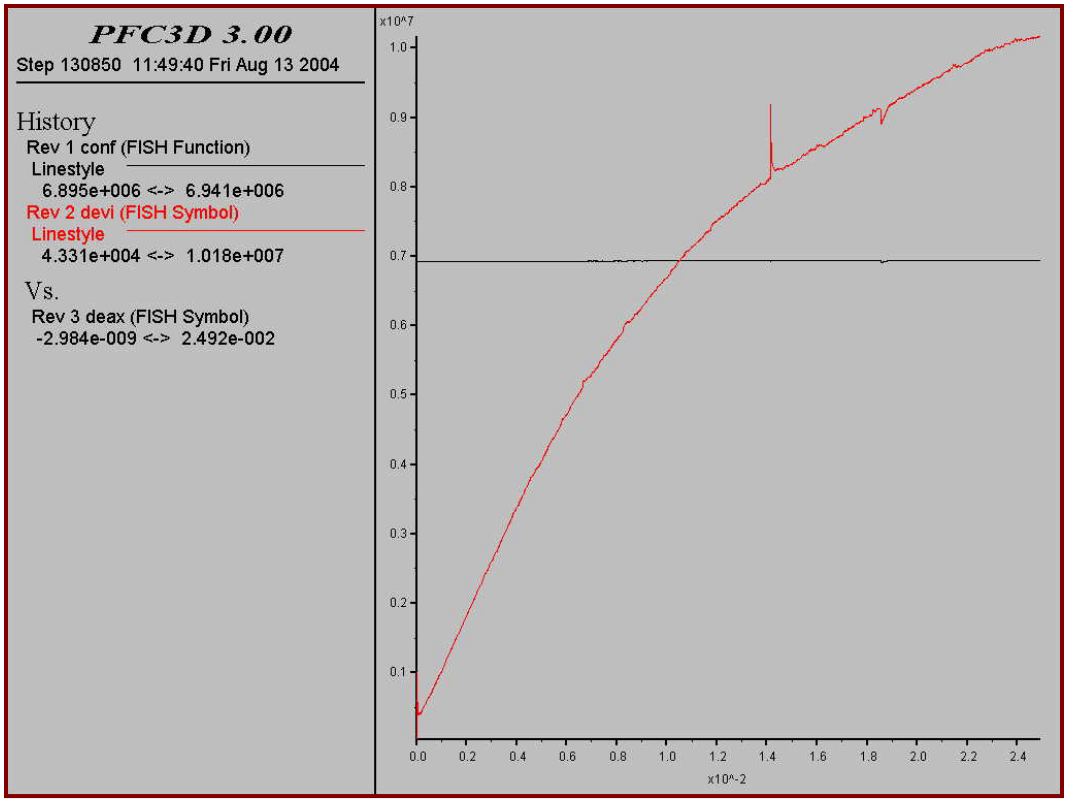

Figure 5-7. Curve of stress (in Pa) vs. strain for Test 3-3, with σ_{conf} = 1,000 psi (6.9 MPa), b_kn=6.9*10^{10} Pa (10^{7} psi), and b_ks=0 Pa (0 psi), see Table 5.4

Test	Simulation Input Parameters						Results
	Frict.	pb_kn, GPa	pb_ks, GPa	pb_rad	pb_nstren MPa	pb_sstren MPa	Elastic modulus GPa (*psi*)
4-1[60]	0.55	1.00*10^{7}	1.00*10^{7}	0.30	1.00	1.00	1.03 (*149,484*)
4-2[61]	0.55	76.00	30.00	0.30	1.00	1.00	1.00 (*145,000*)
4-3[60]	0.55	76.00	30.00	0.50	1.00	1.00	0.90 (*130,337*)
4-4[60]	0.55	76.00	30.00	0.50	3.50	9.30	0.81 (*116,935*)
4-5[60]	0.55	76.00	30.00	0.10	3.50	9.30	1.85(*268,518)*
4-6[60]	0.55	98.00	43.00	0.10	3.50	9.30	2.35 (*341,176*)
4-7[60]	0.55	112.00	52.60	0.10	3.50	9.30	2.78 (*402,777*)
4-8[60]	0.55	112.00	52.60	0.15	3.50	9.30	4.17 (*604,166*)

Table 5-5. Fourth series of simulations; with σ_{conf} = 1,000 psi (6.9 MPa), see footnotes.

[60] With the spheres having normal and shear stiffness equal to 6.9*10^{11} Pa (1.0*10^{8} psi) and 0.0 Pa (0.0 psi), respectively.
[61] With the spheres having normal and shear stiffness equal to 9.4*10^{10} Pa (13.6*10^{6} psi) and 4.0*10^{10} Pa (5.8*10^{6} psi), respectively.

In the table above, Test 4-1 was performed assuming extremely high values of normal stiffness for the particles in the assembly (*b_kn* = 690 GPa = $1.0*10^8$ psi) and for the inter-particle contacts (*pb_kn* = *pb_ks*=$1.0*10^{16}$ Pa = $1.45*10^{12}$ psi). Despite using these unrealistically high values[62], the stiffness of the model was found to be relatively low. This outcome led to the conclusion that it was necessary to assign a non-zero magnitude to the shear stiffness of the spheres while reducing their normal and contact stiffnesses to more reasonable values. Consequently, Tests 4-2 through 4-8 were performed with the particles having normal and shear stiffness values of $9.4*10^{10}$ Pa ($13.6*10^6$ psi) and $4.0*10^{10}$ Pa ($5.8*10^6$ psi), respectively. Comparison of the results on Tests 4-1 and 4-2, allowed observing the effects of such changes (Fig. 5.8 shows the results of Test 4-2). Much lower values of contact stiffness produced similar values of elastic modulus when the assigned value to the spheres shear stiffness is not zero. The results from Test 4-8 were very similar to those reported by Wang et al. (1995) from tests on "real" rocks (see Fig. 5.9).

The outcome from Test 4-2 through 4-5, where the contacts are "softer" than the particles, showed that any increase in the radius of the contacts translates into a decrease in the elastic modulus of the model. By the same token, when the

[62] For Silica the value of Young's and shear moduli are about 94 GPa ($13.6*10^6$ psi) and 34 MPa ($4.9*10^6$ psi), respectively (University of Kansas, 2004; Efunda, 2004).

contacts were stiffer than the particles (Tests 4-6 to 4-8), enlarging the contact radius caused the elastic modulus of the whole sample to increase.

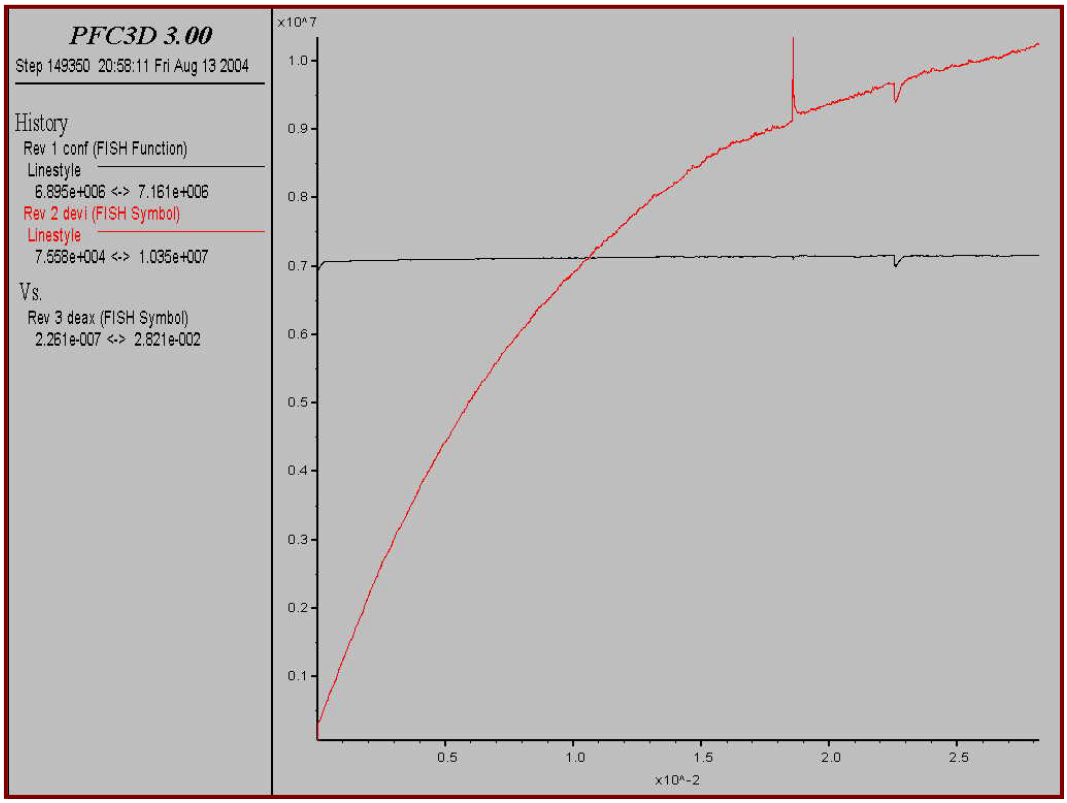

Figure 5-8. Curve of stress (in Pa) vs. strain for Test 4-2, with σ_{conf} = 1,000 psi (6.9 MPa), b_kn=9.4*10^{10} Pa (13.6*10^{6} psi), and b_ks=4.0*10^{10} Pa (5.8*10^{6} psi), see Table 5.5.

The physical explanation for the behavior observed during this series of tests is that larger contacts have relatively more importance on the overall behavior of the rock, due to an increment on their relative volume within the specimen. Thus, the mechanical properties of the model could be increased or decreased by changing the radius of the contacts depending on their relative stiffness with respect to the

stiffness of the spheres. Likewise, increasing the strength of the contacts transfers more load to them, making them increasingly important on the overall model properties, as it is apparent from comparing the outcome of Tests 4-2 and 4-3.

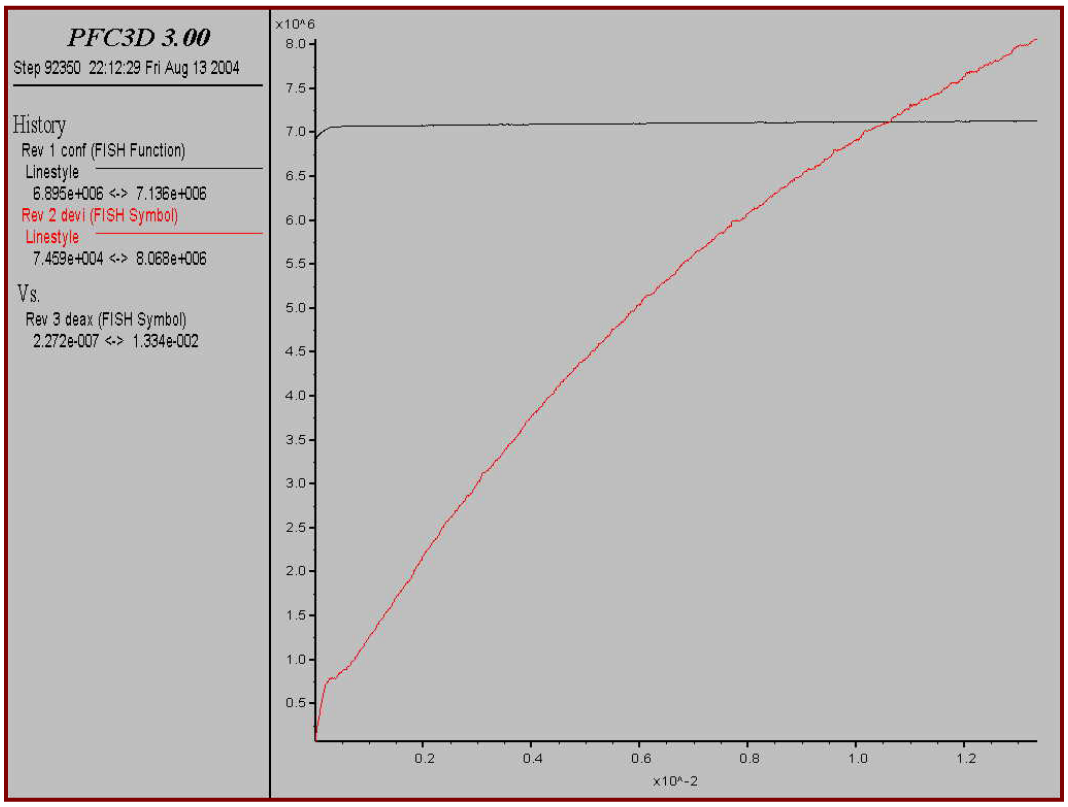

Figure 5-9. Curve of stress (in Pa) vs. strain for Test 4-8, with σ_{conf} = 1,000 psi (6.9 MPa), b_kn=9.4*10^{10} Pa (13.6*10^{6} psi), and b_ks=4.0*10^{10} Pa (5.8*10^{6} psi), see Table 5.5.

Table 5-6 summarizes the results from additional tests run under a confining pressure of 34.48 MPa (5,000 psi). The outcome of the numerical experiments in Table 5-6, indicated that increments in the stiffness of the contacts caused the overall model stiffness to increase. Once again, it was observed that when

contacts were relatively stiffer than the particles, larger contact radii translated into higher values of elastic modulus.

Test	Simulation Input Parameters						Results
	Frict.	pb_kn (GPa)	pb_ks (GPa)	pb_rad	pb_nstren (MPa)	pb_sstren (M Pa)	Elastic modulus Gpa (*psi*)
5-1	0.55	98.0	43.0	0.10	3.50	9.30	4.44 (*644,444*)
5-2	0.55	112.0	52.6	0.10	3.50	9.30	4.65 (*674,418*)
5-3	0.55	112.0	52.6	0.15	3.50	9.30	6.02 (*873,494*)

Table 5-6. Fifth series of simulations; with σ_{conf} = 5,000 psi (34.5 MPa), b_kn=9.4*10^{10} Pa (13.6*10^{6} psi), and b_ks=4.0*10^{10} Pa (5.8*10^{6} psi)

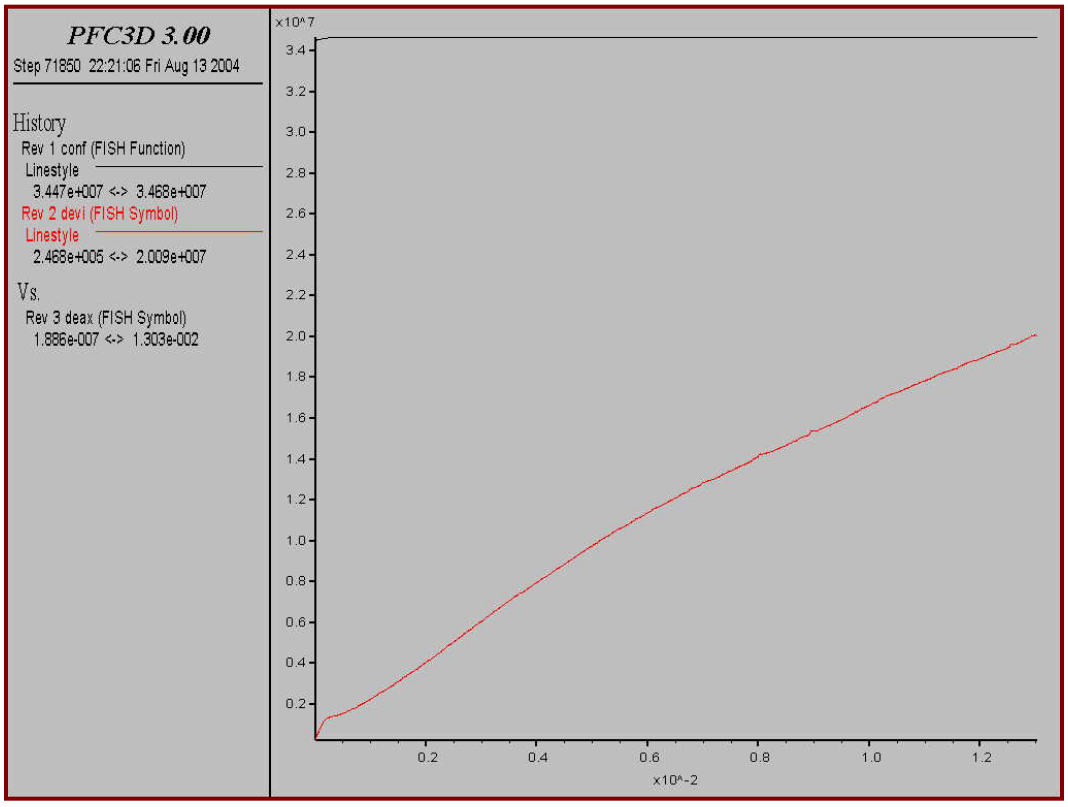

Figure 5-10. Curve of stress (in Pa) vs. strain for Test 5-3, with σ_{conf} = 5,000 psi (34.5 MPa), b_kn=9.4*1010 Pa (13.6*10^{6} psi), and b_ks=4.0*1010 Pa (5.8*10^{6} psi), see Table 5.6.

The parameter values run in Tests 4-8 and 5-3 provided values of elastic modulus that were very similar to those measured in the laboratory by Wang et al. (1995) under the same values of confining stress. In addition to comparing the values of the elastic modulus, the differences in the magnitudes of Poisson's ratio between the "real" and the "virtual" rock were also evaluated. Laboratory measured values of Poisson's ratio for the Antler sandstone range between 0.2 and 0.3 for confining stresses varying between 6.9 and 34.5 MPa (1,000 to 5,000 psi) for both natural and remolded samples (Wang et al., 1995). The results obtained from the numerical tests in this study ranged between 0.256 and 0.396 under the same window of confining stress values; Fig. 5.11 shows the curve of volumetric vs. axial strain for Test 5-3.

The last parameters to be calibrated in this model were the normal and shear strength assigned to the inter-particle contacts. This scheme was followed as these values affect only the magnitude of the y-axis values on the stress-strain curve (Itasca Consulting Group, 2004), i.e. the strength of the contacts affects only the peak strength of the rock and not its shape neither its slope. Up to this point in the study, the values used for the normal and shear strength of the contacts were 3.5 MPa (500 psi) and 9.3 MPa (1,350 psi), respectively. Table 5.7 shows the calibration procedure performed in order to find proper values for the contact strength parameters.

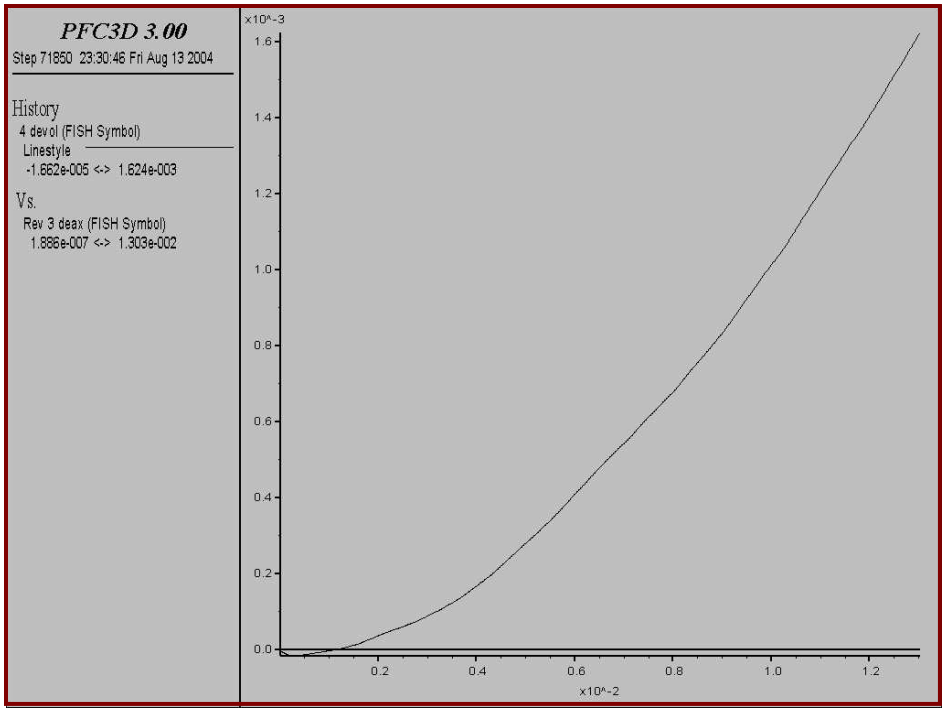

Figure 5-11. Curve of volumetric strain vs. axial strain for Test 5-3, with σ_{conf} = 5,000 psi, b_kn=9.4*1010 Pa (13.6*106 psi), and b_ks=4.0*1010 Pa (5.8*106 psi), see Table 5.6.

Test	Simulation Input Parameters			Results
	Confining pressure MPa (*psi*)	pb_nstren MPa(*psi*)	pb_sstren MPa(*psi*)	Peak deviatoric stress, MPa (*psi*)
6-1	6.89 (*1,000*)	3.50 (*500*)	9.30 (*1,350*)	20.00 (*2,900*)
6-2	6.89 (*1,000*)	34.50 (*5,000*)	41.18 (*5,975*)	24.18 (*3,506*)
6-3	6.89 (*1,000*)	68.96 (*10,000*)	82.37 (*11,950*)	26.78 (*3,883*)
6-4	6.89 (*1,000*)	137.93 (*20,000*)	164.74 (*23,880*)	29.50 (*4,278*)
6-5	34.48 (*5,000*)	3.50 (*500*)	9.30 (*1,350*)	36.34 (*5,270*)
6-6	34.48 (*5,000*)	34.50 (*5,000*)	41.18 (*5,975*)	66.88 (*9,697*)
6-7	34.48 (*5,000*)	68.96 (*10,000*)	82.37 (*11,950*)	82.06 (*11,900*)
6-8	34.48 (*5,000*)	137.93 (*20,000*)	164.74 (*23,880*)	90.01 (*13,050*)

Table 5-7. Calibration of the normal[63] and shear strength of the inter-particle contacts, with constant values of stiffness for both spheres and contacts (see Table 5.6).

[63] In this study, normal strength refers to the tensile strength of the inter-particle contact.

According to experimental data published by Wang et al. (1995), the peak deviatoric stress for Antler sandstone samples varied between 33.1 MPa and 96.5 MPa (4,800 psi to 14,000 psi) for confining pressure varying between 6.9 MPa and 34.5 MPa (1,000 psi to 5,000 psi). Thus, a comparison between the data published in the literature and the data produced from the simulations rendered the selected parameters for strength acceptable for the purpose of this study.

The comparisons above allowed assessing the feasibility of producing reliable results through the model constructed for this study. It was concluded that matching the values of elastic modulus, Poisson's ratio, general shape of the stress-strain curve, and peak strength provided enough confidence on the mechanical accuracy of the model. Table 5-8 summarizes the values for the particle interaction properties that were selected after the calibration process, in order to represent the mechanical behavior of the Antler sandstone.

Selected Values for Input Parameters					
Frict.	**pb_kn GPa (*psi*)**	**pb_ks GPa (*psi*)**	**pb_rad**	**pb_nstren MPa (*psi*)**	**pb_sstren MPa (*psi*)**
0.55	112.00 (*16,240*)	52.60 (*7,627*)	0.15	137.93 (*20,000*)	164.74 (*23,880*)

Table 5-8. Calibrated values for the mechanical interaction parameters used in this study.

The model building and validation processes described above, were performed by running a series of routines written in FISH[64]; this modular programming scheme allowed running several variations of the same model without executing extremely long and complex routines. A complete list of the routines written for this part of the study is provided in Appendix A.

5.3.1.3 Comments on the validation of the model mechanical properties

The results of the validation process for the mechanical properties of the model allowed drawing several conclusions on the effects of changing certain micro-scale properties on the macroscopic properties of the model. It was found that:

i) Contact bonds tend to give a brittle nature to the sample, i.e. the stress-strain curve for the model is characterized by the presence of a sharp peak; which is followed by a very rapid decrease in the load carried by the sample as deformation continues. On the other hand, the presence of inter-granular friction tends to induce weak strain softening (i.e. post-peak plastic behavior).

[64] Exclusive programming language used by PFC[3D].

ii) The initial elastic modulus of the model is proportional to the stiffness of the contact. Parallel bonds are far more efficient than contact bonds in increasing the contact stiffness. The relative values of the contacts stiffness with the respect to the spheres stiffness is also important; for contacts that are relatively stiffer than the particles, larger contact radii translate into higher values of elastic modulus. By the same token, increasing the radii of relatively softer contacts decreases the global elastic modulus of the model.

iii) The effect of the friction strength is proportional to the magnitude of the confining stress. Hence, the material behaves in a more plastic manner under higher confining loads.

Additional guidelines for choosing the micro-scale properties of the contacts are provided in the PFC^{3D} manual (Itasca Consulting Group, 2004).

The main mineral component of the grains in sandstone is quartz. Laboratory tested samples of quartz show measured values of Young's modulus of about 94.3 GPa (13.6*10^6 psi), and magnitudes of shear modulus of up to 34.0 GPa (4.9*10^6 psi) (University of Kansas, 2004). The selected values for the normal and shear stiffness of the particles were 94.0 GPa (13.6*10^6 psi) and 40.0 GPa (5.8*10^6 psi), respectively. The differences between these two sets of values were only about

0.3% for the Young's modulus and 18% for the shear modulus; these discrepancies could be attributed to the presence of minerals other than quartz in the rock being modeled (i.e. in the Antler sandstone). Nonetheless, it was considered that the values found during the validation process for the normal and shear stiffness of the particles were in good agreement with the magnitudes measured in the laboratory.

The radius of the parallel inter-particle bonds obtained from the validation procedure was 0.15, i.e. 15% of the radius of the smaller of the two spheres forming the contact. Results from electronic microscopy images of Antler sandstone showed rounded grains with cementing material at the contacts. It is difficult from the pictures to calculate the radius of the bonds, as it is evident that the bonds vary in size and thickness throughout the rock. Relatively large bonds were found between the grains (Fig. 5.12a), as well as very small coatings at the contact (Fig. 5.12b). Hence, it was concluded that the value used in the simulations (0.15) was acceptable for the purposes of this study.

The values selected from the simulation runs for the normal and shear stiffness of the contacts were 112.0 GPa ($16.24*10^6$ psi) and 52.6 GPa ($7.63*10^6$ psi). At a first glance these values seem to be abnormally high. However, a closer look at the mineral components of the cementing material revealed the presence of

significant amounts of silica, aluminum, and iron; traces of magnesium, potassium, calcium, and titanium were also reported, see Fig. 5.13 (Wang et al., 1995). Reported values for the Young's modulus for the most important minerals in the inter-granular cement ranged between 69 and 196 GPa ($10.00*10^6$ to $28.13*10^6$ psi). Figure 5.14 presents a comparison of the values of stiffness used for the parallel contacts in the model and the values of the stiffness of the mineral components found in the cement of the Antler sandstone. It was apparent that the simulated model had stiffness properties well within the ranges expected for the real rock.

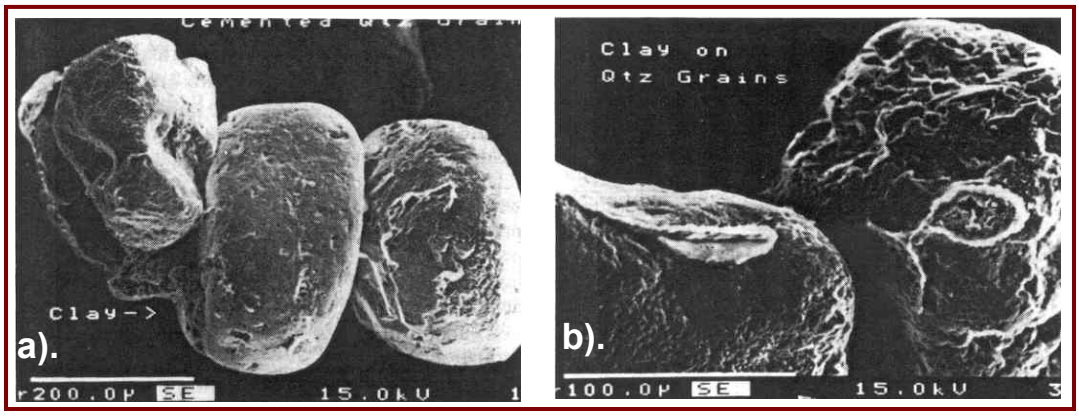

Figure 5-12 . Secondary electron images of the Antler sandstone; a). bonded grains showing what appears to be clay cement (x132);and, b). bonded grains showing white coatings of cementing material (x368), after Wang et al. (1995).

Likewise, the inter-particle strength parameters in the model (i.e. shear and normal strength) were compared to the shear and tensile strength of the mineral components of the cementing material. In this case, it was also found that the

values of normal and shear strength for the inter-particle contacts in the model fell within the limits defined by the mechanical properties of the rock components (see Fig. 5.15).

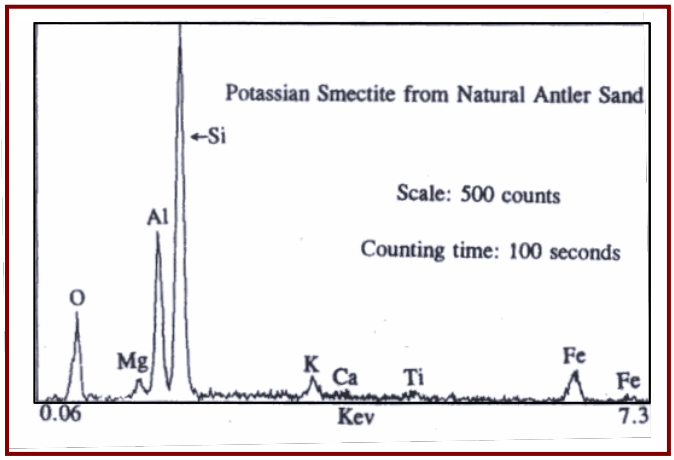

Figure 5-13. EDS-Spectrum display of the cementing materials in a sample of the Antler sandstone (after Wang et al., 1995).

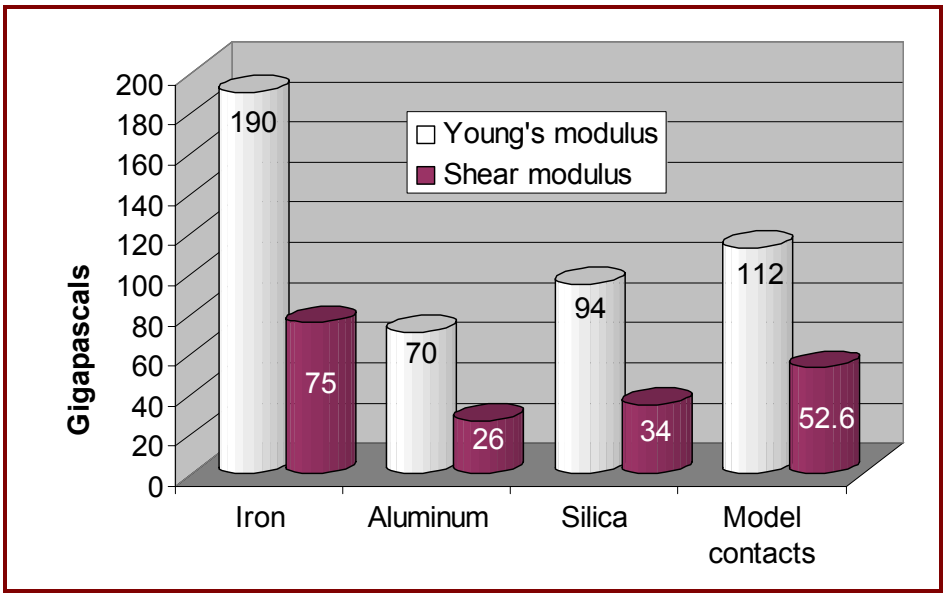

Figure 5-14. Normal and shear stiffness of the minerals in the rock cement and of the simulated model (built with data from University of Kansas (2004) and Efunda (2004).

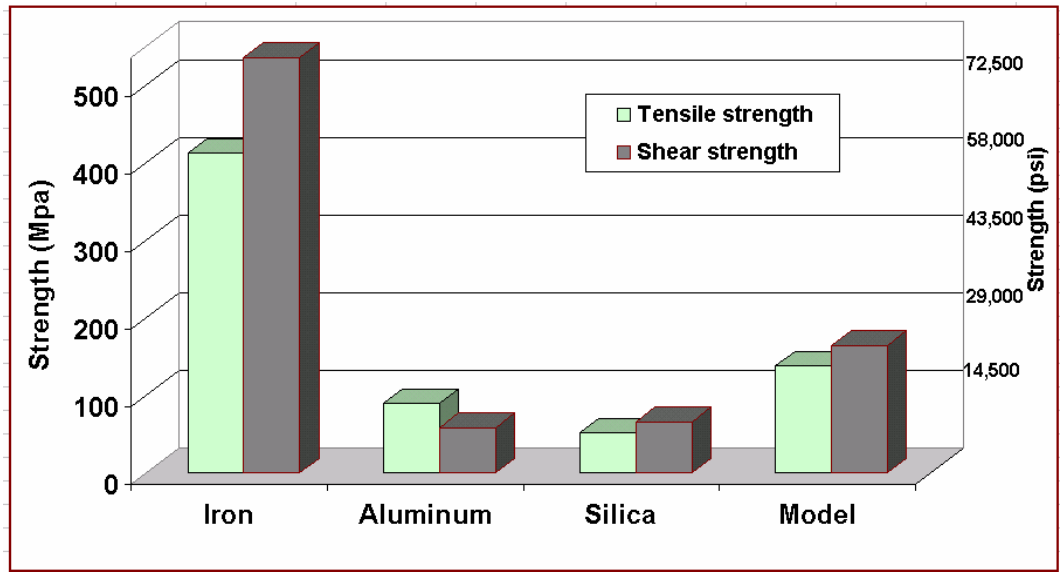

Figure 5-15. Normal[65] and shear strength of the minerals in the rock cement and of the simulated model (built with data from University of Kansas (2004) and Efunda (2004).

5.3.1.4 Hydraulic properties of the model - Validation

In PFC^{3D}, the pore geometry is represented by the void space between individual particles. The entire particle assembly is divided into domains, where each one is defined by a group of four adjacent particles. There are several properties that define a domain in the assembly: pore pressure, volume, change in volume per cycle, and pipes associated to it. The term "pipe" refers to a link between two adjoining domains; this pipe is defined by the small space between the three closest particles at the boundary of the domain. PFC^{3D} represents each pipe as a

[65] Hereby, the expressions normal strength and tensile strength are used interchangeably.

cylinder of length L, and aperture a. According to Poiseuille's law (Munson et al., 2003), the laminar flow rate in a pipe is given by:

$$q = \frac{k\, a^3\, \Delta P}{L} \quad \text{.....(5.3)}$$

where,
- L : distance between the centers of the two domains being linked;
- a : pipe aperture, i.e. diameter;
- k : conductivity factor[66]; and,
- ΔP : pressure difference between two adjacent domains.

The pressure formulation in PFC^{3D} assumes that in one time step, Δt, the change in domain fluid pressure is caused both by an alteration of the fluid volume inside the domain, and by a change of the apparent volume of the domain itself (Itasca Consulting Group, 2004) . Thus, the pressure disturbance within any domain may be calculated as:

$$\Delta P = \frac{K_f}{V_d}\left(\Sigma q\, \Delta t - \Delta V_d\right) \quad \text{.....(5.4)}$$

where K_f is the fluid bulk modulus, and V_d is the apparent volume of the domain being evaluated. The first term represents the net amount of fluid

[66] Defined as $k = \pi a / (16\mu)$; where μ is the fluid viscosity.

entering/leaving the domain; whereas the second term accounts for the change of the domain's volume as a result of changes in the effective stress.

PFC^{3D} uses an explicit solution scheme for solving the coupled fluid/deformation problem that results from fluid injection into a discrete material. First, the flow rate into/out of every domain, as triggered by a pressure disturbance (ΔP_d), is calculated by using Eqn. 5.3. The calculated flow causes a pressure response, ΔP_r, according to Eqn. 5.4. The change in domain volume as result of the applied stress is calculated according to Newton's second law by the main module of PFC^{3D}. For stability purposes ΔP_d is always larger than ΔP_r, the physical implication of this condition is that part of the energy causing the disturbance is lost during every time step (typically, ΔP_r is about $0.8*\Delta P_d$).

The overall rock permeability was the only calibration parameter considered during the validation of the hydraulic properties of the model. Throughout this process, several "virtual" permeability tests were performed by applying a finite pressure difference between the ends of the model. Although very simple, this methodology had a critical drawback: the flowrate (and hence the calculated permeability) was time-dependent at the beginning of the test. Furthermore, reaching steady-state typically took an excessively large number of steps, which made it impractical for calibration purposes. This stabilization time decreased as

the overall model permeability was increased. In order to ensure steady-state behavior, it was decided to apply a fixed logarithmic pressure vs. distance distribution (Earlougher, 1977). This steady state distribution was imposed throughout the sample from the beginning of the test, according to the equation:

$$P = \frac{P_0}{\ln\left(L_0 / L\right)}\left[\ln\left(L_0 / L\right) - \ln\left(L_0 / x\right)\right] + P_1 \quad \text{.....(5.5)}$$

where

- P_0 : pressure at the bottom of the specimen (high pressure end);
- P_1 : pressure at the top of the model (low pressure end);
- L : total distance between the two ends;
- L_0 : length of the specimen having pressure equal to P_0; and,
- x : distance of a given point to the bottom of the model.

For convenience, the values of these parameters were chosen such that $P_0 > P_1$, and $L_0 << L$. The final shape of the pressure vs. distance distribution is shown in Fig. 5.16. The permeability calculation, performed during the validation stage of this study, was carried out by creating a "virtual" surface in the middle of the sample (see Fig. 5.17). The flow rates obtained for all the "pipes" crossing this surface were computed and totalized as the variable Q_T. Then, the value of permeability was computed from Darcy's law as:

$$Perm = \frac{\mu\, Q_T\, x_P}{\pi\, R^2\, \Delta P} \quad \text{.....(5.6)}$$

where,

- μ : viscosity of the saturating fluid;
- Q_T : total flow rate for all the pipes crossing the virtual surface;
- R : model radius;
- x_p : distance of the virtual surface to the model bottom end; and,
- ΔP : pressure drop, $P_0 - P$; with P being the pressure at point x.

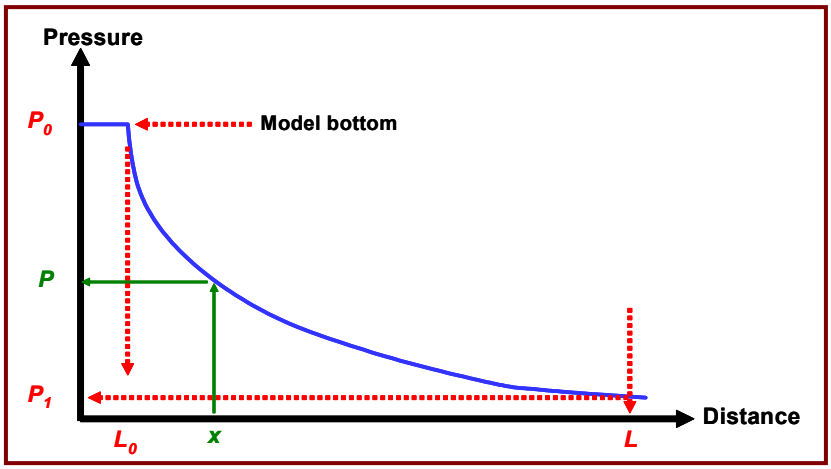

Figure 5-16. Pressure vs. distance (along the model axis) distribution, hydraulic properties validation.

Figure 5.17 also shows a snapshot of the model, taken during a permeability test; the white circles represent the magnitude of the local pore pressure, i.e. larger circles at the bottom correspond to the highest values of fluid pressure. The yellow and black lines symbolize the magnitude of tensile and compressive inter-particle loads, respectively.

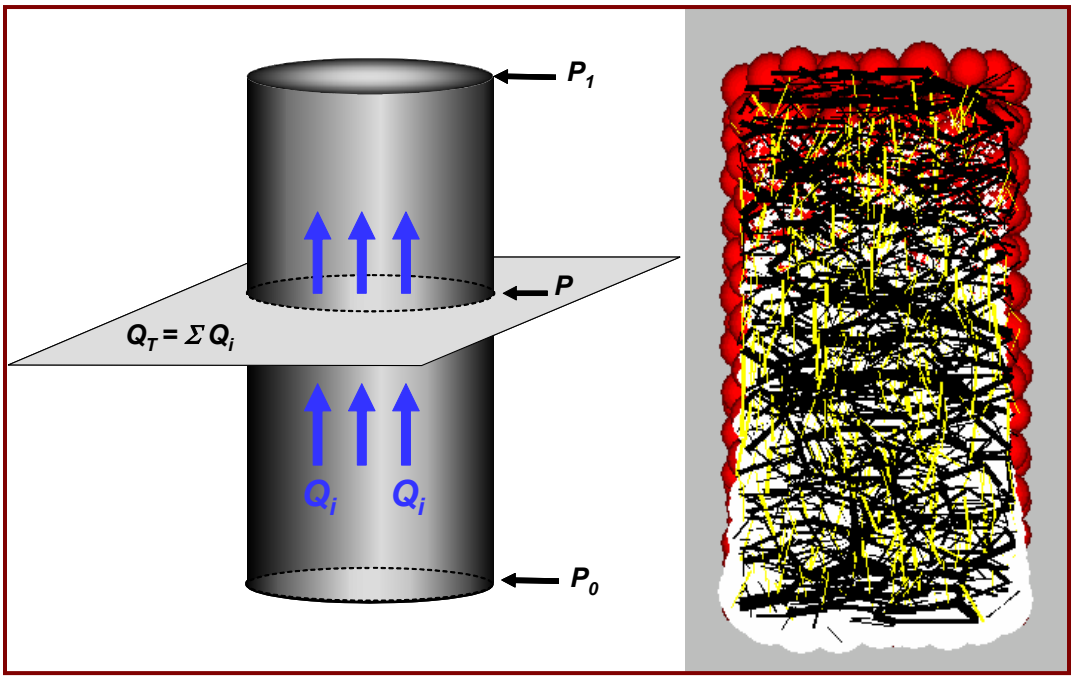

Figure 5-17. Schematic of the "virtual" plane used for permeability measurement (left); snapshot of the model during a permeability test (right)

For the permeability tests, the saturating fluid was assumed to be water; thus, the following fluid properties were used (Engineering toolbox, 2004):

$$\mu = 0.01\ Pa.s = 1\ cP$$
$$K_f = 2.15\ GPa = 312{,}000\ psi$$

PFC^{3D} assumes that the pipes connecting adjacent domains are perfectly straight cylindrical pipes, and that their hydraulic properties are defined by their conductivity factor, k. However, during this study, it was found that the standard

definition of k tended to produce excessively high values for permeability. Thus, a new definition was introduced here to account for the fact that the "pipes" linking contiguous pores are not straight conduits:

$$k = \beta \frac{a}{\mu} \qquad \text{(5.7)}$$

where β is a shape factor[67], a is the average pipe aperture, and μ is the fluid viscosity. The validation procedure was performed by varying the values of both a and β to match the permeability of Antler sandstone measured in the laboratory. Table 5.9 shows a summary of the input and results obtained during the validation process.

Test	INPUT		OUTPUT
	a ***(m)***	**β** ***(dimensionless)***	**Permeability** ***(Darcy)***
7-1	0.0100	0.050	0.289
7-2	0.0050	0.050	0.018
7-3	0.0450	0.050	118.550
7-4	0.0400	0.050	74.090
7-5	0.0045	0.005	1.210
7-6	0.0200	0.050	4.630
7-7	0.0150	0.050	1.459
7-8	0.0120	0.050	0.601
7-9	0.0110	0.050	0.423

Table 5-9. Summary of the tests performed for model permeability calibration.

[67] This factor accounts for the fact that the "pipes" are not straight but rather tortuous.

The application of the explicit solution scheme described by Eqns. (5.3) to (5.5) was not used at this stage of the study, i.e. constant load and pore pressure translate into constant pore volumes; and, hence, into constant permeability. The reported value of permeability for the Antler sandstone is about 300 md (Krishnan et al., 1994); thus, the input values of Test 7-9 were selected as the correct magnitudes of a and β for modeling the hydraulic behavior of the Anther sandstone. A complete listing of the FISH[68] routines used for this part of the study appears in Appendix B.

5.3.1.5 Comments of the validation of the model hydraulic properties

The original definition of the conductivity coefficient in Eqn. (5.3) was modified due to the fact that the obtained values of permeability for the model were unrealistically high[69]. This is likely to be consequence of the fundamental assumption, made in PFC^{3D}, that the pore throats may be considered as cylindrical pipes of constant diameter. In reality, the geometry of the pore network is rather irregular; thus, changes in pore throat diameter as well as tortuosity of the flow path would affect the overall permeability of the porous medium. To the knowledge of the author, a hydraulic calibration (such as the one described here)

[68] Exclusive programming language used by PFC^{3D}.
[69] In the order of thousands of darcies.

has never been attempted on DEM models. Hence, this is the first time limitations on the assumptions regarding the "pipe" network in PFC^{3D} have been exposed.

The calibration of the hydraulic properties of the model proved to be a difficult process as time-dependent processes affected the results. The approach explained in the last section for artificially imposing a steady-state flow to the model is recommended for future studies. It is also recommended performing the calibration of permeability as a function of stress, i.e. matching laboratory measured permeability obtained at different values of stress. This procedure could not be performed in this study as such measurements were not available.

5.3.2 Antler sandstone - Field model

For this part of the study, a parallelepipedic particle assembly was built; this shape was selected for convenience as a three-dimensional system of stress was to be applied to the model. The dimensions of this assembly were obtained by trying different combinations of values for length, width, and height. Two criteria were used for selecting the best set of values: *i)* the dimensions of the model had to ensure minimal boundary effects on the behavior of the model, and *ii)* the total number of particles obtained had to be as little as possible due to computational

limitations[70]. After a series of trials, the following set of values was selected for the model (see Fig. 5.18):

$$Height = 4.572\ m = 15.00\ ft$$
$$Width = 3.429\ m = 11.25\ ft$$
$$Length = 3.429\ m = 11.25\ ft$$

This geometry and dimensions gave a total of 1537 particles, which was considered manageable with the computer resources available throughout this study. In order to better represent stress conditions typically found in-situ, the model was assumed to be buried at a depth of 3,048 m (10,000 ft); hence, the complete stress field was defined as[71]:

$$\sigma_V = 68.96\ MPa = 10{,}000\ psi$$
$$\sigma_H = 58.62\ MPa = 8{,}500\ psi$$
$$\sigma_h = 51.72\ MPa = 7{,}500\ psi$$
$$P_P = 37.93\ MPa = 5{,}500\ psi$$

where σ_v is the total vertical stress, σ_H is the total maximum horizontal stress, σ_h is the total minimum horizontal stress, and P_p is the pore pressure. While constructing and running the model, it was found that working with such large values of stress increased the instability of the model, i.e. large values of pore

[70] The computer used throughout this study was a Pentium 4, with 1.7 GHz, and 540 MB RAM.
[71] The rock was assumed to be slightly overpressure (0.55 psi/ft), a condition of common occurrence in under-consolidated rock.

(interstitial) pressure increased the possibility of having particles separated from the model and "flying out" in space[72]. Thus, it was decided to work with the values of effective stress rather than with the magnitude of the total load. Therefore, the stress field used for the simulations was changed to:

$$\sigma_v^{'} = 31.03\ MPa = 4{,}500\ psi$$
$$\sigma_H^{'} = 20.69\ MPa = 3{,}000\ psi$$
$$\sigma_h^{'} = 13.80\ MPa = 2{,}000\ psi$$

where $\sigma_v^{'}$, $\sigma_H^{'}$, and $\sigma_h^{'}$ represent the magnitudes of the effective stresses in the vertical, minimum horizontal , and maximum horizontal directions, respectively. The model was run following a sequence composed of six main computer routines, described as follows:

1. *Hydrofrac1.DAT*: This program generated the walls that enclosed the space where the particles were to be created. Here, the magnitude of the stiffness was defined for the walls, the particles, and the inter-particle contacts. The porous medium was created by generating particles, inter-

[72] Large interstitial fluid pressure increases the chance of inter-particle bond breaking; this is especially critical for calculation stability if the broken bond is located close to the edges of the model.

particle bonds, and contacts within the previously defined walls (until a given value of porosity was achieved).

2. *Hydrofrac2.DAT*: The results obtained after running *Hydrofrac1.DAT* were loaded by this program, and the complete stress field (σ'_x, σ'_y, and σ'_z) was applied to the particle assembly. This process was made easier by selecting a parallelepipedic geometry for the model; thus, each load was applied perpendicular to a given face of the particle assembly. A particular load magnitude was achieved by means of displacing inwards all the particles located at the edge of the model.

3. *Hydrofrac3.DAT*: This routine deleted the walls in the model and fixed in space the particles located at the edges of the model. The walls were deleted to avoid creating "artificial" loads during the deformation process. For the same reason, the particles located on the faces of the assembly had to be fixed in order to avoid model rotation/displacement in space.

4. *Hydro_DOM_3.fis*: The domains and pipes defining the hydraulic network within the model were created by running this routine. The version of this program used during this study was provided in the manual

of PFC[3D] (Itasca Consulting Group, 2004), and no modifications were made to it at any stage.

5. *Hydro_DOM1_3.fis*: This program calculated the fluid flow at any point within the pipe network built by *Hydro_DOM_3.fis*. The original version of this routine, provided in the PFC[3D] Manual (Itasca Consulting Group, 2004), was improved to include key calculations, such as the volume of each individual pore, and its change at every timestep. It was also modified to impose a logarithmic pressure distribution, and to measure the overall model permeability during the calibration stage.

6. *Inject_Hydro.DAT:* By running this routine, a pressure differential was imposed at the wellbore created within the particle assembly. This pressure differential simulated the injection of fluid into an unconsolidated formation. The number and type of the cracks created due to fluid injection was monitored throughout the test; these are the results that were analyzed in order to describe the hydraulic fracturing processes occurring in poorly-consolidated sandstones. A complete listing of these FISH[73] programs is provided in Appendix C.

[73] Programming language used in PFC[3D].

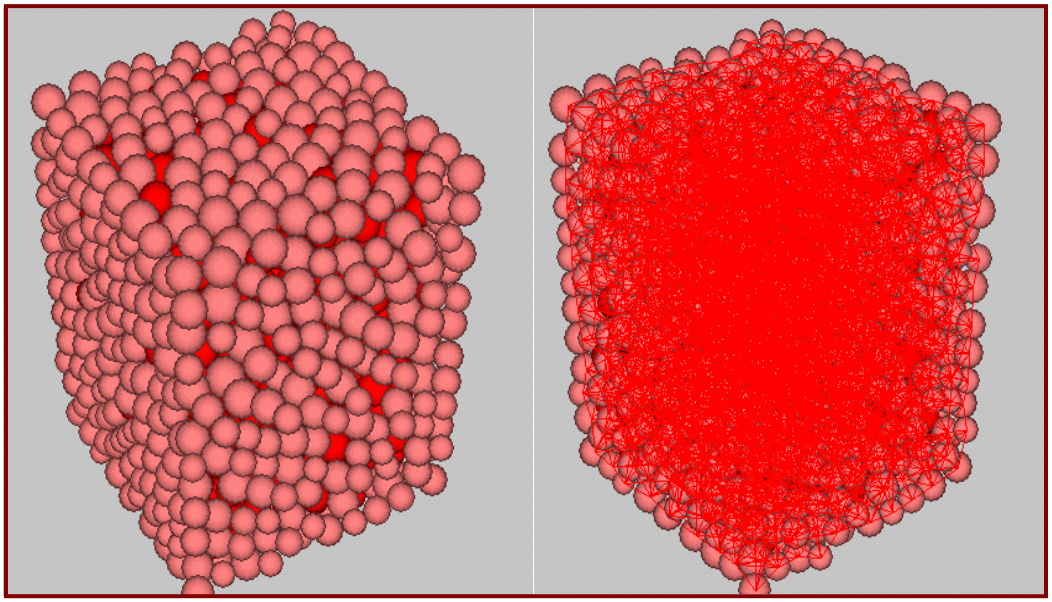

Figure 5-18. Snapshots of the field model used in this study: left, particle assembly; right, particle assembly + pipe network.

5.3.2.1 Testing and results

The main objective in this study was to evaluate the effect of fluid leak-off on the hydraulic fracturing process of unconsolidated formations. Fluid leak-off is dominated mainly by three variables: pressure differential, fluid viscosity, and formation permeability. In this particular study, the permeability of the rock was kept constant at a very high value (400 md approx.). On the other hand, the magnitudes of both fluid viscosity and pressure differential were varied over a wide range. For the case of fluid viscosity, the behavior of the model was evaluated with μ varying between 1 cP and 1,000 cP. Likewise, the pressure difference between the wellbore and the saturating fluid ranged between 0.689

MPa and 17.241 MPa (100 psi to 2,500 psi). Table 5.10 presents a listing of the values used for the parametric study evaluating the effects of changes in both fluid viscosity and pressure differential.

Parameter	**Evaluated values**			
Fluid viscosity, μ, cP	1	200	500	1,000
Pressure differential, ΔP, MPa (*psi*)	0.689 (*100*)	3.448 (*500*)	6.896 (*1,000*)	17.241 (*2,500*)

Table 5-10. Summary of the values of fluid viscosity and pressure differential evaluated in this study.

Rock failure may be induced in the field as consequence of changes in the effective stress affecting the formation solid frame and its bonds; these changes may be triggered by depletion or by fluid injection. The way the model in this study was set up allowed for two types of failure to occur. The first type of failure corresponds to tensile failure, as the strength of the inter-particle bonds is overcome by the tensile stress acting on them; this process is triggered by an increment in the pore pressure due to fluid injection. As the compressive stress acting on the particles is decreased by fluid injection, displacement perpendicular to the contacts may take place, creating the conditions for shear failure to occur. Thus, both tensile and shear failure were monitored throughout the injection tests

performed according to the conditions described in Table 5.10. The final count for the number of shear and tensile cracks obtained for each one of the tests is reported in Table 5.11.

	INPUT			OUTPUT				
Test number	ΔP, (*psi*)	ΔP, *MPa*	Viscosity, *cP*	Tensile cracks		Shear cracks		Shear / Tensile crack ratio
				number	percentage (%)	number	percentage (%)	
8-1	100	0.689	1	356	27.75	927	72.25	2.60
8-2	100	0.689	200	722	35.92	1288	64.08	1.78
8-3	100	0.689	500	680	38.27	1097	61.73	1.61
8-4	100	0.689	1000	690	38.83	1087	61.17	1.58
8-5	500	3.448	1	367	31.31	805	68.69	2.19
8-6	500	3.448	200	748	35.47	1361	64.53	1.82
8-7	500	3.448	500	700	37.61	1161	62.39	1.66
8-8	500	3.448	1000	683	38.57	1088	61.43	1.59
8-9	1,000	6.896	1	709	38.41	1137	61.59	1.60
8-10	1,000	6.896	200	757	36.06	1342	63.94	1.77
8-11	1,000	6.896	500	697	38.00	1137	62.00	1.63
8-12	1,000	6.896	1000	706	38.62	1122	61.38	1.59
8-13	2,500	17.241	1	809	41.02	1163	58.98	1.44
8-14	2,500	17.241	200	808	37.92	1323	62.08	1.64
8-15	2,500	17.241	500	835	40.32	1236	59.68	1.48
8-16	2,500	17.241	1000	810	40.97	1167	59.03	1.44

Table 5-11. Summary of the results obtained from the field model.

Under conditions of relatively low pressure differential, the fluid viscosity played an important role in determining not only the dominating type of failure but also its behavior over time. The shape of the curve representing the number of cracks also changed because of variations in fluid viscosity. For $\mu = 1\ cp$, the slope of the curves corresponding to the number of shear and tensile cracks increased

rapidly over time (Fig. 5.19). This behavior suggests that the fracturing process is rather unstable and that total sample failure eventually occurs. On the other hand, for μ = *1,000 cp* the lines behaved asymptotically, i.e. the slope of the lines tended to zero over time, suggesting that the fracturing process would tend to stabilize (Fig. 5.20). For intermediate values of fluid viscosity, the behavior was transitional as the initially asymptotic behavior became unstable after some time (see Fig. 5.21).

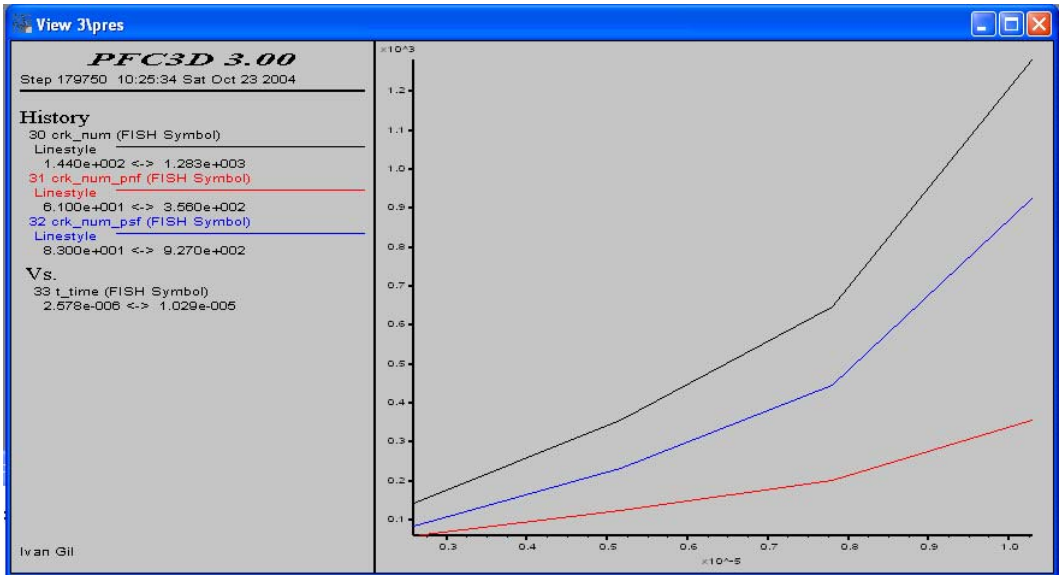

Figure 5-19. Number of cracks vs. time (red → tensile, blue → shear, black → tensile+shear), ΔP = 0.689 MPa= 100 psi & μ = 1 mPa.sec = 1 cP (Test 8-1).

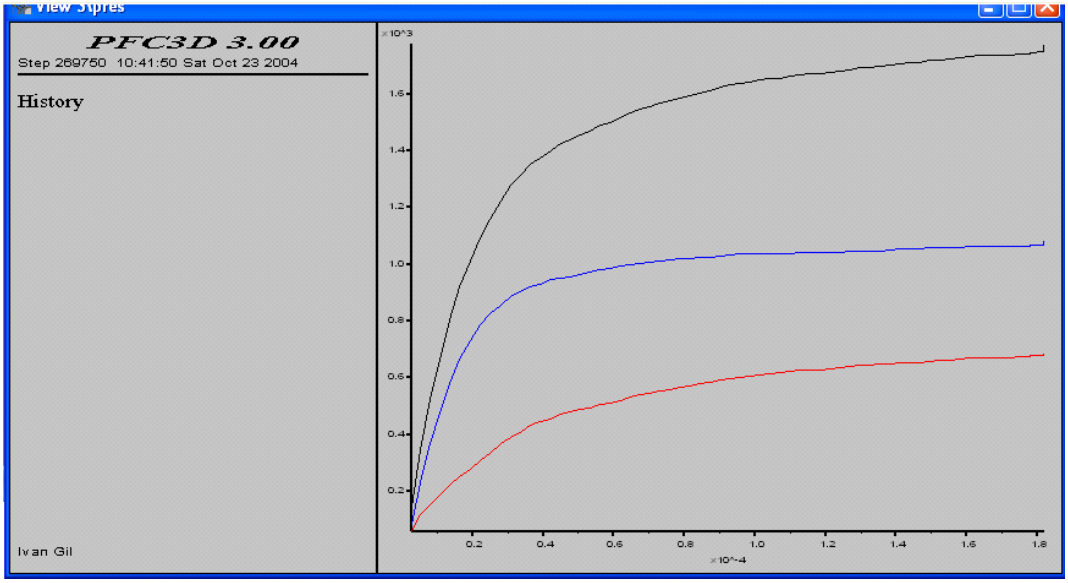

Figure 5-20. Number of cracks vs. time (red → tensile, blue → shear, black → tensile+shear), ΔP = 0.689 MPa= 100 psi & μ = 1,000 mPa.sec = 1,000 cP (Test 8-4).

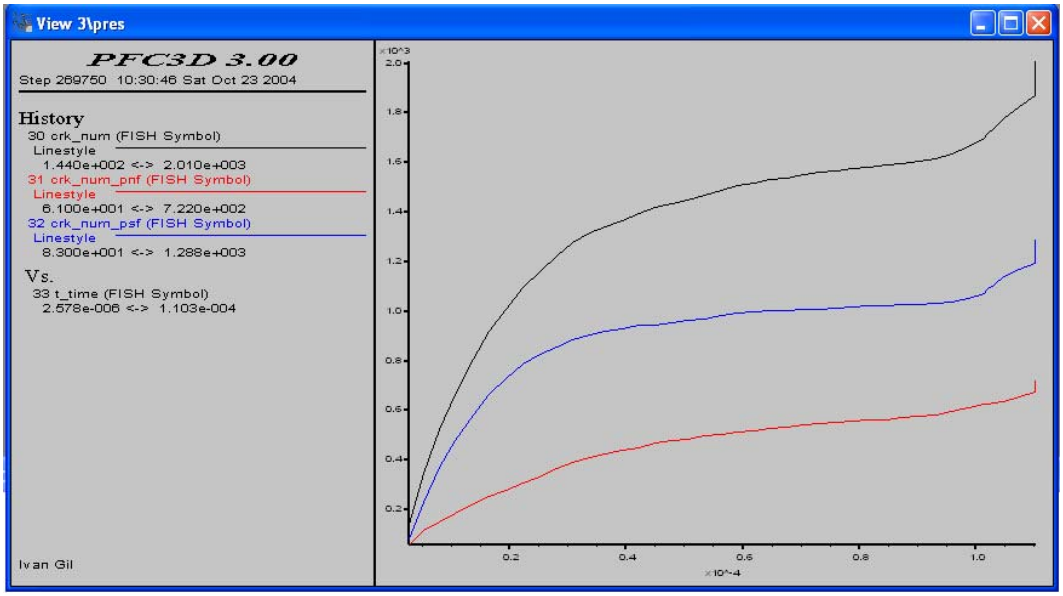

Figure 5-21. Number of cracks vs. time (red → tensile, blue → shear, black → tensile+shear), ΔP = 0.689 MPa= 100 psi & μ = 200 mPa.sec = 200 cP (Test 8-2).

Analysis of the results obtained in this part of the study allowed making several observations on the nature of the hydraulic fracturing process occurring within the model. It was observed that under conditions of relatively low values of pressure differential ($\Delta P \leq 3.448$ MPa = 500 psi), the percentage of created tensile cracks increased asymptotically as the injected fluid became more viscous. No further increment in the number of tensile cracks was found when fluid viscosity increased beyond 200 cP (Fig. 5.22). For large values of pressure differential ($\Delta P \geq 6.896$ MPa = 1,000 psi), the effects of changing fluid viscosity are small.

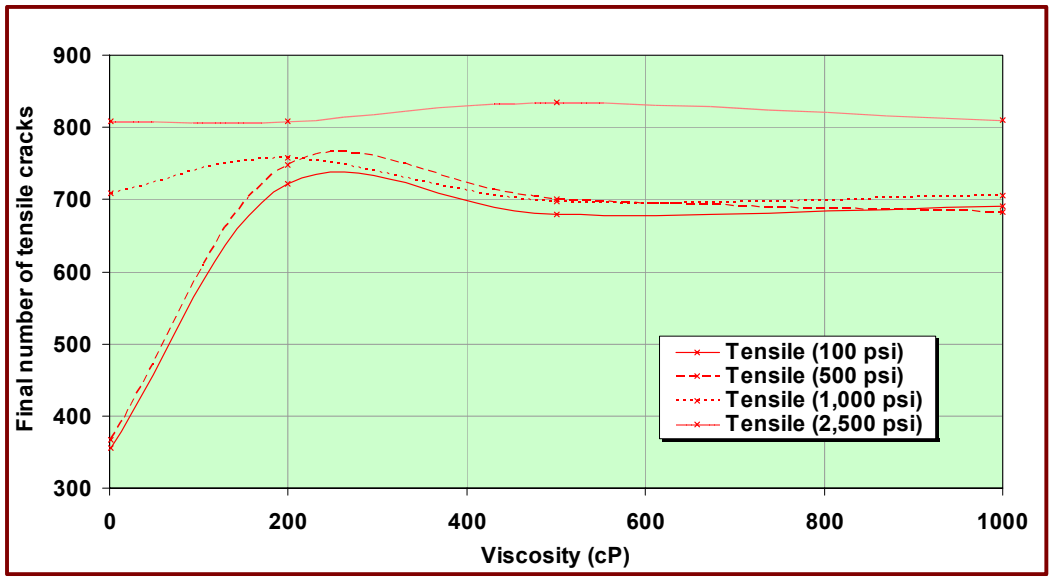

Figure 5-22. Final number of induced tensile cracks – field model.

On the other hand, the number of shear cracks created by fluid injection showed a mixed behavior as a function of fluid viscosity. For low magnitudes of viscosity, the number of shear cracks increased as the fluid became more viscous. However, the curves representing the number of shear cracks reached a maximum at values of viscosity of about 200 cP; after this point, the number of induced shear cracks decreased asymptotically as the fluid became more viscous (Fig. 5.23).

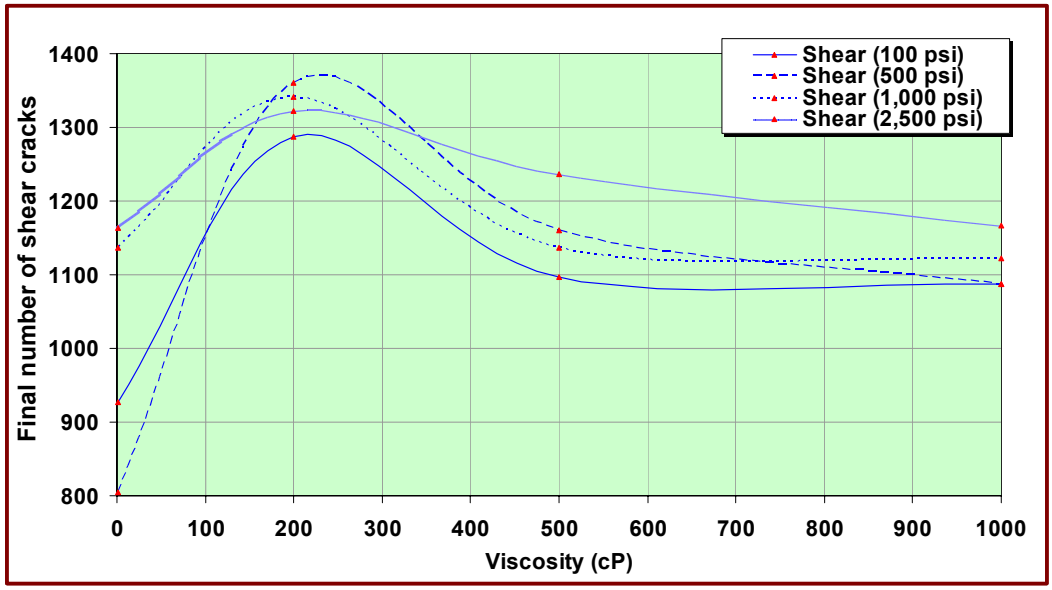

Figure 5-23. Final number of induced shear cracks - field model.

It was also apparent that the number of tensile fractures increased with the applied differential pressure (see difference in the curves in Fig. 5.22). This trend was

somewhat expected as increments in the pressure differential cause the pore pressure to build up more rapidly; hence, creating the conditions for tensile loads to develop. In general, the numbers of induced shear cracks increased as larger values of pressure differential were applied to the sample. However, the curves representing the different values of ΔP, crossed at several values of viscosity. This behavior may be explained by the fact that rising values of pore pressure tend to separate the particles in the model; thus, possibly creating additional normal loads in the direction of shear.

The relative importance of both the shear and tensile failure mechanisms is shown in Fig. 5.24. It was apparent that, for relatively low values of ΔP, the number of induced shear cracks decreased asymptotically with fluid viscosity. Conversely, at relatively low values of differential stress, the percentage of induced tensile cracks increased asymptotically as a function of fluid viscosity. The opposite behavior was observed when the applied differential stress was larger than 6.896 MPa (1,000 psi). Hence, the effect of fluid viscosity seemed to be overshadowed by the effect of the pressure differential when the magnitude of the latter was large, i.e. when $\Delta P \geq 6.896$ MPa = 1,000 psi. In this case, changes in fluid viscosity had little effect on the relative number of both shear and tensile cracks.

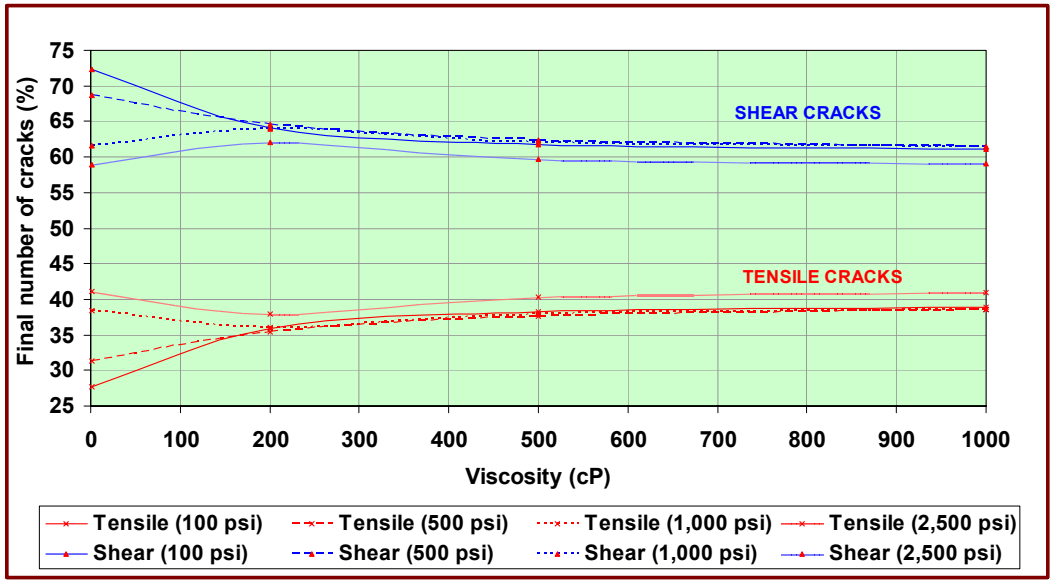

Figure 5-24. Final percentages of shear and tensile cracks induced by fluid injection.

5.3.2.2 Comments on the results obtained from the field model

The parameter values for the numerical experiments in this study (summarized in Table 5.10), were selected by considering the ranges of fluid viscosity and net pressure most commonly found in a hydraulic fracturing stimulation treatment. The results obtained from the field model allowed drawing several conclusions:

i) The shape of the curves representing the number of induced cracks changed as a function of the fracturing fluid viscosity (see Figs. 5.19 through 5.21). Low viscosity fluids (under low ΔP conditions) caused

the curves to be concave upwards, implying unstable crack propagation (see Appendix D). During these tests with low viscosity fluids, it was observed that most cracks were created all around the wellbore, forming a cylindrical cloud around it. Conversely, higher viscosity fluids ($\mu \geq$ 500 cP, regardless of the magnitude of ΔP) produced asymptotic behavior of the same curves; thus, suggesting a more stable crack propagation process. This would imply that in the field, the growth and shape of fractures created on a high leak-off environment would be difficult to control and predict. In addition, most of the cracks would tend to be created near the highest pressure differential zone, without any preferential orientation.

ii) The effect of pressure differential also was found to be important during the fracturing process. Under conditions of large ΔP (larger than 6.896 MPa or 1,000 psi), the effect of viscosity was marginal as all the experiments showed almost the same response, regardless of fluid rheology.

iii) In all the tests, the relative amount of induced shear fractures was always higher than the amount of cracks created by tensile load. The ratio of the number of shear cracks to the number of tensile cracks varied between 1. 44 (under high viscosity, high ΔP conditions) and 2.6 (for low viscosity, low ΔP situations). This conclusion would

imply that the failure mechanism dominating the hydraulic fracturing process in poorly consolidated formations is shear rather than tension, as has been traditionally accepted. It would also explain why the predicted amount of energy (ΔP) necessary for creating hydraulic fractures in unconsolidated rocks is generally much lower than what has been reported in the field.

Chapter 6

Conclusions

The following paragraphs outline the most important conclusions and observations that were reached, based on the literature review and the results obtained throughout this study:

Currently, hydraulic fracturing simulators assume that the value of the elastic parameters of the rock remain constant throughout the stimulation process, regardless of changes in the effective stress as well as in water saturation caused by fluid injection. There is sufficient experimental evidence that this is gross approximation, as the magnitudes of both Young's modulus and Poisson's ratio vary widely as function of both effective stress and rock fluid saturation.

Standard hydraulic fracturing simulators consider that the deformational behavior of the formations being fractured is fully characterized by the values of their Young's modulus and the minimum principal stress acting on them. The assumption of a constant Young's modulus is not particularly applicable in the case of unconsolidated rocksfor which the applied stress and also of the stress-

path followed during rock deformation strongly influence its value. According to results published by Franquet and Economides (1999), the magnitude of Young's modulus for an unconsolidated rock may decrease as much as 60% from its initial value when the corresponding loading stress path, K[74], is equal to zero. On the other hand, the value of Young's modulus may be increased by as much as 125% when the sample is subjected to a loading stress path equal to 1, i.e. both the confining pressure and the axial load are increased at the same rate (Fig. 2.31). Likewise, Poisson's ratio may experience large variations in magnitude as the conditions of stress and loading path are altered (Fig. 2.32). These variations on rock mechanical moduli may cause important changes on the geometry of hydraulically induced fractures in poorly-consolidated materials. Figures 2.55 and 2.56 show a KGD model of a hydraulic fracture, and its expected geometry, in an unconsolidated material with stress-sensitive mechanical properties. Under the same pumping schedule and leakoff conditions, the same fracture volume (shaded area underneath the curve) is to be created for both constant and stress sensitive elastic materials. From this figure, it can be noticed that fractures induced in stress-dependent Young's modulus rocks will tend to be shorter and wider than those created in constant Young's modulus formations.

[74] The stress path, K is defined as: $K = (d\sigma'_3 / dt) / (d\sigma'_1 / dt)$

The effects of changes in fluid saturation on rock strength have long been recognized. It has been observed, from experimental results, that increments in water saturation may cause dramatic reductions in rock strength and also important changes in the elastic moduli of the material (E normally decreases while v tends to increase). Despite the mounting experimental evidence about fluid-triggered weakening processes in rocks, there is still controversy on the causes and severity of each of these mechanisms. Reduction in the surface free energy, as a result of fluid saturation, is considered to be one of the main processes affecting the rock strength and deformation behavior. By definition, the free surface energy is the amount of energy necessary to create a surface unit; thus, it is more related to cracking and fracturing of materials. This may be the case in consolidated formations, where microcracks are formed and extended as the applied stress increases. Nonetheless, processes such as matrix swelling and dissolution, and grain rearrangement also play an important role in the rock strength alteration observed in unconsolidated formations. It has been found that in highly-permeable, weakly-consolidated formations the magnitude of the water weakening effect is strongly influenced by the clay content of the rock. There is also a lack of understanding on the effect of increments in saturation of non-polar fluids, as they also seem to cause rock strength reduction, although to a lesser degree of severity. The need for more comprehensive fluid weakening models specifically designed for weakly-consolidated rocks is becoming more critical as

more unconsolidated hydrocarbon reservoirs are experiencing increments in water saturation due to water injection and depletion.

Stress relaxation during coring, handling and testing procedures has been found to cause important permanent changes in the porosity and mechanical behavior of some core samples. Alterations on the in-situ stress field applied on a rock, due to coring, have the potential to cause permanent "remolding" or rearrangement of the rock fabric and of its pore structure; thus, a new material may be created. The magnitudes of the rock properties measured on this altered material may not necessarily represent the behavior of the original in-situ formation. Techniques such as the application of a axial bias stress, inside the core barrel, show a great potential for core damage prevention. The existence of this artificial stress restrains the expansion of the rock in the axial direction, whereas the lateral expansion of the sample is limited by the core barrel itself. Nevertheless, some knowledge about the in-situ stress and the strength of the formation is necessary, prior to coring, in order to optimize the magnitude of the axially applied bias stress (if the bias stress is too large, compressive failure may be induced within the specimen).

Core damage may also be induced in a core due to freezing/thawing processes. It has been found that, even at temperatures well below 0° C (32° F), some of the

saturating water may remain liquid. This liquid phase has the ability of migrating thorough the rock and collecting as ice somewhere within the pore network. These ice lenses are believed to be responsible for extreme rock expansion, sometimes as high as 100% of the initial rock volume. The relative amount of unfrozen water is a function of the amount of fines in the rock, its pore size distribution, and the clay mineralogy. Even at frost temperatures, clays have the tendency to keep relatively large amounts of unfrozen water within their pores; whereas in sands, the amount of liquid water is almost non existent.

In order for "frost heave" to occur, water needs to be supplied to the system at rates large enough to sustain the ice lenses growth. This is only possible if a large source of unfrozen water is accessible; either from unfrozen water saturating the rock or from the environment. The amount of unfrozen saturating water in "clean" sand cores is rather limited (see Fig. 3.10); as the attraction forces between the grains and the water phase are very small due to the small interfacial contact area. However, in the case of rocks with high clay content, their freezing behavior is more difficult to predict because relatively larger amounts of unfrozen water may be available within the pores for migrating through sample. On the other hand, higher clay content translates into lower rock permeability, which tends to hinder water flow; hence, slowing ice lenses growth (i.e. it is more difficult for the water supply to move through the rock and reach the ice lenses).

For these reasons, frost heaving as seeing on in-situ soils appears to be rather improbable during core freezing operations (unless a large water source is in contact with the sample during the cooling process). Nonetheless, a definitive conclusion cannot be reached at this time due to the lack of published experimental evidence. More specific studies on the effect of freezing on the mechanical properties of cores as function of the clay content are critical to clarify this issue. This would also bring more confidence to the laboratory results that need to be used in the rock characterization process.

As frost heaving[75] is probably not an issue in core freezing procedures, the normal expansion of water due to freezing, which is about 9% of its initial volume, could change the mechanical properties of rock. The effects of changes in the freezing direction on the strength of the rock have been marginally studied. It has been reported that the mechanical response of frozen samples change probably due to alterations in the freezing directions on the samples. Radially frozen samples seemed to be weaker than those frozen in axial direction. The cause of this discrepancy appears to be the presence of stress caused by water expansion during the freezing process. In the radial case, the freezing front advances inwards increasing the pore pressure and locking the saturating fluids within the sample. This condition alters the stress field exerted on the rock and may cause material

[75] Extreme rock expansion due to freezing, sometimes it could be as much as 100% of the rock thawed volume.

"remolding". In contrast, the samples being frozen in axial direction, contract slightly and expel part of the saturating fluids during the process; eliminating any stress induced by the freezing procedure. The results published by Côté et al. (2000) and Côté (2003), were obtained under frozen conditions only, and no comparison to the unfrozen mechanical responses of the specimens was performed. Thus, their findings are inconclusive and additional research on the issue is needed.

The results of the validation process for the mechanical properties of the model, allowed drawing several conclusions:

The main mineral component of the grains in sandstone is quartz. Laboratory tested samples of quartz show measured values of Young's modulus of about 94.3 GPa ($13.6*10^6$ psi), and magnitudes of shear modulus of up to 34.0 GPa ($4.9*10^6$ psi) (University of Kansas, 2004). The selected values for the normal and shear stiffness of the particles were 94.0 GPa ($13.6*10^6$ psi) and 40.0 GPa ($5.8*10^6$ psi), respectively. The differences between these two sets of values were only about 0.3% for the Young's modulus and 18% for the shear modulus; these discrepancies could be attributed to the presence of minerals other than quartz in the rock being modeled (i.e. in the Antler sandstone). Nonetheless, it was considered that the values found during the validation process for the normal and

shear stiffness of the particles were in good agreement with the magnitudes measured in the laboratory.

The radius of the parallel inter-particle bonds obtained from the validation procedure was 0.15, i.e. 15% of the radius of the smaller of the two spheres forming the contact. Results from electronic microscopy images of Antler sandstone showed rounded grains with cementing material at the contacts. It is difficult from the pictures to calculate the radius of the bonds, as it is evident that the bonds vary in size and thickness throughout the rock. Relatively large bonds were found between the grains (Fig. 5.12a), as well as very small coatings at the contact (Fig. 5.12b). Hence, it was concluded that the value used in the simulations (i.e. 0.15) was acceptable for the purposes of this study.

The values selected from the simulation runs for the normal and shear stiffness of the contacts were 112.0 GPa ($16.24*10^6$ psi) and 52.6 GPa ($7.63*10^6$ psi). At a first glance these values seem to be abnormally high. However, a closer look at the mineral components of the cementing material revealed the presence of significant amounts of silica, aluminum, and iron; traces of magnesium, potassium, calcium, and titanium were also reported (see Fig. 5.13). Reported values for the Young's modulus for the most important minerals in the inter-granular cement ranged between 69 and 196 GPa ($10.00*10^6$ to $28.13*10^6$ psi).

Figure 5.14 presents a comparison of the values of stiffness used for the parallel contacts in the model and the values of the stiffness of the mineral components found in the cement of the Antler sandstone. It was apparent that the simulated model had stiffness properties well within the ranges expected for the real rock.

Likewise, the inter-particle strength parameters in the model (i.e. shear and normal strength) were compared to the shear and tensile strength of the mineral components of the cementing material. In this case, it was also found that the values of normal and shear strength for the inter-particle contacts in the model fell within the limits defined by the mechanical properties of the rock components (see Fig. 5.15).

In the future, calibration of the mechanical properties of the model may be performed more efficiently by using initial "guessing" values of inter-particle contact stiffness and strength determined by the mineralogical composition of the rock being modeled.

The original definition of the conductivity coefficient in Eqn. (5.3) was modified due to the fact that the obtained values of permeability for the model were unrealistically high. This is likely to be the consequence of the fundamental assumption, made in PFC^{3D}, that the pore throats may be considered as cylindrical

pipes of constant diameter. In a real rock, the geometry of the pore network is rather irregular; thus, changes in pore throat diameter as well as tortuosity in the flow path would affect the overall permeability of the porous medium. To the best knowledge of the author, a hydraulic calibration (such as the one described here) has never been attempted on DEM models. Hence, this is the first time limitations on the assumptions regarding the "pipe" network in PFC^{3D} have been exposed.

The calibration of the hydraulic properties of the model proved to be a difficult process as time-dependent processes affected the results. The approach explained in the last section for artificially imposing a steady-state flow to the model is recommended for future studies. It is also recommended performing the calibration of permeability as a function of stress, i.e. matching laboratory measured permeability obtained at different values of stress. This procedure could not be performed in this study as such measurements were not available.

The parameters chosen for the numerical experiments in this study (summarized in Table 5.10), were selected by considering the ranges of fluid viscosity and net pressure most commonly found in a field hydraulic fracturing treatment. The results obtained from the hydraulic fracturing tests allowed drawing a number of conclusions:

The shape of the curves representing the number of induced cracks changed as a function of the fracturing fluid viscosity (see Figs. 5.19 through 5.21). Low viscosity fluids (under low ΔP conditions) caused the curves to be concave upwards, implying unstable crack propagation (see Appendix D). During these tests with low viscosity fluids, it was observed that most cracks were created all around the wellbore, forming a cylindrical cloud around it. Conversely, higher viscosity fluids ($\mu \geq 500$ cP, regardless of the magnitude of ΔP) produced asymptotic behavior of the same curves; thus, suggesting a more stable crack propagation process. This would imply that in the field, the growth and shape of fractures created on a high leak-off environment would be difficult to control and predict. In addition, most of the cracks would tend to be created near the highest pressure differential zone, without any preferential orientation.

The effect of pressure differential also was found to be important during the fracturing process, at least in the case of Antler sandstone. Under conditions of large ΔP (larger than 6.896 MPa or 1,000 psi), the effect of viscosity was marginal as all the experiments showed almost the same response, regardless of fluid rheology.

In all the numerical tests performed here, the relative amount of induced shear fractures was always higher than the amount of cracks created by tensile load.

The ratio of the number of shear cracks to the number of tensile cracks varied between 1. 44 (under high viscosity, high ΔP conditions) and 2.6 (for low viscosity, low ΔP situations). This conclusion would imply that the failure mechanism dominating the hydraulic fracturing process in poorly consolidated formations is shear rather than tension, as has been traditionally accepted. It would also explain why the predicted amount of energy (ΔP) necessary for creating hydraulic fractures in unconsolidated rocks is generally much lower than what has been reported in the field.

The modeling effort presented here allows fracture propagation to be a direct consequence of the interaction of shear and tensile microcracks induced in the material during the injection process. Thus, a priori assumptions on the final geometry of the macro-scale fracture were not introduced in this model. For the case of Antler sandstone, shear microcracks seem to have a dominant role during the failure process; thus, a "normal" planar macro-scale fracture was never formed. A "process" zone around the wellbore was found instead. These results suggest that non-planar features encountered in hydraulic fractures in the field could be a consequence of the interaction of shear microcracks created in a zone around the "main" fracture plane defined by tensile failure.

It should be emphasized that the conclusions obtained during this study strictly apply only to Antler sandstone; however, the behavior described here suggests that unconsolidated rocks behave in similar fashion. Thus, it is recommended that more modeling is performed for other poorly consolidated formations in order to check if some of the "discovered" differences (with respect to consolidated formations) can be generalized.

Questions related to the fact that several combinations of inter-particle stiffness/strength parameters could produce the same deformation behavior for the overall samples were not addressed in this study. The possibility of having non-unique solutions during the calibration process exists; however, it was considered that given the number of parameters being matched, the probability of having such problems was small.

Chapter 7

Recommendations

The effects of changes in the freezing direction on the strength of the rock have only been marginally studied despite the fact that they may have a great influence on how to obtain a representative sample from an unconsolidated formation. It has been reported that the mechanical response of frozen samples changes due to alterations in the freezing direction of the sample. However, no comparison between the mechanical response of samples before and after a freezing/thawing cycle has been published. Thus, additional research and laboratory measurements are needed in order to fully understand the effect of freezing on porous media.

It has been proven that coring-induced stress relaxation may cause permanent alteration of the rock mechanical properties. The severity of these changes is a function of the initial rock strength: weak rocks show the highest degree of sensitivity. Thus, it is recommended to implement techniques such as the application of a bias stress to reduce the impact of stress relaxation on the core in order to improve its representativity.

Due to computational constraint, the model proposed in this study had some limitations on the number of particles and overall size it could handle. The availability of faster and more powerful computers brings the possibility of creating larger and more realistic models in which boundary effect will definitively not be an issue. It is also recommended to run the model for a larger number of steps in order to more closely represent field situations.

The necessity of running a field case with data from a real hydraulic fracturing stimulation job would allow for further verification and validation of the model. It would also bring the possibility of creating a commercial hydraulic fracturing simulator specifically tailored for poorly consolidated formations.

In this study, phenomena such as creep and variation of the mechanical properties of the model with saturation were not included. However, there is no theoretical reason why these processes could not be included in future DEM models. Creep may be accounted for if contact stiffness is defined as a time-dependent function of stress. Similarly, changes in mechanical properties due to alterations in fluid saturation may be accounted for if both contact stiffness and strength are defined as function of fluid saturation instead of being assumed constant.

One of the main assumptions in PFC^{3D} is that the particles are rigid bodies that are not allowed to break. In real life however, this may not be always the case as some sand grains (or grain clumps) may fail during the rock deformation process, especially if the inetrgranular cement is unexpectedly strong. This apparent limitation may be overcome if values of strength are used as stress limits for the load being applied to each particle.

During this study, only the final number of cracks being created was used for comparison purposes; however, it would be desirable to study the variation on the number of cracks over time to learn more about the fracture propagation process.

In this work, the volume of a given domain (i.e. pore space) was calculated as the volume of the tetrahedron defined by the center of each one of the four particles forming the domain, thus neglecting a small space occupied by the particles themselves. Additional effort is needed to avoid this limitation and to link the value of the pipe aperture to the geometry of the domain themselves. In the current version of the program, it may be set to a given value regardless of any consideration on the particle and pore size distributions.

The conclusions obtained during this study strictly apply only to Antler sandstone; however, the author believes that the behavior described here suggests

that unconsolidated rocks behave in similar fashion. Thus, it is recommended that similar efforst be made in modeling other poorly consolidated formations in an attempt to generate a database and be able to extend or refute some of the conclusions reached in this dissertation.

References

1. Abou-Sayed, A.S., (1978): "An Experimental Technique for Measuring the Fracture Toughness of Rock under Downhole Stress Condition", *VDI-Berichte*, **v.** 313: pp. 819-824.
2. Abou-Sayed, A.S., Sinha, K.P., and Clifton, R.J. (1984): "Evaluation of the Influence of In-Situ Reservoir Conditions on the Geometry of Hydraulic Fractures Using a 3D Simulator", Part 1-Technical Approach SPE 12877, Part 2- Case Studies SPE 12878, presented at the SPE/DOE/GRI Unconventional Gas Recovery Symposium, Pittsburg, May 13-15.
3. Addis, M.A., Cauley, M.B., and Kuyken, C., (2001): "Brent In-Fill Drilling Programme: Lost Circulation Associated with Drilling Depleted Reservoirs", SPE/IADC paper 67741, presented at the SPE/IADC Drilling Conference, Amsterdam, The Netherlands, February 27 - March 1.
4. American Society for Testing and Materials (ASTM), (1990): *Annual Book of ASTM Standards, Vol. 4.08, Soil and Rock, Dimension Stone, Geosynthetics*, ASTM Designation C666-84, Philadelphia, PA, pp. 314-319.
5. Arakawa, K., (1966): "Theoretical Studies of Ice Segregation in Soil", *Jour. Glaciology*, **Vol. 6**, No. 44, pp. 255-260.
6. Atwater, G.I., and Miller, E.E., (1965): "The Effect of Decrease in Porosity with Depth on Future Development of Oil and Gas Reserves in South Louisiana", *Bull. Am. Assoc. Petrol. Geol*., **v 49**, 334 (Abs).
7. Avseth, P.; Dvorkin, J.; Mavko, G.; and Rykkje, J., (2000): "Rock physics diagnostic of North Sea sands; link between microstructure and seismic properties", *Geophysical Research Letters*, **vol.27**, no.17, pp.2761-2764, 01 September.
8. Baud, P., Zhu, W., and Wong, T.F., (2000): "Failure Mode and Weakening Effect of Water on Sandstone", *J.Geophy. Research*, **v 105**, Solid Earth (B7), pp. 16,371-16,389.
9. Berardi, R., Passalacqua, R., Scavia, C., and Forlatti, F., (1994): "Translational Slope Stabilities in Weak Rock", Rock Mechanics, Nelson & Laubach (eds.), proceedings of the 1st North American Rock Mechanics Symposium, The University of Texas, Austin, TX, June 1-3, pp. 859-865.
10. Beskow, G., (1947); "Soil Freezing and Frost Heaving with Special with Special Applicaton to Roads and railroads", Swedish Geological Society, Series C, No. 375, 26th Year Book N0.3, 1935, (Osterberg, J.O., Trans), Technological Institute, Northwestern Univ., Evanston, Il, pp. 14-21.

11. Bowers, G.L., (2002): "Detecting High Overpressure", *The Leading Edge*, **v.21**, pp.174-177.
12. Boyd, G.E., and Livingston, H.K., (1942): "Adsorption and Energy Changes at Crystalline Solid Surfaces", *Am. Chem. Soc. Jour*., **v. 71**, pp.581-595.
13. Bratli, R.K., and Risnes, R., (1981): "Stability and Failure of Sand Arches", *Society of Petroleum Engineers Journal*, **v. 21**, pp. 236-248.
14. Bratton, T.R., Rezmer-Cooper, I.M., Desroches, J., Gille, Y.-E., Li, Q., and McFayden, M., (2001): "How to Diagnose Drilling-Induced Fractures in Wells Drilled with Oil-Based Muds with Real-Time Resistivity and Pressure Measurements", SPE/IADC paper 67742, presented at the SPE/IADC Drilling Conference, Amsterdam, The Netherlands, February 27- March 1.
15. Brignoli, M., Fanuel, P., Holt, R.M., and Kenter, C.J., (1996): "Effects of Core Quality of a Bias Stress Applied During Coring", SPE/ISRM paper 47262, presented at the 1998 SPE European Rock Mechanics Meeting, Trondheim, Norway, July, 8-10.
16. Brignoli, M., Fanuel, P., Holt, R.M., and Kenter, C.J., (1998): "Effects on Core Quality of a Bias Stress Applied During Coring", SPE/ISRM paper 47262, presented at the SPE/ISRM Eurock 98, Trondheim, Norway, July 5-10.
17. Broek, D., (1986): *Elementary Fracture Mechanics*, Kluwer Academic Publishers, 4th Ed.(rev).
18. Bruno, M.S., (1992): "Subsidence-Induced Well Failure", *SPEDE*, June, pp.148.
19. Bruno, M.S., (2002): "Geomechanical and Decision Analyses for Mitigating Compaction-Related Casing Damage", *SPE Drilling and Completion*, September, pp. 179-188.
20. Bruno, M.S., Bovberg, C.A., and Nakagawa, F.M., (1991): "Anisotropic Stress Influences on the Permeability of Weakly-Cemented Sandstones", Rock mechanics as a multidisciplinary science; proceedings of the 32nd U.S. symposium, Roegiers, Jean-Claude (ed.), Proceedings - Symposium on Rock Mechanics, **vol.32**, pp.375-383.
21. Chan, A.W., and Zoback, M.D., (2002): "Deformation Analysis in Reservoir Space (DARS): A Simple Formalism for Predicting Reservoir Deformation with Depletion", SPE/ISRM paper 78174, presented at the OilRock SPE/ISRM Rock Mechanics Conference, Irving, Texas, October 20-23.
22. Chang, C.T., and Zoback, M.D., (1998): "Viscous Rheology and State of Stress in Unconsolidated Sands", SPE/ISRM paper 47401, presented at the SPE/ISRM Eurock 98, Trondheim, Norway, July 8-10, pp. 465-473.
23. Chhajlani, R., Zheng, Z., Mayfield, D., and MacArthur, B, (2002): "Utilization of Geomechanics for Medusa Filed Development, Deepwater

Gulf of Mexico", SPE paper 77779, presented at the SPE Annual Technical Conference and Exhibition, San Antonio, Texas, September 29 - October 2.
24. Chudnovsky, N., (1984): *Crack Layer Theory*, NASA Report 17463, Case Western University, Cleveland, Ohio.
25. Chudnovsky, N., Fan, J., Shulkin, Y., Dudley, J.W., Shlyapobersky, J., and Shraufnagel, R., (1996): "A New Hydraulic Fracture Tip Mechanism in a Statistically Homogeneous medium", paper SPE 36442, presented at the SPE Annual Technical Conference and Exhibition, Denver CO, October.
26. Cleary, M.P., Wright, C.A., and Wright, T.B., (1991): "Experimental and Modeling Evidence for Major Changes in Hydraulic Fracturing Design and Field Procedures", paper SPE 21494 presented at the SPE Gas Technology Symposium, Houston, Texas, January 23-25.
27. Clifton, R.J., and Abou-Sayed, A.S., (1981): "A Variational Approach to the Prediction of the Three-Dimensional Geometry of Hydraulic fractures", SPE/DOE paper 11627, presented at the Low permeability Gas Reservoirs Symposium, Denver, March.
28. Colback, P.S.B., and Wiid, B.L., (1965): "The Influence of Moisture Content on the Compressive Strength of Rocks", Proc. 3rd Canadian Rock Mechanics Symposium, pp. 65-83.
29. Côté, H., (2003): *Comportement Thermo-Hydro- Mécanique de Geomatériaux Poreux – Approches Expérimentales et Numériques*, Ph.D. Dissertation, Université Catholique de Louvain, Faculté de Sciences Appliquées, Unité de Génie Civil et Environnemental, Louvain-La-Neuve, Belgium.
30. Côté, H., Thimus, J.F., Rijkers, R., and Naaktgeboren, M., (2000): "Soil Behavior During Artificial Freezing – Part I: Frost Heaving 3D tests", Proc. of the International Symposium on Ground Freezing and Frost Action in Soils, Louvain-La-Neuve, Belgium, September 11-13., pp. 69-74.
31. Cottrell, A.H., (1964): *The Mechanical Properties of Matter*, New York, John Wiley and Sons, 430 p.
32. Crockett, A.R., Okusu, N.M., and Cleary, M.P., (1986a): "A Complete Integrated Model for Design and Real-Time Analysis of Hydraulic Fracturing Operations", SPE paper 15069, presented at the 56th California regional Meeting of the SPE, Oakland, California, April 2-4.
33. Crockett, A.R., Vo, H., and Cleary, M.P., (1986b): "Studies of Fluid Flow, Heat Transfer and Induced Stresses in and Around Underground Fractures", Report No. REL-84-1, MIT Resource Extraction laboratory, March.
34. Cundall, P.A., (1974): "A Computer Model for Rock – Mass Behavior using Interactive Graphics for the Input and Output of Geometrical Data", Report MRD-2-74 prepared at The University of Minnesota under Contract number DACW 45-74-C-006, for the Missouri River Division, US Army Corps of

Engineers, available from National Technical Information Service- Report number AD/A-001 602.
35. Cundall, P.A., and Strack, O.D.L., (1979): "A Discrete Numerical Model for Granular Assemblies", *Géotechnique* **29**, No.1, pp. 47-65.
36. Dale, B.A., Narahara, G.M., Stevens, R.M., (1996): "A Case History of Reservoir Subsidence and Wellbore Damage Management in the South Belridge Diatomite Field", SPE paper 35658, presented at the 1996 SPE Western Regional Meeting, Anchorage, Alaska, May 22-24.
37. Dale, B.A., Narhara, G.M., and Stevens, R.M., (1996): "A Case History of Reservoir Subsidence and Wellbore Damage Management in the South Belridge Diatomite Field", prepared for presentation at the SPE Western Regional Meeting held in Anchorage, Alaska, May 22-24.
38. Dash, J.G., Haiying, F., and Wettlauffer, J.S., (1995): "The Premelting of Ice and its Environmental Consequences", *Rep.Prog.Phys*. **58**, 115-67.
39. Davis, N., (2001): *Permafrost: A Guide to Frozen Ground in Transition*, University of Alaska Press, Fairbanks, Alaska, 351 p.
40. Deere, D.U., and Miller, R.P., (1966): "Engineering Classification nad Index Properties for Intact Rock", Univ. of Illinois Contract AF 29(601)-6319, Tech Report AFWL-TR-65-116.
41. Domenico, S.N., (1977): "Elastic Properties of Unconsolidated Porous Sand Reservoirs", *Geophysics*, **v.42**, pp. 1339-1368.
42. Dudley, J.W., Myers, M.T., Shew, R.D., and Arasteh, M.M., (1998): "Measuring Compaction and Compressibilities in Unconsolidated Reservoir Materials by Time-Scaling Creep", SPE Reservoir Evaluation & Engineering, October, pp. 430-437.
43. Dusseault, M.B., and Santarelli, F.J., (1989): "A Conceptual Model for Massive Solids Production in Poorly-Consolidated Sandstones", Rock at Great Depth, Maury & Fourmaintraux (eds.), pp. 789-797.
44. Dusseault, M.B., Bruno, M.S., and Barrera, J., (1998): "Casing Shear: Causes, Cases, Cures", SPE paper 48864, presented at the 1998 SPE International Conference and Exhibit, Beijing, China, November 2-7.
45. Dyke, C.G., and Doberiner, L., (1991): "Evaluating the Strength and Deformability of Sandstones", *Q. J. Engng. Geol*., **v 24**, pp. 123-134.
46. Earlougher, R.C., (1977): *Advances in Well Test Analysis* – SPE Monograph Series, Society of Petroleum Engineers, Dallas, TX.
47. Economides, M.J., Oligney, R.E., and Valkó, P., (2002): *Unified Fracture Design*, Orsa Press.
48. Edwards, S.T., Bratton, T.R., Standifird, W.B., (2002): "Accidental Geomechanics", SPE paper 78205, presented at the SPE/ISRM OilRock, Rock Mechanics Conference, Irving, TX, October 20-23.

49. Efunda, (2004): Engineering Fundamentals Website, url: http://www.efunda.com/materials/common_matl/Common_Matl.cfm?MatlPhase=Solid&MatlProp=Mechanical#Mechanical
50. Engineering Toolbox, (2004): url: www.engineeringtoolbox.com
51. Fahrenthold, E.P., (1984): "Elastic and Plastic Stresses in a Porous Medium Containing Spherical and Cylindrical Cavities", PhD. Thesis, Rice University, Houston.
52. Fahrenthold, E.P., and Cheatham, J.B. Jr., (1986): "Incipient Yielding and Solids Production for Perforated Casing Completions", *Journal of Energy Resources Technology*, **v. 108**, December, pp. 321-325.
53. Fan, Y., White, D.E., Aimar, A., and Satyagraha, M.T., (2001): "Frac/Pack Modeling for High Permeability Viscous Oil Reservoirs of the Duri Field, Indonesia", *SPE Production & Facilities,* August, pp. 189-196.
54. Fatt, I., (1958): "Compressibility of sandstones at low to moderate pressures", *Bulletin of the American Association of Petroleum Geologists*, **vol.42**, no.8, pp.1924-1957, Aug 1958
55. Finkbeiner, T., and Zoback, M.D., (1998): "In-Situ Sress, pore pressure, and Hydrocarbon Migrations in The South Eugene Island Field – Gulf of Mexico", SPE paper 47212, presented at the 1998 SPE European Rock Mechanics Meeting, Trondheim, Norway, July, 8-10.
56. Fitzner, B., (1990): "Porosity Analysis, a Method for the Characterization of Building Stones in Different Weathering States", Proc. of Engineering Geology of Ancient Works, Monuments and Historic Sites, Marinos, P.G. & Koukis, B.S. (eds.), Balkema, Rotterdam, pp. 2031-2037.
57. Fjær, E., (1999): "Static and Dynamic Moduli of Weak Sandstones", Rock Mechanics for Industry; Amadei, Kranz, Scott & Smeallie (eds.), proceedings of the 37th U.S. Rock Mechanics Symposium, Vail, Colorado, **vol. 2**, pp. 675-681.
58. Fjær, E., Holt, R.M., and Raaen, A.M., (1989): "Rock Mechanics and Rock Acoustics", Rock at Great Depth; Maury and Fourmaintraux (eds.), Pau, France, **vol. 1,** pp. 355-362.
59. FracproPT Manual (2003): Documentation provided with FracproPT V. 10.2.23.0., Pinnacle Technologies.
60. Frame, R.G., (1952): "Earthquake Damage, Its Cause and Prevention in the Wilmington Oil Field", *California Oil Fields*, Thirty-eighth Annual Report, Dept. of Natural Resources, Division of Oil and Gas, California.
61. Franquet, J., and Economides, M.J., (1999): "Effect of Stress and Stress Path on Young´s Modulus and Poisson Ratio of Unconsolidated Rocks: A New Idea for Hydraulic Fracturing", SPE paper 54012, presented at the 1999 SPE Latin American and Caribbean Petroleum Engineering Conference held in Caracas, Venezuela, 21–23 April.

62. Fredich, J.T., Arguello, J.G., Thorne, B.J., Deitrick, G.L., de Roufignac, E.P., Myer, L.R., and Bruno, M.S., (1996): "Three Dimensional Geomechanical Simulation of Reservoir Compaction and Implications for Wellbore Failures in the Belridge Diatomite", SPE paper 36698, presented at the SPE Annual Technical Conference and Exhibition, Denver, Colorado, October 6-9.
63. Fu., G.-F., Morita, N., Boyd, P.A., and McGoffin, S.J., (1992): "A New Approach to Preventing Lost Circulation while Drilling", SPE paper 24599, presented at the 67th SPE Annual Technical Conference and Exhibition, Washington, DC, October 4-7.
64. Fukuda, M., (1983): "The Pore Pressure Profile in Porous Rocks During Freezing", Proc. of the 4th Int. Conf. on Permafrost, Fairbanks, Alaska, Acad. Press., Washington, D.C., pp. 322-327.
65. Geertsma, J., and Haafkens, R., (1979): "A Comparison of the Theories for Predicting Width and Extent of Vertical Hydraulically Induced Fractures", Trans. ASME (March), **101**, 8-19.
66. Gulrajani, S.N., Tibbles, R.J., and Nolte, K.G., (1997): "Evaluation of Calibration Treatments, for Frac Pack Completions in Offshore West Africa", SPE paper 38192, presented at the 1997 SPE European Formation damage Conference, The Hague, The Netherlands, June 2-3.
67. Hadizadeh, J., and Law, R.D., (1991): "Water-Weakening of Sandstone and Quartzite Deformed at Various Stress and Strain Rates", *Int. J. of Rock Mech. Min. Sci. & Geomech. Abstr*., **Vol. 28**, No. 5, pp. 431-439.
68. Hainey, B.W., and Troncoso, J.C., (1992): "Frac-Pack: An Innovative Stimulation and Sand Control Technique", SPE paper 23777, presented at the Formation Damage Control Symposium, Lafayette, Louisiana, February 26-27.
69. Hale, P.A., and Shakoor, A., (2003): "A Laboratory Investigation of the Effects of Cyclic Heating and Cooling, Wetting and Drying, and Freezing and Thawing on the Compressive Strength of Selected Sandstones", *Environmental and Engineering Geoscience*, **Vol. IX**, Number 2, May, pp. 117-130.
70. Hawkins, A.B., and McConnell, B.J., (1992): "Sensitivity of Sand Stone Strength and Deformability to Changes in Moisture Content", *Q.J. Engng. Geol*., **v 25**, pp. 115-130.
71. Hoekstra, P., (1969): "Water Movement and Freezing Pressures", *Soil Sci. Soc. Amer. Proc*., **Vol. 33**, pp. 512-518.
72. Holt, R.M., (1990): "Permeability Reduction Induced by a Nonhydrostatic Stress Field", *SPE Formation Evaluation* (also in SPE paper 19595), December, pp.444-448.

73. Holt, R.M., and Kenter, C.J., (1992): "Laboratory Simulation of Core Damage Induced by Stress Release", Proc. of the 33rd U.S. Rock Mechanics Symposium, Tillerson & Waversik (eds.), Santa Fe, June 3-5, pp. 959-968.
74. Holt, R.M., Brognoli, M., Fjær, E., Unander, T.E., and Kenter, C.J., (1994): "Core Damage Effects on Compaction Behavior", SPE/ISRM paper 28027, presented at the SPE/ISRM Rock Mechanics in Petroleum Engineering Conference, Delft, The Netherlands, August 29-31.
75. Huang, A.B., Liao, J.J., Pan, Y.W., Cheng, M.H., Hsieh, S.Y., and Peng, J.K., (2000): "Characterization of Soft Rocks in Taiwan", Pacific Rocks 2000, Rock Around the Rim; Girard, Liebman, Breeds & Doe (eds.), Seattle, WA, July 31-August 3, pp. 83-90.
76. Huffman, A.R., and Castagna, J.P., (2001): "The Petrophysical Basis for Shallow Water Flow Prediction Using Multicomponent Seismic Data", *The Leading Edge*, **v. 20**, pp. 1030-1035, 1052.
77. International Society of Rock Mechanics, (1981): *Rock Characterization, Testing and Monitoring* (ISRM Suggested Methods), Pergamon, New York, 211 p.
78. Ishizaki, T., (2000): "Frost Deterioration of Historical Stone Monuments and Brick Buildings and Its Preventive Measures", Proc. of the International Symposium on Ground Freezing and Frost Action in Soils, Louvain-La-Neuve, Belgium, September 11-13, pp. 79-83.
79. Itasca Consulting Group, (2004): PFC3D manual, Documentation provided with PFC3D V. 3.00-174,.
80. Jaeger, J.C., and Cook, N.G.W., (1976): *Fundamentals of Rock Mechanics*, John Wiley & Sons Inc (eds.), London, UK.
81. Jeremic, M.L., (1981): "Elements of Rock-Weakening of Coal-Bearing Strata of the Canadian Plains Region", Proceedings of the International Symposium on Weak Rock, Tokyo, Japan, September 21-24, pp. 43-48.
82. Joiner, S.D., Kreisa, R.D., Bloch, R.B., and Paul, J.B. (1999): "Defining Reservoir-Rock Properties, Deep-Water Depositional Facies of the Qua Iboe Member, Pliocene, Offshore Nigeria", SPE paper 56859, presented at the Annual Technical Conference and Exhibition, Houston, TX, October 3-6.
83. Jones, J.F., Taylor, G.D., and Barree, R.D., (2001): "Succesfully Managing Drilling-Fluid Losses in Multiple Highly Depleted Sands", OTC paper 13107, presented at the 2001 OTC, Houston, Texas, April 30 – May 3.
84. Kaplar, C.W., (1968): "New Experiments to Simplify Frost Susceptibility Testing of Soils", *Highway Research Record*, **Number 215**, pp. 48-59.
85. Kilmer, N.H., Morrow, N.R., and Pitman, J.K., (1987): "Pressure Sensitivity of Low Permeability Sandstones", *J. Pet. Sci. & Eng.*, **v.1**, pp. 65-81.
86. Klein, A.L., Aldea, C., Bruton, J.R., Dobbs, W.R., (2003): "Field Verification: Invert Mud Performance from Water-Based Mud in Gulf of Mexico Shelf",

SPE paper 84314, presented at the SPE Annual Technical Conference and Exhibition, Denver, Colorado, October 5-8.
87. Konrad, J.-M., (2000): "Assessment of Subgrade Frost Susceptibility from Soil Index Properties", Proc. of the International Symposium on Ground Freezing and Frost Action in Soils, Louvain-La-Neuve, Belgium, September 11-13, pp. 89-94.
88. Krishnan, G.R., Zhao, X.L., and Wang, H., (1994): "Properties of Unconsolidated Materials using Hydrostatic Tests, Acoustic Measurements, Pulse Techniques, and Fracture Tests, Progress Report, Rock Mechanics Consortium, The University of Oklahoma, Norman, OK.
89. Lade, P.V., (1999): "Instability of Granular Materials", Physics and Mechanics of Soil Liquefaction", Lade & Yamamuro (eds.), Balkerma, Rotterdam, pp. 3-16.
90. Lam, K.Y., Barr, D.T., and Cleary, M.P., (1986): "A Complete Three-Dimensional Simulator for Analysis and Design of Hydraulic Fracturing", SPE paper 15266, presented at the SPE Unconventional Gas Recovery Symposium, Louisville, Kentucky, May.
91. Larsen, I, Fjær, E., and Renlie, L., (2000); "Static and Dynamic Poisson's Ratio of Weak Sandstones", Pacific Rocks 2000, Rock Around the Rim; Girard, Liebman, Breeds & Doe (eds.), Seattle, WA, July 31-August 3, pp. 77-82.
92. Lee, M.W., (2003): "Elastic Properties of Overpressured and Unconsolidated Sediments", *U.S. Geological Survey Bulletin 2214*, November (available online at: http://geology.cr.usgs.gov/pub/bulletins/b2214/)
93. Lewis, D. W., Dolch, W.L., and Woods, K.B., (1953): "Porosity Determinations and the Significance of Pore Characteristics and Aggregates", *ASTM Proceedings*, **Vol. 52**, pp. 949-958.
94. Li, L., and Holt, R.M., (2002): "Simulating Stress Dependent Permeability of Granular Media with a Fluid-Coupled Particle Model", in Particle Scale Reservoir Mechanics, pp. 1-30, L. Li (ed.), Trondheim.
95. Li, X., Mitchum, F.L., Bruno M., Pattillo, P.D., and Willson, S.M., (2003): "Compaction, Subsidence, and Associated Casing Damage and Well Failure Assessment for the Gulf of Mexico Shelf Matagorda Island 623 Field", SPE paper 84553, presented at the SPE Annual Technical Conference and Exhibition, Denver, Colorado, October 5-8.
96. Lienhart, D.A., (1988): "The Geographic Distribution of Intensity and Frequency of Freeze-Thaw Cycles, Bulletin Association of Engineering Geologists, Vol. 25, No.4, pp. 465-469.
97. Litvan, G.G., (1984): " Frost Action in Porous Systems", in Séminaire: Durabilité des Beton et des Pierres, Séminaire Organisé avec la Collaboration

de l'UNESCO par le Collège International des Sciences de la Construction, National Research Council of Canada DBR 1176, pp. 95-108.
98. Marsala, A.F., Ragazzini, G., Meazza, O., Brignoli, M., and Santarelli, F.J., (1994): "Basin scale rock mechanics; logs and core measurements", Eurock 94 (also in SPE paper 28034), SPE/ISRM Rock Mechanics in Petroleum Engineering Conference, Delft, The Netherlands, pp.105-112.
99. Martin, A.N., (2000): "Crack Tip Plasticity: A Different Approach to Modeling Fracture Propagation in Soft Formations", paper SPE 63171, presented at the SPE Annual Technical Conference and Exhibition, Dallas Texas, October.
100. McGregor, K.W., Park, E.I., Sincock, K.J., and Piekenbrock, E.J., (1991): "Effective Unconsolidated Core Preservation in the Artic Environment: An Aid to Accurate Reservoir Evaluation", SPE paper 22128, presented at the International Artic Technology Conference, Anchorage, Alaska, May 29-31.
101. Meredith P.G., and Atkinson, B.K., (1985): "Fracture Toughness and Subcritical Growth During High Temperature Tensile Deformation of Westerly Granite and Black Gabbro", Physics of the Earth and Planetary Interiors, **vol. 39**, no. 1, pp.33-51, June.
102. Meyer, B.R., (1989): "Three-Dimensional Hydraulic Fracturing Simulation on Personal Computers: Theory and Comparison Studies", SPE paper 19329, presented at the SPE Eastern regional Meeting, Morgantown, West Virginia, October 24-27.
103. Meyer, B.R., Cooper, G.D., and Nelson, S.G., (1990): "Real-Time 3-D Hydraulic Fracturing Simulation: Theory and Field case Studies", SPE paper 20658, presented at the 65th Annual Technical Conference and Exhibition, New Orleans, September 23-26.
104. MFrac Online Manual, (2004): http://www.mfrac.com/documentation.shtml , Meyer & Associates Inc.
105. Morita, N., and Ross, C.K., (1993): "Core-Based Horizontal or Highly-Inclined Well Stability Analysis for Unconsolidated formations", SPE paper 26332, presented at the 68th Annual Technical Conference and Exhibition, Houston, TX, October 3-6.
106. Morita, N., Whitfill, D.L., and Wahl, H.A., (1988): "Stress-Intensity Factor and Fracture Cross-Sectional Shape Predictions from a 3-D Model for Hydraulically Induced fractures", *Journal of Petroleum Technology*, pp. 1329-1342, October.
107. Mullen, M.E., Stewart, B.R., and Norman, W.D., (1994): "Evaluation of Bottom Hole Pressures in 40 Soft Rock Frac-Pack Completions in the Gulf of Mexico", SPE paper 28532, presented at the Annual Technical Conference and Exhibition, New Orleans, Louisiana, September 25-26.

108. Munson, B.R., Young, D.F., and Okiishi, T.H., (2003): *Fundamentals of Fluid Mechanics*, 4th Ed., John Wiley & Sons, Inc., New York.
109. Mustoe, G., (2004): The Discrete Element Method, webpage: http://egweb.mines.edu/dem/ .
110. Nicholson, E.D., Goldsmith, G., and Cook, J.M., (1998): "Direct Observation and Modeling of Sand Production Processes in Weak Sandstone", SPE/ISRM paper 47328, presented at the SPE/ISRM Eurock 98, Trondheim, Norway, July 8-10, pp. 97-106.
111. Ong, Seehong, May, A., and George, I., (2000): "An Accurate Characterization of Sand Strength in Weak and Unconsolidated Formations Aids Offshore Production Test Designs – A Bohai Bay Case Study", SPE paper 64738, presented at the SPE International Oil and Gas Conference and Exhibition in China, Beijing, China, November 7-10.
112. Orowan, E., (1949): "Fracture and Strength of Solids", *Reports on Progress in Physics*, **v. 12**, pp. 185-232.
113. Ostermeier, R.M., (1993): "Deepwater Gulf of Mexico Turbidites: Compaction Effects on Porosity and Permeability", SPE paper 26468, presented at the 68th SPE Annual Technical Conference and Exhibition, Houston, TX, October 3-6.
114. Ostermeier, R.M., (1995): "Stressed Oil Permeability of Deepwater Gulf of Mexico Turbidite Sands: Measurements and Theory", SPE paper 30606, presented at the 1995 SPE Annual Technical Conference and Exhibition, Dallas, TX, October 22-25.
115. Ostermeier, R.M., Pelletier, J.H., Winker, C.D., and Nicholson, J.W., (2001): "Trends in Shallow Sediment Pore Pressure – Deepwater Gulf of Mexico", SPE/IADC paper 67772, presented at the SPE/IADC Drilling Conference, Amsterdam, The Netherlands, February 27 - March 1.
116. Pak. A., (1997): Numerical Modeling of Hydraulic Fracturing, Ph.D. Thesis, Department of Civil and Environmental Engineering, University of Alberta, Canada.
117. Palmer, I. D., and Carroll, H.B., Jr., (1983): "3D Hydraulic Fracture Propagation in the Presence of Stress Variations", *Soc. Pet. Engr. J.*, December.
118. Palmer, I.D. and Veatch, R.W., (1987): "Abnormally High Fracturing Pressure in Step-Rate Tests", paper SPE 16902 presented at the 62nd Annual Technical Conference and Exhibition, Dallas, Texas.
119. Papanastasiou, P., (1997): The Influence of Plasticity in Hydraulic Fracturing, *Int. J. Fracture*, **84**: 61-79.
120. Parks, G.A., (1984): "Surface and Interfacial Free Energies of Quartz", *Journal of Geophysical Research*, **Vol. 89**, No. B6, pp. 3997-4008, June 10.

121. Pauget, L, Specia, F., and Boubazine, A., (2002): "Reliability of Laboratory Porosity and Pore Compressibility Obtained on Unconsolidated Deep Off-Shore and Heavy-Oil Reservoirs", SPE paper 77639, presented at the 2002 SPE Annual Technical Conference and Exhibition, San Antonio, TX, September 29-October 2.
122. Penner, E., (1960): "The Importance of Freezing Rate on Frost Action in Soils", *Proc. ASTM*, **Vol. 60**, pp. 1151-1165.
123. Penner, E., (1972): "Influence of Freezing Rate on Frost Heaving", *Highway Research Records*, **Number 393**, Frost Action in Soils, Highway Research Board - Division of Engineering, National Research Council, National Academy of Sciences, pp. 56-64.
124. Perkins, T.K., and Weingarten, J.S., (1988): "Stability and Failure of Spherical Cavities in Unconsolidated Sand and Weakly Consolidated Rock', SPE paper 18244, presented at the 63rd Annual Technicval Conference and Exhibition, Houston, Texas, October 2- 5.
125. Powell, K.R., Hathcock, R.L., Mullen, M.E., Norman, W.D., and Baycroft, P.D., (1997): "Productivity Comparisons of High rate water Pack and Frac-Pack Completion Techniques", SPE paper 38592, presented at the SPE Annual Technical Conference and Exhibition, San Antonio, Texas, October 5-8.
126. Prasad, M., (2002): "Acoustic Measurements in Unconsolidated Sands at Low Effective Pressure and Overpressure Detection", *Geophysics*, **v.67**, pp. 405-412.
127. Prats, M., (1961): "Effect of Vertical Fractures on Reservoir Behavior – Incompressible Fluid Case", *SPEJ*, June, pp. 105-117.
128. Proctor, K.E., (1974): "The Petrography and Gas-Reservoir Potential of Stanley-Jackfork Sandstones, Ouachita Mountains, Arkansas and Oklahoma", MSc. Thesis, Northern Illinois University, Dekalb, Illinois.
129. Ramamurthy, T., (2001): "Shear Strength Response of Some Geological Materials in Triaxial Compression", *International Journal of Rock Mechanics & Mining Sciences*, **v. 38**, pp. 683-697.
130. Rebinder, P.A., and Lichtman, V., (1957):"Effect of Surface Active Media on Strain and Rupture of Solids", Proceedings of the 2nd International Congress on Surface Activity, New York, Academic Press, v. 3, pp. 563-580.
131. Reimers, D.R., and Clausen, R.A., (1991): "High-Permeability Fracturing at Prudhoe Bay, Alaska", SPE paper 22835, presented at the SPE Annual Technical Conference and Exhibition, Dallas, Texas, October 6-9.
132. Rhett, D.W., and Lord, C.J., (2001): ""Water Weakening in Sedimentary Rocks", Rock Mechanics in the National Interest, Elsworth, Tinucci & Heasley (eds.), Proceedings of the 38th U.S. Rock Mechanics Symposium, DC Rocks, Washington D.C., pp. 121-128.

133. Risnes, R., Brattli, R.K., and Horsrud, P., (1982): "Sand Stress around a Wellbore", SPE Journal, December, pp. 883 – 898.
134. Roegiers, J.-C, (2004a): Personal Communication.
135. Roegiers, J.-C,: (2004b): *Rock Mechanics for the Petroleum Engineer*, in print.
136. Roegiers, J.-C., and Zhao, X.L., (1991): "Rock Fracture Tests in Simulated Downhole Conditions", Rock Mechanics as a Multidisciplinary Science, Proceedings of the 32nd U.S. Rock Mechanics Symposium, Norman, Oklahoma, pp. 221-230.
137. Roodhart, L.P., Fokker, P.A., and Davies, D.R., (1993): "Frac and Pack Stimulation: Application, Design, and Field Experience from the Gulf of Mexico to Borneo", SPE paper 26564, presented at the 68th Annual Technical Conference and Exhibition, Houston, Texas, October 3-6.
138. Sandia National Laboratories, (2004): Fact sheet: "Discrete Element Modeling", http://www.nwmp.sandia.gov/wlp/factsheets/dem.pdf .
139. Santarelli, F.J., (1987): Theoretical and Experimental Investigation of the Stability of the Axisymmetric Borehole", Ph.D. Thesis, the University of London, London, 472 p.
140. Santarelli, F.J., and Dusseault, M.B. (1991): "Core Quality Control in Petroleum Engineering", Proceedings of the 32nd U.S. Rock Mechanics Symposium, Rock Mechanics as a Multidisciplinary Science, Roegiers (ed.), Norman, Oklahoma, pp. 111-120.
141. Sapegin, D.D., Karpov, N.M., and Petrosyan, G.M., (1981): "Study of Physico-Mechanical Properties of Weak Rock Underlying Structure Foundations", Proceedings of the International Symposium on Weak Rock, Tokyo, Japan, September 21-24.
142. Saucier, R.J., (1974): "Considerations in Gravel Pack Design", *Journal of Petroleum Technology*, February, pp. 205-212.
143. Scherer, M., (1987): "Parameters Influencing Porosity in Sandstones: A Model for Sandstone Porosity Prediction", *The American Association of Petroleum Geologists Bulleti*n, **v. 71**, No. 5, May, pp. 485-491.
144. Schmidt, R.A., and Hurdle, C.W., (1977): "Effect of Confining Pressure on Fracture Toughness of Indiana Limestone", *International Journal of Rock Mechanics and Mining Science and Geomechanics Abstracts*, **v.** 14, pp. 289-293.
145. Schmidt, V., McDonald, A., and Platt, R.L., (1997): "Pore Geometry and Reservoir Aspects of Secondary porosity in Sandstones", *Bulletin of Canadian Petroleum Geology*, **v.25**, pp. 271-290.
146. Schön, J.H., (1996): *Physical Properties of Rocks*, Pergamon, 583 p.

147. Sclater, J.C., and Christie, P.A.F., (1980): "Continental Stretching: AN Explanation of the Post-mid Cretaceous Subsidence of the Central North Sea Basin", *Journal of Geophysical Research*, **v. 85**, pp. 3711-3739.
148. Seifert, P., Geller, J.T., Johnson, L., (1998): "Effect of P-Wave Scattering on Velocity and Attenuation in Unconsolidated Sand saturated with Immiscible Liquids"*, Geophysics*, **Vol. 63**, January-February, pp. 161-170.
149. Selley, R.C., (1978): "Porosity Gradients in North Sea Oil Bearing Sandstones", *Journal of the Geological Society of London*, v.135, pp. 119-132.
150. Settari, A., and Cleary, M.P., (1982); "Development and Testing of a Pseudo-Three-Dimensional Model of Hydraulic Fracture Geometry (P3DH)", SPE paper 10505.
151. Shakoor, A., West, T.R., and Scholer, C.F., (1982): "Physical Characteristics of some Indiana Argillaceous Carbonates Regarding Their Freeze-Thaw Resistance in Concrete", *Bulletin Association of Engineering Geologists*, **Vol. 19**, No.4, pp. 371-384.
152. Shlyapobersky, J., (1985): "Energy Analysis of Hydraulic Fracturing", Proc. 26th U.S. Symposium on Rock Mechanics, pp.539-546
153. Shlyapobersky, J., Isaa, M.A., Issa, M.A., Dudley, J.W., Shulkin, Y., and Chudnovsky, A., (1998): "Scale Effects on Fracture Growth Resistance in Poroelastic Materials", SPE paper 48929, presented at the SPE Annual Technical Conference and Exhibition, New Orleans, LA, September 27-30.
154. Shlyapobersky, J., Wong, G.K., and Walhaugh, W.W., (1988): "Overpressure-calibrated design of Hydraulic Fracture Stimulations", paper SPE 18194, presented at the 63rd SPE Technical Conference and Exhibition, Houston, Texas, October.
155. Smith, M.B., (2004): Personal communication.
156. Smith, M.B., Miller II, W.K., and Haga, J., (1987): "Tip Screenout Fracturing: A Technique for Soft, Unstable Formations", *SPE Production Engineering*, May, pp. 95-103.
157. Snoeyink, V.L., and Weber, W.J., (1972): "Surface Functional Groups on Carbon and Silica"*, Surf. Membr. Sci*., **V. 5**, pp. 63-119.
158. Stewart, B.R., Mullen, M.E., Ellis, R.C., Norman, W.D., and Miller, W.K., (1995): "Economic Justification for Fracturing Moderate to High Permeability Formations in Sand Control Environments", SPE paper 30470, presented at the SPE Annual Technical Conference and exhibition, Dallas, Texas, October 22-25.
159. Stimplan Manual, (2004): Documentation provided with Stimplan V.5.20., NSI Technologies.
160. Strandenes, S., and Blangy, J.P., (1991): "Integrated Reservoir Characterization of a Field from the North Sea: Part I. The Rock Physics

Model", 61st Annual International SEC Meeting, Houston, TX, November, 10-14.
161. Suman, G.O., Jr., Ellis, R.C., and Snyder, R.E., (1983): *Sand Control Handbook*, Gulf Publishing Co., Houston, 89 p.
162. Swolfs, H.S., (1971): "Chemical Effects of Pore Fluids on Rock Properties", Proceedings of the Underground Waste Management and Environmental Implications symposium, Houston, TX, December 6-9, pp.224-233.
163. Thiercelin, M., (1987): "Fracture Toughness under Confining Pressure Using the Modified Ring Test", Proceedings of the 28th U.S. Rock Mechanics Symposium, pp. 149-156.
164. Thimus, J.F., (1989): Caractéristiques Physiques, Mécaniques et Rhéologiques d'un Sol Argileux Lors de sa Congélation, Ph.D. Dissertation, Université Catholique de Louvain, Faculté de Sciences Appliquées, Unité de Génie Civil et Environnemental, Louvain-La-Neuve, Belgium.
165. Tutuncu, A.N., Dvorkin, J., and Nur, A., (1997): "Influence of Cementation and Permeability on Wave Velocities in Poorly Consolidated Sands", Int. J. Rock Mech. & Min. Sci., paper No.313, Vol. 34, No. 3-4.
166. U.S. Army, Corps of Engineers,(1958): Cold Room Studies- Third Interim Report, Tech. Rep. 43.
167. University of Kansas, (2004): University of Kansas website, url: http://www.eng.ku.ac.th/~mat/MatDB/source/Prop/def/young/young.htm
168. Valkó, P., and Economides, M.J., (1993): "Continuum Damage Mechanics Model of Hydraulic Fracturing", J*PT*, pp. 198-205.
169. van Dam, D.B., Papanastasiou, P., and de Pater, C.J., (2000): "Impact of Rock Plasticity on Hydraulic Fracture propagation and Closure", SPE paper 63172, presented at the SPE Annual Technical Conference and Exhibition, Dallas, Texas, October 1-4.
170. van Oort, E., Gradishar, J., Ugeto, G., Cowan, K.M., Barton, K.K., and Didely, J.W., (2003): "Accessing Deep Reservoirs by Drilling Severely Depleted Formations', SPE/IADC paper 79861, presented at the SPE/IADC Drilling Conference, Amsterdam, The Netherlands, February 19-21.
171. Wang, H., Khrishnan, G.R., Zaman, M., and Roegiers, J.C., (1995): "Behavior of Natural and remolded Antler Sandstone: Sample Preparation and Grain Crushing Aspects", Rock Mechanics, proceedings of the 35th U.S. Rock Mechanics Symposium, Daemen & Schultz (eds.), Reno, Nevada, June 5-7, pp. 127-133.
172. Warpinski, N.R. and Teufel, L.M., (1987): "Influence of Geologic Discontinuities on Hydraulic Fracture Propagation", *JPT*, pp. 209-220
173. Weng, X., (1991): "Incorporation of 2D Fluid Flow into a Pseudo-3D Hydraulic Fracturing Simulator", SPE paper 21849, presented at the Rocky

Mountain Regional Meeting and Low-Permeability Reservoirs Symposium, Denver, Colorado, April 15-17.

174. WesternGeco website, (2004): A Shallow Water Flow Study, Gulf of Mexico, http://www.westerngeco.com/content/resources/casestudies/europa.asp

175. Williams, P.J., and Smith, M.W., (1989): *The Frozen Earth*, Cambridge University Press, Cambridge, 306 p.

176. Willson, S.M., Edwards, S., Heppard, P.D., Li, X., Coltrin, G., Chester, D.K., Harrison, H.L., and Cocales, B.W., (2003): "Wellbore Stability Challenges in the Deep Water, Gulf of Mexico: Case History Examples from the Pompano Field", SPE paper 84266, presented at the SPE Annual Technical Conference and Exhibition, Denver, Colorado, October 5-8.

177. Wu, B., and Tan, C.P., (2000): "Relationship Between Thick-Walled Cylinder and Unconfined Compressive Strength for Application in Sand Prediction", Pacific Rocks 2000, Rock Around the Rim; Girard, Liebman, Breeds & Doe (eds.), Seattle, WA, July 31-August 3, pp. 287-294.

178. Wu, B., and Tan, C.P., (2001): ""Effect of Water-Cut on Sandstone Strength and Implications in Sand Production Prediction", Rock Mechanics in the National Interest, Elsworth, Tinucci & Heasley (eds.), Proceedings of the 38th U.S. Rock Mechanics Symposium, DC Rocks, Washington D.C., pp. 27-34.

179. Yale, D.P., (1984): "Network Modeling of Flow, Storage and Deformation in Porous Rocks", PhD dissertation, Stanford U., Stanford, CA.

Appendix A – Fish Routines used during the validation of the model mechanical properties

```
;fname: triax_1.DAT Creation and packing of particles - triaxial sample
;
new
SET random ; reset random-number generator
; ------------------------------------------------
def make_walls ; create walls: a cylinder and two plates
        extend = 0.1
        rad_cy = 0.5*width
        w_stiff= 1e8
        _z0 = -extend
        _z1 = height*(1.0 + extend)
        command
                wall type=cylinder id=1 kn=w_stiff end1 0.0 0.0 _z0 end2 0.0 0.0
_z1 &
                rad rad_cy rad_cy
        end_command
        _x0 = -rad_cy*(1.0 + extend)
        _y0 = -rad_cy*(1.0 + extend)
        _z0 = 0.0
        _x1 = rad_cy*(1.0 + extend)
        _y1 = -rad_cy*(1.0 + extend)
        _z1 = 0.0
        _x2 = rad_cy*(1.0 + extend)
        _y2 = rad_cy*(1.0 + extend)
        _z2 = 0.0
        _x3 = -rad_cy*(1.0 + extend)
        _y3 = rad_cy*(1.0 + extend)
        _z3 = 0.0
        command
                wall id=5 kn=w_stiff face (_x0,_y0,_z0) (_x1,_y1,_z1)
(_x2,_y2,_z2) &
                (_x3,_y3,_z3)
        end_command
        _x0 = -rad_cy*(1.0 + extend)
```

```
        _y0 = -rad_cy*(1.0 + extend)
        _z0 = height
        _x1 = -rad_cy*(1.0 + extend)
        _y1 = rad_cy*(1.0 + extend)
        _z1 = height
        _x2 = rad_cy*(1.0 + extend)
        _y2 = rad_cy*(1.0 + extend)
        _z2 = height
        _x3 = rad_cy*(1.0 + extend)
        _y3 = -rad_cy*(1.0 + extend)
        _z3 = height
        command
                wall id=6 kn=w_stiff face (_x0,_y0,_z0) (_x1,_y1,_z1)
(_x2,_y2,_z2) &
                (_x3,_y3,_z3)
        end_command
end
; ------------------------------------------------
def assemble ; assemble sample
        s_stiff=0.0 ; initial stiffnesses
        n_stiff=1e8
        tot_vol = height * pi * rad_cy^2.0
        rbar = 0.5 * (rlo + rhi)
        num = int((1.0 - poros) * tot_vol / (4.0 / 3.0 * pi * rbar^3))
        mult = 1.6 ; initial radius multiplication factor
        rlo_0 = rlo / mult
        rhi_0 = rhi / mult
        command
                gen id=1,num rad=rlo_0,rhi_0 x=-1.0,1.0 y=-1.0,1.0 z=0.0,height
&
                filter ff_cylinder
                prop dens=1000 ks=s_stiff kn=n_stiff
        end_command
        ii = out(string(num)+' particles were created')
        sum = 0.0 ; get actual porosity
        bp = ball_head
        loop while bp # null
                sum = sum + 4.0 / 3.0 * pi * b_rad(bp)^3
                bp = b_next(bp)
        end_loop
        pmeas = 1.0 - sum / tot_vol
```

```
        mult = ((1.0 - poros) / (1.0 - pmeas))^(1.0/3.0)
        command
                ini rad mul mult
                cycle 1000
                prop ks=1e8 fric 0.25
                cycle 250
        end_command
end
; ------------------------------------------------
def cws ; change lateral wall stiffnesses
        command
                wall type cylinder id 1 kn=w_stiff
        end_command
end
; ------------------------------------------------
def ff_cylinder
        ff_cylinder = 0
        _brad = fc_arg(0)
        _bx = fc_arg(1)
        _by = fc_arg(2)
        _bz = fc_arg(3)
        _rad = sqrt(_bx^2 + _by^2)
        if _rad + _brad > rad_cy then
                ff_cylinder = 1
        end_if
end
; ------------------------------------------------
macro zero 'ini xvel 0 yvel 0 zvel 0 xspin 0 yspin 0 zspin 0'
SET height=4.0 width=2.0 rlo=0.075 rhi=0.100 poros=0.4
make_walls
assemble
SET w_stiff= 1e7 ; make lateral wall stiffness=1/10 of ball stiffness
cws
cyc 500
zero
plot create assembly
plot set cap size 25
plot set mag 1.5
plot set rot 30 0 40
plot add ball lorange
plot show
```

```
save tt_ass.SAV
return
```

;fname: **triax_2_1_1000psi.DAT** Servo-control and initial stress state - triax sample

```
res tt_ass_1.SAV ; restore compacted assembly
; ------------------------------------------------
def get_ss ; determine average stress and strain at walls
        new_rad = w_radend1(wadd1)
        rdif = new_rad - rad_cy
        zdif = w_z(wadd6) - w_z(wadd5)
        new_height = height + zdif
        wsrr = -w_radfob(wadd1) / (new_height * 2.0 * pi * new_rad)
        wszz = 0.5*(w_zfob(wadd5) - w_zfob(wadd6)) / (pi * new_rad^2.0)
        werr = 2.0 * rdif / (rad_cy + new_rad)
        wezz = 2.0 * zdif / (height + new_height)
        wevol = wezz + 2.0 * werr
end
; ------------------------------------------------
def get_gain ; determine servo gain parameters for axial and lateral motion
        alpha = 0.5 ; relaxation factor
        count = 0
        avg_stiff = 0
        cp = contact_head ; find avg. number of contacts on lateral walls
        loop while cp # null
                if c_gobj2(cp) = wadd1
                        count = count + 1
                        avg_stiff = avg_stiff + c_kn(cp)
                end_if
                cp = c_next(cp)
        end_loop
        avg_stiff = avg_stiff / count
        gr = alpha * height * pi * rad_cy * 2.0 / (avg_stiff * count * tdel)
        count = 0
        avg_stiff = 0
        cp = contact_head ; find avg. number of contacts on top/bottom walls
        loop while cp # null
                if c_gobj2(cp) = wadd5
                        count = count + 1
                        avg_stiff = avg_stiff + c_kn(cp)
```

```
                end_if
                if c_gobj2(cp) = wadd6
                        count = count + 1
                        avg_stiff = avg_stiff + c_kn(cp)
                end_if
                cp = c_next(cp)
        end_loop
        ncount = count / 2.0
        avg_stiff = avg_stiff / count
        gz = alpha * pi * rad_cy^2.0/ (avg_stiff * ncount * tdel)
end
; ------------------------------------------------
def servo
        while_stepping
        get_ss ; compute stresses & strains
        udr = gr * (wsrr - srrreq)
        w_radvel(wadd1) = -udr
        if z_servo = 1 ; switch stress servo on or off
                udz = gz * (wszz - szzreq)
                w_zvel(wadd5) = udz
                w_zvel(wadd6) = -udz
        end_if
end
; ------------------------------------------------
def iterate
        loop while 1 # 0
                get_gain
                if abs((wsrr - srrreq)/srrreq) < sig_tol then
                        if abs((wszz - szzreq)/szzreq) < sig_tol then
                                exit
                        end_if
                end_if
                command
                        cycle 100
                end_command
        end_loop
end
; ------------------------------------------------
def wall_addr
        wadd1 = find_wall(1)
        wadd5 = find_wall(5)
```

```
        wadd6 = find_wall(6)
end
; ------------------------------------------------
wall_addr
zero
SET srrreq=-6.896e6 szzreq=-6.896e6 sig_tol=0.005 z_servo=1
iterate ; get all stresses to requested state
sav tt_str_1_1000psi.SAV
return
```

```
;fname: triax_3_1_1000psi.DAT Preparation for upcoming tests.
res tt_str_1_1000psi.sav ; restore initial stressed assembly
;
; ------------------------------------------------
def set_ini ; set initial strains
        wezz_0 = wezz
        wevol_0 = wevol
end
; ------------------------------------------------
def conf ; variables for histories
        devi = wszz - wsrr ; deviatoric stress
        deax = wezz - wezz_0 ; axial strain
        devol = wevol - wevol_0 ; volumetric strain
        conf = wsrr ; confining stress
end
; ------------------------------------------------
def accel_platens
        ; ----- Accelerates the platens to achieve vel of _vfinal in _nsteps,
        ; using _nchunks
        _niter = _nsteps / _nchunks
        loop _chnk (1,_nchunks)
                if _close = 1 then
                        _vel = _chnk*(_vfinal/_nchunks)
                else
                        _vel = -_chnk*(_vfinal/_nchunks)
                end_if
                _mvel = -_vel
                command
                        wall id 5 zvel= _vel
                        wall id 6 zvel= _mvel
```

```
                    cycle _niter
                end_command
            end_loop
end
; ------------------------------------------------
set_ini
history id=1 conf
history id=2 devi
history id=3 deax
history id=4 devol
history id=11 werr
history id=12 wezz
SET hist_rep=50
SET z_servo=0
zero
sav tt_init_1_1000psi.SAV ; ready for modulus and failure tests
return
```

;fname: **triax_5.DAT** (determine elastic properties)

```
res tt_init.sav
prop fric 1.0 s_bond=1e15 n_bond=1e15
set _vfinal= 0.1 _nsteps= 2000 _nchunks= 80
set _close = 1 ; load
accel_platens
cyc 2000
zero
set _close = 0 ; unload
accel_platens
cyc 2000
save triax_5.SAV
return
```

Appendix B – Fish Routines used during the validation of the model hydraulic properties

; FNAME: **bhx_3.dat**

```
new
set random

def setup
  CR      = 1.3716
  CH      = 4.572
  lo_rad  = 0.150
  hi_rad  = 0.210
  x_min   = -CR + hi_rad
  x_max   = CR - hi_rad
  y_min   = -CR + hi_rad
  y_max   = CR - hi_rad
  poros   = 0.4
  s_stiff = 4.0e10
  n_stiff = 9.4e10
end
setup
def ff_cylinder
  ff_cylinder = 0
  _brad = fc_arg(0)
  _bx   = fc_arg(1)
  _by   = fc_arg(2)
  _rad  = sqrt(_bx^2 + _by^2)
  if _rad + _brad > CR then
    ff_cylinder = 1
  end_if
end
def make_model
  ;--- Create assembly ---
  command
    wall type cylinder rad CR,CR end1 0.0,0.0,0.0  end2 0.0,0.0,CH &
      kn n_stiff ks=s_stiff  id 1
```

```
end_command
_x0 = -CR
_y0 = -CR
_z0 = 0.0
_x1 = CR
_y1 = -CR
_z1 = 0.0
_x2 = CR
_y2 = CR
_z2 = 0.0
_x3 = -CR
_y3 = CR
_z3 = 0.0
command
  wall id=2 kn=n_stiff ks=s_stiff &
    face (_x0,_y0,_z0) (_x1,_y1,_z1) (_x2,_y2,_z2) (_x3,_y3,_z3)
end_command
_x0 = -CR
_y0 = -CR
_z0 = CH
_x1 = -CR
_y1 = CR
_z1 = CH
_x2 = CR
_y2 = CR
_z2 = CH
_x3 = CR
_y3 = -CR
_z3 = CH
command
  wall id=3 kn=n_stiff ks=s_stiff &
    face (_x0,_y0,_z0) (_x1,_y1,_z1) (_x2,_y2,_z2) (_x3,_y3,_z3)
end_command
;--- Derived and internal data ---
V_sum  = CR^2.0*pi*CH    ;Initial volume of the specimen
rmult  = 1.6
Vmean  = 4.0/3.0*pi*(hi_rad+lo_rad)^3/8 ;Mean volume of balls
nball  = (1.0 - poros) * V_sum / Vmean ; Ball number
r1red  = lo_rad / rmult
r2red  = hi_rad / rmult
command
```

```
    gen id=1,nball x=x_min,x_max y=y_min,y_max z=0.0,CH rad=r1red,r2red &
      filter ff_cylinder
    prop dens 2650 ks=s_stiff kn=n_stiff
    ini rad mul rmult
    pl wall whi ball whi
  end_command
end
make_model

cyc 1000
prop fric 0.1
solve av=0.001 max=0.001
save preflt.sav
call pcflt_3.fis
prop s_bond 1.0e15 n_bond 1.0e15
del wall 2
del wall 3
ini xv 0 yv 0 zv 0 xspin 0 yspin 0 zspin 0
solve av=0.001 max=0.001
ini xv 0 yv 0 zv 0 xspin 0 yspin 0 zspin 0
call fishcall.fis
call crk.fis
crk_init

;--- Fixing the particles along the side wall ---
def test
  bp = ball_head
  loop while bp # null
    b_zfix(bp) = 0
    b_color(bp)= 0
    cp    = b_clist(bp)
    loop while cp # null
      b1    = c_ball1(cp)
      b2    = c_ball2(cp)
      if b1 = bp
        if pointer_type(b2) = 101 ; Must be wall!
          b_zfix(bp) = 1
        endif
        cp = c_b1clist(cp)
      else
        cp = c_b2clist(cp)
```

```
    endif
   endLoop
   if b_zfix(bp) = 1
    b_xfix(bp)  = 1
    b_yfix(bp)  = 1
    b_rxfix(bp) = 1
    b_ryfix(bp) = 1
    b_rzfix(bp) = 1
    ; b_color(bp) = 1
   endif
   bp = b_next(bp)
  endLoop
end
test

del wall 1
plo create qqq
plo add ball red lred
save bhx_3.sav
ret
; EOF: bhx_3.dat
```

```
; FNAME: dom_3.fis
new
res bhx_3.sav
;****************** Define calculational conditions ******************
def ball_number ;Total ball number
  idmax = 0
  bp = ball_head
  loop while bp # null
    idmax = idmax + 1
    bp = b_next(bp)
  end_loop
  pipemax = idmax * 60
  connectmax = idmax * 20
  saf =1.3 ; Safety factor
end
ball_number
;------------------ Make arrays -------------------------------------
```

```
def make_array
  array pipe(pipemax)     ;Header to objects in a pipe
  array connect(connectmax) ;Header to objects in a connecter
  array v1(3,3)
  array v2(3,3)
  array vc1(3)
  array vc2(3)
end
make_array
;------------------ Create memory access number ------------------------
def connect_symbols
  CONNECT_BALL1 = 1 ; Pointer to domain 1
  CONNECT_BALL2 = 2 ; Pointer to domain 2
end
connect_symbols
def pipe_symbols
  PIPE_BALL1   = 1  ;  Pointer to a ball comprising a pipe
  PIPE_BALL2   = 2  ;  Pointer to a ball comprising a pipe
  PIPE_BALL3   = 3  ;  Pointer to a ball comprising a pipe
  PIPE_X       = 4
  PIPE_Y       = 5
  PIPE_Z       = 6
  PIPE_DOM1    = 7  ;  Pointer to domain 1
  PIPE_DOM2    = 8  ;  Pointer to domain 2
  PIPE_AP_ZERO = 9  ;  Residual aperture
  PIPE_PERM    = 10 ;  Permeability constant
  PIPE_ACTIVE  = 11 ;  = 1 if pipe is active, else 0
end
pipe_symbols
;******************                    Create                    connecters
**********************************
def make_connect
  n = 1
  loop i(1,idmax-1)
    bpi = find_ball(i)
    loop j(i+1,idmax)
      bpj = find_ball(j)
      maxdis = (b_rad(bpi)+b_rad(bpj))*saf
      distance =          (b_x(bpj)-b_x(bpi))^2
      distance = distance + (b_y(bpj)-b_y(bpi))^2
      distance = distance + (b_z(bpj)-b_z(bpi))^2
```

```
      distance = sqrt(distance)
      if distance < maxdis
        connect(n) = get_mem(3)
        mem(connect(n)+CONNECT_BALL1) = bpi
        mem(connect(n)+CONNECT_BALL2) = bpj
        n = n + 1
      end_if
    end_loop
  end_loop
  connectmax = n-1
end
make_connect
;------------------ Display for linked balls --------------------------
def ball_item_connect
  loop n(1,connectmax)
    id1 = b_id(mem(connect(n)+CONNECT_BALL1))
    id2 = b_id(mem(connect(n)+CONNECT_BALL2))
    command
      pro co 2 range id id1
      pro co 2 range id id2
    end_command
  end_loop
end
;ball_item_connect
;plot ball white red yellow ;ra color 2
;------------------ Display for lines ---------------------------------
def line_item_connect
  plot_item
  loop n(1,connectmax)
    vc1(1) = b_x(mem(connect(n)+CONNECT_BALL1))
    vc1(2) = b_y(mem(connect(n)+CONNECT_BALL1))
    vc1(3) = b_z(mem(connect(n)+CONNECT_BALL1))
    vc2(1) = b_x(mem(connect(n)+CONNECT_BALL2))
    vc2(2) = b_y(mem(connect(n)+CONNECT_BALL2))
    vc2(3) = b_z(mem(connect(n)+CONNECT_BALL2))
    status = draw_line(vc1,vc2)
  end_loop
end
;plot add fish line_item_connect red
;******************                Create                pipes
************************************
```

```
def make_pipe
  k = 1
  loop n(1,connectmax)
    v12_x = b_x(mem(connect(n)+CONNECT_BALL2))
    v12_x = v12_x - b_x(mem(connect(n)+CONNECT_BALL1))
    v12_y = b_y(mem(connect(n)+CONNECT_BALL2))
    v12_y = v12_y - b_y(mem(connect(n)+CONNECT_BALL1))
    v12_z = b_z(mem(connect(n)+CONNECT_BALL2))
    v12_z = v12_z - b_z(mem(connect(n)+CONNECT_BALL1))
    loop i(1,idmax)
      bp = find_ball(i)
      ;Vector from ball 1 to ball i
      v1i_x = b_x(bp)-b_x(mem(connect(n)+CONNECT_BALL1))
      v1i_y = b_y(bp)-b_y(mem(connect(n)+CONNECT_BALL1))
      v1i_z = b_z(bp)-b_z(mem(connect(n)+CONNECT_BALL1))
      ;Vector from ball 2 to ball i
      v2i_x = b_x(bp)-b_x(mem(connect(n)+CONNECT_BALL2))
      v2i_y = b_y(bp)-b_y(mem(connect(n)+CONNECT_BALL2))
      v2i_z = b_z(bp)-b_z(mem(connect(n)+CONNECT_BALL2))
      ip1i = v12_x * v1i_x + v12_y * v1i_y + v12_z * v1i_z
      if ip1i > 0.0
        ip2i = -v12_x * v2i_x - v12_y * v2i_y - v12_z * v2i_z
        if ip2i > 0.0
          distance = sqrt(v1i_x^2+v1i_y^2+v1i_z^2)
          distance = distance + sqrt(v2i_x^2+v2i_y^2+v2i_z^2)
          maxdis = b_rad(mem(connect(n)+CONNECT_BALL1))
          maxdis = maxdis + b_rad(mem(connect(n)+CONNECT_BALL2))
          maxdis = maxdis + b_rad(bp)*2
          maxdis = maxdis * saf
          if distance < maxdis
            pipe(k) = get_mem(12)
            mem(pipe(k)+PIPE_BALL1) = mem(connect(n)+CONNECT_BALL1)
            mem(pipe(k)+PIPE_BALL2) = mem(connect(n)+CONNECT_BALL2)
            mem(pipe(k)+PIPE_BALL3) = bp
            tmem = b_x(mem(connect(n)+CONNECT_BALL1))
            tmem = tmem + b_x(mem(connect(n)+CONNECT_BALL2))
            tmem = tmem + b_x(bp)
            mem(pipe(k)+PIPE_X) = tmem / 3.0
            tmem = b_y(mem(connect(n)+CONNECT_BALL1))
            tmem = tmem + b_y(mem(connect(n)+CONNECT_BALL2))
            tmem = tmem + b_y(bp)
```

```
          mem(pipe(k)+PIPE_Y) = tmem / 3.0
          tmem = b_z(mem(connect(n)+CONNECT_BALL1))
          tmem = tmem + b_z(mem(connect(n)+CONNECT_BALL2))
          tmem = tmem + b_z(bp)
          mem(pipe(k)+PIPE_Z) = tmem / 3.0
          mem(pipe(k)+PIPE_ACTIVE) = 1
          k = k + 1
        end_if
      end_if
    end_if
   end_loop
  end_loop
  pipemax = k-1
end
make_pipe
;------------------ Exclude excess pipes -----------------------------
def exclude_pipe
  loop n(1,pipemax-1)
    ii=out('Checked Pipe No. = ' +string(n))
    loop p(n+1, pipemax)
      distance = (mem(pipe(n)+PIPE_X)-mem(pipe(p)+PIPE_X))^2
      distance = distance + (mem(pipe(n)+PIPE_Y)-mem(pipe(p)+PIPE_Y))^2
      distance = distance + (mem(pipe(n)+PIPE_Z)-mem(pipe(p)+PIPE_Z))^2
      if distance < 1e-6
        mem(pipe(p)+PIPE_ACTIVE) = 0
      end_if
    end_loop
  end_loop
  k=1
  loop n(1,pipemax)
    if mem(pipe(n)+PIPE_ACTIVE) = 1
      pipe(k) = pipe(n)
      k=k+1
    end_if
  end_loop
  pipemax = k-1
end
exclude_pipe
;------------------ Display for pipes ---------------------------------
def poly_item_pipe
  plot_item
```

```
  loop n(1,pipemax)
    v1(1,1)=b_x(mem(pipe(n)+PIPE_BALL1))
    v1(2,1)=b_y(mem(pipe(n)+PIPE_BALL1))
    v1(3,1)=b_z(mem(pipe(n)+PIPE_BALL1))
    v1(1,2)=b_x(mem(pipe(n)+PIPE_BALL2))
    v1(2,2)=b_y(mem(pipe(n)+PIPE_BALL2))
    v1(3,2)=b_z(mem(pipe(n)+PIPE_BALL2))
    v1(1,3)=b_x(mem(pipe(n)+PIPE_BALL3))
    v1(2,3)=b_y(mem(pipe(n)+PIPE_BALL3))
    v1(3,3)=b_z(mem(pipe(n)+PIPE_BALL3))
    status = draw_poly(v1,3,1)
  end_loop
end
plot add fish poly_item_pipe red
save pipe_3.sav
;****************** Define calculational conditions ******************
def variable
  dommax = pipemax * 5
  sfa = 1.2
end
variable
;------------------ Make arrays -------------------------------------
def dom_make_arrays
  array dom(dommax) ;Header to objects in a domain
  array poly1(3,3)
  array poly2(3,3)
  array poly3(3,3)
  array poly4(3,3)
end
dom_make_arrays
;------------------ Create memory access number -----------------------
def dom_symbols
  DOM_BALL1  = 1  ; Pointer to list of balls comprising domain
  DOM_BALL2  = 2
  DOM_BALL3  = 3
  DOM_BALL4  = 4
  DOM_X      = 5  ;  X coordinate (not updated automatically)
  DOM_Y      = 6  ;  Y coordinate
  DOM_Z      = 7  ;  Z coordinate
  DOM_PRESS  = 8  ;  Pressure
  DOM_FIX    = 9
```

```
  DOM_VSUM   = 10 ;  Flow volume-sum
  DOM_VOL    = 11 ;  Domain volume
  DOM_ACTIVE = 12 ;  = 1 if domain is active; else 0
  DOM_PIPE   = 13 ;  Bottom pipe of a domain
end
dom_symbols
;******************                    Create                    domains
************************************
def make_domain
  loop n(1,pipemax)
    mem(pipe(n)+PIPE_DOM1) = null
    mem(pipe(n)+PIPE_DOM2) = null
  end_loop
  k = 1
  loop n(1,pipemax)
    ii=out('Pipe No. = ' +string(n))
;------------------ Make a normal vector on the triangle --------------
    v12_x = b_x(mem(pipe(n)+PIPE_BALL2))-b_x(mem(pipe(n)+PIPE_BALL1))
    v12_y = b_y(mem(pipe(n)+PIPE_BALL2))-b_y(mem(pipe(n)+PIPE_BALL1))
    v12_z = b_z(mem(pipe(n)+PIPE_BALL2))-b_z(mem(pipe(n)+PIPE_BALL1))
    v13_x = b_x(mem(pipe(n)+PIPE_BALL3))-b_x(mem(pipe(n)+PIPE_BALL1))
    v13_y = b_y(mem(pipe(n)+PIPE_BALL3))-b_y(mem(pipe(n)+PIPE_BALL1))
    v13_z = b_z(mem(pipe(n)+PIPE_BALL3))-b_z(mem(pipe(n)+PIPE_BALL1))
    vpn_x = v12_y * v13_z - v12_z * v13_y
    vpn_y = v12_z * v13_x - v12_x * v13_z
    vpn_z = v12_x * v13_y - v12_y * v13_x
    bp4 = null
    bp5 = null
    maxdis1 = b_rad(mem(pipe(n)+PIPE_BALL1))
    maxdis1 = maxdis1 + b_rad(mem(pipe(n)+PIPE_BALL2))
    maxdis1 = maxdis1 + b_rad(mem(pipe(n)+PIPE_BALL3))
    maxdis1 = maxdis1 + hi_rad*3.0
    maxdis1 = maxdis1 * sfa
    maxdis2 = maxdis1
    loop i(1,idmax)
      bp=find_ball(i)
      v1i_x = b_x(bp)-b_x(mem(pipe(n)+PIPE_BALL1))
      v1i_y = b_y(bp)-b_y(mem(pipe(n)+PIPE_BALL1))
      v1i_z = b_z(bp)-b_z(mem(pipe(n)+PIPE_BALL1))
      v2i_x = b_x(bp)-b_x(mem(pipe(n)+PIPE_BALL2))
      v2i_y = b_y(bp)-b_y(mem(pipe(n)+PIPE_BALL2))
```

```
  v2i_z = b_z(bp)-b_z(mem(pipe(n)+PIPE_BALL2))
  v3i_x = b_x(bp)-b_x(mem(pipe(n)+PIPE_BALL3))
  v3i_y = b_y(bp)-b_y(mem(pipe(n)+PIPE_BALL3))
  v3i_z = b_z(bp)-b_z(mem(pipe(n)+PIPE_BALL3))
  ip = vpn_x * v1i_x + vpn_y * v1i_y + vpn_z * v1i_z
  distance =           sqrt(v1i_x^2+v1i_y^2+v1i_z^2)
  distance = distance + sqrt(v2i_x^2+v2i_y^2+v2i_z^2)
  distance = distance + sqrt(v3i_x^2+v3i_y^2+v3i_z^2)
  if ip > 1e-6
    if distance < maxdis1
      maxdis1 = distance
      bp4 = bp
    end_if
  end_if
  if ip < -1e-6
    if distance < maxdis2
      maxdis2 = distance
      bp5 = bp
    end_if
  end_if
end_loop
if bp4 # null
  dom(k) = get_mem(14)
  mem(dom(k)+DOM_BALL1) = mem(pipe(n)+PIPE_BALL1)
  mem(dom(k)+DOM_BALL2) = mem(pipe(n)+PIPE_BALL2)
  mem(dom(k)+DOM_BALL3) = mem(pipe(n)+PIPE_BALL3)
  mem(dom(k)+DOM_BALL4) = bp4
  mem(dom(k)+DOM_ACTIVE) = 1
  mem(dom(k)+DOM_PIPE)  = pipe(n)
  mem(pipe(n)+PIPE_DOM1) = dom(k)
  k=k+1
end_if
if bp5 # null
  dom(k) = get_mem(14)
  mem(dom(k)+DOM_BALL1) = mem(pipe(n)+PIPE_BALL1)
  mem(dom(k)+DOM_BALL2) = mem(pipe(n)+PIPE_BALL2)
  mem(dom(k)+DOM_BALL3) = mem(pipe(n)+PIPE_BALL3)
  mem(dom(k)+DOM_BALL4) = bp5
  mem(dom(k)+DOM_ACTIVE) = 1
  mem(dom(k)+DOM_PIPE)  = pipe(n)
  mem(pipe(n)+PIPE_DOM2) = dom(k)
```

```
    k=k+1
   end_if
  end_loop
  dommax = k-1
  ;  -------------------------------  Domain volume calculation --------
  loop j(1, dommax)
   v12_xx                    =                    b_x(mem(dom(j)+DOM_BALL2))-
b_x(mem(dom(j)+DOM_BALL1))
   v12_yy                    =                    b_y(mem(dom(j)+DOM_BALL2))-
b_y(mem(dom(j)+DOM_BALL1))
   v12_zz                    =                    b_z(mem(dom(j)+DOM_BALL2))-
b_z(mem(dom(j)+DOM_BALL1))
   v13_xx                    =                    b_x(mem(dom(j)+DOM_BALL3))-
b_x(mem(dom(j)+DOM_BALL1))
   v13_yy                    =                    b_y(mem(dom(j)+DOM_BALL3))-
b_y(mem(dom(j)+DOM_BALL1))
   v13_zz                    =                    b_z(mem(dom(j)+DOM_BALL3))-
b_z(mem(dom(j)+DOM_BALL1))
   Area_123                                                                  =
(V12_xx^2+V12_yy^2+v12_zz^2)*(V13_xx^2+V13_yy^2+v13_zz^2)/2
   vpn_xx = v12_yy*v13_zz - v12_zz*v13_yy
   vpn_yy = v12_zz*v13_xx - v12_xx*v13_zz
   vpn_zz = v12_xx*v13_yy - v12_yy*v13_xx
   d_plane = vpn_xx*b_x(mem(dom(j)+DOM_BALL1))
   d_plane = d_plane +  vpn_yy*b_y(mem(dom(j)+DOM_BALL1))
   d_plane = d_plane +  vpn_zz*b_z(mem(dom(j)+DOM_BALL1))
   d_plane = -d_plane
   nd_plane = vpn_xx*b_x(mem(dom(j)+DOM_BALL4))
   nd_plane = nd_plane + vpn_yy*b_y(mem(dom(j)+DOM_BALL4))
   nd_plane = abs (nd_plane + vpn_zz*b_z(mem(dom(j)+DOM_BALL4)) +
d_plane)
   dd_plane = sqrt (vpn_xx^2 + vpn_yy^2 + vpn_zz^2)
   dto_plane = nd_plane / dd_plane
   mem(dom(j)+DOM_VOL) = Area_123*dto_plane / 3
   ii= out ('Domain volume = '+ string (mem(dom(j)+DOM_VOL)))
  end_loop
end
make_domain
;------------------ Exclude excess domains ----------------------------
def exc_domain
  ;------------ Center of a domain ------------
```

```
 loop n(1,dommax)
   tmem                                                                    =
b_x(mem(dom(n)+DOM_BALL1))+b_x(mem(dom(n)+DOM_BALL2))
   tmem                          =                 tmem                    +
b_x(mem(dom(n)+DOM_BALL3))+b_x(mem(dom(n)+DOM_BALL4))
   mem(dom(n)+DOM_X) = tmem / 4.0
   tmem                                                                    =
b_y(mem(dom(n)+DOM_BALL1))+b_y(mem(dom(n)+DOM_BALL2))
   tmem                          =                 tmem                    +
b_y(mem(dom(n)+DOM_BALL3))+b_y(mem(dom(n)+DOM_BALL4))
   mem(dom(n)+DOM_Y) = tmem / 4.0
   tmem                                                                    =
b_z(mem(dom(n)+DOM_BALL1))+b_z(mem(dom(n)+DOM_BALL2))
   tmem                          =                 tmem                    +
b_z(mem(dom(n)+DOM_BALL3))+b_z(mem(dom(n)+DOM_BALL4))
   mem(dom(n)+DOM_Z) = tmem / 4.0
 end_loop
 ;------------ Distance between centers --------------
 loop n(1,dommax-1)
  ii=out('Checking Dom No. = ' +string(n))
  loop p(n+1,dommax)
    distance =          (mem(dom(n)+DOM_X)-mem(dom(p)+DOM_X))^2
    distance = distance + (mem(dom(n)+DOM_Y)-mem(dom(p)+DOM_Y))^2
    distance = distance + (mem(dom(n)+DOM_Z)-mem(dom(p)+DOM_Z))^2
    if distance < 1e-6
      mem(dom(p)+DOM_ACTIVE) = 0
      if mem(mem(dom(p)+DOM_PIPE)+PIPE_DOM1)=dom(p)
        mem(mem(dom(p)+DOM_PIPE)+PIPE_DOM1)=dom(n)
      end_if
      if mem(mem(dom(p)+DOM_PIPE)+PIPE_DOM2)=dom(p)
        mem(mem(dom(p)+DOM_PIPE)+PIPE_DOM2)=dom(n)
      end_if
    end_if
  end_loop
 end_loop
 ;------------ Replace excess domains -------------
 k=1
 loop n(1,dommax)
  if mem(dom(n)+DOM_ACTIVE) = 1
    dom(k) = dom(n)
    k=k+1
```

```
    end_if
  end_loop
  dommax = k-1
  loop n(1,pipemax)
    mem(pipe(n)+PIPE_ACTIVE) = 0
    if mem(pipe(n)+PIPE_DOM1) # null
      if mem(pipe(n)+PIPE_DOM2) # null
        mem(pipe(n)+PIPE_ACTIVE) = 1
      endif
    endif
  endloop
end
exc_domain
;----------------- Display for domains --------------------------------
def poly_item_domain
  plot_item
  loop n(1,dommax)
    poly1(1,1)=b_x(mem(dom(n)+DOM_BALL1))
    poly1(2,1)=b_y(mem(dom(n)+DOM_BALL1))
    poly1(3,1)=b_z(mem(dom(n)+DOM_BALL1))
    poly1(1,2)=b_x(mem(dom(n)+DOM_BALL2))
    poly1(2,2)=b_y(mem(dom(n)+DOM_BALL2))
    poly1(3,2)=b_z(mem(dom(n)+DOM_BALL2))
    poly1(1,3)=b_x(mem(dom(n)+DOM_BALL3))
    poly1(2,3)=b_y(mem(dom(n)+DOM_BALL3))
    poly1(3,3)=b_z(mem(dom(n)+DOM_BALL3))
    status = draw_poly(poly1,3,1)
    poly2(1,1)=b_x(mem(dom(n)+DOM_BALL1))
    poly2(2,1)=b_y(mem(dom(n)+DOM_BALL1))
    poly2(3,1)=b_z(mem(dom(n)+DOM_BALL1))
    poly2(1,2)=b_x(mem(dom(n)+DOM_BALL2))
    poly2(2,2)=b_y(mem(dom(n)+DOM_BALL2))
    poly2(3,2)=b_z(mem(dom(n)+DOM_BALL2))
    poly2(1,3)=b_x(mem(dom(n)+DOM_BALL4))
    poly2(2,3)=b_y(mem(dom(n)+DOM_BALL4))
    poly2(3,3)=b_z(mem(dom(n)+DOM_BALL4))
    status = draw_poly(poly2,3,1)
    poly3(1,1)=b_x(mem(dom(n)+DOM_BALL2))
    poly3(2,1)=b_y(mem(dom(n)+DOM_BALL2))
    poly3(3,1)=b_z(mem(dom(n)+DOM_BALL2))
    poly3(1,2)=b_x(mem(dom(n)+DOM_BALL3))
```

```
    poly3(2,2)=b_y(mem(dom(n)+DOM_BALL3))
    poly3(3,2)=b_z(mem(dom(n)+DOM_BALL3))
    poly3(1,3)=b_x(mem(dom(n)+DOM_BALL4))
    poly3(2,3)=b_y(mem(dom(n)+DOM_BALL4))
    poly3(3,3)=b_z(mem(dom(n)+DOM_BALL4))
    status = draw_poly(poly3,3,1)
    poly4(1,1)=b_x(mem(dom(n)+DOM_BALL3))
    poly4(2,1)=b_y(mem(dom(n)+DOM_BALL3))
    poly4(3,1)=b_z(mem(dom(n)+DOM_BALL3))
    poly4(1,2)=b_x(mem(dom(n)+DOM_BALL1))
    poly4(2,2)=b_y(mem(dom(n)+DOM_BALL1))
    poly4(3,2)=b_z(mem(dom(n)+DOM_BALL1))
    poly4(1,3)=b_x(mem(dom(n)+DOM_BALL4))
    poly4(2,3)=b_y(mem(dom(n)+DOM_BALL4))
    poly4(3,3)=b_z(mem(dom(n)+DOM_BALL4))
    status = draw_poly(poly4,3,1)
  end_loop
end
plot add fish poly_item_domain red
save dom_3.sav
; EOF: dom_3.fis
```

```
; FNAME: dom1_3.fis
new
res dom_3.sav
;****************** Set properties for flow cal. **********************
def flow_props
  loop n(1,pipemax)
    if mem(pipe(n)+PIPE_ACTIVE) = 1
      mem(pipe(n)+PIPE_AP_ZERO) = ap_zero ;Set in Darcy_fis_3
      mem(pipe(n)+PIPE_PERM)    = perm    ;Set in Darcy_fis_3
    endif
  endLoop
end
;****************** Set flow-calc boundary flag & pressure ************
def flow_bc
  ; Range specified with (x1_bc .. x2_bc) and (y1_bc .. y2_bc)
  ;  and (z1_bc .. z2_bc)
  ; flow_set:  1  .. fix pressure
  ;            2  .. free pressure
```

```
;           3  .. set pressure to p_given
;           4  .. linear pressure distribution between pp_1 and pp_2
;           5  .. logarithmic pressure distribution between pp_1 and pp_2
 len0 = z1_bc + 0.05*(z2_bc-z1_bc)
 lenlog = ln (len0/z2_bc)
 loop n(1,dommax)
  tmem                                                                    =
b_x(mem(dom(n)+DOM_BALL1))+b_x(mem(dom(n)+DOM_BALL2))
  tmem                          =                     tmem                +
b_x(mem(dom(n)+DOM_BALL3))+b_x(mem(dom(n)+DOM_BALL4))
  mem(dom(n)+DOM_X) = tmem / 4.0
  tmem                                                                    =
b_y(mem(dom(n)+DOM_BALL1))+b_y(mem(dom(n)+DOM_BALL2))
  tmem                          =                     tmem                +
b_y(mem(dom(n)+DOM_BALL3))+b_y(mem(dom(n)+DOM_BALL4))
  mem(dom(n)+DOM_Y) = tmem / 4.0
  tmem                                                                    =
b_z(mem(dom(n)+DOM_BALL1))+b_z(mem(dom(n)+DOM_BALL2))
  tmem                          =                     tmem                +
b_z(mem(dom(n)+DOM_BALL3))+b_z(mem(dom(n)+DOM_BALL4))
  mem(dom(n)+DOM_Z) = tmem / 4.0
  xdom = mem(dom(n)+DOM_X)
  ydom = mem(dom(n)+DOM_Y)
  zdom = mem(dom(n)+DOM_Z)
  if xdom > x1_bc
   if xdom < x2_bc
    if ydom > y1_bc
     if ydom < y2_bc
      if zdom > z1_bc
       if zdom < z2_bc
        caseOf flow_set
         case 1
          mem(dom(n)+DOM_FIX) = 1
         case 2
          mem(dom(n)+DOM_FIX) = 0
         case 3
          mem(dom(n)+DOM_PRESS) = p_given
         case 4
          zdom = mem(dom(n)+DOM_Z)
          if zdom > len0
```

```
                mem(dom(n)+DOM_PRESS) = pp_1 + (pp_2-pp_1)/(z2_bc-
len0)*(zdom-len0)
              else
                mem(dom(n)+DOM_PRESS) = pp_1
              endif
            case 5
              zdom = mem(dom(n)+DOM_Z)
              if zdom > len0
                mem(dom(n)+DOM_PRESS) = pp_2 + pp_1/lenlog * (lenlog -
ln(len0/zdom))
              else
                mem(dom(n)+DOM_PRESS) = pp_1
              endif
          endCase
        endif
      endif
    endif
  endif
 endloop
end
;************ Plot pressures as filled circles with various rad. *****
def pressure
 plot_item
 array pvec(dim)
 ;----- First, get max pressure --------
 press_max = 0.0
 loop n(1,dommax)
  press_max = max(press_max,mem(dom(n)+DOM_PRESS))
 end_loop
 if press_max = 0.0
  exit
 end_if
 loop n(1,dommax)
  pvec(1) = mem(dom(n)+DOM_X)
  pvec(2) = mem(dom(n)+DOM_Y)
  pvec(3) = mem(dom(n)+DOM_Z)
  rad = 0.3 * mem(dom(n)+DOM_PRESS) / press_max
  if rad > 0.01
   status = fill_circle(pvec,rad)
```

```
   endif
  endloop
end
;****************** Run flow calculation
*****************************
def flow_run
  while_stepping
  n_rep = n_rep + 1
  if n_rep < 10 ; 10 flow calculation at a pfc cycle
    exit
  endif
  n_rep=0
  summflow=0.0
  flow_dt=0.1
  ;-------------------- Flow in pipes ----------------------
  loop n(1,pipemax)
    if mem(pipe(n)+PIPE_ACTIVE) = 1
      dom1 = mem(pipe(n)+PIPE_DOM1)
      dom2 = mem(pipe(n)+PIPE_DOM2)
      rsum =        (mem(dom1+DOM_X)-mem(dom2+DOM_X))^2
      rsum = rsum + (mem(dom1+DOM_Y)-mem(dom2+DOM_Y))^2
      rsum = rsum + (mem(dom1+DOM_Z)-mem(dom2+DOM_Z))^2
      rsum = sqrt(rsum)
      pdiff = mem(dom1+DOM_PRESS) - mem(dom2+DOM_PRESS)
      per_fac = mem(pipe(n)+PIPE_PERM)
      fnorm = 0.0
      cp = b_clist(mem(pipe(n)+PIPE_BALL1))
      loop while cp # null
        if c_ball1(cp) = mem(pipe(n)+PIPE_BALL1)
          if c_ball2(cp) = mem(pipe(n)+PIPE_BALL2)
            fnorm = fnorm + c_nforce(cp)
            cp = c_b1clist(cp)
          else
            if c_ball2(cp) = mem(pipe(n)+PIPE_BALL3)
              fnorm = fnorm + c_nforce(cp)
              cp = c_b1clist(cp)
            else
              cp = c_b1clist(cp)
            endif
          endif
        else
```

```
        if c_ball1(cp) = mem(pipe(n)+PIPE_BALL2)
          fnorm = fnorm + c_nforce(cp)
          cp = c_b2clist(cp)
        else
          if c_ball1(cp) = mem(pipe(n)+PIPE_BALL3)
            fnorm = fnorm + c_nforce(cp)
            cp = c_b2clist(cp)
          else
            cp = c_b2clist(cp)
          endif
        endif
      endif
    endloop
    cp = b_clist(mem(pipe(n)+PIPE_BALL2))
    loop while cp # null
      if c_ball1(cp) = mem(pipe(n)+PIPE_BALL2)
        if c_ball2(cp) = mem(pipe(n)+PIPE_BALL3)
          fnorm = fnorm + c_nforce(cp)
          cp = c_b1clist(cp)
        else
          cp = c_b1clist(cp)
        endif
      else
        if c_ball1(cp) = mem(pipe(n)+PIPE_BALL3)
          fnorm = fnorm + c_nforce(cp)
          cp = c_b2clist(cp)
        else
          cp = c_b2clist(cp)
        endif
      endif
    endloop
    fnorm = fnorm/3.0
    aper0 = mem(pipe(n)+PIPE_AP_ZERO)
    if fnorm > 0.0
      aper = aper0 * Fap_zero / (fnorm + Fap_zero)
    else
      if gap_mul = 0.0
        aper = aper0
      else
        xdif12=b_x(mem(pipe(n)+PIPE_BALL1))-
b_x(mem(pipe(n)+PIPE_BALL2))
```

```
        ydif12=b_y(mem(pipe(n)+PIPE_BALL1))-
b_y(mem(pipe(n)+PIPE_BALL2))
        zdif12=b_z(mem(pipe(n)+PIPE_BALL1))-
b_z(mem(pipe(n)+PIPE_BALL2))
        xdif13=b_x(mem(pipe(n)+PIPE_BALL1))-
b_x(mem(pipe(n)+PIPE_BALL3))
        ydif13=b_y(mem(pipe(n)+PIPE_BALL1))-
b_y(mem(pipe(n)+PIPE_BALL3))
        zdif13=b_z(mem(pipe(n)+PIPE_BALL1))-
b_z(mem(pipe(n)+PIPE_BALL3))
        xdif23=b_x(mem(pipe(n)+PIPE_BALL2))-
b_x(mem(pipe(n)+PIPE_BALL3))
        ydif23=b_y(mem(pipe(n)+PIPE_BALL2))-
b_y(mem(pipe(n)+PIPE_BALL3))
        zdif23=b_z(mem(pipe(n)+PIPE_BALL2))-
b_z(mem(pipe(n)+PIPE_BALL3))
        expdif =         b_rad(mem(pipe(n)+PIPE_BALL1))
        expdif = expdif + b_rad(mem(pipe(n)+PIPE_BALL2))
        expdif = expdif + b_rad(mem(pipe(n)+PIPE_BALL3))
        expdif = expdif * 2.0
        gap =       sqrt(xdif12^2+ydif12^2+zdif12^2)
        gap = gap + sqrt(xdif13^2+ydif13^2+zdif13^2)
        gap = gap + sqrt(xdif23^2+ydif23^2+zdif23^2)
        gap  = gap - expdif
        aper = aper0 + gap_mul * gap
      endif
    endif
    qpipe = 0.196325*pdiff * per_fac * aper^4 / rsum
    ; ---------------- Calculation of optimum flow_dt ---------------------
    vol_averg = (mem(dom1+DOM_VOL)+mem(dom2+DOM_VOL))/2
    dt_opt = 5.09 * rsum * vol_averg / (bulk_w * aper^4)
    if dt_opt < flow_dt
       flow_dt = dt_opt
    endif
    dvol  = qpipe * flow_dt
    mem(dom1+DOM_VSUM) = mem(dom1+DOM_VSUM) - dvol
    mem(dom2+DOM_VSUM) = mem(dom2+DOM_VSUM) + dvol
    ;---------------- Permeability of the whole model ---------------------
    height1=mem(dom1+DOM_Z)
    height2=mem(dom2+DOM_Z)
    if height2 > 2.5
```

```
        if height1 < 2.5
          summflow = summflow+qpipe
        endif
      endif
      if height1 > 2.5
        if height2 < 2.5
          summflow = summflow+qpipe
        endif
      endif
    end_if
  endLoop
  Totalperm = 0.001*summflow*2.2714/(3.1415926*1.143^2*4.03e4)
  ;---------------- Pressure-changes in domains --------------------
  loop n(1,dommax)
    if mem(dom(n)+DOM_FIX) = 0
      delta_p = mem(dom(n)+DOM_VSUM) * bulk_w /
mem(dom(n)+DOM_VOL)  ;assume vol <> 1
      mem(dom(n)+DOM_PRESS) = mem(dom(n)+DOM_PRESS) + delta_p
    endif
    mem(dom(n)+DOM_VSUM) = 0.0
  endLoop
  ;-------------------------- Pressure on balls ----------------------
  bp = ball_head
  loop while bp # null
    b_xfap(bp) = 0.0
    b_yfap(bp) = 0.0
    b_zfap(bp) = 0.0
    bp = b_next(bp)
  endloop
  loop n(1,dommax)
    ppp = mem(dom(n)+DOM_PRESS)
    bp1 = mem(dom(n)+DOM_BALL1)
    bp2 = mem(dom(n)+DOM_BALL2)
    bp3 = mem(dom(n)+DOM_BALL3)
    bp4 = mem(dom(n)+DOM_BALL4)
    ;------------ Applied force acting on ball 1 ---------
    v12_x = b_x(bp2)-b_x(bp1)
    v12_y = b_y(bp2)-b_y(bp1)
    v12_z = b_z(bp2)-b_z(bp1)
    v13_x = b_x(bp3)-b_x(bp1)
    v13_y = b_y(bp3)-b_y(bp1)
```

```
v13_z = b_z(bp3)-b_z(bp1)
v14_x = b_x(bp4)-b_x(bp1)
v14_y = b_y(bp4)-b_y(bp1)
v14_z = b_z(bp4)-b_z(bp1)
v12   = sqrt(v12_x^2 + v12_y^2 + v12_z^2)
v13   = sqrt(v13_x^2 + v13_y^2 + v13_z^2)
v14   = sqrt(v14_x^2 + v14_y^2 + v14_z^2)
b12_x = b_x(bp1) + v12_x/v12 * b_rad(bp1)
b12_y = b_y(bp1) + v12_y/v12 * b_rad(bp1)
b12_z = b_z(bp1) + v12_z/v12 * b_rad(bp1)
b13_x = b_x(bp1) + v13_x/v13 * b_rad(bp1)
b13_y = b_y(bp1) + v13_y/v13 * b_rad(bp1)
b13_z = b_z(bp1) + v13_z/v13 * b_rad(bp1)
b14_x = b_x(bp1) + v14_x/v14 * b_rad(bp1)
b14_y = b_y(bp1) + v14_y/v14 * b_rad(bp1)
b14_z = b_z(bp1) + v14_z/v14 * b_rad(bp1)
a = sqrt((b12_x-b13_x)^2+(b12_y-b13_y)^2+(b12_z-b13_z)^2)
b = sqrt((b12_x-b14_x)^2+(b12_y-b14_y)^2+(b12_z-b14_z)^2)
c = sqrt((b13_x-b14_x)^2+(b13_y-b14_y)^2+(b13_z-b14_z)^2)
s = (a+b+c)/2.0
s1 = sqrt(s*(s-a)*(s-b)*(s-c))
vf1_x = b_x(bp1)-(b12_x+b13_x+b14_x)/3.0
vf1_y = b_y(bp1)-(b12_y+b13_y+b14_y)/3.0
vf1_z = b_z(bp1)-(b12_z+b13_z+b14_z)/3.0
f1 = sqrt(vf1_x^2+vf1_y^2+vf1^2)
b_xfap(bp1) = b_xfap(bp1) + ppp * vf1_x/f1
b_yfap(bp1) = b_yfap(bp1) + ppp * vf1_y/f1
b_zfap(bp1) = b_zfap(bp1) + ppp * vf1_z/f1
;------------ Applied force acting on ball 2 ---------
v21_x = -v12_x
v21_y = -v12_y
v21_z = -v12_z
v23_x = b_x(bp3)-b_x(bp2)
v23_y = b_y(bp3)-b_y(bp2)
v23_z = b_z(bp3)-b_z(bp2)
v24_x = b_x(bp4)-b_x(bp2)
v24_y = b_y(bp4)-b_y(bp2)
v24_z = b_z(bp4)-b_z(bp2)
v21   = v12
v23   = sqrt(v23_x^2+v23_y^2+v23_z^2)
v24   = sqrt(v24_x^2+v24_y^2+v24_z^2)
```

```
b21_x = b_x(bp2) + v21_x/v21 * b_rad(bp2)
b21_y = b_y(bp2) + v21_y/v21 * b_rad(bp2)
b21_z = b_z(bp2) + v21_z/v21 * b_rad(bp2)
b23_x = b_x(bp2) + v23_x/v23 * b_rad(bp2)
b23_y = b_y(bp2) + v23_y/v23 * b_rad(bp2)
b23_z = b_z(bp2) + v23_z/v23 * b_rad(bp2)
b24_x = b_x(bp2) + v24_x/v24 * b_rad(bp2)
b24_y = b_y(bp2) + v24_y/v24 * b_rad(bp2)
b24_z = b_z(bp2) + v24_z/v24 * b_rad(bp2)
a = sqrt((b21_x-b23_x)^2+(b21_y-b23_y)^2+(b21_z-b23_z)^2)
b = sqrt((b21_x-b24_x)^2+(b21_y-b24_y)^2+(b21_z-b24_z)^2)
c = sqrt((b23_x-b24_x)^2+(b23_y-b24_y)^2+(b23_z-b24_z)^2)
s = (a+b+c)/2.0
s2 = sqrt(s*(s-a)*(s-b)*(s-c))
vf2_x = b_x(bp2)-(b21_x+b23_x+b24_x)/3.0
vf2_y = b_y(bp2)-(b21_y+b23_y+b24_y)/3.0
vf2_z = b_z(bp2)-(b21_z+b23_z+b24_z)/3.0
f2 = sqrt(vf2_x^2+vf2_y^2+vf2^2)
b_xfap(bp2) = b_xfap(bp2) + ppp * vf2_x/f2
b_yfap(bp2) = b_yfap(bp2) + ppp * vf2_y/f2
b_zfap(bp2) = b_zfap(bp2) + ppp * vf2_z/f2
;------------ Applied force acting on ball 3 ---------
v31_x = -v13_x
v31_y = -v13_y
v31_z = -v13_z
v32_x = -v23_x
v32_y = -v23_y
v32_z = -v23_z
v34_x = b_x(bp4)-b_x(bp1)
v34_y = b_y(bp4)-b_y(bp1)
v34_z = b_z(bp4)-b_z(bp1)
v31   = v13
v32   = v23
v34   = sqrt(v14_x^2 + v14_y^2 + v14_z^2)
b31_x = b_x(bp3) + v31_x/v31 * b_rad(bp3)
b31_y = b_y(bp3) + v31_y/v31 * b_rad(bp3)
b31_z = b_z(bp3) + v31_z/v31 * b_rad(bp3)
b32_x = b_x(bp3) + v32_x/v32 * b_rad(bp3)
b32_y = b_y(bp3) + v32_y/v32 * b_rad(bp3)
b32_z = b_z(bp3) + v32_z/v32 * b_rad(bp3)
b34_x = b_x(bp3) + v34_x/v34 * b_rad(bp3)
```

```
b34_y = b_y(bp3) + v34_y/v34 * b_rad(bp3)
b34_z = b_z(bp3) + v34_z/v34 * b_rad(bp3)
a = sqrt((b31_x-b32_x)^2+(b31_y-b32_y)^2+(b31_z-b32_z)^2)
b = sqrt((b32_x-b34_x)^2+(b32_y-b34_y)^2+(b32_z-b34_z)^2)
c = sqrt((b31_x-b34_x)^2+(b31_y-b34_y)^2+(b31_z-b34_z)^2)
s = (a+b+c)/2.0
s3 = sqrt(s*(s-a)*(s-b)*(s-c))
vf3_x = b_x(bp3)-(b32_x+b31_x+b34_x)/3.0
vf3_y = b_y(bp3)-(b32_y+b31_y+b34_y)/3.0
vf3_z = b_z(bp3)-(b32_z+b31_z+b34_z)/3.0
f3 = sqrt(vf3_x^2+vf3_y^2+vf3^2)
b_xfap(bp3) = b_xfap(bp3) + ppp * vf3_x/f3
b_yfap(bp3) = b_yfap(bp3) + ppp * vf3_y/f3
b_zfap(bp3) = b_zfap(bp3) + ppp * vf3_z/f3
;------------ Applied force acting on ball 4 ---------
v41_x = -v14_x
v41_y = -v14_y
v41_z = -v14_z
v42_x = -v24_x
v42_y = -v24_y
v42_z = -v24_z
v43_x = -v34_x
v43_y = -v34_y
v43_z = -v34_z
v41   = v14
v42   = v24
v43   = v34
b41_x = b_x(bp4) + v41_x/v41 * b_rad(bp4)
b41_y = b_y(bp4) + v41_y/v41 * b_rad(bp4)
b41_z = b_z(bp4) + v41_z/v41 * b_rad(bp4)
b42_x = b_x(bp4) + v42_x/v42 * b_rad(bp4)
b42_y = b_y(bp4) + v42_y/v42 * b_rad(bp4)
b42_z = b_z(bp4) + v42_z/v42 * b_rad(bp4)
b43_x = b_x(bp4) + v43_x/v43 * b_rad(bp4)
b43_y = b_y(bp4) + v43_y/v43 * b_rad(bp4)
b43_z = b_z(bp4) + v43_z/v43 * b_rad(bp4)
a = sqrt((b41_x-b42_x)^2+(b41_y-b42_y)^2+(b41_z-b42_z)^2)
b = sqrt((b41_x-b43_x)^2+(b41_y-b43_y)^2+(b41_z-b43_z)^2)
c = sqrt((b42_x-b43_x)^2+(b42_y-b43_y)^2+(b42_z-b43_z)^2)
s = (a+b+c)/2.0
s4 = sqrt(s*(s-a)*(s-b)*(s-c))
```

```
    vf4_x = b_x(bp4)-(b42_x+b43_x+b41_x)/3.0
    vf4_y = b_y(bp4)-(b42_y+b43_y+b41_y)/3.0
    vf4_z = b_z(bp4)-(b42_z+b43_z+b41_z)/3.0
    f4 = sqrt(vf4_x^2+vf4_y^2+vf4^2)
    b_xfap(bp3) = b_xfap(bp3) + ppp * vf3_x/f3
    b_yfap(bp3) = b_yfap(bp3) + ppp * vf3_y/f3
    b_zfap(bp3) = b_zfap(bp3) + ppp * vf3_z/f3
  endloop
end
hist id=10 Totalperm
hist id=11 summflow
save dom1_3.sav
; EOF: dom1_3.fis
```

; FNAME: **darcy_fis_3.dat**

```
; "Darcy" flow test  - FISH formulation
set echo off
res dom1_3.sav
;------------------ Variable setting ----------------------------------
set ap_zero=0.01 perm=0.05  gap_mul=0.0 Fap_zero=1e10
set bulk_w=2.15e9 flow_dt=0.1
prop n_bond=1e2 s_bond=1e2
;prop pb_nstren=3.5e15 pb_sstren=9.3e15 pb_rad=0.15 fric=0.55
;prop pb_kn=9.8e10 pb_ks=4.3e10
flow_props
def put_walls
  _x0 = -CR
  _y0 = -CR
  _z0 = 0.0
  _x1 = CR
  _y1 = -CR
  _z1 = 0.0
  _x2 = CR
  _y2 = CR
  _z2 = 0.0
  _x3 = -CR
  _y3 = CR
  _z3 = 0.0
  command
```

```
    wall id=2 kn=n_stiff ks=s_stiff &
      face (_x0,_y0,_z0) (_x1,_y1,_z1) (_x2,_y2,_z2) (_x3,_y3,_z3)
  end_command
  _x0 = -CR
  _y0 = -CR
  _z0 = CH
  _x1 = -CR
  _y1 = CR
  _z1 = CH
  _x2 = CR
  _y2 = CR
  _z2 = CH
  _x3 = CR
  _y3 = -CR
  _z3 = CH
  command
    wall id=3 kn=n_stiff ks=s_stiff &
      face (_x0,_y0,_z0) (_x1,_y1,_z1) (_x2,_y2,_z2) (_x3,_y3,_z3)
  end_command
end
put_walls
;----------------- Set boundary pressure conditions -------------------
set    flow_set=1    x1_bc=-1.143    x2_bc=1.143    y1_bc=-1.143    y2_bc=1.143
z1_bc=0.0  z2_bc=4.572
flow_bc ; Model fix condition
set flow_set=5 pp_1=2.0e5 pp_2=0.0 ;  Logarithmic pressure distribution
flow_bc ;
;------------------ Pressure circle display --------------------------
plo crea pres
plo add ball red red
plo add fish pressure white
plo add cforce black yellow
plo add vel blue
plo sho
plot set distance 15.0
;----------------- Profile of pressure in z direction -----------------
def prof
  z_step = CH / nslice
  loop n (1,nslice)
    ytable(1,n)     = 0     ; accumulates count
    ytable(nsnap,n) = 0.0   ; accumulates pressure
```

```
    zmin = (n-1)*z_step
    zmax = n*z_step
    loop k(1,dommax)
      zz = mem(dom(k)+DOM_Z)
      if zz > zmin
        if zz < zmax
          ytable(nsnap,n) = ytable(nsnap,n) + mem(dom(k)+DOM_PRESS)
          ytable(1,n) = ytable(1,n) + 1
        endif
      endif
    endloop
    ytable(nsnap,n) = ytable(nsnap,n)/ytable(1,n)
    xtable(nsnap,n) = zmin + z_step/2.0
  endloop
  command
    plot add table nsnap line xmin 0.5 xmax 9.5 ymin 0 ymax 1.0
  endcommand
end
;----------------- Flow & Pressure calculation -----------------------
set nslice = 10
cycle 5000
set nsnap = 2
prof
cycle 5000
set nsnap = 3
prof
cycle 5000
set nsnap=4
prof
cycle 5000
set nsnap=5
prof
cycle 5000
set nsnap=6
prof
cycle 5000
set nsnap=7
prof
cycle 5000
set nsnap=8
prof
```

```
cycle 70000
set nsnap=9
prof
;
; ------------------------------------------------------------
def setTime
  oldtime = clock
end
def getTime
  getTime = float(clock-oldTime)/100.0
end
setTime
cycle 20000
print getTime
plo sho
save darcy_fis14_3.sav
ret
; EOF: darcy_fis_3.dat
```

Appendix C – Fish Routines used during the hydraulic fracturing tests

```
;fname: Hydrofrac_1.DAT Creation and packing of particles - triaxial sample
;
new
SET random ; reset random-number generator
; ------------------------------------------------
def make_walls ; create walls: a cylinder and two plates
          extend = 0.1
          rad_cy = 0.5*width
          w_stiff= 9.4e10
          _x0 = width/2.0
          _y0 = width/2.0
          _z0 = -extend
       _x1 = width/2.0
          _y1 = width/2.0
          _z1 = height
          _x2 = -width/2.0
          _y2 = width/2.0
          _z2 = height
          _x3 = -width/2.0
          _y3 = width/2.0
          _z3 = -extend
       command
                    wall id=1 kn=w_stiff ks=w_stiff face (_x0,_y0,_z0) (_x1,_y1,_z1)
(_x2,_y2,_z2) &
                    (_x3,_y3,_z3)
          end_command
       _x0 = -width/2.0
          _y0 = width/2.0
          _z0 = -extend
       _x1 = -width/2.0
          _y1 = width/2.0
          _z1 = height
          _x2 = -width/2.0
```

```
        _y2 = -width/2.0
        _z2 = height
        _x3 = -width/2.0
        _y3 = -width/2.0
        _z3 = -extend
      command
                wall id=2 kn=w_stiff ks=w_stiff face (_x0,_y0,_z0) (_x1,_y1,_z1)
(_x2,_y2,_z2) &
                (_x3,_y3,_z3)
        end_command
      _x0 = -width/2.0
        _y0 = -width/2.0
        _z0 = -extend
      _x1 = -width/2.0
        _y1 = -width/2.0
        _z1 = height
        _x2 = width/2.0
        _y2 = -width/2.0
        _z2 = height
        _x3 = width/2.0
        _y3 = -width/2.0
        _z3 = -extend
      command
                wall id=3 kn=w_stiff ks=w_stiff face (_x0,_y0,_z0) (_x1,_y1,_z1)
(_x2,_y2,_z2) &
                (_x3,_y3,_z3)
        end_command
      _x0 = width/2.0
        _y0 = -width/2.0
        _z0 = -extend
      _x1 = width/2.0
        _y1 = -width/2.0
        _z1 = height
        _x2 = width/2.0
        _y2 = width/2.0
        _z2 = height
        _x3 = width/2.0
        _y3 = width/2.0
        _z3 = -extend
      command
```

```
                wall id=4 kn=w_stiff ks=w_stiff face (_x0,_y0,_z0) (_x1,_y1,_z1)
(_x2,_y2,_z2) &
                (_x3,_y3,_z3)
        end_command
    _x0 = width*(1.0 + extend)/2.0
        _y0 = width*(1.0 + extend)/2.0
        _z0 = 0.0
        _x1 = -width*(1.0 + extend)/2.0
        _y1 = width*(1.0 + extend)/2.0
        _z1 = 0.0
        _x2 = -width*(1.0 + extend)/2.0
        _y2 = -width*(1.0 + extend)/2.0
        _z2 = 0.0
        _x3 = width*(1.0 + extend)/2.0
        _y3 = -width*(1.0 + extend)/2.0
        _z3 = 0.0
        command
                wall id=5 kn=w_stiff ks=w_stiff face (_x0,_y0,_z0) (_x1,_y1,_z1)
(_x2,_y2,_z2) &
                (_x3,_y3,_z3)
        end_command
        _x0 = width*(1.0 + extend)/2.0
        _y0 = -width*(1.0 + extend)/2.0
        _z0 = height
        _x1 = -width*(1.0 + extend)/2.0
        _y1 = -width*(1.0 + extend)/2.0
        _z1 = height
        _x2 = -width*(1.0 + extend)/2.0
        _y2 = width*(1.0 + extend)/2.0
        _z2 = height
        _x3 = width*(1.0 + extend)/2.0
        _y3 = width*(1.0 + extend)/2.0
        _z3 = height
        command
                wall id=6 kn=w_stiff ks=w_stiff face (_x0,_y0,_z0) (_x1,_y1,_z1)
(_x2,_y2,_z2) &
                (_x3,_y3,_z3)
        end_command
    _z0 = height_well*(1.0 + extend)
        _z1 = height*(1.0 + extend)
        command
```

```
                wall type=cylinder id=7 kn=w_stiff end1 0.0 0.0 _z0 end2 0.0 0.0
_z1 &
                rad well_rad well_rad
        end_command
end
; -----------------------------------------------------
def assemble ; assemble sample
        s_stiff=4.0e10 ; initial stiffnesses
        n_stiff=9.4e10
        tot_vol = (height * width^2.0) - (height_well*pi*well_rad^2)
        rbar = 0.5 * (rlo + rhi)
        num = int((1.0 - poros) * tot_vol / (4.0 / 3.0 * pi * rbar^3))
        mult = 1.6 ; initial radius multiplication factor
        rlo_0 = rlo / mult
        rhi_0 = rhi / mult
        command
                gen id=1,num rad=rlo_0,rhi_0 x=-1.7145,1.7145 y=-1.7145,1.7145
z=0.0,height &
                filter ff_cylinder
                prop dens=1.25 ks=s_stiff kn=n_stiff
        end_command
        ii = out(string(num)+' particles were created')
        sum = 0.0 ; get actual porosity
        bp = ball_head
        loop while bp # null
                sum = sum + 4.0 / 3.0 * pi * b_rad(bp)^3
                bp = b_next(bp)
        end_loop
        pmeas = 1.0 - sum / tot_vol
        mult = ((1.0 - poros) / (1.0 - pmeas))^(1.0/3.0)
        command
                ini rad mul mult
                cycle 1000
                prop ks=1e10 fric 0.25
                cycle 250
        end_command
end
; -----------------------------------------------------
def cws ; change lateral wall stiffnesses
        command
                wall type cylinder id 7 kn=w_stiff
```

```
        end_command
end
; ------------------------------------------------
def ff_cylinder
        ff_cylinder = 0
        _brad = fc_arg(0)
        _bx = fc_arg(1)
        _by = fc_arg(2)
        _bz = fc_arg(3)
        _rad = sqrt(_bx^2 + _by^2)
        if _rad - _brad < well_rad then
        ff_cylinder = 1
        end_if
end
; ------------------------------------------------
macro zero 'ini xvel 0 yvel 0 zvel 0 xspin 0 yspin 0 zspin 0'
SET height=4.572 width=3.429 rlo=0.15 rhi=0.21 poros=0.30
SET height_well= 2.286 well_rad=0.1143
make_walls
assemble
SET w_stiff= 9.4e9 ; make lateral wall stiffness=1/10 of ball stiffness
cws
cyc 500
zero
plot create assembly
plot set cap size 25
plot set mag 1.5
plot set rot 30 0 40
plot add ball lorange
plot show
save hydro_ass.SAV
return
```

;fname: **Hydrofrac2.DAT** Servo-control and initial stress state - triax sample

```
res hydro_ass.SAV ; restore compacted assembly
; ------------------------------------------------
def get_ss ; determine average stress and strain at walls
      xdif = w_x(wadd4) - w_x(wadd2)
      ydif = w_y(wadd1) - w_y(wadd3)
      zdif = w_z(wadd6) - w_z(wadd5)
```

```
      new_widthx = width + xdif
      new_widthy = width + ydif
      new_height = height + zdif
      wsxx = 0.5*(w_xfob(wadd2) - w_xfob(wadd4)) / (new_widthy*new_height)
      wsyy = 0.5*(w_yfob(wadd3) - w_yfob(wadd1)) / (new_widthx*new_height)
      wszz = 0.5*(w_zfob(wadd5) - w_zfob(wadd6)) / (new_widthx*new_widthy)
      ii = out('sigma x=' + string(wsxx))
      ii = out('sigma y=' + string(wsyy))
      ii = out('sigma z=' + string(wszz))
         wexx = 2.0 * xdif / (width + new_widthx)
      weyy = 2.0 * ydif / (width + new_widthy)
      wezz = 2.0 * xdif / (height + new_height)
         wevol = wexx + weyy + wezz
end
; ------------------------------------------------
def get_gain ; determine servo gain parameters for axial and lateral motion
         alpha = 0.1 ; relaxation factor
         count_x = 0
      count_y = 0
      count_z = 0
         avg_stiff = 0.0
         cp = contact_head ; ---------find avg. number of contacts on walls perpend.
to x ---------------
         loop while cp # null
                  if c_gobj2(cp) = wadd2
                           count_x = count_x + 1
                           avg_stiff = avg_stiff + c_kn(cp)
                  end_if
            if c_gobj2(cp) = wadd4
                           count_x = count_x + 1
                           avg_stiff = avg_stiff + c_kn(cp)
                  end_if
                  cp = c_next(cp)
         end_loop
         ncount_x = count_x / 2.0
         avg_stiff = avg_stiff / count_x
         gx = alpha * height * width / (avg_stiff * ncount_x * tdel)
      ; ------------------------- find avg. number of contacts on walls perpend. to y --
-------------
         avg_stiff = 0.0
         cp = contact_head
```

```
        loop while cp # null
                if c_gobj2(cp) = wadd3
                        count_y = count_y + 1
                        avg_stiff = avg_stiff + c_kn(cp)
                end_if
                if c_gobj2(cp) = wadd1
                        count_y = count_y + 1
                        avg_stiff = avg_stiff + c_kn(cp)
                end_if
                cp = c_next(cp)
        end_loop
        ncount_y = count_y / 2.0
        avg_stiff = avg_stiff / count_y
        gy = alpha * height * width / (avg_stiff * ncount_y * tdel)
    ; ------------------------ find avg. number of contacts on walls perpend. to z ---
----------
        avg_stiff = 0.0
    cp = contact_head
        loop while cp # null
                if c_gobj2(cp) = wadd5
                        count_z = count_z + 1
                        avg_stiff = avg_stiff + c_kn(cp)
                end_if
                if c_gobj2(cp) = wadd6
                        count_z = count_z + 1
                        avg_stiff = avg_stiff + c_kn(cp)
                end_if
                cp = c_next(cp)
        end_loop
        ncount_z = count_z / 2.0
        avg_stiff = avg_stiff / count_z
        gz = alpha * width^2.0/ (avg_stiff * ncount_z * tdel)
end
; -------------------------------------------------
def servo
        while_stepping
    if iter_switch = 1
         get_ss ; compute stresses & strains
         udx = gx * (wsxx - sxxreq)
      udy = gy * (wsyy - syyreq)
         w_xvel(wadd4) = -udx
```

```
        w_xvel(wadd2) = udx
        w_yvel(wadd1) = -udy
        w_yvel(wadd3) = udy
           if z_servo = 1 ; switch stress servo on or off
                 udz = gz * (wszz - szzreq)
                 w_zvel(wadd5) = udz
                 w_zvel(wadd6) = -udz
           end_if
      endif
end
; ---------------------------------------------------
def iterate
  if iter_switch = 1
        loop while 1 # 0
                 get_gain
                 if abs((wsxx - sxxreq)/sxxreq) < sig_tol then
                          if abs((wsyy - syyreq)/syyreq) < sig_tol then
                                   if abs((wszz - szzreq)/szzreq) < sig_tol then
                                       exit
                                end_if
                          end_if
                 end_if
                 command
                          cycle 100
                 end_command
        end_loop
  endif
end
; ---------------------------------------------------
def wall_addr
        wadd1 = find_wall(1)
        wadd2 = find_wall(2)
        wadd3 = find_wall(3)
        wadd4 = find_wall(4)
        wadd5 = find_wall(5)
        wadd6 = find_wall(6)
      ;wadd7 = find_wall(7)
end
; ---------------------------------------------------
wall_addr
zero
```

```
SET iter_switch = 1
SET    sxxreq=-20.69e6        syyreq=-13.80e6    szzreq=-31.03e6    sig_tol=0.005
z_servo=1
iterate ; get all stresses to requested state
sav hydro_str.SAV
return
```

; FNAME: **Hydrofrac3.dat**

```
new
res hydro_str.SAV
SET iter_switch = 0
;
prop fric 0.55
hist diagnostic muf
hist diagnostic mcf
save hydro_preflt.sav
set alpha=0.1
call pcflt_3.fis
;prop s_bond 1.0e15 n_bond 1.0e15
prop pb_nstren=68.96e10 pb_sstren=82.37e10 pb_rad=0.1 fric=0.55
prop pb_kn=9.8e10 pb_ks=4.3e10
ini xv 0 yv 0 zv 0 xspin 0 yspin 0 zspin 0
SET iter_switch = 1
SET    sxxreq=-20.69e6        syyreq=-13.80e6    szzreq=-31.03e6    sig_tol=0.005
z_servo=1
step 10000
SET iter_switch = 0
prop pb_nstren=137.93e6 pb_sstren=164.74e6 pb_rad=0.15 fric=0.55
;
;--- Fixing the particles along  all the walls  ---------------------------
def test
  bp = ball_head
  loop while bp # null
    b_zfix(bp) = 0
    b_color(bp)= 0
    section
      cp = b_clist(bp)
      loop while cp # null
        b2 = c_gobj2(cp)
```

```
      if pointer_type(b2) = 101 then
        b_xfix(bp) = 1
        b_yfix(bp) = 1
        b_zfix(bp) = 1
        b_color(bp) = 1
        exit section
      endif
      if c_gobj1(cp) = bp
        cp = c_go1clist(cp)
      else
        cp = c_go2clist(cp)
      endif
    endLoop
  end_section
  bp = b_next(bp)
 endLoop
end
; ------------------------------------------------------------
test
; Replace unbalanced forces with applied forces -------------
def replace
 bp = ball_head
 loop while bp # null
  if b_xfix(bp) = 1
    b_xfap(bp) = -b_xfob(bp)
    b_yfap(bp) = -b_yfob(bp)
    b_zfap(bp) = -b_zfob(bp)
  endif
 bp = b_next(bp)
 end_loop
end
; ------------------------------------------------------------
replace
;del wall 5
;del wall 6
del wall 7
;
;del wall 1
;del wall 2
;del wall 3
;del wall 4
```

```
step 10000
ini xv 0 yv 0 zv 0 xspin 0 yspin 0 zspin 0
call fishcall.fis
call crk.fis
crk_init
plot create qqq
plot add ball red lred
plot show
save hydro_bhx.sav
ret
; EOF: bhx_3.dat
```

; FNAME: **HYDRO_DOM_3.FIS** → Same file named DOM_3.FIS, listed in Appendix B

; FNAME: **HYDRO_DOM_1_3.FIS** → Same file named DOM_1_3.FIS, listed in Appendix B

```
; FNAME: inject_hydro.dat
new
rest hydro_dom1.sav
plo crea pres
plo show
plot set distance=15.0
plot add axes black
plo add fish pressure white
;plot set back=white
;plo add cforce yellow cyan
set crk_ctype=0
set ap_zero=0.01 perm=0.05 gap_mul=0.0 Fap_zero=1e10
set bulk_w=2.15e9 flow_dt=0.1
find_flow_dt
flow_props
```

```
make_walls
wall_addr
set iter_switch = 0
; -------------------------------------------------------------
ini xvel 0 yvel 0 zvel 0 xs 0 ys 0 zs 0
plo add fish crk_item white black blue red
save inject_hydro_ini1.sav              ; ****************SAVING MODEL
; -------------------------------------------------------------
prop pb_nstrength=103.44e6 pb_sstrength=123.55e6 pb_rad=0.15 fric=0.55
prop pb_kn=1.2e11 pb_ks=5.26e10
set flow_set=3 p_given=0.0; ----- Setting Pp=0.0 Mpa
set x1_bc=-1.7145 x2_bc=1.7145
set y1_bc=-1.7145 y2_bc=1.7145
set z1_bc=0 z2_bc=4.572
flow_bc
set flow_set=2              ; ----- Setting all Pp free to change
flow_bc
set flow_set=1              ; ----- Fixing Pp
set x1_bc=-0.2286 x2_bc=0.2286
set y1_bc=-0.2286 y2_bc=0.2286
set z1_bc=2.26  z2_bc=4.572
flow_bc                     ; ----- Setting higher Pp=500 psi at the wellface
set flow_set=3 p_given=3.448e6
flow_bc ; pressure
set gap_mul=0.02
set t_time = 0.0
save inject_hydro_pre500.sav                ; ****************SAVING MODEL
hist id=30 crk_num
hist id=31 crk_num_pnf
hist id=32 crk_num_psf
hist id=33 t_time
cyc 1000000
save  inject_hydro_after500.sav                         ;  ****************SAVING
MODEL
ret
; EOF: inject_hydro.dat
```

Appendix D – Results of numerical experiments using the field model

	INPUT			OUTPUT				
Test number	ΔP, (psi)	ΔP, MPa	Viscosity, cP	Tensile cracks		Shear cracks		Total number of cracks
				number	percentage (%)	number	percentage (%)	
8-1	100	0.689	1	356	27.75	927	72.25	1283
8-2	100	0.689	200	722	35.92	1288	64.08	2010
8-3	100	0.689	500	680	38.27	1097	61.73	1777
8-4	100	0.689	1000	690	38.83	1087	61.17	1777
8-5	500	3.448	1	367	31.31	805	68.69	1172
8-6	500	3.448	200	748	35.47	1361	64.53	2109
8-7	500	3.448	500	700	37.61	1161	62.39	1861
8-8	500	3.448	1000	683	38.57	1088	61.43	1771
8-9	1,000	6.896	1	709	38.41	1137	61.59	1846
8-10	1,000	6.896	200	757	36.06	1342	63.94	2099
8-11	1,000	6.896	500	697	38.00	1137	62.00	1834
8-12	1,000	6.896	1000	706	39.00	1122	61.00	1828
8-13	2,500	17.241	1	809	41.02	1163	58.98	1972
8-14	2,500	17.241	200	808	37.92	1323	62.08	2131
8-15	2,500	17.241	500	835	40.32	1236	59.68	2071
8-16	2,500	17.241	1000	810	40.97	1167	59.03	1977

Table D-0-1. Results of the numerical experiments performed on the field model

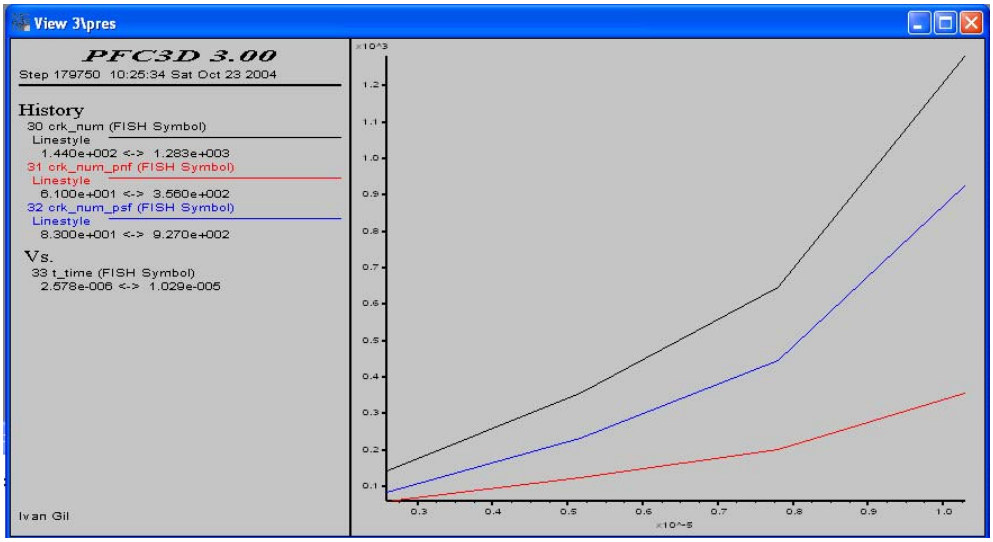

Figure D-1. Number of cracks vs. time (red → tensile & blue → shear), ΔP = 0.689 MPa= 100 psi & μ = 1 mPa.sec = 1 cP (Test 8-1).

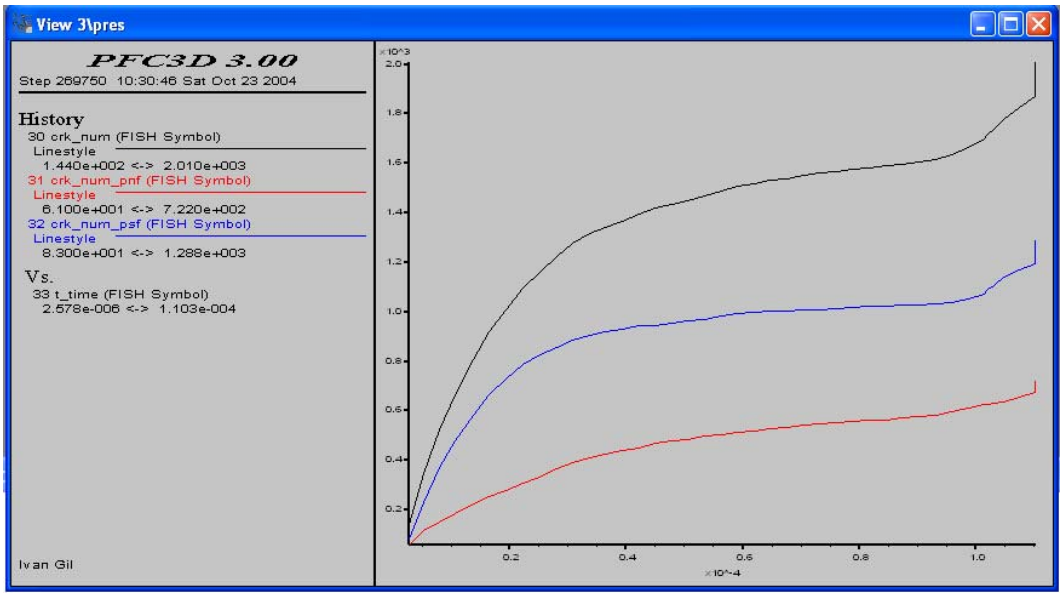

Figure D-2. Number of cracks vs. time (red → tensile & blue → shear), ΔP = 0.689 MPa= 100 psi & μ = 200 mPa.sec = 200 cP (Test 8-2).

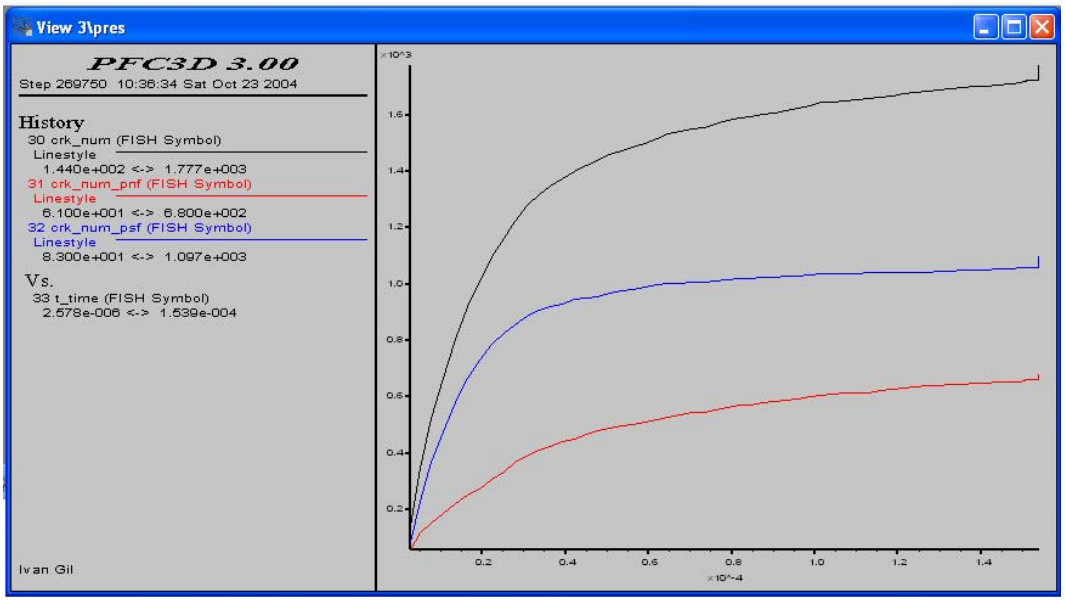

Figure D-3. Number of cracks vs. time (red → tensile & blue → shear), ΔP = 0.689 MPa= 100 psi & μ = 500 mPa.sec = 500 cP (Test 8-3).

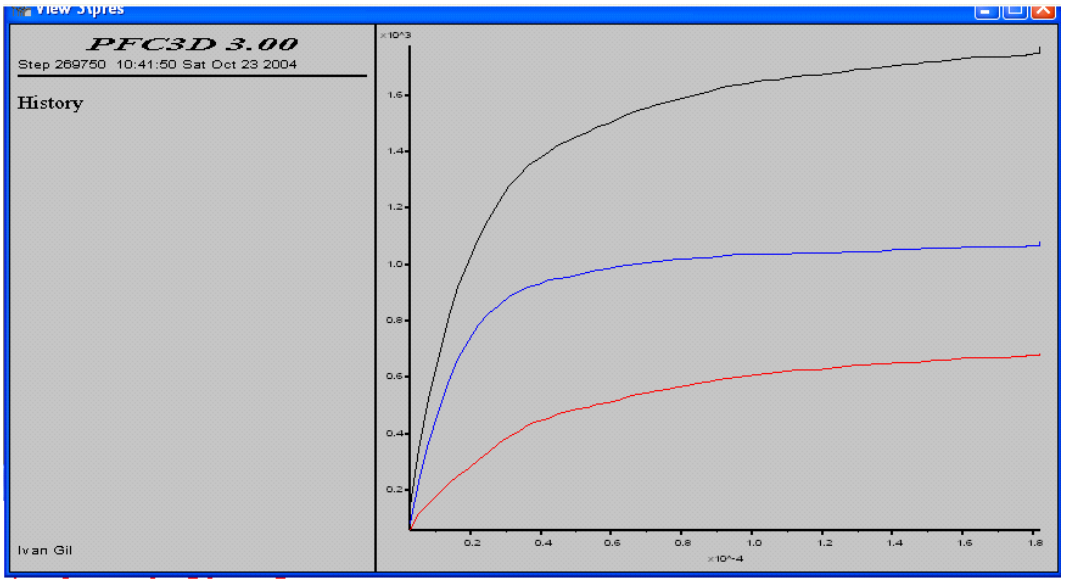

Figure D-4. Number of cracks vs. time (red → tensile & blue → shear), ΔP = 0.689 MPa= 100 psi & μ = 1,000 mPa.sec = 1,000 cP (Test 8-4).

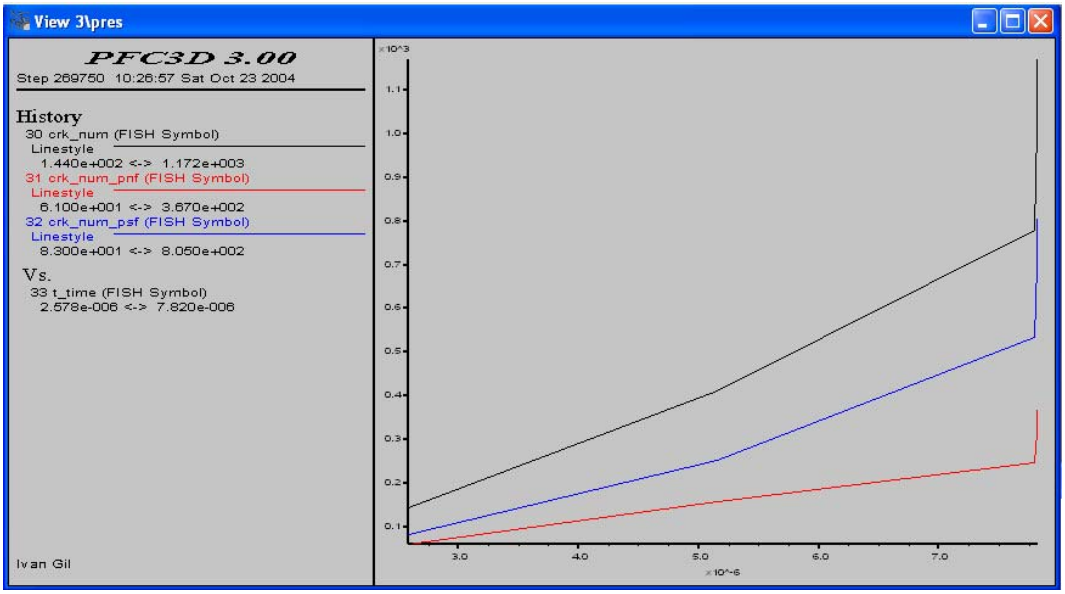

Figure D-5. Number of cracks vs. time (red → tensile & blue → shear), ΔP = 3.448 MPa= 500 psi & μ = 1 mPa.sec = 1 cP (Test 8-5).

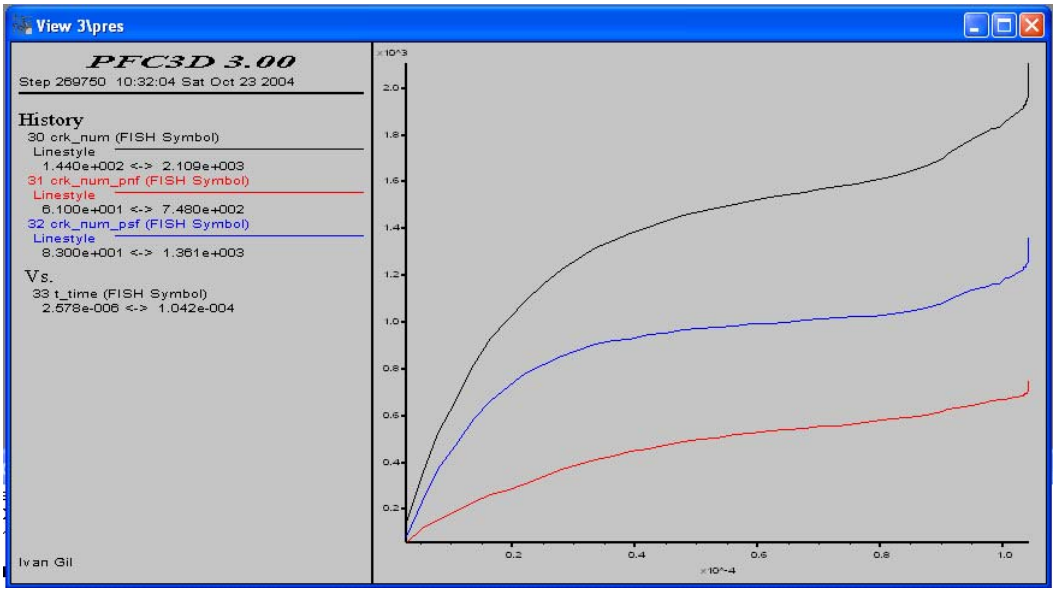

Figure D-6. Number of cracks vs. time (red → tensile & blue → shear), ΔP = 3.448 MPa= 500 psi & μ = 200 mPa.sec = 200 cP (Test 8-6).

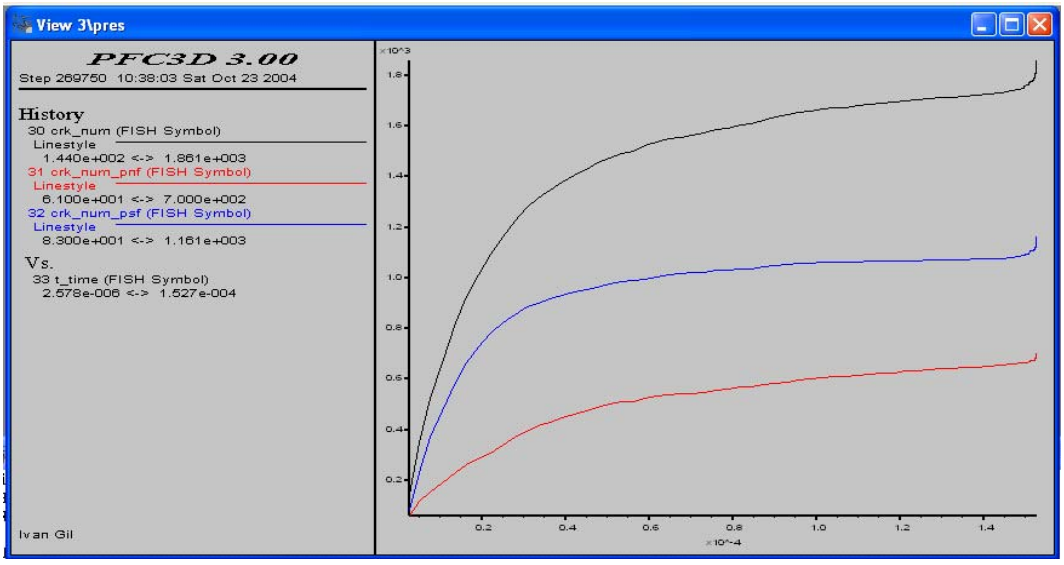

Figure D-7. Number of cracks vs. time (red → tensile & blue → shear), ΔP = 3.448 MPa= 500 psi & μ = 500 mPa.sec = 500 cP (Test 8-7).

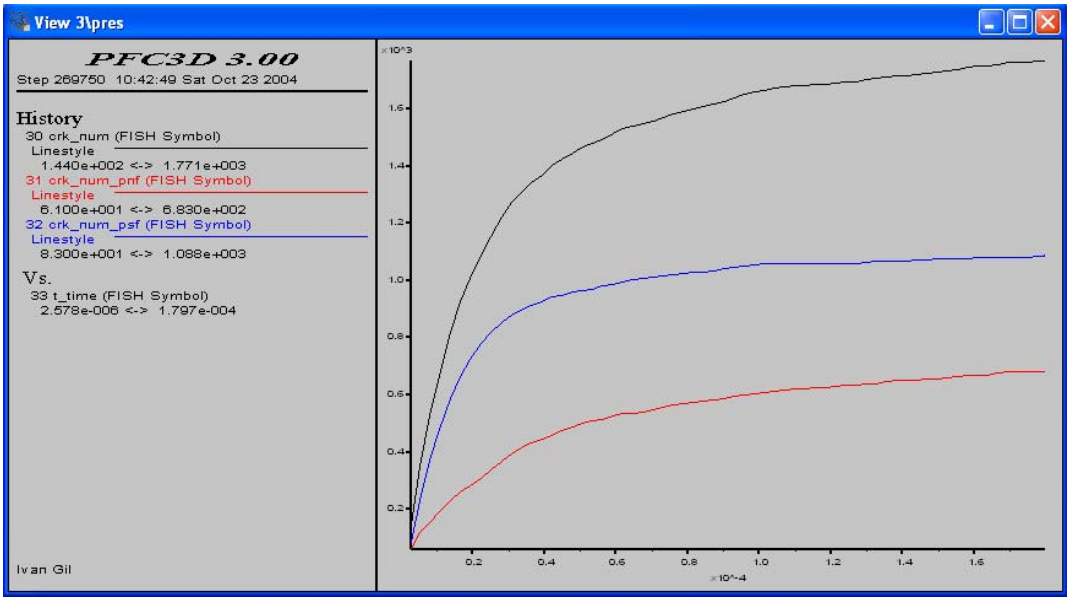

Figure D-8. Number of cracks vs. time (red → tensile & blue → shear), ΔP = 3.448 MPa= 500 psi & μ = 1,000 mPa.sec = 1,000 cP (Test 8-8).

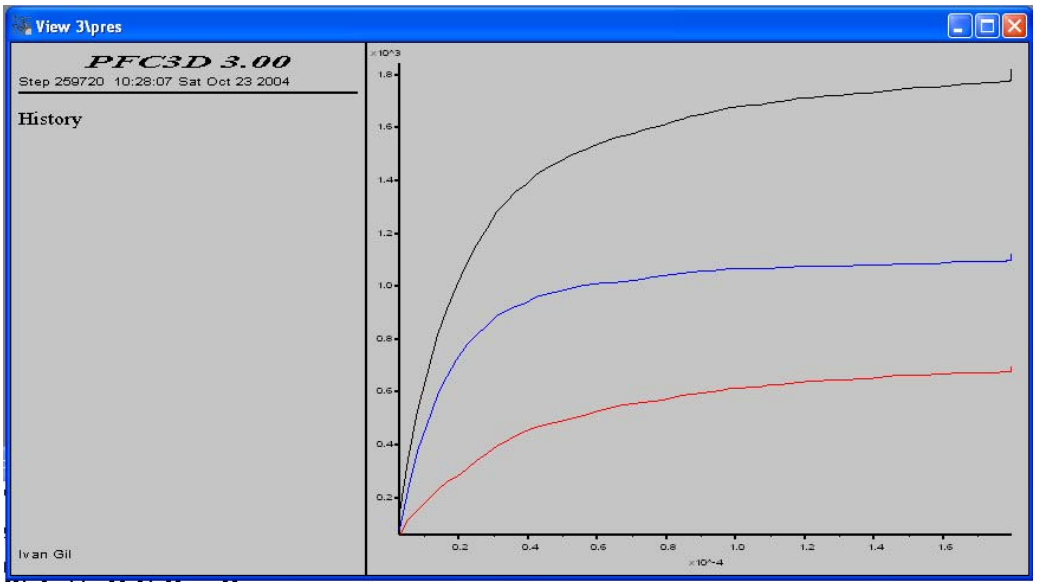

Figure D-9. Number of cracks vs. time (red → tensile & blue → shear), ΔP = 6.896 MPa= 1,000 psi & μ = 1 mPa.sec = 1 cP (Test 8-9).

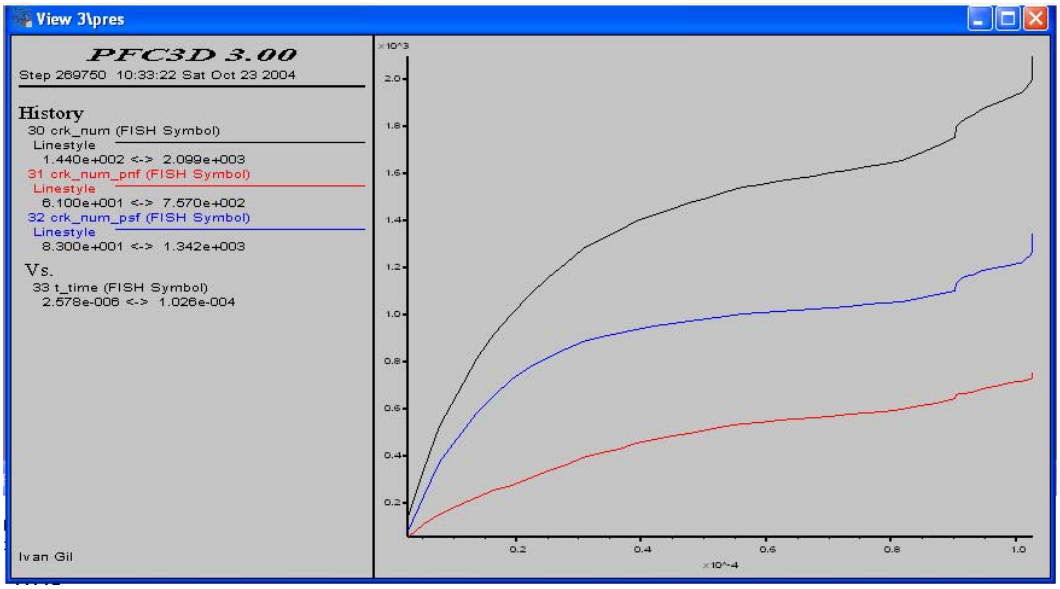

Figure D-10. Number of cracks vs. time (red → tensile & blue → shear), ΔP = 6.896 MPa= 1,000 psi & μ = 200 mPa.sec = 200 cP (Test 8-10).

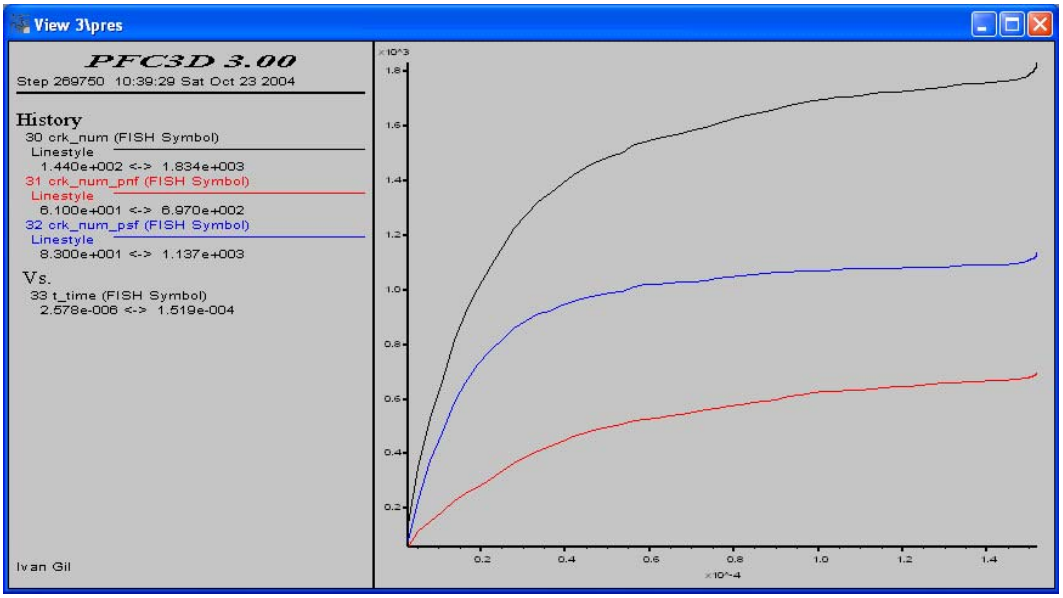

Figure D-11. Number of cracks vs. time (red → tensile & blue → shear), ΔP = 6.896 MPa= 1,000 psi & μ = 500 mPa.sec = 500 cP (Test 8-11).

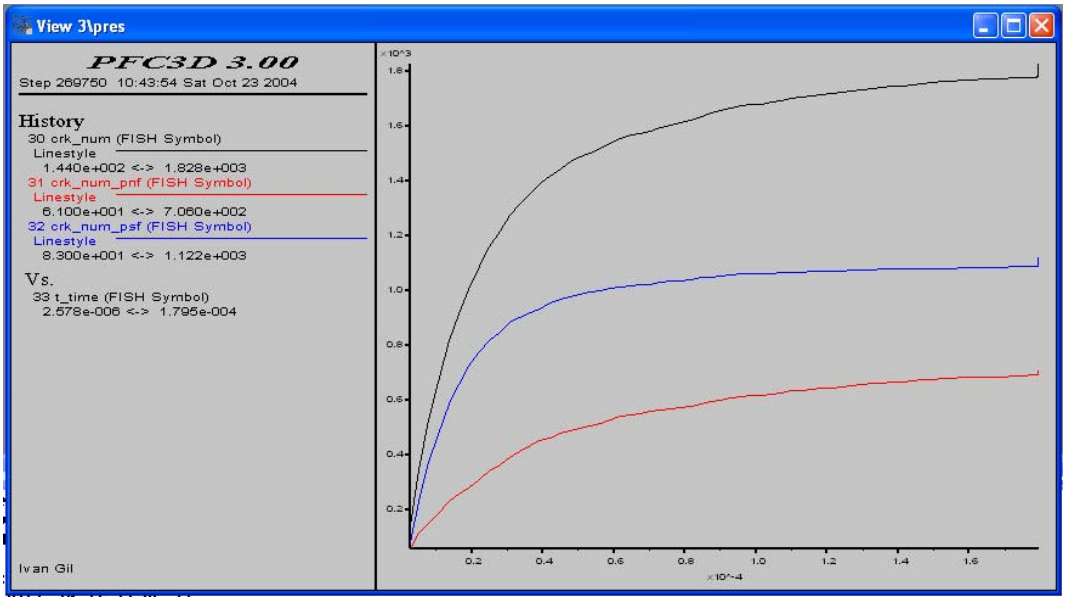

Figure D-12. Number of cracks vs. time (red → tensile & blue → shear), ΔP = 6.896 MPa= 1,000 psi & μ = 1,000 mPa.sec = 1,000 cP (Test 8-12).

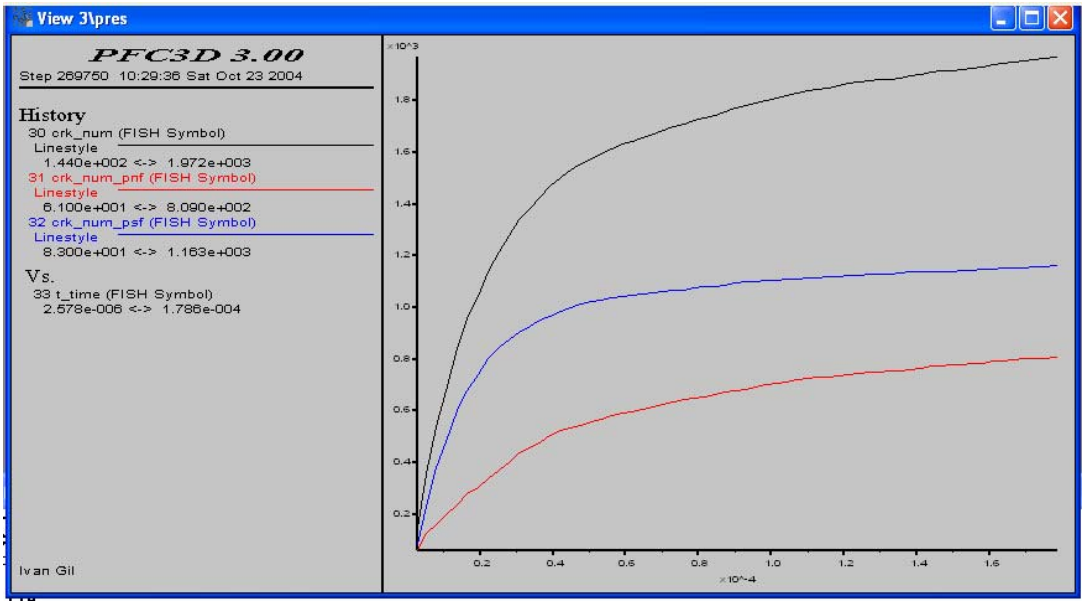

Figure D-13. Number of cracks vs. time (red → tensile & blue → shear), ΔP = 17.241 MPa= 2,500 psi & μ = 1 mPa.sec = 1 cP (Test 8-13).

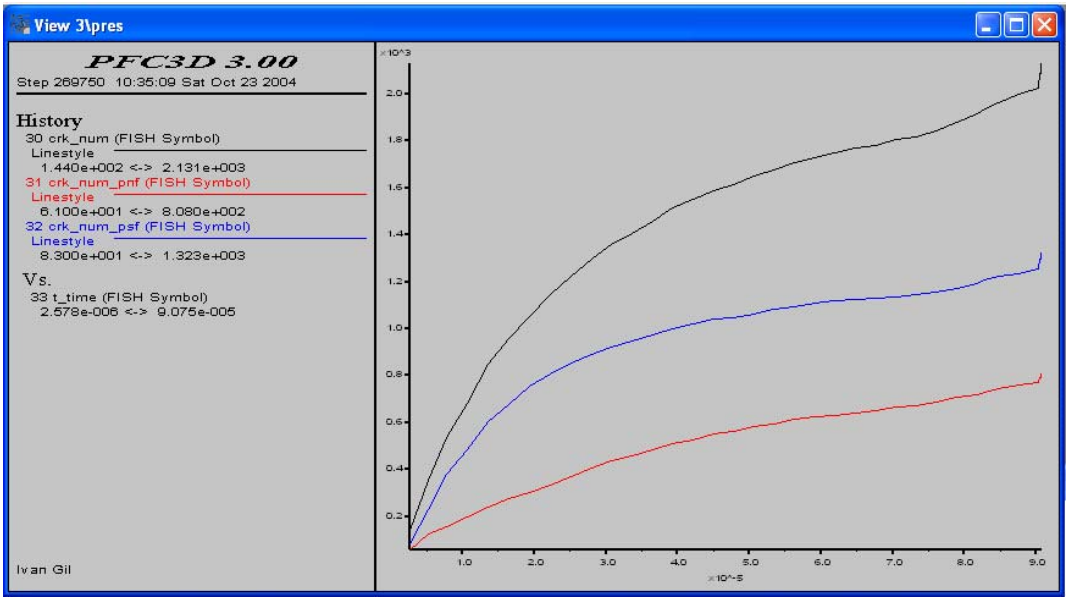

Figure D-14. Number of cracks vs. time (red → tensile & blue → shear), ΔP = 17.241 MPa= 2,500 psi & μ = 200 mPa.sec = 200 cP (Test 8-14).

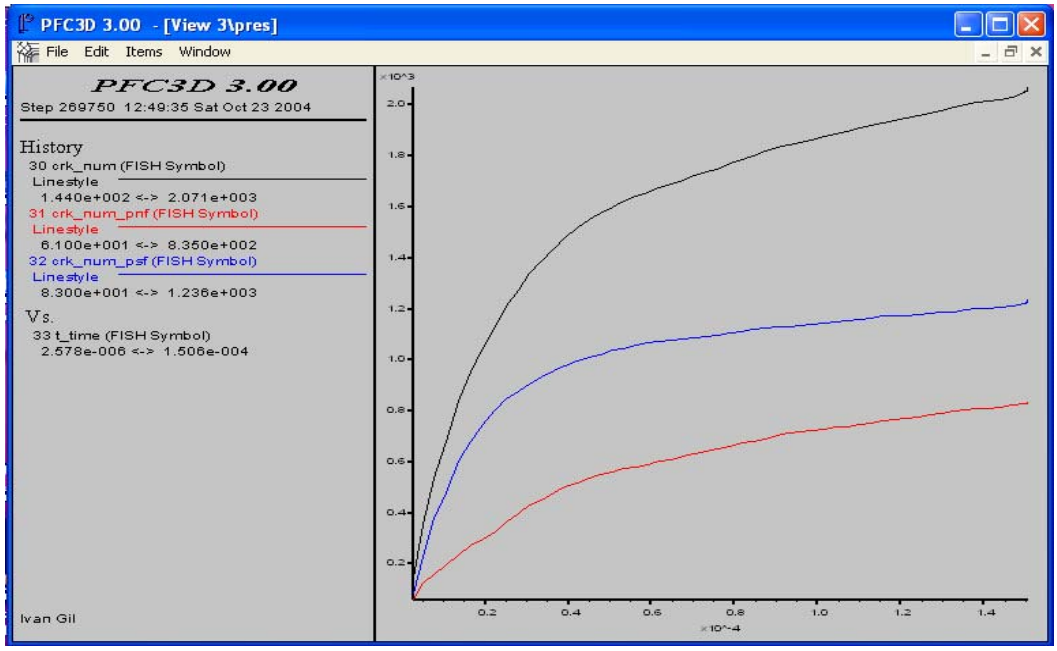

Figure D-15. Number of cracks vs. time (red → tensile & blue → shear), ΔP = 17.241 MPa= 2,500 psi & μ = 500 mPa.sec = 500 cP (Test 8-15).

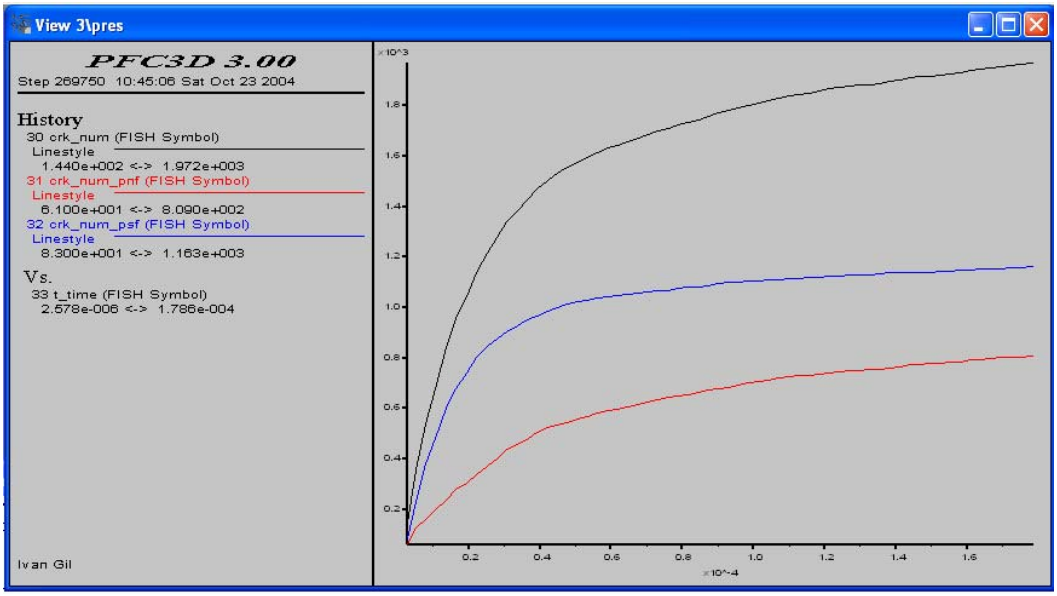

Figure D-16. Number of cracks vs. time (red → tensile & blue → shear), ΔP = 17.241 MPa= 2,500 psi & μ = 1,000 mPa.sec = 1,000 cP (Test 8-16).